Measurements and modeling of ozone fluxes in and above Norway spruce canopies

Dissertation
zur Erlangung des Grades
„Doktor der Naturwissenschaften“

am Fachbereich Physik, Mathematik und Informatik
der Johannes Gutenberg Universität
in Mainz

Linda Voß

geb. in Oldenburg (Oldb.)
Mainz, den 28. April 2015

Datum der mündlichen Prüfung: 29. Juli 2015
D77 – Mainzer Dissertationen

Abstract

Ozone (O_3) is an important oxidation and greenhouse gas in the Earth's atmosphere, having an influence on climate and air quality, affecting human health and vegetation. Ecosystems like forest canopies are sinks for tropospheric ozone. In a future climate system forests will be more heterogeneous due to wind, pests and changes in land use. These heterogeneities are assumed to decrease the uptake of greenhouse gases by an ecosystem with significant feedback on the climate system. The atmosphere-biosphere exchange of ozone is controlled by stomatal uptake, deposition to plant surfaces and soil, as well as chemical transformations. Understanding these processes and quantifying the ozone exchange for different ecosystem types are prerequisites to upscale from local measurements towards regional ozone fluxes.

Vertical turbulent ozone fluxes are measured by the eddy-covariance technique. In order to ensure high quality fluxes obtained with closed-path eddy-covariance systems based upon a fast chemiluminescence ozone sensor, side-by-side measurements have been performed to provide insight to factors affecting ozone flux estimates. Systematic differences between individual sensors and the impact of different sampling tube lengths were investigated by analyzing frequency spectra and determining correction factors for the ozone fluxes with the cospectral correction method. The experimentally determined correction factors were found to show no significant difference to correction factors determined from theoretic transfer functions, which verified the applicability of the theoretic factors for the correction of ozone fluxes.

In summer 2011, measurements have been performed in the frame of the EGER (ExchanGE processes in mountainous Regions) project to contribute to a better understanding of the atmosphere-biosphere ozone exchange in disturbed ecosystems. Ozone fluxes have been measured on both sides of a forest edge separating a Norway spruce canopy and a wind-throw area in the mountains of the Fichtelgebirge, South-East Germany. On the road-like clearing, generated by the winter storm "Kyrill" (2007), secondary vegetation developed, which differed in its phenology and leaf physiology from the original Norway spruce. The averaged nighttime flux above the spruce forest was -6 to -7 nmol m^{-2} s^{-1} and decreased to -13 nmol m^{-2} s^{-1} around noon. The measured ozone fluxes showed a strong dependency on canopy transpiration and CO_2 assimilation, indicating that during daytime most ozone was absorbed by plant stomata. The relatively large nighttime deposition was caused by non-stomatal deposition. The deposition above the forest was about twice as high as above the clearing over the entire diel cycle, which agrees with the ratio of the plant area indices (PAI) measured during EGER-IOP3. Thus, the disturbance of the ecosystem reduced the capability of the canopy to act as a sink for tropospheric ozone. The significant differences between ozone depositions for the two canopy types have challenging implications for the regionalization of ozone fluxes for heterogeneously forested areas.

Furthermore, the experimental results have been compared to simulations with the chemistry model MLC-CHEM. In order to evaluate the model regarding the calculation of ozone fluxes, measured and modeled fluxes at two positions within the EGER site have been used. Although the order of magnitude of the fluxes agreed, the results showed a significant difference between measured and modeled fluxes. Moreover, there was a clear dependency of the difference between measurement and modeling on relative humidity, with decreasing difference with increasing relative humidity, showing that the model needs further improvement in advance of a more extensive use for ozone flux modeling studies.

Zusammenfassung

Ozon (O_3) ist ein wichtiges Oxidierungs- und Treibhausgas in der Erdatmosphäre. Es hat Einfluss auf das Klima, die Luftqualität sowie auf die menschliche Gesundheit und die Vegetation. Ökosysteme, wie beispielsweise Wälder, sind Senken für troposphärisches Ozon und werden in Zukunft, bedingt durch Stürme, Pflanzenschädlinge und Änderungen in der Landnutzung, heterogener sein. Es ist anzunehmen, dass diese Heterogenitäten die Aufnahme von Treibhausgasen verringern und signifikante Rückkopplungen auf das Klimasystem bewirken werden. Beeinflusst wird der Atmosphären-Biosphären-Austausch von Ozon durch stomatäre Aufnahme, Deposition auf Pflanzenoberflächen und Böden sowie chemische Umwandlungen. Diese Prozesse zu verstehen und den Ozonaustausch für verschiedene Ökosysteme zu quantifizieren sind Voraussetzungen, um von lokalen Messungen auf regionale Ozonflüsse zu schließen.
Für die Messung von vertikalen turbulenten Ozonflüssen wird die Eddy Kovarianz Methode genutzt. Die Verwendung von Eddy Kovarianz Systemen mit geschlossenem Pfad, basierend auf schnellen Chemilumineszenz-Ozonsensoren, kann zu Fehlern in der Flussmessung führen. Ein direkter Vergleich von nebeneinander angebrachten Ozonsensoren ermöglichte es einen Einblick in die Faktoren zu erhalten, die die Genauigkeit der Messungen beeinflussen. Systematische Unterschiede zwischen einzelnen Sensoren und der Einfluss von unterschiedlichen Längen des Einlassschlauches wurden untersucht, indem Frequenzspektren analysiert und Korrekturfaktoren für die Ozonflüsse bestimmt wurden. Die experimentell bestimmten Korrekturfaktoren zeigten keinen signifikanten Unterschied zu Korrekturfaktoren, die mithilfe von theoretischen Transferfunktionen bestimmt wurden, wodurch die Anwendbarkeit der theoretisch ermittelten Faktoren zur Korrektur von Ozonflüssen bestätigt wurde.
Im Sommer 2011 wurden im Rahmen des EGER (ExchanGE processes in mountainous Regions) Projektes Messungen durchgeführt, um zu einem besseren Verständnis des Atmosphären-Biosphären Ozonaustauschs in gestörten Ökosystemen beizutragen. Ozonflüsse wurden auf beiden Seiten einer Waldkante gemessen, die einen Fichtenwald und einen Windwurf trennt. Auf der straßenähnlichen Freifläche, die durch den Sturm "Kyrill" (2007) entstand, entwickelte sich eine Sekundärvegetation, die sich in ihrer Phänologie und Blattphysiologie vom ursprünglich vorherrschenden Fichtenwald unterschied. Der mittlere nächtliche Fluss über dem Fichtenwald war -6 bis -7 nmol m^{-2} s^{-1} und nahm auf -13 nmol m^{-2} s^{-1} um die Mittagszeit ab. Die Ozonflüsse zeigten eine deutliche Beziehung zur Pflanzenverdunstung und CO_2 Aufnahme, was darauf hinwies, dass während des Tages der Großteil des Ozons von den Pflanzenstomata aufgenommen wurde. Die relativ hohe nächtliche Deposition wurde durch nicht-stomatäre Prozesse verursacht. Die Deposition über dem Wald war im gesamten Tagesverlauf in etwa doppelt so hoch wie über der Freifläche. Dieses Verhältnis stimmte mit dem Verhältnis des Pflanzenflächenindex (PAI) überein. Die Störung des Ökosystems verringerte somit die Fähigkeit des Bewuchses, als Senke für troposphärisches Ozon zu fungieren. Der deutliche Unterschied der Ozonflüsse der beiden Bewuchsarten verdeutlichte die Herausforderung bei der Regionalisierung von Ozonflüssen in heterogen bewaldeten Gebieten.
Die gemessenen Flüsse wurden darüber hinaus mit Simulationen verglichen, die mit dem Chemiemodell MLC-CHEM durchgeführt wurden. Um das Modell bezüglich der Berechnung von Ozonflüssen zu evaluieren, wurden gemessene und modellierte Flüsse von zwei Positionen im EGER-Gebiet verwendet. Obwohl die Größenordnung der Flüsse übereinstimmte, zeigten die Ergebnisse eine signifikante Differenz zwischen gemessenen und modellierten Flüssen. Zudem gab es eine klare Abhängigkeit der Differenz von der relativen Feuchte, mit abnehmender Differenz bei zunehmender Feuchte, was zeigte, dass das Modell vor einer Verwendung für umfangreiche Studien des Ozonflusses weiterer Verbesserungen bedarf.

Contents

List of Figures

List of Tables

1 Introduction

1.1 Fundamentals

Ozone (O_3) is an important oxidation and greenhouse gas in the Earth's atmosphere, which influences climate and air quality, affecting human health and vegetation. The highest ozone concentrations can be found in the stratosphere, where it forms the ozone layer. Within the stratosphere, above 11 km up to 50 km (Kraus, 2004), about 90 % of the total atmospheric ozone is present. The stratospheric ozone absorbs about 99 % of the dangerous UV radiation from entering the troposphere, resulting in a cooling below and enabling life on Earth. The tropospheric ozone has the opposite effect (Forster et al., 2007). In the troposphere, the remaining 10 % of atmospheric ozone are found. Although ozone occurs in the atmosphere only as a trace gas, it has a large contribution to the radiative forcing. According to Forster et al. (2007), it is the third most important greenhouse gas, following CO_2 and methane. While the concentration of stratospheric ozone decreased due to increased emissions of air pollutants, thus increasing the UV radiation reaching the Earth's surface, there is an increase in tropospheric ozone concentrations, particularly in rural areas downwind of urban areas. In addition to advection, ozone can be locally generated by photochemistry as a result of natural trace gas emissions like nitrogen oxides and volatile organic compounds (VOCs). In the last few decades the release of ozone precursors like carbon monoxide, hydrocarbons and nitrogen oxide increased due to human activities (Solomon et al., 2007; Derwent et al., 2007). Ozone is one of the main sources of the hydroxyl radical (OH), thus influencing the oxidizing capacity of the atmosphere, governing the oxidative properties and self-cleansing mechanism of the troposphere (Monks, 2005). Other ozone sinks, apart from chemical reactions, are stomatal uptake and deposition to plants and surfaces/soils. It is a secondary and most phototoxic air pollutant, which affects plants, and causes damage to the photosynthetic apparatus (Ashmore, 2005; Wittig et al., 2009). Above a certain concentration, tropospheric ozone becomes harmful for humans, animals and plants (WHO, 2003), and can cause adverse health effects in humans and vegetation (Ashmore, 2005; Fuhrer, 2009). Among air pollutants, ozone is the most important stressor to vegetation. There is incidence of ozone-induced ecological changes (Reich, 1987), since many plant species are sensitive to ozone as it causes cell damage and reduces growth. Reported effects are a decrease in crop yield (Heck et al., 1982) as well as a decline in net photosynthesis in trees and crops (Reich and Amundson, 1985). According to Sandermann Jr (1996), the arising injuries have been related to the stomatal uptake of ozone into the substomatal cavity and oxidative effects damaging the internal leaf tissue. The consequences for the plant depend on whether the ozone is removed by reactions inside the mesophyll or outside at the foliage surface. Therefore, it is crucial to know the partitioning of the ozone uptake, meaning where in the canopy and which parts of it react with the O_3 molecules. The main penetration location of ozone molecules into the leaves are the stomata, while the ozone uptake by the cuticles is comparably small (Kerstiens and

Lendzian, 1989), as they are covered by waxes, isolating and thus protecting the tissues from external agents. To estimate the effect of ozone on air quality and ecosystem health, there is a need to distinguish between the processes contributing to the ozone transport.

In order to understand the ozone transfer between atmosphere and vegetation, the interaction between atmospheric chemistry, meteorology, transport and vegetation uptake mechanisms needs to be considered. The parameters characterizing the transfer are the ozone mixing ratios, deposition velocities and fluxes. They provide information about how much ozone is present in the atmosphere and the strength of its transport. Ozone is known to be transported vertically downward from the above-canopy atmospheric surface layer. The sink strength is determined by the combined effect of all removal pathways for ozone, which are the stomatal uptake and the removal at the various canopy and forest surfaces. As ozone is quite an unstable molecule, it is likely to decompose when brought in contact with a solid surface, such as bare soil, tree trunks, water, dead organic matter, etc., resulting in a net sink (e.g. Fowler et al., 2001; Hanisch and Crowley, 2003). The dry deposition sink provides one of the key uncertainties in the tropospheric ozone budget through its influence on ambient ozone concentrations, which in turn results in uncertainties of photochemical processes and the tropospheric ozone budget in general. Chemical reactions of ozone with some biogenic volatile organic compounds (VOCs) and nitrogen oxides also play an important role in the ozone sink process near the surface (Goldstein et al., 2004).
Ozone transfer to a surface depends on the mixing ratio in the atmosphere above, which in turn depends on transport, local formation and destruction in photochemical and other reactions, and on volume and mixing conditions of the boundary layer. The flux of ozone towards a plant canopy is governed by the turbulent properties of the air flow around and within the canopy, the transfer at the diffusive boundary layer of the surface as well as the characteristics of the sinks by which ozone is ultimately removed and/or deposited. Although the ozone flux is affected by plant activity, there is no known biological use to the flux of ozone. Transport phenomena act by controlling the access of ozone to potential reaction partners. Turbulent transport faciliates such access through canopy scale mixing whereas molecular diffusion is less efficient, but controls the transport at smaller scales, e.g. close to surfaces. The ozone destruction in the atmosphere is much influenced by temperature, light and humidity, surface reactions, NO and VOC emissions. The biological part of the ozone deposition is described by the stomatal behavior, thus the above mentioned factors have often been examined (Meyers et al., 1998; Wesely and Hicks, 2000; Mikkelsen et al., 2004). The dynamics of stomatal aperture govern the deposition during the active season and explain most of the daily and annual pattern (Baldocchi et al., 1987; Meyers et al., 1998; Simpson et al., 2003). If turbulent and diffusive transport is taken into account, the stomatal uptake is not sufficient to predict the magnitude of the canopy sink. To explain the disagreement, so-called non-stomatal sinks have been invoked. These sinks can be in the order of 50 to 70 %, as reported from canopy scale measurements. It was studied for a variety of forest ecosystems as spruce-fir (Zeller and Nikolov, 2000) or ponderosa pine (Kurpius and Goldstein, 2003) as well as low vegetation like moorland (Fowler et al., 2001), barley field (Gerosa et al., 2004) and miscellaneous Mediterranean sites (Cieslik, 2004). The non-stomatal deposition covers several processes, such as gas-phase and/or heterogeneous chemical sinks inside and above the canopy. Furthermore, NO emitted from the soil may result in a significant consumption of O_3 (Duyzer et al., 1983; Pilegaard, 2001). Another factor is the quenching of organic volatiles in the atmosphere

(Kurpius and Goldstein, 2003; Goldstein et al., 2004; Mikkelsen et al., 2000, 2004), including reactions leading to aerosol formation (Bonn and Moortgat, 2003). The intensity of these reactions and their relevance as ozone sinks depends on the presence and relative abundance of the various reactants. Forest ecosystems are known to play an important role in the uptake and destruction of tropospheric ozone. Ozone deposition into forest canopies and sink mechanisms at night are not well understood so far. Several studies assume that stomatal deposition of ozone at night is negligible and surface reactions are responsible for ozone removal from air (Mikkelsen et al., 2004). Other studies point out the role of gas-phase chemical reactions (Goldstein et al., 2004). Findings indicate that ozone deposition is affected by humidity conditions of surfaces (Altimir et al., 2006). Prevailing low turbulence at stable conditions at night complicates ozone deposition studies by micrometeorological methods. The flux is underestimated at night, as low turbulence conditions limit the turbulent exchange and advective transport becomes important.
For the analysis of ozone fluxes into the leaf, the analog resistance technique derived from Ohm's law can be used (Leuning et al., 1979). For the discussion of chemical fluxes to and from the surface as well as the influence of meteorological factors, the resistance controlling the deposition is traditionally subdivided into $R = R_{\mathrm{a}} + R_{\mathrm{b}} + R_{\mathrm{c}}$, which are the aerodynamic, quasi-laminar boundary layer and surface resistance, respectively. The meteorological influence on R_{a} is mainly through the intensity of the turbulence and the involvement of the Monin-Obukhov scaling. The resistance R_{b} at the leaf boundary layer depends on the wind speed and the molecular diffusivity of ozone in air. A range of external factors influence the surface resistance R_{c}, especially in the case of exchange through the stomata (Pilegaard et al., 1998). For a harvested wheat field with sparse vegetation cover, Pilegaard et al. (1998) showed that the aerodynamic resistance accounted for 23-28 $\%$ of the total resistance during the day and 16-26 $\%$ during the night. The laminar boundary layer resistance accounted for 8-11 $\%$ during the day and 4-7 $\%$ during the night. More than 60 $\%$ of the total resistance during the day and slightly more during the night were due to the dominating surface resistance in their study.

The atmosphere-biosphere exchange can change within a short time period due to severe disturbances such as fire (Amiro et al., 2006; Dore et al., 2012), harvest (Schmid et al., 2006; Yanai et al., 2003), insect outbreaks (Seidl et al., 2008) or strong storms (Amiro et al., 2010; Knohl et al., 2002; Lindauer et al., 2014). The disturbances affect a wide range of ecosystem characteristics such as stand structure, leaf area, species composition, ecophysiology, rates of decomposition and microclimate. They have potentially large and long lasting effects on carbon, water and energy fluxes (Williams et al., 2012, 2014). In addition, the damage of forest ecosystems caused by storms, insects, and fires is expected to increase due to climate change (Running, 2008; Seidl et al., 2011; Spathelf et al., 2014). Forests in a future climate system will thus be more heterogeneous due to wind and pests. Especially for such forest ecosystem heterogeneities, current landscape studies poorly describe scale transitions and interactions. Erisman and Draaijers (2003) found that forest edges may affect the surface exchange of energy and matter between atmosphere and forest vegetation on a local scale. Therefore, it must be assumed that these heterogeneities (e.g. forest – clear-cut) decrease the uptake of greenhouse gases by an ecosystem with significant feedback on the climate system (Serafimovich et al., 2011). Hence, disturbances of forest ecosystems have to be considered to accurately determine the contribution of forests to the global ozone budget.

Ozone flux measurements are performed in various ecosystems. They have been carried out over Norway spruce (Picea abies) from the northern boreal region (Pilegaard et al., 1995; Mikkelsen et al., 2000, 2004) and other coniferous trees, e.g. Scots pine (Aurela et al., 1996; Tuovinen et al., 2001; Keronen et al., 2003). Ozone flux measurements have also been performed for low vegetation like grassland and moorland species (Cieslik, 1998; Fowler et al., 2001; Cieslik, 2004). Large uncertainty as well as temporal and spatial variability of ozone fluxes have been reported by the mentioned studies, and they have been related either to biogeochemical processes and/or several systematic and random error sources of the measurement. The temporal and spatial variability is also due to a large variation in soil and vegetation properties such as soil moisture or leaf area index (LAI: portion of plant surfaces per surface area; Foken, 2008). The large variation of fluxes to different ecosystem types emphasizes the impact of disturbed forest ecosystems on the atmosphere-biosphere exchange and the associated effect on the climate system.

The increased focus on climate research during the last years raised the need for reliable measurements of transpiration and CO_2 uptake of forests as well as fluxes of other trace gases. High quality flux measurements are the only way to directly quantify fluxes and help to understand destruction processes and the relationship to atmospheric and biological conditions. The measurement of fluxes and the estimation of deposition velocities and surface resistances are important for surface-atmosphere exchange modelling (Grünhage et al., 2000) as well as for model validation and development (Bassin et al., 2004). Measurement results form the basis of parameterizations of deposition schemes in regional and global models. While the values of parameters as mean wind, temperature and humidity can directly be obtained from measurements, fluxes can be calculated in a variety of ways (Stull, 1988). To measure fluxes of chemical species between the atmosphere and the surface, several micrometeorological (aerodynamic) methods have been used (Wesely, 1989; Dabberdt et al., 1993; Rinne et al., 2001; Altimir et al., 2002; Guenther et al., 1996). These methods can rely on measuring the vertical concentration profile (profile method), the concentration difference between up- and downward directed air-drafts (eddy accumulation and relaxed eddy accumulation methods) or the concurrent turbulent fluctuations of vertical wind speed and concentration (eddy-covariance and disjunct eddy-covariance method). In order to calculate fluxes with the profile and accumulation methods, flux-profile and flux-concentration difference relationships are needed. The eddy-covariance (EC) method obtains the flux directly from the covariance between wind speed and concentration data, and by sampling the motions of the air sufficiently fast (preferably 10 times per second, or faster) and over a sufficiently long time (30 to 60 minutes), an averaged flux density of gas exchange between a vegetated canopy and the atmosphere can be determined (Baldocchi, 2014). In the micrometeorological community, the estimation of turbulent fluxes of energy and chemical species between land surfaces and the atmosphere by the eddy-covariance technique is well established and one of the most accepted and widespread methods (Baldocchi et al., 2001). EC flux measurements are the optimal method to determine atmosphere-biosphere exchange of reactive compounds and biogenic aerosols. However, the requirement of fast-response sensors limits its application to very few chemical species.
One of the chemical species, for which fast-response sensors are available, is ozone. Therefore, the EC method is applicable for the measurement of ozone fluxes. A variety of suitable analyzers exist for ozone measurements, all of which are based on chemilumi-

nescence. The reagents can be either in liquid, solid or gaseous form and hence the type of chemiluminescence is called wet, dry and gas-phase chemiluminescence, respectively. The use of the wet chemiluminescence method has advantages over the dry method (e.g. regarding signal drift and water vapor influence), but the sensitivity can be lower than for the dry method. Gas-phase chemiluminescence (GPC) is generally based on the homogeneous reaction with NO (Pearson Jr, 1990). One of the main practical disadvantages of GPC is that NO is a toxic compound and is required as compressed gas during operation. The dry chemiluminescence (DC) method has been used most regularly and successfully in a variety of environments and settings (Tuovinen et al., 1998; Bauer et al., 2000; Gallagher et al., 2001; Bassin et al., 2004; Rummel et al., 2007). In DC analysis air passes over a disc coated with reagents, which produce photon emissions in the blue spectral range when reacting with ozone. High flow rates are used to draw in air from the inlet to the analyzer, operate in the flow-independent regime and achieve the fast response times required for eddy-covariance measurements (Güsten et al., 1992). Ozone fluxes have been measured by DC for many years using an analyzer originally developed as an ozone sonde by GFAS ("Gesellschaft Für Angewandte Systemtechnik"; Güsten et al., 1992), which has since then been reproduced by other groups (e.g. by NOAA-ATDD as detailed in Bauer et al., 2000; enviscope GmbH as described in Zahn et al., 2012).
Many groups of micrometeorologists and tower network (FLUXNET) sites around the world use EC systems, where scalar concentration analyzer and wind measurement are separated by up to several tens of meters (Goulden et al., 1997; Hollinger et al., 1999; Loescher et al., 2003; Moncrieff et al., 1997; Pilegaard, 2001). To transport a gas sample to the fast-response analyzer, a tube system is used. The application of these closed-path systems suffers from lags and attenuation of high-frequency fluctuations. However, for some trace species like O_3, this closed-path approach is the only method of making EC measurements, as no open-path analyzers are available so far, and the approach allows easier access and protection of measurement equipment. The low-pass filtering effects in closed-path EC systems can partly be explained by mixing effects in tubes (Lenschow and Raupach, 1991; Leuning and Judd, 1996; Leuning and Moncrieff, 1990; Massman, 1991). The damping of higher frequencies is due to differential advection caused by the radial variation of the mean velocity and simultaneous radial diffusion of the sample gas (Lenschow and Raupach, 1991; Taylor, 1953, 1954; Massman and Ibrom, 2008). Therefore, concentration fluctuations introduced into the tube are smeared as they advect down the tube. The result is an increasing attenuation of the signal with increasing frequency and tube length. The effect of signal reduction on the flux determination is described in several recent studies (Philip, 1963a,b; Lenschow and Raupach, 1991) and the attenuation has received some physically based theoretical modeling based on passive tracer formulations in a tube flow system (Lenschow and Raupach, 1991; Massman, 1991; Massman and Ibrom, 2008). Physical adsorption and desorption at the tube walls, as in the case of water vapor, leads to an increased high-frequency attenuation (e.g. Ammann et al., 2006; Ibrom et al., 2007; Massman and Ibrom, 2008; Runkle et al., 2012), which was shown for first-order sorption (or destruction) of ozone at the tube wall in an EC ozone flux sampling tube by Massman (1991). When no interaction between the solute and the tube wall is occuring, fluctuations are usually attenuated less by turbulent tube flow than by laminar tube flow (Massman, 1991). Therefore, turbulent flow is typically maintained to minimize the effect of attenuation of fluctuations (Lenschow and Raupach, 1991). The above men-

tioned studies found the attenuation to be dependent on tube length and diameter, flow Reynolds number and molecular Schmidt number of the particular gas. In order to insure the accuracy of the closed-path approach, it is important to account for the attenuation of fluctuations caused by the flow within the tube. Consequently, the attenuated and phase-shifted concentration fluctuations and covariances need to be corrected.
As a result of the finding of low-pass filtering effects by the inlet tubing, different methods have been developed to correct the data either in spectral (Aubinet et al., 2000, 2001; Massman, 2000; Moncrieff et al., 1997; Moore, 1986; Ibrom et al., 2007; Ammann et al., 2006; Moravek et al., 2013) or in time space (Goulden et al., 1997; Hollinger et al., 1999). For the post-processing of closed-path EC system data, empirical transfer functions are applied to compensate for attenuation effects of long tubing (Lenschow and Raupach, 1991; Leuning and Judd, 1996; Massman, 1991), or a correction factor is determined by comparing attenuated and unattenuated frequency spectra (Aubinet et al., 2001; Ibrom et al., 2007; Leuning and King, 1992). Another possibility is to estimate a cospectrum for each block averaging period by Fourier transform, correct the cospectrum, and integrate the corrected cospectrum to obtain the desired flux. This cospectral correction method may be the best method of all because it requires the fewest assumptions. However, it is numerically intensive and therefore impractical for long duration experiments comprising many block averaging periods. In order to determine the effect of the inlet tubing on the attenuation of fluctuations, spectral analyses have been performed for several measurements, especially for closed-path CO_2 and H_2O instruments. The resulting spectra of measurements with open- and closed-path instruments have been compared (Ibrom et al., 2007; Runkle et al., 2012; Leuning and Moncrieff, 1990; Leuning and King, 1992; Massman, 2000) or the cospectrum of the closed-path instrument has been compared with the ideal sensible heat flux cospectrum (Aubinet et al., 2001; Massman, 2004; Ammann et al., 2006; Ibrom et al., 2007; Mammarella et al., 2009). For ozone fluxes measured with closed-path EC systems, the effect of attenuation of fluctuations has been analyzed by Keronen et al. (2003) and Cieslik (1998) for individual instruments and Zhu (2008) showed the importance of the correction for the determination of ozone flux profiles, which showed the expected trend with height only after correcting for differences of the sensors.

As flux measurements are restricted to a limited number of sites and time periods, models are applied to determine fluxes for larger areas. Furthermore, the application of a model is required for the analysis of surface or boundary layer observations of reactive compounds and aerosols in terms of surface sources, sinks and transport. Models for the exchange of gases between the atmosphere and the biosphere are used for transpiration modeling and, regarding climate change, for the modeling of CO_2 exchange. Models have the advantage of being able to extrapolate measurements towards larger regions and their results can be used to close gaps in the measurements if the model has been validated for the respective site. For the determination of the turbulent exchange between the atmosphere and the biosphere, layer models of different levels are applied. One-layer models ("big leaf" models) consider soil, plant and the atmosphere above. The plant lies like a big leaf above the soil and is not divided in more detailed layers. These models contain surface layer physics and consist in some cases of several layers. Multi-layer models divide the atmosphere into several horizontal layers. Models with boundary layer coupling are state of the art. Atmosphere-biosphere exchange models are usually based on the resistance approach (Wesely, 1989; Ganzeveld and Lelieveld, 1995; Fig. 4.2). Fluxes are related to

concentrations through resistances by analogy with an electric circuit. The easiest concept is the comparison with Ohm's law $I = U/R$, where the flux is compared to the current and the concentration to the voltage. The resistance opposed to the flux can be displayed as a circuit of the single resistances. For the analysis of surface layer observations of concentrations and fluxes, the individual contributions by emission, dry deposition, chemical transformations and turbulent transport as well as interactions between these processes inside and above the canopy need to be considered by the model.

1.2 Motivation and outline

The previous section outlined the importance of precise ozone flux measurements for the analysis of the atmosphere-biosphere ozone exchange as well as for model validation purposes. This thesis presents ozone flux measurements during two distinct measurement campaigns within three different ecosystems: a grassland site in Mainz, Germany, and a Norway spruce forest as well as a mixed clear-cut vegetation in the Fichtelgebirge.

Ozone interaction with vegetation is controlled by stomatal uptake, deposition to plant surfaces and soil, as well as chemical transformations. Understanding these processes and quantifying the ozone exchange for different ecosystem types are prerequisites to upscale from local measurements towards regional ozone fluxes. The investigations are related to disturbed ecosystems as landscape studies suffer poor description of scale transitions in case of such heterogeneities. The objectives of this work are to give answers to the following questions:

- How do disturbed ecosystems affect the atmosphere-biosphere ozone exchange?
- Is the Multi-Layer Canopy CHemistry Exchange Model MLC-CHEM able to reproduce the measured ozone fluxes?

This is done by analyzing the difference in atmosphere-biosphere exchange between a spruce forest ecosystem and a canopy with low heterogeneous vegetation. To this end, within the scope of the EGER (ExchanGE processes in mountainous Regions) project, O_3 exchange was measured by the eddy-covariance method. The time series and diurnal cycles of trace substances in the soil-vegetation-boundary layer system are analyzed. Finally, for evaluation purposes, the EC fluxes (simultaneous measurements of an undisturbed forest and a clear-cut) are compared with those obtained from a modeling study, and recommendations how to improve the model output are given.

In some field campaigns, it is not possible to mount the gas-analyzer close to the sonic and the use of a longer inlet tube is unavoidable. Previous studies performed under field conditions already noted an underestimation of the EC flux caused by the attenuation of ozone concentration fluctuations in a tube (Keronen et al., 2003; Zhu, 2008). For a correct interpretation of the measured fluxes it is important to estimate the error that is produced by the EC system, consisting of sensor and inlet tube, which is not involved in the corrections by eddy-covariance software packages. If there are distinctive differences between the EC setups or even individual instruments, it is not sufficient to apply the same corrections and quality criteria. In theoretical corrections, the effects of different sensor flow rates or differing tube lengths between EC systems are considered, and not applying the correction

after the determination of fluxes by the software could lead to misinterpretations when comparing fluxes from different campaigns, ecosystems and sites. However, it needs to be justified that the correction is applicable for ozone flux measurement systems, as Aubinet et al. (2000) have shown that transfer functions predicted by theory can significantly depart from the ones estimated experimentally. Therefore, the results of experimentally estimated correction factors will be compared with the results of a transfer function for a laminar flow through a straight tubing. The main objective of this thesis is to answer the following question:

- Are the existing theoretic transfer functions derived for other species suitable to correct for the underestimation of the measured ozone fluxes?

To the best knowledge of the author, so far no comparison of theoretically and experimentally estimated correction factors was performed for ozone.
The limits of EC flux measurements of ozone are explored using state-of-the art equipment within a grassland ecosystem in Mainz, Germany. The performance of different EC systems is investigated using the cospectral correction method and the effect of wind speed on the EC flux correction is explored. A recommendation for the post-processing of the data of future ozone flux measurements is derived under the assumption that the results are representative for other EC ozone systems.

The sites where the measurements for these investigations were performed is described in chapter 2. Chapters 3 and 4 will describe the applied methods of measurement and modeling as well as the post-processing of the data. In chapter 5 the results of the measurement for the validation of the flux correction method will be analyzed. The measurement and modeling at the EGER site will be presented and discussed in chapter 6. The conclusions and an outlook for further investigations will be given in chapter 7.

2 Experimental setup: Field campaigns

The data used for the analysis of ozone fluxes of different ecosystems was collected during two field campaigns. The setup of the EGER campaign in summer 2011 and the experiment at the airfield Mainz-Finthen in summer 2013 will be described in the following sections.

2.1 ExchanGE processes in mountainous Regions (EGER)

As part of the DFG funded EGER (ExchanGE processes in mountainous Regions) project, the ozone exchange between the atmosphere and the biosphere was investigated during the third intensive observation period of the project (EGER-IOP3) in summer 2011. In the first project phase, two IOPs have been performed (Serafimovich et al., 2008a,b) with results published by Foken et al. (2011) and Foken et al. (2012). In the second phase, the focus of EGER was on disturbed ecosystems and their effect on the trace gas exchange. The main focus of the analysis of ozone fluxes was on the differences in exchange between a spruce forest canopy and a wind-throw vegetation. IOP3 was conducted from June 15 to July 25, 2011 at the research site of the Bayreuth Centre of Ecological and Environmental Research (BayCEER). The experiment site was located in a spruce forest ecosystem surrounding the FLUXNET (Baldocchi et al., 2001) site DE-Bay (Waldstein-Weidenbrunnen) in the Fichtelgebirge mountains in south-east Germany. The Fichtelgebirge is a low mountain range in north-eastern Bavaria, Germany. "Waldstein" is a hillside in the north-western part of the Fichtelgebirge mountains. The site is in the upper catchment of the stream "Lehstenbach" between the hilltops of "Großer Waldstein" (879 m a.s.l.) in the south-west and "Bergkopf" (857 m a.s.l.) in the north-east. The surrounding topography is described in Thomas and Foken (2007). The complete experiment site of EGER-IOP3 consists of an area of 4 km ^{2} differing in topography and vegetation cover.
Due to a wind-throw by the storm "Kyrill" on January 18, 2007, it was possible to use the FLUXNET site for the analysis of the effect of a disturbed ecosystem. The measurement site (50°8' N, 11°52' E, ~775 m a.s.l) containes a spruce forest (Picea abies) patch as well as a clearing south of the forest edge (see Fig. 2.1(a)) and the terrain is moderately sloped towards the south with about 3°. The clearing can be attributed to the wind-throw by the storm "Kyrill" and the northern border of the clearing is artificially straightened.

Ozone measurements have been performed on two masts, one on the main tower (M1, see Fig. 2.1(c) and Tab. 2.1) above the forest and the other one on the turbulence mast (M4, see Fig. 2.1(e) and Tab. 2.1) on the wind-throw. On M1 eddy-covariance measurements of fluxes of sensible and latent heat, carbon dioxid (CO_2) and ozone were carried out at 32 m height and on M4 at 5.5 m height in both cases about 5 m above the canopy top. Only the ozone measurements were performed by the author, all other flux measurements

Table 2.1: Characteristics of the ozone measurement sites.

	M1	M4
surface type	spruce forest	wind-throw
h_{meas} [m]	32	5.5
h_{canopy} [m]	27	0.4
PAI [$m^2\,m^{-2}$]	6.0	3.34

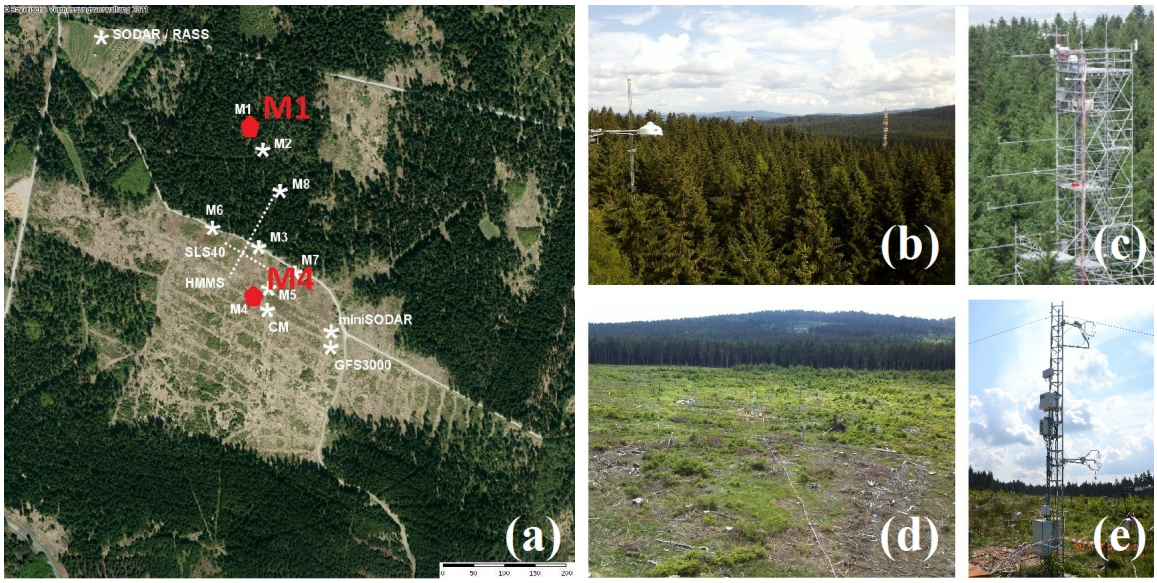

Figure 2.1: Masts M1 and M4 and their surrounding vegetation. (a) Positions of the masts M1 and M4, where the ozone measurements were performed; (b), (c) main tower M1 and its surrounding vegetation; (d), (e) turbulence mast M4 and its surrounding vegetation.

were conducted by participants from the Department of Micrometeorology, University of Bayreuth, Germany.

For the measurements of vertical velocity, a USA-1 (METEK GmbH, Germany) sonic anemometer was installed at 32.5 m height on M1 (see Fig. 2.1(b),(c)) and a CSAT3 (Campbell Scientific Inc., USA) sonic anemometer was mounted on M4 at 5.5 m (see Fig. 2.1(d),(e)). Ozone fluctuations were measured with fast response ozone sensors (enviscope GmbH, Germany; Zahn et al., 2012). For the calibration of the ozone data, UV absorption based slow response ozone monitors (Model 205, 2B Technologies, Inc.) were applied. To measure CO_2 and water vapor fluxes, a Li7000 was mounted at M1 and a Li7500 at M4.

The high frequency data was sampled at 20 Hz. The measurement frequency of the sonics was 20 Hz. The fast ozone sensors were run with a frequency of 10 Hz until power outages occured, whereafter the frequency changed to 25 Hz. The inlets of both ozone instruments were mounted alongside each other directly beneath the sonic on both masts and protected from rain and insects by a net and a funnel. More information about the installation of the instruments is given in Table 2.2. The data aquisition and recording for M1 was done with the tcopy logging program on a computer based in a hut at the bottom of the tower. At M4, a Campbell logger (CR3000) was installed. The calculation of fluxes and turbulence

statistics is performed by the eddy-covariance software TK3 (Mauder and Foken, 2011). The chemical discs inside the fast ozone sensors were exchanged every two days, resulting in data gaps of a few seconds. The respective and subsequent half-hour fluxes were excluded from analysis. Three calibrations of the ozone monitor were performed (June 14, July 08, July 23) with an Ozone Calibration Source (Model 306, 2B Technologies, Inc.) and they were taken into account during post-processing by linear interpolation between the calibration checks. In the 30-minute interval of the calibration, no absolute ozone mixing ratio measurement is available and for the flux calculation the average of the previous and following half-hour values was taken. Additional data gaps resulted from power outages.

Table 2.2: Installation information of the ozone instruments at M1 and M4.

	M1	M4
sampling frequency of ozone monitor	0.5 Hz	0.5 Hz
sampling frequency of ozone sensor	25 Hz (up to 01.07. 10 Hz)	25 Hz (up to 06.07. 10 Hz)
vertical displacement of inlets	30 cm	31 cm
horizontal displacement of inlets	19 cm	14 cm
tube length of ozone sensor	7.0 m	9.5 m

From July 26 (10:50 CET) to July 27, 2011 (14:00 CET), the two enviscope ozone sensors were run side-by-side to investigate their consistency. They were mounted at the turbulence mast M4 in a height of 2.25 m above ground and the data was collected with the CR3000 logger, applied for the data from the 5 m measurements during IOP3. Each sensor remained on the setup (same tube and tube length) as during the main measurement campaign.

For the determination of the vegetation structure, which is necessary for the analysis and the modeling of fluxes, forest inventories were performed at 30 positions within the experiment site. The plant area index (PAI, last row of table 2.1) was measured by the LAI-2200 plant canopy analyzer (LI-COR, Lincoln, USA) at all 30 forest plots. The PAI is determined by spectral radiation measurements in the photosynthetic active radiation (PAR) range by comparing the radiation underneath the biomass with the uninfluenced radiation. At 15 of the 30 plots tree positions, trees per hectar, tree circumferences and tree heights were determined as well. On the clearing, only main cover types were measured (Picea, Calamagrostis, Deschampsia, Vaccinium, Juncus, Alnus and other deciduous trees, dead wood). For these species, averaged height and the coverage were determined by vegetation transects. Therefore, three sites were chosen along the forest edge consisting of five plots each. The transects had a length of 30 m with a 100-110° orientation, which is parallel to the forest edge, and the five transects were 10 m apart from each other in perpendicular direction. The PAI of the selected species was measured with the LAI-2200 (LI-COR, Lincoln, USA) at the three sites on June 16, July 02, 14 and 25. The results of the transect

Table 2.3: Distribution of main cover types on the clear-cut (modified after Serafimovich et al., 2011).

	Ground Cover [%]	Height [m]	PAI [$m^2\ m^{-2}$]
Deschampsia	21.7 ± 18.8	0.17 ± 0.05	2.65 ± 1.08
Picea	21.4 ± 13.7	1.21 ± 0.50	8.67 ± 2.29
Vaccinium	15.9 ± 11.4	0.27 ± 0.10	3.46 ± 1.05
Calamagrostis, Agrostis	9.0 ± 11.3	0.42 ± 0.10	3.43 ± 1.07
Juncus, Carex	3.1 ± 6.5	0.74 ± 0.13	1.77 ± 0.60
other herbaceous	1.6 ± 2.5	-	-
moss	0.9 ± 1.9	-	-
dead grass, bare soil	7.2 ± 11.0	-	-
dead wood (harvest residuals)	18.8 ± 14.2	-	-
water	0.2 ± 0.6	-	-

measurements are summarized in Table 2.3.
In addition, airborne LIDAR (laser scanner) measurements (Trimble/Toposys) were performed to document the spatial distribution of trees at the Weidenbrunnen site and in order to parameterize models for even larger areas (4 km^2 from Großer Waldstein up to Köhlerloh and Weidenbrunnen). The LIDAR elevation and vegetation surface data is available in 1 m resolution.

A more detailed description of the site and all measurements performed during the campaign can be found in Serafimovich et al. (2011).

2.2 Airfield Mainz-Finthen

Based on the differences found for fluxes measured with different ozone sensor setups during the two days of instrument comparison at the end of the EGER-IOP3 campaign with two enviscope ozone sensors, a second more extended side-by-side field campaign was performed from July to August 2013 to investigate the consistency and to analyse systematic deviations between ozone sensors.
The experiment site was located at the estate of the airfield Mainz-Finthen (49.9685 N, 8.1481 E, ~185 m a.s.l.) in Rhine Hessen (Germany). The airfield is located south-west of the city of Mainz and the main landcover in the other directions is agricultural area. The vegetation type is classified as a nutrient poor steppe-like grassland ecosystem with a mean canopy height of 0.6 m. Due to hot and dry conditions before and during the measurements, the vegetation was dry, thus reducing the expectable stomatal deposition.

The measurements were performed using an eddy-covariance setup. The vertical velocity was measured with a USA-1 (METEK GmbH, Germany) sonic anemometer, which was installed at a height of 2.8 m. Only one sonic was applied for the determination of ozone

fluxes during the campaign. This was done to avoid a potential influence of different sonics on the result of the flux measurement. For the side-by-side comparison, up to 7 fast-response ozone sensors (enviscope GmbH, Germany) measured fluctuations of the ozone mixing ratio (see Fig. 2.2). Due to broken fans inside the sensors, only four of them were running throughout the whole campaign. As the ozone sensors provide only ozone fluctuations, they have been calibrated by a slow-response ultraviolet photometric analyzer (TEI 49, Thermo Environmental Instruments Inc., Franklin, MA, USA) as reference. The inlets of all ozone sensors were mounted next to each other on the mast, together with the inlet of the monitor for the absolute ozone measurements. As the sensors draw in a large volume of air, they were installed in some distance from the center of the sonic to not disturb the wind measurements. Therefore, the horizontal and vertical displacement was 85 cm and 15 cm, respectively. The air was transported from the inlets to the instruments through black 3/8" PFA tubing (inner diameter (ID) of 7.52 mm). For the comparison of the sensors, all sensors were equipped with tubes of the same length (l = 3 m) from July 19 until July 29. For the investigation of the effect of the tube length on the flux underestimation, all sensors were equipped with tubes of different lengths (l = 3, 5, 7, 10 m) from August 01 until August 12.
The sonic and the ozone sensors were mounted in south-east and north-west direction from the mast, respectively, as the main wind directions of the site are south-west and north-east. For the further analysis, data belonging to wind directions where the mast is in-between the sonic - ozone sensor path is neglected otherwise the mast would influence the turbulence field.
The chemical discs inside the fast ozone instruments were replaced twice a week and the respective and subsequent half-hour data of this exchange period was excluded from further analysis.
The reinstallation of an afore broken ozone sensor on August 01 led to the appearance of single unrealistic large and small relative mixing ratios in the time series of all ozone sensors receiving power by the same power line. This affected all ozone instruments until the end of the experiment. The spikes could be distinguished from normal fluctuations, but caused gaps in the time series.

The data of the sonic anemometer and the ozone instruments was sampled with a frequency of 50 Hz using two CR3000 Campbell data loggers. One of them collected the data from the sonic, the other one from the fast ozone sensors and the slow ozone monitor. Due to the large amount of data recorded by the second data logger, a time delay occured, resulting in an increasing lag time between the data from the sonic and the ozone instruments with time. This was corrected during post-processing by determining the time shift, where the sonic and ozone data show the best correlation. A third Campbell data logger recorded the data of a weather station, which was mounted on a second mast north-west of the main mast. It provided meteorological data at intervals of 10 minutes.
The eddy-covariance software TK3 (Mauder and Foken, 2011) was used for the calculation of fluxes and turbulence statistics.

Figure 2.2: Setup of the instruments at the airfield Mainz-Finthen. On the left side the main mast is displayed with the sonic and the ozone sensors (red boxes), on the right side the weather station is on a second mast. The picture is taken in south-western direction.

3 Measurement of ozone fluxes

This chapter gives an overview of the technique used for the measurement of ozone fluxes. In addition to the theory of the technique, the instruments applied for the measurement and the data processing is presented. For the determination of ozone, CO_2, sensible and latent heat fluxes the eddy-covariance technique is applied. The instruments used for the measurement of the required quantities are described in section 3.1 and the method is demonstrated in section 3.2. Section 3.3 presents the necessary steps of the data processing. As different eddy-covariance systems for the measurement of ozone fluxes give different results, the steps on how to investigate the comparability between different eddy-covariance systems are introduced in section 3.4.

3.1 Instrumentation for flux measurements

As eddies of different spatial scales contribute to the flux, the instruments need to be able to capture the bulk of eddies passing the sensor.
Fast fluctuations of wind velocity and temperature are measured with sonic anemometers. Ultrasonic sound waves are used for the measurement of wind velocity and the result is based on the time of flight of sonic pulses between pairs of transducers. Sonics are also used as thermometers, as the speed of sound is temperature dependent. Two different kinds of anemometers are applied, a USA-1 (METEK GmbH, Germany) sonic anemometer (main tower M1 during EGER and on airfield Mainz-Finthen) and a CSAT3 (Campbell Scientific Inc., USA) sonic anemometer (turbulence mast M4 during EGER). The sonics differ in the alignment of the three arms and in their maximum sampling frequency. The instrument that is used in addition to the sonic anemometer should be placed beneath the middle of the measurement path of the sonic rather than above (Kristensen et al., 1997).
In order to measure turbulent ozone fluxes, the instruments need to capture fast fluctuations of ozone mixing ratio. For the measurement, fast-response ozone sensors (enviscope GmbH, Germany; Zahn et al., 2012) have been applied, which are dry chemiluminescence instruments. The sensor was designed as a cooperation between enviscope GmbH and the Institute for Meteorology and Climate Research (IMK) of the Research Center Karlsruhe (KIT) and Figure 3.1 shows the sensor and its mechanical setup. First sensors of this type were produced by Güsten et al. (1992). The measurement principle is based upon the chemical reaction of ozone with the organic dye coating of a reaction plate inside the instrument. The plate is placed in front of a photomultiplier and is exposed to the stream of ambient air through the instrument. The chemical reaction leads to the emittance of light within the visible wavelength range (~500 nm), which is detected by a photomultiplier. The instrument can be used for the measurement of fast ozone concentration fluctuations due to the very fast reaction and subsequent electronic analysis of the light signal (Zahn et al., 2012). Its sensitivity depends on the used sensor disc and decreases during the use. Sensor discs

with a more constant sensitivity have recently been produced by Ermel et al. (2013). Due to the non-constant sensitivity of the chemical plates, the sensor can only give the mixing ratio in arbitrary units (0-5 V) and parallel measurements of absolute ozone mixing ratios are needed to calibrate the output signal. In addition, the sensitivity of the measurement depends on the humidity of the sensor discs, thus there is a cross-sensitivity regarding water vapor in the air. An increase in sensitivity is reported by Schurath et al. (1991) after a relaxation time to adjust to the enhancement factor. To activate the dye coated plates, they have to be pre-ozonised ahead of their application with air of high ozone concentration to get the sensitivity to its maximum. When the sensor disc is changed, small gaps appear in the time series. The instrument allows a sampling frequency of up to 50 Hz (20 ms). If

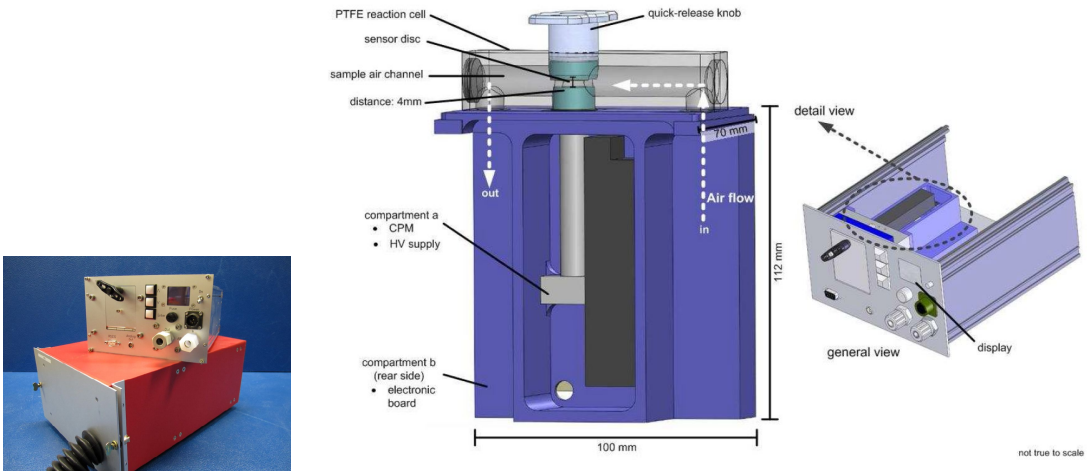

(a) (b)

Figure 3.1: Mechanical setup of the applied fast ozone analyzer. In (a) the entire ozone instrument is displayed and (b) shows the two compartments with the channel photomultiplier (CPM) and the high-voltage (HV) supply as well as the electronics (taken from Zahn et al., 2012).

a lower frequency is chosen, the single measurements can be averaged to a lower output frequency (1, 10, 25 Hz) and thus the data is smoothed. For example, if a 10 Hz frequency is chosen, five subsequent measurements are averaged. The precision of the instrument depends on the number of photons reaching the photomultiplier. It is given with about 0.4 ppbv at a measurement frequency of 50 Hz and 0.09 ppbv at 1 Hz for dry air at an ambient mixing ratio of 45/50 ppbv (Zahn et al., 2012 and instruction manual as of July 01, 2010, respectively).

As the dry chemiluminescence technique is not absolute, a frequent calibration with absolute mixing ratios is needed. The slow-response measurement of ozone mixing ratios is performed with UV absorption based slow-response ozone monitors (Model 205, 2B Technologies, Inc.; during EGER) and a slow-response UV photometric analyzer (TEI 49, Thermo Environmental Instruments Inc., Franklin, MA, USA; at airfield Mainz-Finthen). A low-pressure mercury lamp with a principal emission wavelength of 254 nm is used. This is the wavelength, where the ozone molecule has its absorption maximum. The measurement is based on the attenuation of light and the concentration is determined after the Beer-Lambert Law. The 2B Technologies instrument can measure with a frequency of up

to 0.5 Hz, which is too slow for the direct use in EC measurements.

3.2 The eddy-covariance method

In general a flux is defined as how much of something moves through a unit area per unit time (Burba and Anderson, 2010). The turbulent flux can be considered as a superposition of eddies of different sizes (frequencies) transporting air with varying composition. The eddy-covariance method is one of the most applied techniques for the determination of fluxes (e.g. sensible and latent heat flux, CO_2, methane, ozone and other trace gas fluxes). It is a direct approach for the measurement of fluxes and no empirical coefficients need to be applied (Foken et al., 1995; Kaimal and Finnigan, 1994; Lee et al., 2004).
The method is based on a number of assumptions. The most important assumptions for the exact application of the technique are horizontal homogeneity of the surface and stationary atmospheric conditions. The derivation of the mathematical algorithms is based on these assumptions and simplifications, and the quality of the result depends on how good the assumptions are fulfilled, on physical phenomena, instrumental problems, specificies of the terrain and the setup (Burba and Anderson, 2010). Therefore, for the definition of the measurement site, the exclusion of internal boundary layers and influence of obstacles and the identification of the footprint area (area surrounding the sensor that influences the result of the measurement) are of special importance. As state-of-the-art measurement systems give precise data, the quality of the measurement does not depend on the instrumentation, but on the operating conditions and the application of necessary corrections. In forested areas the characteristics of high vegetation also need to be considered for the finding of the measurement site (Foken, 2008).

In order to obtain fluxes from the measured quantities, a mathematical algorithm needs to be determined. A vertical turbulent flux is defined as the time average of the product of the vertical wind velocity w and the concentration of the substance c. The instantaneous values can be decomposed into a mean and a fluctuating part (Reynolds decomposition), thus the flux F_c is (after Webb et al., 1980):

$$F_c = \overline{w \cdot c} = \overline{(\overline{w} + w') \cdot (\overline{c} + c')} = \overline{w} \cdot \overline{c} + \overline{w' \cdot c'} = \overline{w' \cdot c'} \; . \tag{3.1}$$

The overbar denotes a time average and primes the fluctuating parts. The derivation of Equation 3.1 is based on $\overline{w}$=0, $\overline{w'}$=0 and $\overline{c'}$=0. Therefore, the EC method can give the flux as a direct result as from the time series of each measured quantity, a time series of perturbations can be yielded. Multiplying the respective values and averaging gives the covariance (Stull, 1988). The EC method is valid for non-reactive gases like CO_2, but for reactive trace gases the technique can only be applied if the gases are present with high concentration and if the reactions do not play an important role. This is the case for daytime ozone deposition in rural areas.

From the turbulent deposition flux of ozone, the deposition velocity v_d can be determined. The formulation of the dry deposition assumes that the deposition flux is directly proportional to the local concentration c at the measurement height and is only valid if $c(z = 0) = 0$:

$$F_c = -v_d \cdot c \; . \tag{3.2}$$

The deposition velocity v_d is a proportionality factor, it indicates the combined effect of all physical, chemical and physiological processes causing the flux, regardless of concentration (Keronen et al., 2003). Since the deposition velocity is determined by dividing the flux by the mean concentration, it can be interpreted as a normalized flux. The deposition velocity can be calculated directly from the measurement of fluctuations, even if those have no absolute unit:

$$v_d = -\frac{\overline{w's'}}{\overline{s}} \; ; \qquad s\text{: sensor output (e.g. voltage)} \; . \tag{3.3}$$

The turbulent fluctuations need to be sampled with a high frequency to cover the frequency spectrum up to frequencies of 10-20 Hz. The time period for the measurement is depending on the atmospheric stability, the wind velocity and the measurement height. For daytime unstable stratification the time period is lower than for nighttime stable conditions. In most cases a time window of 30 minutes is taken for the whole day. For shorter periods the longwave contribution to the flux is missing and for longer periods the conditions might not be considered as stationary.

3.3 Data processing

For the processing of measured data, a variety of software packages is available, which have been tested in inter-comparison experiments (Mauder et al., 2008). They differ slightly in the application of corrections and quality control measures.
For this work, the fluxes are calculated by the well-known eddy-covariance software TK3 from the University of Bayreuth (for a detailed description see Mauder and Foken, 2011). The software applies lag correction, coordinate rotation and spectral corrections. In addition, it also performs a spike detection in advance and it has a module for quality assurance and quality control (QA/QC), which checks for stationarity and well-developed turbulence. The application of corrections is closely connected to the quality control. Furthermore, the output of an estimate for the random error is included, which consists of a stochastic error after Finkelstein and Sims (2001) and instrumental noise according to Lenschow et al. (2000). The new software including the error estimation is described by Mauder et al. (2013). As the software's ozone channel is not fully implemented yet, the ozone data was inserted into the N_2O channel and the resulting flux was converted into the ozone flux by considering the different molecular weights.
The results of the TK3 software package were compared with those obtained with a MATLAB code, which was developed at Max Planck Institute for Chemistry (MPIC) by Z. Zhu (Institute for Geographic Sciences and Natural Resources Research, Chinese Academy of Sciences (CAS), Beijing, China). The code was used for the evaluation of ozone fluxes during the first phase of the EGER project (EGER-IOP1&2). The same corrections as in TK3 are performed, but no spike detection is done and it includes no error estimation or QA/QC module. The MPIC code was partly rewritten by the author to be compatible with the data from EGER-IOP3.

As most measurement sites do not meet all assumptions for the EC technique (like horizontal homogeneous surface or simultaneous measurement of all variables at exactly the

same place), some corrections have to be applied, which are described in section 3.3.2. The estimation of the flux error and the quality control measures are described in sections 3.3.3 and 3.3.4.

3.3.1 Pre-processing of the data

The raw data obtained by the measurements is not necessarily correct due to nonmeteorological events like bug strikes of the sensor or voltage surges in the power supply. To get physical correct data, pre-processing steps are applied on the time series (Mauder and Foken, 2011). The first step is to get rid of spikes in the time series, which are unrealistically large or small values associated with nonmeteorological events (Stull, 1988). Therefore, plausibility tests are applied on the measured time series. Electronic and meteorological plausibility tests recognize wrong values. Those and missing values shall be neglected. For all measured variables (like concentrations, wind speeds, temperature) consistency limits are given and measurements exceeding these values are excluded from the flux calculation. Technical problems are not seperable from inappropriate meteorological influences and both have to be exposed.
Two different approaches are used to detect spikes. Following Vickers and Mahrt (1997) and Hojstrup (1993) the spike detection is performed for the data of the airfield Mainz-Finthen. Spikes are defined as values exceeding 4.5 times the standard deviation in a shifting window of 15 values, provided that this is not fulfilled for more than three values in a row. The spike elimination is run 5 times, increasing the standard deviation threshold by 0.1 in each round. Another method of detecting spikes, which is utilized by the eddy-covariance software package TK3, is the use of Median Absolute Deviation (MAD). The advantage of this method, compared to the afore mentioned, is its lower computational cost as it avoids iterations. A data point x_i is flagged as a spike if it is not in the range

$$\langle x \rangle - \frac{q \cdot \mathrm{MAD}}{0.6745} \leq x_i \leq \langle x \rangle + \frac{q \cdot \mathrm{MAD}}{0.6745} \,. \tag{3.4}$$

$\langle x \rangle$ denotes the median of x, $\mathrm{MAD} = \langle |x_i - \langle x \rangle \,| \rangle$ and q is a threshold value which is set to 7. MAD is a more robust statistical metric than the test by Vickers and Mahrt (1997) (Mauder et al., 2008).

Due to the transfer of sampled air from the inlet to the instrument, the application of closed-path instruments results in a time lag in the order of seconds. To consider the influence of the drift of turbulent eddies with the wind through anemometers and additional sensors and to adjust for slightly changing tube delay of closed-path sensors, a cross-correlation analysis is performed for a time window of ± 20 timesteps around a given lag time estimated by tube length and flow rate (Mauder and Foken, 2011). After the analysis, the time series of the signal is shifted against that of the vertical wind velocity by the time lag matching the maximum of the cross-correlation (Foken, 2008). The cross-correlation also corrects for the time it takes for an eddy to get from one sensor to the other, if there is a sensor separation in longitudinal wind direction (Moore, 1986). For the correction of the lateral separation the angle between the sensors and the wind direction have to be known.

Missing values are not replaced by interpolation, but they are marked as missing values and excluded from the calculations. A time series should not consist of more than 10 $\%$

missing values, otherwise the half-hour data is discarded (Mauder and Foken, 2011). In the case of spectral calculations, no missing values are allowed in-between the time series and respective 30 minute periods are neglected.

3.3.2 Corrections

From the pre-processed data series variances, covariances and other statistical moments are calculated. Due to violations of assumptions of the underlying theory, several corrections are necessary for eddy-covariance flux measurements (Mauder and Foken, 2011). A detailed description can be found in Foken (2008) and Mauder and Foken (2011) and in the following sections only the corrections having an effect on the ozone flux will be introduced.

3.3.2.1 Coordinate rotation

The eddy-covariance method requires a zero mean vertical velocity. In order to fulfill this prerequisite, the data is corrected by a rotation into the mean wind (Foken, 2008). Therefore, a transformation is performed from the sonic anemometer coordinate system (index m) to a coordinate system with $\overline{w} = 0$. This is done by matrix multiplication with a rotation matrix **A**. The full coordinate transformation consists of three rotations around the three axes of the coordinate system, described by three rotation matrices (**B**, **C**, **D**) and three angles, with $\mathbf{A} = \mathbf{BCD}$:

$$\begin{bmatrix} u_m \\ v_m \\ w_m \end{bmatrix} = \mathbf{A} \begin{bmatrix} u \\ v \\ w \end{bmatrix} \quad . \tag{3.5}$$

To receive a zero vertical velocity, two different methods to determine the rotation angles are available, which work on different time scales. The first one is the Planar Fit method after Wilczak et al. (2001), which is applied on the data of EGER-IOP3. The vertical wind velocity is averaged to zero over the whole data set or a longer time range (days to weeks). The rotations are directed to the mean stream lines for a site with unchanged setup of the sonic anemometer. The angles of the rotation are calculated by multiple linear regression and the steps of the coordinate rotation are shown in Fig. 3.2(b). An advantage is that it covers a wide range of wind directions, with a large diversity of points to fit the plane. In many cases, a turbulence data set of five days is long enough.
The second method is the Double Rotation method after Kaimal and Finnigan (1994), where $\overline{w}$ is set to zero for each half-hour period, indicated by the upper part of Figure 3.2(a). The coordinate system is turned to follow the stream lines. In tilted areas those are not necessarily normal to gravity. McMillen (1988) proposed a third rotation which should make the covariance between the vertical component and the component normal to the horizontal wind vanish (Kaimal and Finnigan, 1994). It has only minor impact on the fluxes and can create unrealistic values, thus only the first two steps are recommended (Aubinet et al., 2000). In case of disturbed periods (free convection, moving of the sensor), the Double Rotation method should be used, as those disturbances do not allow a rotation over a longer time period (Mauder and Foken, 2011). Therefore, the latter method was used for the coordinate rotation of the data of the airfield Mainz-Finthen.

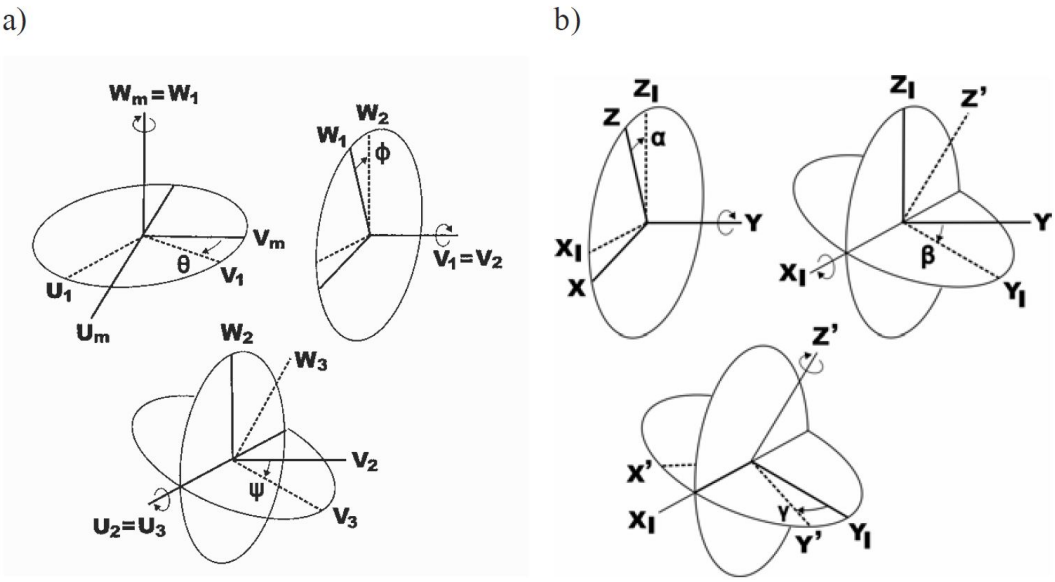

Figure 3.2: Steps of the coordinate rotation methods. (a) Double Rotation and (b) Planar Fit (taken from Foken, 2008).

Eddy-covariance software packages do not apply the coordinate rotation on the raw data, but on the already calculated averages, variances and covariances. In Equation 3.6 this is exemplarily shown for the horizontal and vertical flux of the temperature:

$$\begin{bmatrix} \overline{u'_m T'} \\ \overline{v'_m T'} \\ \overline{w'_m T'} \end{bmatrix} = \mathbf{A} \begin{bmatrix} \overline{u'T'} \\ \overline{v'T'} \\ \overline{w'T'} \end{bmatrix} \quad . \tag{3.6}$$

A detailed description of the coordinate rotation methods can be found in Foken (2008) and Mauder and Foken (2011), giving the respective rotation angles and matrices.

3.3.2.2 Spectral correction

The next step in the correction procedure is to adjust the spectral resolution of the measurement system to the actual turbulence spectrum. The characteristic distribution of the turbulence elements by their size can be described by the turbulence spectrum, which is the energy distribution of turbulent eddies according to their wave number or frequency. Turbulent kinetic energy (TKE), which consists of the contributions of the energy of the different size eddies, is produced by buoyant forces or by shear of the mean flow. Initially, this energy passes over to large turbulence elements. In the power spectrum, which is shown in Figure 3.3, this range is called production range **P** and contains the energy-containing eddies (f about 10^{-4} Hz). In the inertial subrange **I** the energy is passed from the larger to smaller scales down to the molecular range in a cascade process. The energy coming from energy-containing eddies is in equilibrium with the net energy cascading to smaller eddies, resulting in a constant decay of energy density with frequency. The decrease of energy density by the decay of larger into smaller elements happens after Kolmogorov's

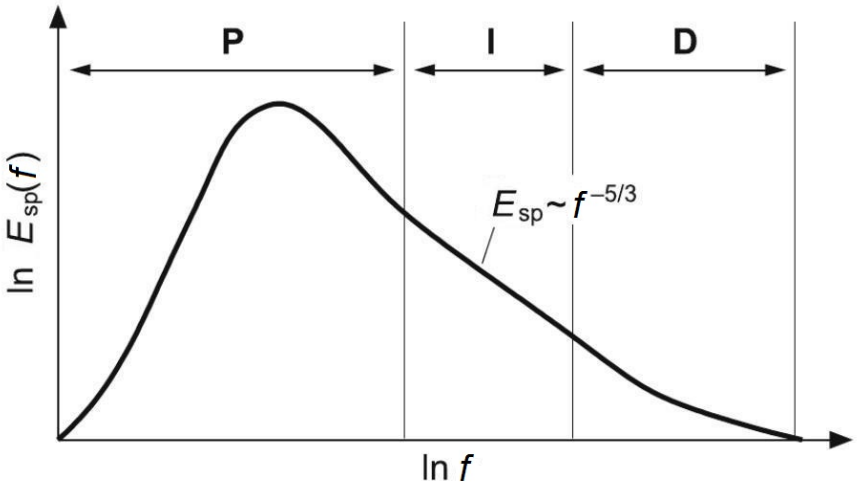

Figure 3.3: Schematic presentation of a power spectrum of the atmospheric boundary layer related to the frequency. Indicated is the range of production **P**, the inertial subrange **I** and the range of dissipation **D** (following Kraus, 2008).

$-5/3$ law (Kolmogorov, 1941), which describes the spectral energy E_{sp} in relation to the frequency f:

$$E_{\text{sp}}(f) \propto f^{-\frac{5}{3}} \, . \tag{3.7}$$

In contrast to TKE, the cospectral density of fluxes decreases with $f^{-7/3}$ in the inertial subrange (Foken, 2008). In the dissipation range **D** (f about 10-30 Hz) the transition of energy to frictional heat (by the decay of the smallest eddies) takes place due to molecular friction. The largest portion of the total energy is contained in the large eddies, the small eddies provide only a minor contribution to the total energy (see Fig. 3.3). The position of the peak and the general level of the (co)spectral energy or density is dependent on the meteorological quantities, the stability (stratification of the ABL), the height and the wind velocity (Foken, 2008). Under unstable conditions, when the potential temperature decreases with height, the atmosphere is well mixed by turbulence. An increasing potential temperature with height characterizes a stable stratification. Due to the limited turbulence under stable conditions, the impact of smaller eddies increases and the peak in the spectrum is shifted to higher frequencies.

It is beyond the power of measurements to capture the complete (co)spectrum. There are several sources for underestimating the flux due to the instrumentation and the setup of the measurement system. Long instrument response times (of gas analyzers) cause imperfect response of the system to high-frequency fluctuations. A displacement between the sensors and spatial averaging of the wind speed values along the sound pulse measuring path also affect the high frequencies and concentration fluctuations are attenuated during the transport through long sample lines.
In the longwave range a limitation is that a measurement time of 30 minutes is not necessarily sufficient to capture all longwave fluxes. An extension of the averaging interval could counteract this limitation, but longwave events, which are not connected to the turbulent flux, might add to the determined flux.

The corrections of the spectral loss are performed following Moore (1986) and the error $\frac{\Delta F}{F}$ can be expressed by (Mauder and Foken, 2011):

$$\frac{\Delta F}{F} = 1 - \frac{\int_0^\infty T_{x(y)}(f) \cdot S_{x(y)}(f) df}{\int_0^\infty S_{x(y)}(f) df} \,, \tag{3.8}$$

where ΔF is the correction of the flux F. To evaluate the error, the theoretic (co)spectrum S of the variable x (in case of cospectrum of the variables x and y), as well as the specific transfer function $T_{x(y)}$ have to be known, which are both functions of the natural frequency f. $\frac{\Delta F}{F}$ is a factor applied to the fluxes in order to correct for the underestimation of the flux due to the inability of the system to respond to the high frequencies (Aubinet et al., 2001).

To apply the correction given by Equation 3.8, the eddy-covariance software packages use modeled instead of measured spectra. That way, the computational cost of the spectra calculation is reduced. The stability dependent spectra are taken from Kaimal et al. (1972) and rely on the measurements during the Kansas experiment. In order to correct mass fluxes of e.g. H_2O, CO_2, O_3, the cospectrum of the sensible heat flux $\overline{w'T'}$ is used, as for the temperature flux no frequency loss is assumed. Furthermore, spectral similarity between the temperature and the scalars of interest is expected. Therefore, only the cospectrum between the vertical wind velocity w and the temperature T is exemplarily shown. For unstable stratification it is modeled after Kaimal et al. (1972):

$$\frac{f \cdot S_{wT}(f)}{\overline{w'T'}} = \begin{cases} \dfrac{11n}{(1+13.3n)^{1.75}} & n < 1 \\ \dfrac{4.4n}{(1+3.8n)^{2.4}} & n \geq 1 \end{cases} \tag{3.9}$$

and the stable cospectrum is also parameterized after Kaimal et al. (1972):

$$\frac{f \cdot S_{wT}(f)}{u_* T_*} = \frac{0.88 \dfrac{n}{n_0}}{1 + 1.5 \left(\dfrac{n}{n_0}\right)^{2.1}} \,, \tag{3.10}$$

$$n_{0,wT} = 0.23 \cdot \left(1 + 6.4 \frac{z}{L}\right)^{0.75} \,, \tag{3.11}$$

$$n = \frac{f \cdot z}{\overline{u}} \,, \tag{3.12}$$

where n is the normalized frequency. $\overline{u}$ is the mean horizontal velocity and z is the height above zero-plane displacement. The displacement height is the height within the canopy, where the logarithmic wind profile would become 0. z/L represents the stability with the Obukhov length L. For the normalization of the stable spectrum, the friction velocity u_* and the scaling temperature T_* are used.

The transfer function for a measurement of vertical velocity w and a scalar quantity c is defined as the product of single transfer functions for the temporal resolution with the time constant of the sensor response τ, the sampling path length p and the separation length between the instruments s:

$$T_{w,c}(f) = \sqrt{T_{\tau,w}(f)} \cdot \sqrt{T_{\tau,c}(f)} \cdot \sqrt{T_{p,w}(f)} \cdot \sqrt{T_{p,c}(f)} \cdot T_{s,w,c}(f) \,. \tag{3.13}$$

Transfer functions for the high-frequency losses due to path length averaging are given by Moore (1986) for vertical velocity w (also valid for horizontal wind velocity u)

$$T_{p,w}(n) = \frac{2}{\pi n} \cdot \left(1 + \frac{e^{-2\pi n}}{2} - \frac{3(1 - e^{-2\pi n})}{4\pi n}\right) \tag{3.14}$$

and scalars c (T, H_2O, CO_2)

$$T_{p,c}(n) = \frac{1}{2\pi n} \cdot \left(3 + e^{-2\pi n} - \frac{4(1 - e^{-2\pi n})}{2\pi n}\right) , \tag{3.15}$$

$$n = \frac{f \cdot p}{\overline{u}} , \tag{3.16}$$

where n is a normalized frequency with the path length p and the mean horizontal velocity $\overline{u}$.
For the high-frequency loss due to the separation of the sensors s, the theoretic transfer function is also given by Moore (1986):

$$T_{s,w,c}(n) = e^{-9.9n^{1.5}} , \tag{3.17}$$

$$n = \frac{f \cdot s}{\overline{u}} . \tag{3.18}$$

For the lateral separation between wind and scalar sensor $s_{lateral}$, Eq. 3.17 can only be used in the unstable case, if the separation is less than 10 % of the aerodynamic measurement height. The separation should not be greater than 0.7 % of the Obukhov length under stable stratification. The separation lateral to the wind direction is calculated from the total separation s_{total} by

$$s_{lateral} = s_{total} \cdot |sin(dir)| , \tag{3.19}$$

where dir is the wind direction. If there is only a vertical displacement between the instruments, $s = s_{lateral} = s_{total}$ is valid. A correction of the longitudinal separation only needs to be applied, if no cross-correlation was performed before.
Additional high-frequency losses can occur due to the instrument response time and can be corrected if the response time τ is known by:

$$T_{\tau,w}(f) = T_{\tau,c}(f) = \left[1 + (2\pi f \tau)^2\right]^{-0.5} . \tag{3.20}$$

The eddy-covariance software package TK3 performs no flux correction for the attenuation of fluctuations in the sampling tube. This correction is described in section 3.4.

3.3.3 Estimation of the flux error

Flux measurements are prone to systematic and random errors. Random errors originate from the stochastic nature of turbulence and the instrumental noise as well as uncertainty attributable to changes in footprint (Mauder et al., 2013). The first one is called stochastic error and is due to inevitable sampling limitations resulting from a finite sampling time (Lenschow et al., 1994). To capture the entire statistical ensemble of a turbulent flux, one would have to measure at an infinite number of masts on an infinite plane above a

homogeneous canopy for an infinite time period under stationary conditions. Stochastic errors can be reduced by increasing the number of measurements. The instrumental noise can be understood as the scatter of the wind measurement under zero wind conditions (Lenschow and Kristensen, 1985). It is estimated by analyzing the high-frequency data series. The error due to changes in the footprint can only be determined if fluxes are known for all land cover types surrounding the sensor. Based on footprint modeling it can be decided if a flux estimate is representative for the ecosystem of interest.
The random error is recognized in the high-frequency part of the variance spectrum and can be estimated by integrating a certain percentage of the high-frequency end of the spectrum (e.g. 0.8-1.0 times the Nyquist frequency f_N). Another possibility is to receive it from the signal cross-correlation using the property of white noise beeing uncorrelated. A quantity x can be decomposed into its mean part $\overline{x}$, the deviation from the mean x' and a white noise term ϵx: $x = \overline{x} + x' + \epsilon x$. The second-order auto-covariance between the measurement and the time-shifted measurement is calculated depending on the time shift. If the noise is uncorrelated with the signal, its term only appears at zero lag in the auto-covariance. Thus, the variance of the noise error can be estimated. The instrumental noise of the covariance $cov(x, y)$ of variables x and y with errors ϵx and ϵy is calculated by error propagation with N beeing the number of observations used for the calculation of the covariance:

$$\sigma^{\text{noise}}_{cov(x,y)} = \sqrt{\frac{1}{N}} \sqrt{\overline{\epsilon x^2 y'^2} + \overline{\epsilon y^2 x'^2}} \,. \tag{3.21}$$

Following the algorithm of Finkelstein and Sims (2001) to receive the statistical variance of the covariance, the stochastic error is determined:

$$\sigma^{\text{stoch}}_{cov(x,y)} = \sqrt{\frac{1}{N} \sum_{p=-m}^{m} (\overline{x'x'_p} \cdot \overline{y'y'_p} + \overline{x'y'_p} \cdot \overline{y'x'_p})} \,, \tag{3.22}$$

where the index p denotes the time-shifted variable, which is shifted between $-m$ and m time steps against the measurement. The summation bound should be $m = N/2$ or it should be at least the integral time scale of the auto-covariances.
Random errors are partly corrected by the corrections described in section 3.3.2.2.

Systematic errors can be caused by e.g. an insufficient length of the time series for the flux determination, flow distortion by the anemometer, a time shift between wind speed and gas concentration data, imperfect frequency response of the concentration measurement instrumentation, changes in analyzer's sensitivities and horizontal inhomogeneity of the surface (McMillen, 1988; Lenschow et al., 1994; Kaimal and Finnigan, 1994; Foken and Wichura, 1996). Systematic errors either have a positive or a negative sign. If the error results from a recognized effect, it can be quantified and a correction can be applied to compensate for the effect. There are errors resulting from unmet assumptions or from instrumental calibration and errors associated with data processing. The two latter ones can be minimized by calibration and application of all required corrections. For the first one quality tests can be applied.

3.3.4 Quality assurance and quality control (QA/QC)

The quality assurance is a combination of the application of corrections and the exclusion of meteorological influences like internal boundary layers, gravity waves and intermittent turbulence. The goal is to prove that the applied simplifications of the eddy-covariance method are justified under the given micrometeorological conditions.
One assumption of the EC method is the existence of stationary conditions. According to Foken and Wichura (1996), this can be tested by comparing fluxes of different averaging intervals. On the one hand, the flux is determined for M (= 6) short intervals of 5 minutes and than averaged:

$$\begin{aligned} \left(\overline{x'y'}\right)_i &= \frac{1}{N-1}\left[\sum_j x_j \cdot y_j - \frac{1}{N}\left(\sum_j x_j \cdot \sum_j y_j\right)\right] \\ \overline{x'y'} &= \frac{1}{M}\sum_i \left(\overline{x'y'}\right)_i , \end{aligned} \tag{3.23}$$

where N is the number of measuring points within the short interval. On the other hand the flux is calculated for the whole 30 minute interval. The conditions can be estimated as stationary if both fluxes differ by less than 30 $\%$. A classification of the quality is gained by subdividing the differences into percentage classes.
Another main prerequisite of the EC method is that the turbulence is well developed. The fulfillment of this prerequisite is investigated by flux-variance-similarity (Foken and Wichura, 1996). Integral turbulence characteristics (ITC) of the measurement are compared with those of model presentations and the quality is assigned by the magnitude of the deviation (Foken, 2008):

$$ITC_\sigma = \left| \frac{\left(\frac{\sigma_c}{c_*}\right)_{\text{model}} - \left(\frac{\sigma_c}{c_*}\right)_{\text{measurement}}}{\left(\frac{\sigma_c}{c_*}\right)_{\text{model}}} \right| . \tag{3.24}$$

It is tested whether the ratio of the standard deviation of a turbulence parameter and its turbulent flux is nearly constant or a function of e.g. the stability. Functions determined by Foken et al. (1991) are used for the test after Foken and Wichura (1996). The functions depend on stability and resemble standard deviations of wind components

$$\frac{\sigma_{u,v,w}}{u_*} = c_1 \cdot \left(\frac{z}{L}\right)^{c_2} , \tag{3.25}$$

where u is the horizontal or longitudinal wind component, v the lateral wind component, u_* is the friction velocity and L the Obukhov length. The standard deviations for scalar fluxes are normalized by their dynamical parameters c_* (e.g. T_* for the temperature)

$$\frac{\sigma_c}{c_*} = c_1 \cdot \left(\frac{z}{L}\right)^{c_2} . \tag{3.26}$$

The coefficients c_1 and c_2 depend on stability and are given by e.g. Mauder and Foken (2011). The test can be performed for the ITC of both parameters used to determine the

Table 3.1: Combination of single quality tests to an overall quality flag after Foken (1999).

Quality flag	Stationarity	ITC
1	1	1-2
2	2	1-2
3	1-2	3-4
4	3-4	1-2
5	1-4	3-5
6	5	$\leq$5
7	$\leq$6	$\leq$6
8	$\leq$8	$\leq$8
9	9	9

covariance and according to the value of ITC_σ it can be said if well developed turbulence can be assumed and the covariances are classified (Mauder and Foken, 2011).

The results of the single quality test are combined to an overall flag using the scheme after Foken (1999) shown in Table 3.1 with quality flags between 1 and 9. The quality flag for a flux composes of the result of the steady state test and the ITC-test. Highest priority is given to the test on stationarity. An overall flag of 1-3 indicates high quality of the data and the fluxes can be used for fundamental research. Fluxes with flags of 4-6 can be employed for continuous measurements, fluxes with flags of 7-8 should only be used for orientation and fluxes with a flag of 9 should always be excluded. For the further analysis only fluxes with flags of 1 to 6 are considered.

Moreover, poor quality of the data can be caused by e.g. rain, which cannot be identified by the previously described methods. In order to exclude these data, the raw data of the ozone sensors is checked manually for time periods where the sensors give wrong values and the fluxes for those periods are neglected. This is mainly the case during or after rain events. In addition to these high-humidity events, there are discs that produce data with a lot of fluctuations not originating from atmospheric ozone fluctuations during their entire runtime or discs with a very low sensitivity, whose data is excluded from the analysis.

3.4 Comparability of ozone flux measurement systems

Ozone fluxes are measured by systems using closed-path instruments, where the sampled air is transported from the inlet close to the sonic to the instrument through tubing. During field experiments it is not always possible to mount the instrument close to the sonic and the use of longer inlet tubes is inevitable. However, to derive fluxes, precise measurements of the scalar concentrations are crucial (Massman, 1991). An imperfect frequency response of the concentration measurement due to the attenuation of fluctuations in the tubing is the reason for a systematic error (Keronen et al., 2003). The systematic difference between individual experimental setups applying different chemiluminescence sensors and tube lengths needs to be investigated. This is necessary to ensure accuracy, precision and

comparability of eddy-covariance systems. Comparisons of measurement instruments are a basic requirement for their reliable use, and to determine the underestimation of the flux, it is useful to validate the measured flux with independent and reliable methods. For closed-path CO_2 instruments this is achived by comparisons with open-path instruments, which are not influenced by tranfer times through a tube. As for the measurement of ozone fluctuations no open-path instrument is available, intercomparisons of several closed-path instruments are performed instead.
To be able to discuss individual characteristics of ozone flux measurement systems, power- and cospectra are calculated by fast Fourier transform (FFT). In advance of this calculation some data pre-processing steps need to be taken.

3.4.1 Attenuation of fluctuations in the inlet tube

In section 3.3.2.2 the spectral corrections implemented in eddy-covariance software packages are described, but for the determination of ozone fluxes also the attenuation of concentration fluctuations inside the inlet tube affects the accuracy of the measurement. In closed-path instruments, the sampling tubes act as high-frequency filters and the damping of fluctuations takes place due to the radial variation in streamwise air velocity and because of radial diffusion (Leuning and King, 1992). Radial diffusion is increased by turbulence, which decreases the filtering effects of differing advection rates as a function of the tube radius (Leuning and King, 1992). The state of the turbulence in the tube is defined by the Reynolds number, which gives the ratio of inertial to viscous forces and indicates when statically neutral flow becomes turbulent ($Re \geq Re_{\text{crit}}$ ~2300; Stull, 1988). The damping effect of a tube is reduced by a smaller radius of the tube or an increased volumetric flow rate. Furthermore, reducing the length of the sampling tube improves the frequency response, as it reduces the time available for damping of fluctuations in the tube. The theory behind the attenuation and the derivation of the transfer functions for flux attenuation is described by Massman (1991), Lenschow and Raupach (1991) and Leuning and King (1992). The transfer function is derived from the convective diffusion equation to describe lateral and longitudinal dispersion of a solute or a trace gas being convected along a straight horizontal tube. It results in theoretic functions for turbulent and laminar (Re lower than critical Reynolds number) flow. The theoretic transfer function for low-pass filtering in an inlet tubing with turbulent flow $T^{\text{theo}}_{x,\text{turb}}$ after Lenschow and Raupach (1991) is found in Leuning and King (1992) with a minor change:

$$T^{\text{theo}}_{x,\text{turb}}(f) = e^{-160 Re^{-1/8} a l U^{-2} f^2} \tag{3.27}$$

with the Reynolds number $Re = 2Q/(\pi a \nu)$, where Q is the volumetric flow rate in the tube, a is the radius of the tube and ν is the kinematic viscosity of air. U is the mean flow velocity in the tube and l is the length of the tube.
Closed-path ozone instruments applied with a low flow rate and/or a large tube radius result in a laminar flow in the tube. The transfer function for laminar flow is given by Lenschow and Raupach (1991):

$$T^{\text{theo}}_{x,\text{lam}}(f) = e^{-0.41 (ReSc) a l U^{-2} f^2}\ , \tag{3.28}$$

where Sc is the Schmidt number with $Sc = \frac{\nu_{air}}{\nu_{O_3}} = 0.85$, according to Zahn et al. (2012).

3.4.2 Processing of the measured time series

For the determination of correction factors for the underestimation of the flux, spectra have to be calculated. Before calculating spectra, some pre-processing steps need to be performed on the raw time series of ozone, temperature and vertical wind velocity fluctuations, resembling those of the flux calculation procedure presented in section 3.3. These steps consist of despiking of the raw data after Vickers and Mahrt (1997), performing a coordinate rotation (double rotation), detrending of the time series and a lag correction. A linear detrending is performed on fixed five minute intervals. In addition to the usual despiking procedure, an additional routine is run for the data from the second phase of the experiment at the airfield Mainz-Finthen to remove erroneous data due to the malfunctioning instrument mounted at the beginning of this phase of the experiment (see section 2.2). The erroneous data in the time series can easily be distinguished from unaffected data. A simple approach is used to get rid of this data. All data points being outside of $\bar{x} \pm 0.25\bar{x}$ on five minute averaging intervals are eliminated. Afterwards the data is detrended by subtracting the average value using the same five minute window. To correct for noise and aliasing, low-pass filtering can be performed by applying a moving average of different lengths on the raw data. A time lag between the measurement of the vertical wind velocity and the ozone fluctuations is determined by maximizing the cross-correlation around the fixed lag time determined by flow rate measurements. From the pre-processed time series fluxes are calculated, which are spectrally corrected for sensor separation and path-length averaging of the sonic.
As the calculation of eddy-covariance fluxes is performed for 30 minute periods, also the time series for the calculation of spectra are divided into sections of 30 minutes, which are processed individually. To transform the discrete measured data from physical space to phase space the fast Fourier transform (FFT) is applied (Stull, 1988). That way, spectra for the specific setup of the measurement system are determined. To fit the points of the time series, it is broken into a finite number of sine and cosine waves of different frequencies, which are associated with eddies of different sizes. The largest frequency that can be resolved is the Nyquist frequency $f_N = N/2$ as a minimum of two data points per period or wavelength is necessary to resolve a wave (Stull, 1988). Integrating the energy density spectrum S_x of a variable x corresponds to the total variance of a time series and $S_x(f)$ can be interpreted as the portion of the variance, which can be explained by eddies of the frequency f. The frequency spectrum between two variables x and y is called cross-spectrum and its real part is the cospectrum Co_{xy}. Integrating the cospectral density spectrum over all frequencies yields the covariance.
Only spectra under certain conditions are considered in the analysis. An important prerequisite to calculate spectra is a time series, which is free of gaps, as those are not allowed for the spectra calculation. The quality flag has to be between 1 and 6 for the ozone and latent heat flux. The ozone flux also has to be negative as positive fluxes are physically incorrect and a good quality of the chemical disc in the ozone sensor is assured by only using positive mV-signals. For the selection of the time periods, also meteorological conditions are accounted for. For the temperature a range of 20-30 °C is chosen. The limit for the relative humidity is set to $\leq$65 % to neglect high humidity conditions, which could have an effect on the inside of the tube. Mammarella et al. (2009) have shown that the attenuation of water vapor fluxes in a tube is dependent on the relative humidity by increasing

the attenuation with relative humidity due to adsorption/desorption processes at the tube walls. In addition, the sensitivity of the chemical disc in the ozone sensor is dependent on humidity and a high humidity leads to distorted signals. Noticeable outliers are excluded as well, which are set as correction factors smaller than -5 or larger than 10.

3.4.3 High-frequency loss correction procedure

After the calculation of the cospectra, the cospectra of vertical wind velocity and temperature as well as ozone are compared. If measured with adequate accuracy, the heat flux cospectrum is expected to represent the ideal shape of the cospectrum and assuming scalar similarity the true unattenuated ozone flux cospectrum would look the same (Mammarella et al., 2009). As in the spectral correction procedure presented in section 3.3.2.2, the correction is determined as the ratio between unattenuated and attenuated spectrum. According to Moore (1986) the frequency correction factor ϵ_x is determined by

$$\epsilon_x = \frac{\int_0^\infty Co_{wx}(f)df}{\int_0^\infty T_x(f)Co_{wx}(f)df} , \tag{3.29}$$

where Co_{wx} is the cospectral density of the vertical wind velocity w and the scalar quantity x (ozone mixing ratio) and $T_x(f)$ is the total transfer function of the eddy-covariance system. The numerator in Eq. 3.29 is the flux that should be measured if the system was perfect and the denominator gives the flux that is really measured. Theoretic descriptions of transfer functions are given by Moore (1986), Leuning and Moncrieff (1990), Leuning and King (1992) and in section 3.3.2. For closed-path systems the correction depends to a large extent on the attenuation of concentration fluctuations down the sampling tube.
If the transfer function is known, the correction factor can be estimated by Eq. 3.29 using the cospectrum Co_{wx} parameterized after Kaimal et al. (1972). Under unstable and near neutral conditions, the cospectrum Co_{wx} depends only on the measurement height and the horizontal wind velocity. Thus, for a system placed at a fixed height, the correction factor is only a function of wind velocity (see Eq. 3.9). Under stable stratification the stability factor z/L needs to be considered as well (see Eq. 3.10).
For the side-by-side intercomparison at the airfield Mainz-Finthen, the transfer functions of the measurement systems consisting of ozone sensor and inlet tube are unknown and need to be determined from the measurement. In this case, the transfer function and the correction factor can be determined from measured cospectra following Aubinet et al. (2001) and the transfer function is defined as

$$T_x^{\text{exp}}(f) = \frac{Co_{wx}^{\text{exp}}(f)}{Co_{wx}} , \tag{3.30}$$

where Co_{wx} is the unattenuated ozone flux spectrum. As no attenuation of the temperature is assumed, the cospectrum of sensible heat (Co_{wT}^{exp}) is taken as ideal unattenuated spectrum and is compared to the ozone flux spectrum (Co_{wx}^{exp}) affected by attenuation. Taking the heat flux cospectrum is an idealized assumption as the sonic anemometer dampens the temperature and vertical wind velocity signal due to spatial averaging and electronic restrictions. Over rough surfaces in the boundary layer and measurements above the dis-

placement height, these effects are negligible. Thus Eq. 3.30 can be rewritten to

$$T_x^{\text{exp}}(f) = \frac{Co_{wx}^{\text{exp}}(f)/Co_{wx}}{Co_{wT}^{\text{exp}}(f)/Co_{wT}} \,. \tag{3.31}$$

The ratio of real cospectral densities can be replaced by the ratio of covariances, if the exchange processes of sensible heat and ozone are assumed similar:

$$T_x^{\text{exp}}(f) = \frac{\overline{w'T'}Co_{wx}^{\text{exp}}(f)}{\overline{w'x'}Co_{wT}^{\text{exp}}(f)} \,. \tag{3.32}$$

The low-pass filtering due to the high-frequency attenuation reduces the covariance of the measured scalar (Ibrom et al., 2007) and the covariance is potentially enhanced by the sensor's noise. As the measured covariance $\overline{w'x'}$ is lower than the real one, the relation in Eq. 3.32 cannot be used directly. The ratio of covariances is alternatively replaced by a ratio of normalization factors:

$$T_x^{exp}(f) = \frac{N_T Co_{wx}^{exp}(f)}{N_x Co_{wT}^{exp}(f)} \,, \tag{3.33}$$

where the ratio is defined as

$$\frac{N_T}{N_x} = \frac{\int_{f'}^{f''} Co_{wT}^{exp}(f)df}{\int_{f'}^{f''} Co_{wx}^{exp}(f)df} \,. \tag{3.34}$$

The upper frequency limit f'' of the integration is chosen to be low enough for the attenuation to be negligible in the integrals in Eq. 3.34, but high enough to capture a sufficient number of data points to estimate the integral to keep a low uncertainty of the normalization factor. Both cospectra are affected by attenuation in the low-frequency range due to the 30 minute cut-off of the flux measurement period and due to the detrending procedure. Therefore, the integral for the determination of the ratio of normalization factors is not started at 0 Hz, but at an unattenuated lower limit frequency f'. In addition, to exclude the effect of different attenuations in the low-frequency range from the determination of the transfer function and the correction factor, the portion of the covariance between w and O_3 up to f'' is set equal to that of the heat flux cospectrum, as only the high-frequency loss is of interest.
Some frequency loss factors that concern both the heat flux as well as the ozone flux cospectra (i.e. path averaging of sonic) are not considered by the transfer function, but the function contains the effects of sensor separation and attenuation of fluctuations in the tube, which are most important factors for closed-path systems (Aubinet et al., 2001). To consider only the effect of attenuation of concentration fluctuations down the tube, the theoretic transfer function for sensor separation can be applied to the heat flux spectrum. A correction for sensor separation is usually performed by eddy-covariance software packages, but the packages do not correct for the attenuation of fluctuations in the tube.

The upper and lower limit frequencies used for the normalization factors during the experiment at the airfield Mainz-Finthen are slightly shifted as they cannot be determined exactly. Thus, mean values and standard deviations of the correction factor are obtained. For the lower limit frequency values of 0.04, 0.05 and 0.06 Hz are used and the upper limit

frequency varies between 0.14, 0.15 and 0.16 Hz. Thus, a total number of $N = 9$ correction factors is gained for each half hour. During the EGER side-by-side measurement the frequency range was set to 0.007-0.07 Hz, due to longer inlet tubes, which cause a dampening of the spectrum already at lower frequencies.

4 Modeling of atmosphere-biosphere exchange of trace gases

For the analysis of surface layer observations of concentrations and fluxes in terms of surface sources, sinks and transport, the application of a model is required. Models have the advantage of being able to extrapolate measurements towards larger regions and their results can be used to close gaps in measured time series if the model has been validated before. For EGER-IOP3 modeling studies are performed in addition to the measurements as ozone fluxes have been measured at only three positions on a 4 km^2 measurement site.

This chapter introduces the model applied for the modeling of ozone fluxes during the EGER campaign. Section 4.1 describes the implemented processes and settings. Section 4.2 describes the setup of the modeling studies.

4.1 The Multi-Layer Canopy CHemistry Exchange Model MLC-CHEM

The Multi-Layer Canopy CHemistry Exchange Model (MLC-CHEM) is used for modeling studies of the ozone exchange between atmosphere and biosphere. It is based on the implementation of canopy exchange processes in the Earth system model EMAC (ECHAM5/ MESSy Atmospheric Chemistry model, e.g. Ganzeveld et al., 2010). MLC-CHEM is a stand-alone multi-layer canopy exchange model, which simulates the exchange of reactive compounds and aerosol inside and above vegetation canopies and allows the analysis of exchange measurements. The model is designed for the analysis of reactive compound observations in terms of emissions, deposition, chemistry and turbulence. A specific feature, distinguishing the model from other canopy exchange models, is the possibility of application for site-scale analysis and for explicit simulation of atmosphere-biosphere exchange in large-scale models.
The model calculates the different relevant processes determining atmosphere-biosphere fluxes of reactive compounds as O_3, NO_x and VOCs as well as aerosols. It can be used to analyze surface layer observations of tracer concentrations and fluxes as a function of the observed micrometeorology and vegetation cover. As the model is based on the implementation in global-scale models, rather strong constraints are made to the model structure such that the process description is highly parameterized and coarse vertical and temporal resolution is applied. The approach is based on a large number of observations of dry deposition velocities of trace gases such as ozone and sulfur dioxide (Hicks et al., 1987). The effective exchange between the canopy and the above-lying atmosphere is determined by canopy interactions including biogenic emissions, chemical transformations (gas-phase

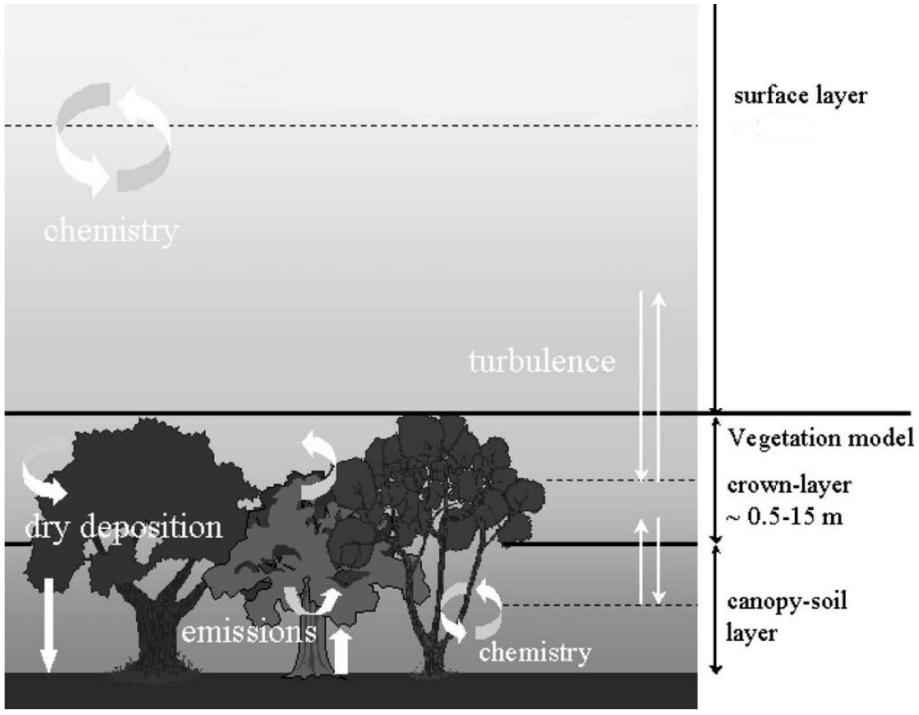

Figure 4.1: Schematic overview of the 2-layer vegetation model used to calculate the canopy top fluxes for the vegetation and wet skin fraction. Contributions of biogenic emissions, dry deposition and turbulence to the concentration changes at the refernce height of the canopy layers and surface layer (dotted lines) are calculated using the sub time step (STS), whereas chemistry calculations use the time step of the input data (modified after Ganzeveld et al., 2002b).

chemistry), dry deposition and turbulence. However, the prevailing processes differ between the canopy and the atmosphere above, which is presented in Figure 4.1.

In the layer above the canopy, the atmospheric surface layer (SL), the concentration tendency is calculated from the temporal derivatives over the vegetation, wet skin (ws) and bare soil fraction $fr_{\text{veg/ws/soil}}$ (Ganzeveld et al., 2002b):

$$\left(\frac{dc}{dt}\right)_{\text{SL}} = fr_{\text{veg}}\left(\frac{\partial c}{\partial t}\right)_{\text{veg}} + fr_{\text{ws}}\left(\frac{\partial c}{\partial t}\right)_{\text{ws}} + fr_{\text{soil}}\left(\frac{\partial c}{\partial t}\right)_{\text{soil}} . \tag{4.1}$$

In the surface layer over the bare soil fraction, the concentration tendency is calculated according to

$$\left(\frac{\partial c}{\partial t}\right)_{\text{soil}} = \left(\frac{\partial c}{\partial t}\right)_{\text{turb}} + \left(\frac{\partial c}{\partial t}\right)_{\text{emis}} + \left(\frac{\partial c}{\partial t}\right)_{\text{dep}} + \left(\frac{\partial c}{\partial t}\right)_{\text{chem}} . \tag{4.2}$$

This reflects the contributions by turbulent transport between the SL and the layer aloft, biogenic as well as anthropogenic emissions, dry deposition and chemical transformations. No chemical advection is considered, but providing surface layer concentrations can be interpreted as adding an advection term to the model.
The coupling with the biosphere is explicitely calculated by the vegetation model and the

equation for the surface layer above the vegetation and wet skin fraction is reduced to

$$\left(\frac{\partial c}{\partial t}\right)_{\text{veg/ws}} = \left(\frac{\partial c}{\partial t}\right)_{\text{turb}} + \left(\frac{\partial c}{\partial t}\right)_{\text{chem}} . \tag{4.3}$$

The change in the concentrations due to turbulence reflects the turbulent exchange between the surface layer and the layer aloft as well as the turbulent exchange between the surface layer and the canopy-top layer of the vegetation model.
Within the canopy, the temporal derivative of the concentration due to turbulent exchange, emissions, dry deposition and chemical transformations is calculated by:

$$\left(\frac{dc}{dt}\right)_{\text{canopy}} = \frac{\Delta F_{\text{turb}} + F_{\text{emis}} - F_{\text{dep}}}{\Delta z} + P_{\text{chem}} , \tag{4.4}$$

where Δz is the depth of the canopy layer. F_{emis} is the biogenic emission flux, F_{dep} the dry deposition flux and P_{chem} denotes the chemical production or destruction. The turbulent flux F_{turb} inside the canopy and between the canopy and surface layer is calculated based on local closure theory with the eddy diffusivity for heat K_H and the concentration gradient between the reference heights of the surface and canopy layers $\frac{\partial c}{\partial z}$:

$$F_{\text{turb}} = -K_H \frac{\partial c}{\partial z} . \tag{4.5}$$

The profile of the eddy diffusivity is estimated as the quotient between the height difference of the reference heights Δz and the aerodynamic resistance R_a in or above the vegetation.

4.1.1 Deposition, emission and photochemistry

The contribution of the dry deposition flux F_{dep} to the total flux is calculated from the surface layer concentration and the dry deposition velocity v_d:

$$F_{\text{dep}} = -c_z v_d = -\frac{c_z}{R_a + R_b + R_c} , \tag{4.6}$$

where c_z is the concentration at the reference height z. v_d is assumed to be independent on the respective trace gas concentration, while it is related to the atmospheric conditions and specific characteristics of the surface described in the following. For the calculation of v_d the resistance approach is applied (see Fig. 4.2). The flux is opposed to the resistances mounted in series. The meanings of the respective resistances are:

- R_a is the resistance of the turbulent air layer
- R_b is the resistance of the quasi-laminar air layer close to the surface elements
- R_c is the resistance of the surface, a combination of all pathways playing a role in the uptake of trace gases by the surface (stomatal, cuticle, mesophyll, wet surface, ocean water and bare soil resistance)

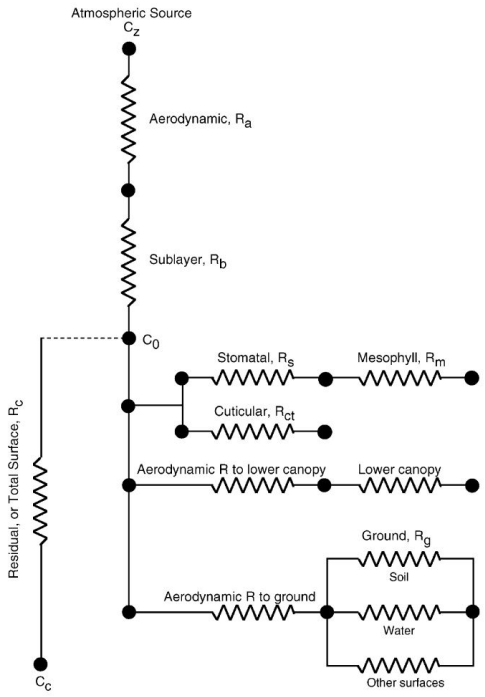

Figure 4.2: Schematic representation of resistances for some of the pathways for the dry deposition, where R represents resistances, c_z is the ambient concentration of the substance of interest, c_0 is the concentration near the surface and c_c represents a bulk tracer concentration, usually assumed to be zero in deposition velocity parameterizations (taken from Wesely and Hicks, 2000).

The aerodynamic resistance to turbulent transport in the canopy is calculated by:

$$R_a = \frac{14 \cdot \mathrm{LAI} \cdot h_c}{u_*} \,, \tag{4.7}$$

where h_c is the height of the canopy.
The quasi-laminar boundary layer resistance, which represents the diffusion through a thin layer close to the leaf surface, is calculated from the wind speed profile according to Meyers (1987):

$$R_b = \frac{2}{k u_*} \left(\frac{Sc}{Pr} \right)^{2/3} = 180 \sqrt{\frac{0.07}{u}} \,, \tag{4.8}$$

where k is the van Karman constant (0.4) and Pr is the Prandtl number (0.72) (Hicks et al., 1987; Ganzeveld and Lelieveld, 1995). To correct for the difference in diffusivity between ozone and water vapor, the resistance is multiplied by a factor of 1.2. This factor is determined by the ratio of the Schmidt number Sc, which is defined as the ratio of the kinematic viscosity for air and the molecular diffusivity of the trace gas.
The total surface resistance R_c of sea and wet skin reservoirs as well as bare soil is defined by

$$R_c = r_{\text{ws/soil}} \,, \tag{4.9}$$

where the constant resistances r of the single surfaces are given in Table 4.1. Over vegetation the surface resistance is given by the reciprocal value of the vegetation resistance for

each canopy layer

$$R_c = \frac{1}{\mathrm{LAI}/r_{\mathrm{leaf}} + 1/r_{\mathrm{soil}}} \,, \tag{4.10}$$

where r_{leaf} is the leaf/needle resistance, which is the resulting resistance of the serial mesophyll and stomatal resistance (r_{mes} and r_{stom}) and a parallel cuticular resistance (r_{cut}) (Ganzeveld and Lelieveld, 1995):

$$r_{\mathrm{leaf}} = \frac{1}{\frac{1}{r_{\mathrm{cut}}} + \frac{1}{r_{\mathrm{stom}}+r_{\mathrm{mes}}}} \,. \tag{4.11}$$

For wet vegetation, the cuticular resistance is replaced by the wet surface resistance

$$r_{\mathrm{leaf,wet}} = \frac{1}{\frac{1}{r_{\mathrm{ws}}} + \frac{1}{r_{\mathrm{stom}}+r_{\mathrm{mes}}}} \,. \tag{4.12}$$

The importance of r_{soil} to the surface resistance increases with decreasing LAI. The uptake resistances are calculated according to the parameterization after Wesely (1989) and are based on the compounds solubility and reactivity. The resistance values according to Ganzeveld and Lelieveld (1995) and Ganzeveld et al. (1998) replaced a number of these resistances. While the other resistances contributing to the surface resistance are given as constant values (see Tab. 4.1), the stomatal resistance r_{stom} is calculated as a function of photosynthetically active radiation (PAR; wavelength of 400-700 nm) and the available water in the root zone, expressed by the soil moisture stress attenuation function $F(W_s)$. The stomatal resistance of the canopy to water vapor is according to Sellers et al. (1986):

$$r_{\mathrm{stom}} = \frac{kc}{\left[\frac{b}{d\mathrm{PAR}} ln\left(\frac{de^{k\mathrm{LAI}}+1}{d+1}\right) - ln\left(\frac{d+e^{-k\mathrm{LAI}}}{d+1}\right)\right] F(W_s)} \,, \tag{4.13}$$

with $d = (a + b \cdot c)/(c \cdot \mathrm{PAR})$, k = 0.9, a = 5000 J m^{-3}, b = 10 W m^{-2} and the minimum stomatal resistance c = 130 s m^{-1}. To determine the stomatal resistance for the trace gas of interest for a leaf/needle of any vegetation type, a LAI of 1 is used and r_{stom} is corrected for differences in molecular diffusivity between H_2O and the specific trace gas. For ozone a factor of 1.6 is used, which is calculated by dividing the square root of the molar mass of ozone by the square root of the molar mass of H_2O. To determine the soil moisture status, the soil moisture is combined with the maximum soil moisture, expressed by the field capacity. A correction function $F(W_s)$ is calculated, which ranges between 0 and 1. For a soil moisture level at the field capacity, the value is 1, there is no soil moisture stress and the leaves take up at a maximum level. With decreasing soil moisture the value decreases. Under a critical soil moisture level, the critical wilting point, there is no stomatal uptake and the value becomes 0. In addition, the effect of a vapor pressure deficit on the stomatal resistance is considered using a correction factor, which increases the resistance with increasing deficit.

To consider the vapor pressure deficit for the determination of the stomatal resistance, observations of the relative humidity are necessary. If no relative humidity observations are available, a fixed relative humidity of 90 % was assumed. This fixed value is replaced by a calculation of relative humidity from temperature T, pressure p and specific humidity q:

$$RH = \frac{e}{E} = \frac{\frac{qp}{0.62+0.378q}}{6.1094 \ \mathrm{hPa} \cdot exp(\frac{17.625(T-273.15)}{243.04+(T-273.15)})} \,, \tag{4.14}$$

where e is the vapor pressure and E is the saturation vapor pressure. The vapor pressure deficit determined from relative humidity is used to calculate a correction factor for the stomatal resistance. The relative humidity is also applied to calculate the wet skin fraction (fr_{ws}) after Lammel (1999) (Table A2):

$$fr_{\mathrm{ws}}(RH) = \begin{cases} 0 & RH < 0.8 \\ \dfrac{RH - 0.8}{0.2} & 0.8 \leq RH < 1 \\ 1 & RH = 1 \end{cases} . \tag{4.15}$$

The relation between relative humidity and wet skin fraction was determined from leaf wetness measurements. Afterwards the bare soil fraction is recalculated as it is depending on wet skin fraction.
As the photochemistry, the stomatal resistance is a function of the radiation. For the calculation of the stomatal resistance a constant radiation was assumed within the canopy resulting also in a constant stomatal resistance throughout the canopy. In order to account for larger removal rates of sunlit leaves and to receive a more realistic profile of the stomatal resistance, the calculation of a resistance profile is added, using the radiation profile calculated for the isoprene emission (see below).

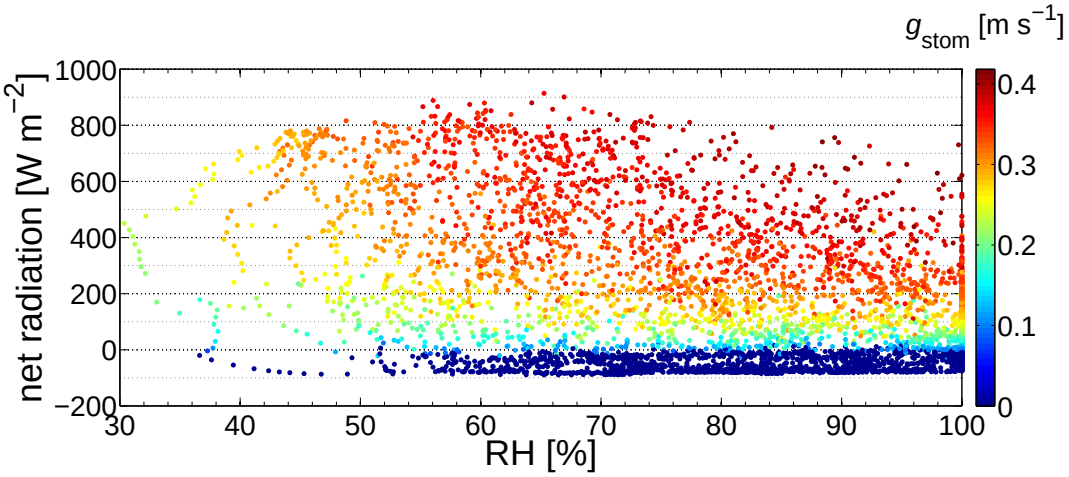

Figure 4.3: Relation of the stomatal conductance to ozone on relative humidity and net radiation.

The stomatal deposition is the main sink for ozone during the day and its strength is expressed by the stomatal conductance, which is the reciprocal of the resistance. The dependency of the stomatal conductance of ozone to net radiation and relative humidity is displayed in Figure 4.3 for the conditions during EGER-IOP3. It shows that the radiation has the largest effect on the conductance. With increasing radiation the conductance increases as well, from close to 0 m s^{-1} for nighttime negative net radiation to up to 0.4 m s^{-1} for a net radiation of about 900 W m^{-2}. The relative humidity causes smaller changes in the stomatal conductance. For a constant net radiation, the conductance varies by less than 0.2 m s^{-1} over the presented humidity range. The stomatal conductance decreases with decreasing RH. A low relative humidity increases the vapor pressure deficit, which leads to a closing of the stomata. There is some dependence between radiation and relative

Table 4.1: Resistance of single surfaces to ozone, needed for the calculation of the total surface resistance to ozone.

Surface	Resistance [s m^{-1}]
Soil	400
Water	2000
Wet skin reservoir	2000
Mesophyll	1
Cuticle	100000

humidity. High RH conditions are usually connected to cloudy conditions and thus a low net radiation. Highest radiation is observed for lower RH conditions. This relationship can also be seen in Figure 4.3, where no observations are available in the upper right corner for high relative humidity and high net radiation. Due to the wet surface at the site, the conductance is affected by the soil moisture only to a minor extent for the considered time period.
The bulk dry deposition velocities are scaled with the leaf area density (LAD) profile for two layers in order to account for the biomass distribution.
The dry deposition of aerosols is calculated after Stier et al. (2005) with no further explanations as it will not be applied in this thesis.

For some gases, the deposition velocities do not only reflect a biological sink but also a source from biogenic emissions within the canopy. The soil biogenic emission flux is calculated according to Yienger and Levy (1995). Emissions of BVOCs as isoprene by the vegetation are calculated according to Guenther et al. (1995) as a function of ecosystem specific emission factors, surface radiation, temperature, the foliar density and its vertical distribution. More details concerning the calculation of biogenic emissions can be found in Ganzeveld et al. (2002a).

In addition to emission and deposition processes, the trace gas concentration is also affected by chemical reactions. The implementation of the role of gas-phase chemistry is based on a modified version of the Carbon Bond 4 mechanism (CBM4) chemistry scheme. The tracer list comprises 62 tracers, but the model can also be run with a limited number of 16 tracers or without the consideration of gas-phase chemistry. The scheme considers standard methane photochemistry (O_3, NO_x, CH_4, CO), but also the role of non-methane hydrocarbons including isoprene (C_5H_8) and a selection of hydrocarbon oxidation products (Roelofs and Lelieveld, 2000).
The photochemistry within the canopy is controlled by radiation. Therefore, the extinction of radiation in the canopy due to interception by biomass needs to be considered. Radiation profiles are used to estimate photodissociation rates within the canopy from above canopy PAR and the surface layer photodissociation rate. The approach implies that the spectral leaf transmission of photodissociation rates is similar to that of PAR. Direct and diffusive PAR profiles and fraction of sunlit and shaded leaves are used to calculate isoprene emission fluxes for crown and canopy-soil layer. The vertical profile of radiation within the canopy is calculated according to Norman (1979) and Weiss and Norman (1985).
An important element of photochemistry is the role of non-methane hydrocarbons (NMHC),

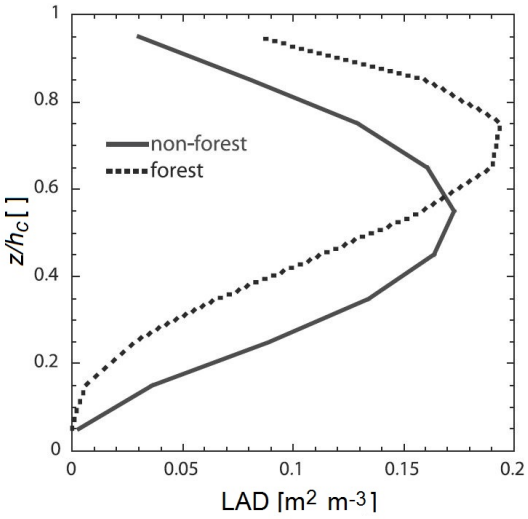

Figure 4.4: Assumed leaf area density profiles for forest and other canopies as a function of the height z normalized by the canopy height h_c (modified after Ganzeveld et al., 2002a).

e.g. isoprene, in the production/destruction of ozone (Ganzeveld et al., 2002a). The deposition of ozone to leaves might involve leaf-scale interactions between emitted BVOCs and O_3.

4.1.2 Canopy structure in MLC-CHEM

To calculate emissions, dry deposition, turbulence and chemistry in the multi-layer vegetation model, a characterization of the biosphere is required. In addition to biogeochemical parameters, e.g. emission factors, the model is initialized by biogeophysical parameters such as the leaf area index (LAI), canopy height, surface roughness and the vertical distribution of biomass expressed by a leaf area density profile. To distinguish between forest and non-forest canopies, two different leaf area density profiles are assigned, which are shown in Figure 4.4. For the forest, the biomass is concentrated in the top, while the biomass shows a more evenly vertical distribution for non-forest canopies. In order to consider these different canopy structures, the canopy module distinguishes two canopy layers.

4.1.3 Spatial and temporal resolution

For the calculation of the contributions of the different processes shown in Figure 4.1 to the concentration changes within the canopy and surface layer, the atmosphere-biosphere trace gas exchange model distinguishes one atmospheric surface layer and two canopy layers of equal thickness, a crown and a canopy-soil layer. The use of two canopy layers has the advantage of an analytical solution of the set of equations to calculate canopy concentrations and fluxes, which makes the model more efficient. The application of more canopy layers coupled to an atmospheric surface layer shows no significant change in the

modeled fluxes and concentrations (Ganzeveld et al., 2002b). An exception is made for the radiation profiles distinguishing four canopy layers, since there is a large sensitivity of simulated VOC emission fluxes to radiation gradients in the top of the canopy, requiring a high vertical resolution in the canopy crown. The canopy-crown and canopy-soil VOC emission flux is subsequently interpolated from these four layers. The reference heights z of the lower and upper canopy layer are set to 0.25 and 0.75 of the total canopy height (h_c), respectively. The reference height of the surface layer corresponds to the height in which above-canopy measurements have been performed.

The time step of the model is set according to the time resolution of the observations to continuously nudge the model solution to the observations. In the coupled differential equations for turbulent transport, dry deposition and emissions a sub time step is considered. The sub time step (Δt_{sub}) is determined from the turbulent and dry deposition timescale to account for short timescales of processes involved for relatively thin canopy layers (Ganzeveld et al., 2002a). To remove potential numerical inaccuracies, the turbulent and dry deposition timescales (ts) are calculated separately from the depth of the canopy layers and the eddy diffusivity as well as dry deposition velocity, respectively:

$$ts_{\text{dd}} = \frac{0.5 \cdot h_c}{0.01 \cdot v_{\text{d, veg}}} \,, \tag{4.16}$$

$$ts_{\text{turb}} = \frac{(0.5 \cdot h_c)^2}{K_H} \,. \tag{4.17}$$

The sub time step is taken as 10 $\%$ of the smallest timescale.

4.1.4 Model settings

In order to simulate the dynamical evolution of the canopy exchange, input parameters are given. The parameters are separated in land cover properties, which are kept constant throughout the simulation, and micrometeorological as well as hydrological drivers of atmosphere-biosphere exchange, which can change over time. The land cover properties include latitude, roughness and canopy structure parameters like canopy height, LAD profile as well as amount of biomass, given as leaf area index. These properties affect the calculation of surface exchange processes. For the meteorological and hydrological conditions, which are not given from measurements, a diurnal cycle is introduced by using simple scaling functions (e.g. simple sinus shape for mixed layer height). If data gaps are present in the observations, the scaling functions are also used to continue the simulation. By switching on and off the processes contributing to the canopy exchange, the role of biogenic emission, dry deposition, in-canopy chemistry and turbulence in explaining the observed temporal variability of the observations can be investigated. Furthermore, the sensitivity of the simulated concentrations and fluxes to different assumptions about canopy structure can be analyzed.

Table 4.2: Input parameters for MLC-CHEM. M1 (main tower), M4 (clearing) and Pflanzgarten (clearing north-west of M1) give the locations from where observations are taken as input for the modeling.

	Pflanzgarten	M1	M4
Temperature	✓	✓	✓
Radiation	-	✓	-
Pressure	-	✓	-
Humidity (RH/q)	✓	✓	-
Precipitation	✓	✓	-
Wind	-	✓	✓
O_3	✓	✓	✓
NO_x	✓	-	✓
Soil wetness	-	✓	-

4.2 Setup of the simulations with MLC-CHEM

To use the model for the analysis of atmosphere-biosphere ozone exchange over Norway spruce canopies during EGER-IOP3 in 2011, the model is evaluated with the ozone flux measurements performed during the campaign. Therefore, the model is initialized by site-specific surface and meteorological conditions.
The reference height for all simulations is set to 5 m above the canopy top, as this corresponds to the measurement height. As input for the modeling studies 10 minute averaged measurements of meteorological and chemical variables are used to replace the idealized daily cycles. Observations are provided for temperature, wind velocity (u, v), friction velocity (u_*), radiation, pressure, humidity, surface moisture, precipitation and mixing ratios of NO_x as well as O_3. The time series of temperature, humidity and wind velocity are shown in Figure 6.1 and Figure 6.6 presents the mixing ratios of ozone. The observational data is obtained from continuous meteorological measurements on the main tower M1, as well as chemical measurements on the Pflanzgarten clearing. In addition, for the campaign period, measurements from the clear-cut around M4 are available. The input variables and their source areas are summarized in Table 4.2. If available, the observational data from M1 is used to model the area around the main tower. The same applies for the clear-cut and the M4 measurements. If the necessary observational data is not available at M1, the data from the Pflanzgarten is used. For the clearing, the measurements from M1 are used in this case.
The initialization of the biosphere characterization is done with available site specific canopy characteristics to ensure a realistic comparison. Canopy structure parameters as plant area index (PAI), canopy height, forest fraction and roughness are provided by observations (see section 2.1). Table 2.1 gives the observed values for PAI, canopy and measurement height. For the modeling of the spruce forest canopy, the forest leaf area density profile (see Fig. 4.4) is used, while for the LAD profile on the clearing the LAI, heights and fractions of the occuring species are considered (see Tab. 2.3), assuming a constant distribution of the LAI of each plant species with height. Compared to the LAD profiles in Figure 4.4, most of the leaf area is accumulated in the lower part of the canopy. The

portion of PAI in each of four canopy layers is distributed as follows: 57.8 % in the lowest layer, 14.4 % in the layer above and 13.9 % in each of the uppermost layers. Despite the mean canopy height of 0.4 m, for the modeling a canopy height of 2 m is employed, which is about the height of the largest spruce trees on the clearing. The forest fraction on the clearing is 21.4 % (spruce trees) and the vegetation fraction is 73.8 % (excluding water and dead wood/grass).

5 Comparability of ozone sensors

A comparison of ozone sensors is performed to ensure that ozone sensor systems give comparable results. This is particularly important for the analysis and interpretation of ozone fluxes measured at different sites. Therefore, a spectral analysis is performed and correction factors for the measured ozone fluxes are determined and compared to theoretical correction factors. The applied cospectral correction method is intended to reconstruct the part of the real turbulent ozone flux which cannot be measured with an imperfect O_3 sensor. The analysis comprises the results of the side-by-side experiment at the end of EGER-IOP3 as well as the results of the experiment at the airfield Mainz-Finthen.

5.1 Meteorological conditions during the Finthen experiment

The experiment at the airfield Mainz-Finthen was separated into two phases with different setups of the EC systems. The first phase was from July 19 until July 29, 2013, and the second phase from August 01 until August 12, 2013.
The hot and dry summer in 2013 resulted in a sere vegetation with water stress conditions for the plants. The first phase of the Finthen experiment was still dominated by hot and dry conditions. Figure 5.1 shows the time series of temperature, relative humidity, wind speed and direction for the first phase of the experiment. The maximum temperatures during daytime were above 25 °C, except for the last day. The nighttime temperatures were mainly between 15 and 20 °C. After July 24, the conditions were more humid, accompanied by slightly lower temperatures. Until July 24, the relative humidity was lower than afterwards with values down to about 30 $\%$ on some days. It exhibited values of up to 90 $\%$ during some nights after July 24. On July 28 and 29 the relative humidity increased to its highest values. During the first days of the experiment, the wind was directed from the north-east at a speed of about 3 $\mathrm{m\,s^{-1}}$. On the following days, the wind direction was fluctuating with low wind speeds of mainly between 1 and 2 $\mathrm{m\,s^{-1}}$. On the last days, the wind speed was again slightly higher at an average speed of about 2 $\mathrm{m\,s^{-1}}$ and the wind was directed from the south-west.
The site was under high pressure influence until the night of July 24/25, when an occlusion passed the site. Alike the occlusion, a cold front on July 28 was accompanied by rain.

Figure 5.2 presents the measurements of the weather station for the second phase of the experiment. In the course of the second phase of the experiment, the daytime temperatures decreased from above 30 °C at the beginning to around 20 °C at the end. The day- as well as nighttime relative humidity was lower during the first half of the phase and increased in the second half. The wind speed reached higher values compared to the first phase, with winds mainly from the south and south-west, and only short time periods where the wind

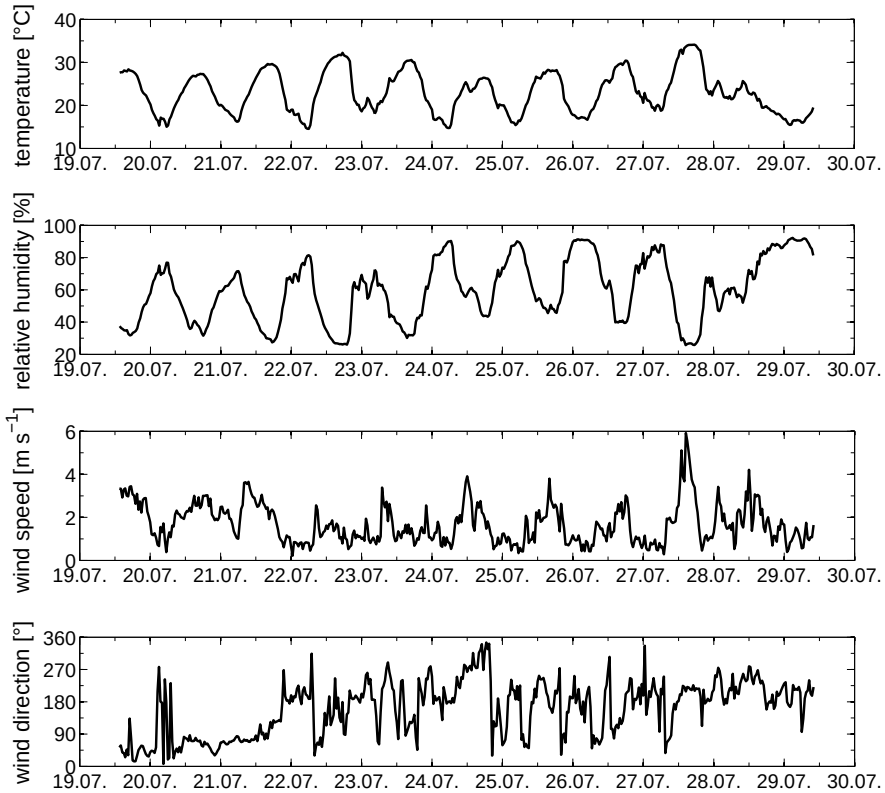

Figure 5.1: Meteorological conditions during the first phase of the side-by-side experiment at the airfield Mainz-Finthen in summer 2013. Displayed from top to bottom are the time series of 10 minute averages of temperature, relative humidity, wind speed and wind direction measured by the weather station.

turned to the north-east.
The second phase showed more rainy periods than the first phase due to the passage of a cold front on August 03, a front located over Germany between August 05 and 07 and the passage of an occlusion on August 10.

For the further analysis, periods with rain are not considered. In addition, only a certain temperature and relative humidity range is included in the analysis (see section 3.4.2).

5.2 Laminar versus turbulent tube flow

For the measurement of O_3 fluxes by EC, a tube is necessary for the transport of sample air from the inlet to the sensor. During the field campaigns four fast ozone instruments were run, which are of the same type, however, measurements of the flow rate in the tubing show that they differ in some system characteristics (see Tab. 5.1).
The flow rate was measured for three of the four sensors. The fourth sensor FXM4 was bro-

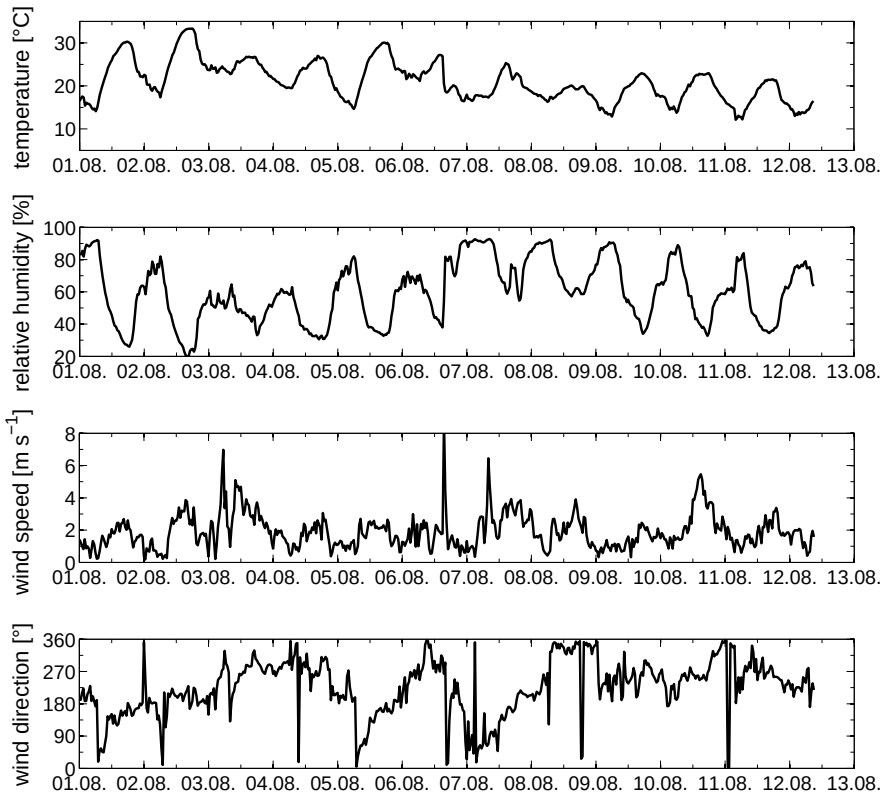

Figure 5.2: Meteorological conditions during the second phase of the side-by-side experiment at the airfield Mainz-Finthen in summer 2013. Displayed from top to bottom are the time series of 10 minute averages of temperature, relative humidity, wind speed and wind direction measured by the weather station.

ken at the time of the flow rate measurement, thus, its flow rate is estimated as the average of three sensors with a fan as old as the one of FXM4. For a largely unaffected transport of fluctuations through the tubing, a turbulent tube flow should be maintained. In order to evaluate whether the flow inside the tube is laminar or turbulent, the Reynolds number is used, determined by means of the flow rate. In addition, the tube diameter is needed. The enviscope instrument has a fitting for 3/8 inch tubes. The applied black PFA tubes have an inner diameter of 7.52 mm (A. Kamps, Saint-Gobain Performance Plastics Isofluor GmbH, personnel communication). In combination with the standard integrated fan of the instrument, this results in an expected laminar flow inside the tube, with Reynolds numbers lower than 1000, which is well below the critical Reynolds number for turbulent flow (~2300 for straight tubing; Lenschow and Raupach, 1991). In order to receive a turbulent flow inside the tube, either the flow rate needs to be increased or the diameter of the tube needs to be decreased. However, as the flow rate of the fans is fixed, the reduction of the tube diameter is the only way to increase the Reynolds number. The maximum inner diameter of a tube still resulting in turbulent tube flow with the given flow rate is listed in Table 5.1. The diameters are well below the diameters of the typically applied tubes (1/4" or 3/8"). Thus,

Table 5.1: Characteristics of the fast ozone instruments. During the flow rate measurement, sensor FXM4 was broken and for its flow rate an average value of sensors with a fan of the same age (FXM2, ITR1 and another ozone sensor, which was not used during the campaign) is used.

Ozone sensor	Flow rate [l min^{-1}]	Mean velocity [m s^{-1}]	Max. turbulent diameter [mm]
FXM1 (EGER-M4)	3.45	1.29	2.0
FXM2 (EGER-M1)	4.51	1.69	2.6
FXM4	4.4	1.65	2.6
ITR1	4.34	1.63	2.5

despite the laminar flow in the tube, the large 3/8" tubes have been applied for the ozone flux measurements, but they need to be corrected for.
To emphasize the difference in the correction of fluxes between laminar and turbulent tube flow, the relation between the correction factor ϵ_x and the wind speed u is determined under unstable conditions. This is done by using the model cospectra after Kaimal et al. (1972) and the theoretic transfer functions for tube attenuation (see section 3.4.1). Theoretically, the relation between ϵ_x and u is linear and approximated by $\epsilon_x = 1 + au$, where a only depends on system characteristics and on the measurement height. The sensitivity of the flux loss to the wind speed results from the shift of the cospectrum to higher frequencies as the wind speed increases and hence there is a greater attenuation of fluctuations in the

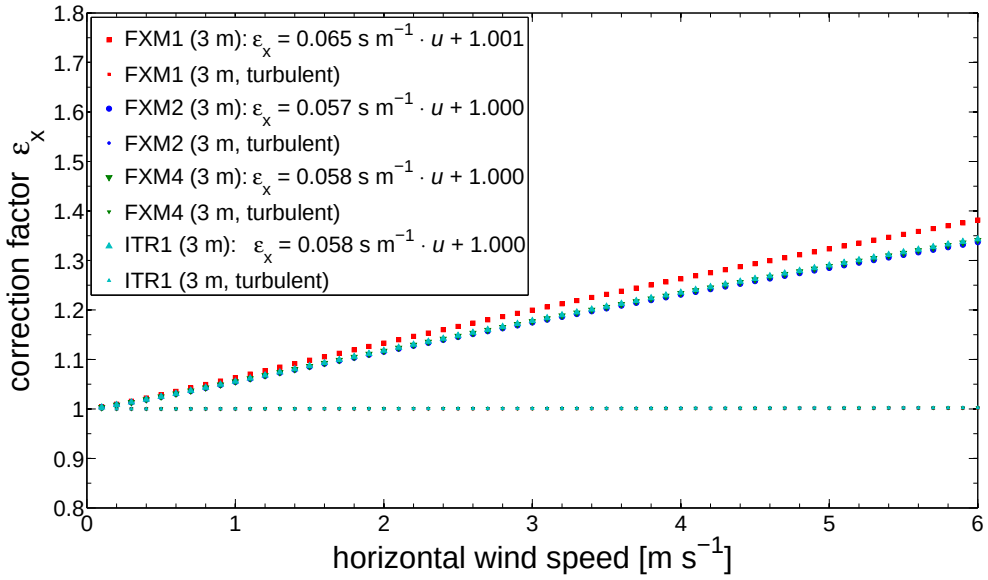

Figure 5.3: Relation between the correction factor and the horizontal wind speed for the sensor systems with same tube lengths. Correction factors are given for laminar as well as turbulent tube flow. The symbols for the turbulent case are hidden behind those for ITR1 (turbulent). Linear regressions for the laminar case are given in the plot.

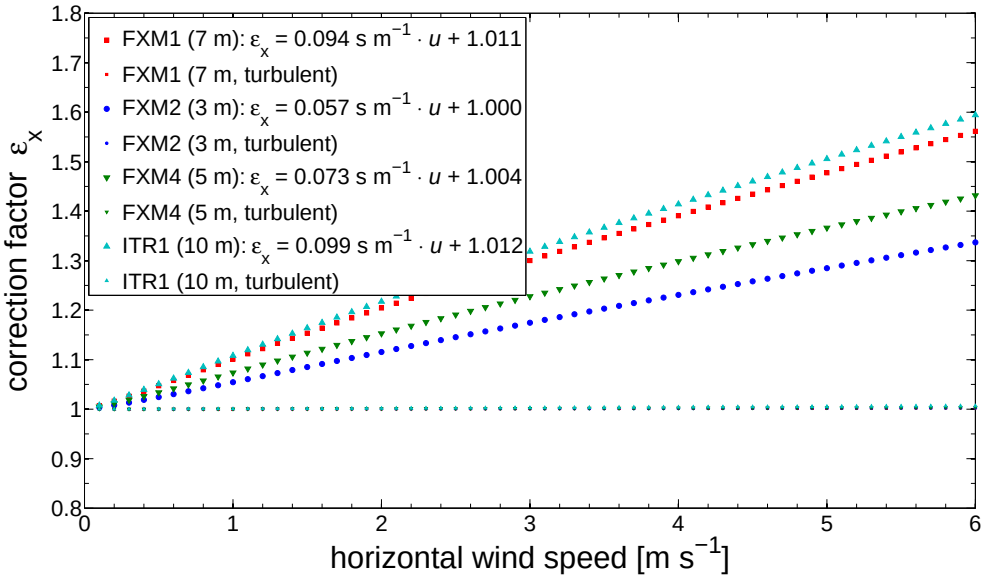

Figure 5.4: Relation between the correction factor and the horizontal wind speed for the sensor systems with different tube lengths. Correction factors are given for laminar as well as turbulent tube flow. The symbols for the turbulent case are hidden behind those for ITR1 (turbulent). Linear regressions for the laminar case are given in the plot.

sampling tube (Leuning and Moncrieff, 1990). In the laminar case, the theoretic correction factor is calculated using the characteristics of the systems applied during the experiments, while for the turbulent case a theoretic sensor system is presented. For this sensor system, the theoretic transfer functions for turbulent tube flow are applied with the tube diameters of Table 5.1. Figure 5.3 shows the theoretic relation between correction factor and horizontal wind speed for the laminar and turbulent systems with same tube length of 3 m, while Figure 5.4 shows the relation for the systems with different tube lengths, both for the measurement height of 2.8 m during the Finthen experiment. The correction using the theoretic transfer function for turbulent tube flow shows correction factors close to 1 for all wind speeds and all tube lengths and thus, no remarkable effect on the resulting flux. Therefore, for an effective transport along the tube, a turbulent tube flow is desired, as it reduces the attenuation of high-frequency fluctuations. Consequently, for a turbulent tube flow no correction for the attenuation of fluctuations in the tubing is necessary and the tube length only needs to be considered in the determination of the lag time.
For laminar tube flow, Figures 5.3 and 5.4 show that the correction factor increases with increasing wind speed, and the equations of linear regressions are displayed in the figures. For the systems with same tube length the correction factors are similar for three of the sensors (FXM2, FXM4, ITR1), while only the sensor FXM1 gives higher correction factors, which is due to the lower flow rate of this sensor. The theoretic functions show that for a horizontal wind speed of 6 m s^{-1} the flux needs to be corrected by 30 to 40 %. Moreover, Figure 5.4 indicates that increasing the tube length increases the correction factor. The correction factors for FXM1 (tube length of 7 m) and ITR1 (tube length of 10 m) are similar as the correction for FXM1 is not only increased by the longer tube, but also due to the lower flow rate. Increasing the tube length from 3 m to 10 m would increase the correction

at 6 m s^{-1} by about 25 %.
The high theoretic correction factors for laminar tube flow compared to the turbulent case demonstrate the need to correct for the attenuation of fluctuations in laminar tube flow. However, in advance of the application of the theoretic correction factors, the accordance between the theoretic corrections and those obtained by measurements needs to be confirmed.

5.3 Side-by-side measurement during EGER

In order to be able to compare the fluxes measured on the masts M1 and M4 during EGER-IOP3, a short side-by-side comparison of ozone sensors was performed on two days at the end of the EGER campaign. Two ozone sensors were compared, which were also used in the more extended field comparison at the airfield Mainz-Finthen. The sensor from M1 is FXM2 and that from M4 is FXM1 in the second campaign. For the intercomparison, the response of the two EC ozone systems to fast ozone fluctuations and the resulting

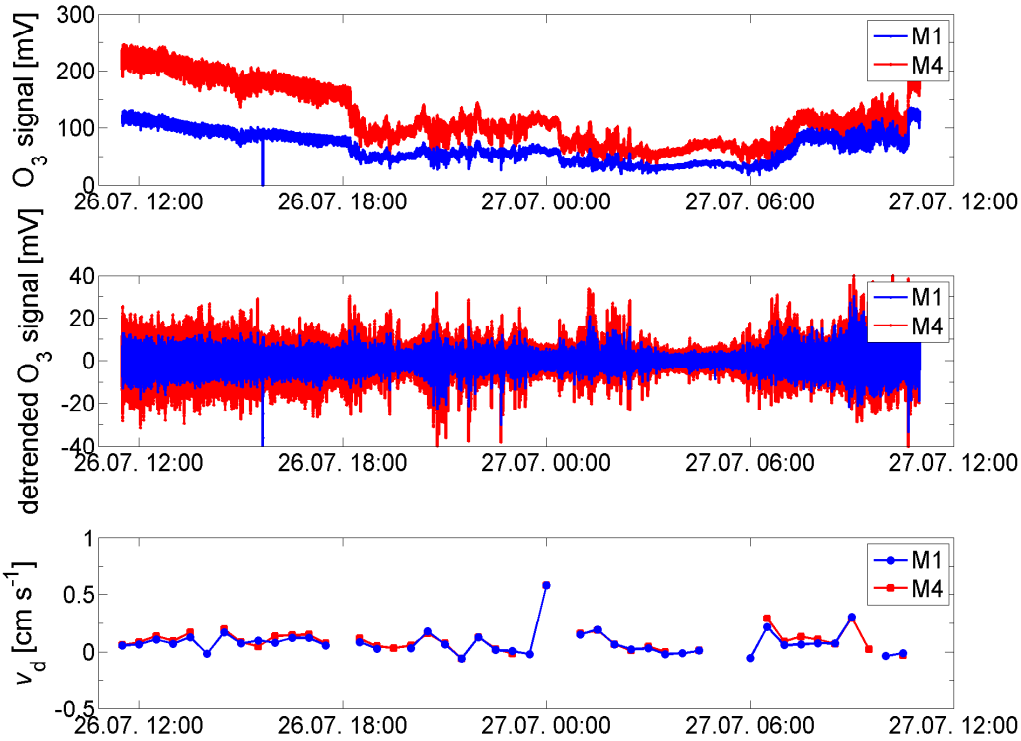

Figure 5.5: Time series of the signals of the ozone sensors applied during the side-by-side comparison at the end of EGER-IOP3 at a height of 2.25 m on M4. The first plot shows the raw and the second plot the detrended (linear trend over 5 minute segments removed) 20 Hz signals. The third plot gives the time series of the calculated deposition velocities.

deposition velocities are analyzed.

The first plot of Figure 5.5 shows the time series of the raw signals of the two ozone sensors applied during the EGER campaign. The signals show the same overall trend, with largest values during the day and decreasing values throughout the night. The detrended signals, by removing the linear trend over 5 minute segments, in the second plot show the same time-dependence for the amplitude of fast fluctuations, with the largest fluctuations during daytime. The larger values and fluctuations given by the M4 sensor indicate a higher sensitivity of the chemical disc inside this sensor. The third plot of Figure 5.5 displays the deposition velocities calculated from the fluctuations of ozone mixing ratio and vertical wind speed. The deposition velocities show no distinct diel cycle and the signals from both ozone sensors give only slight differences in the determined deposition velocity.

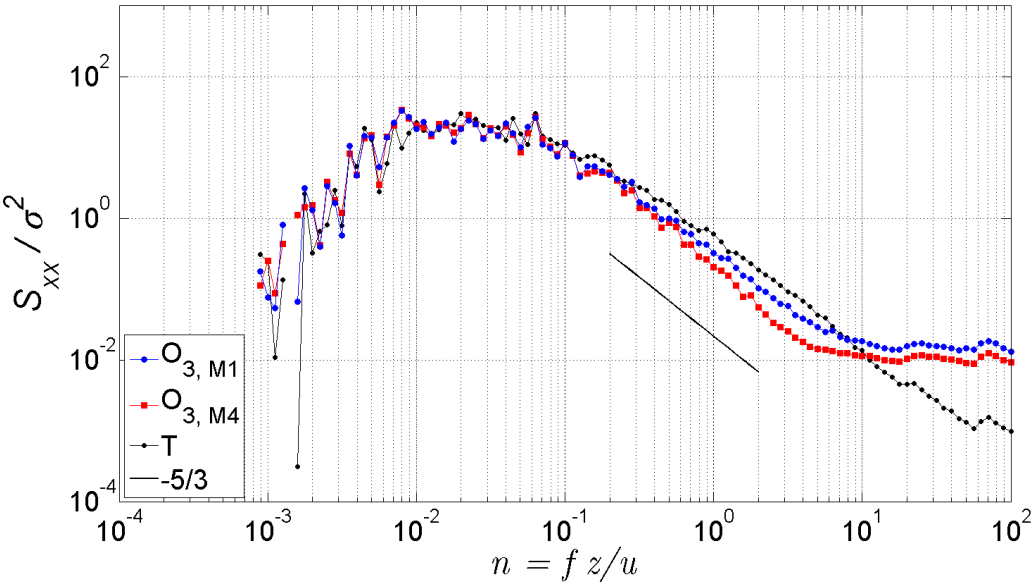

Figure 5.6: Averaged power spectral densities of temperature (T) as well as O_3 plotted against normalized frequency for the side-by-side experiment at the end of EGER-IOP3. Power spectra of the two ozone sensors applied during EGER-IOP3, labeled M1 and M4, are shown. The spectra are normalized by the variance σ^2 of the scalar concentration x (either T or O_3). The measurement length for one power spectrum was 30 minutes and 17 power spectra are averaged. The measurement height was 2.25 m. The straight black solid line gives the theoretical slope of -5/3.

To investigate the different performance of both EC systems, power- and cospectral densities are calculated. Figure 5.6 shows the averaged power spectra, while Figure 5.7 presents the averaged cospectra for the side-by-side experiment. The spectral densities are plotted against the normalized frequency $n = fz/u$, where z is the measurement height and u is the mean horizontal wind speed. Individual spectra are determined from 30 minute time series. In order to ensure that the averaged spectra of the side-by-side experiment include the same meteorological conditions, only those 30 minute time periods are considered, when

there are spectra for all sensors. Moreover, to improve the representation, values are averaged to bins, which are equidistant on the logarithmic scale. Figure 5.6 shows averaged power spectra for temperature as well as ozone signals of the M1 and M4 sensor normalized by their respective variance. In addition, the theoretic slope in the inertial subrange is given. The temperature spectrum agrees well with the theoretic $n^{-5/3}$ slope in the inertial subrange. The power spectra of temperature and the two ozone sensors agree well up to a normalized frequency of about 0.1. For higher frequencies the spectra of the two ozone sensors show a slightly steeper decline than the spectrum of the temperature, with the M4 sensor showing a steeper decline than that of M1. The steeper decline is caused by the attenuation of high-frequency fluctuations in the sensor system. Both ozone spectra show relatively constant values for normalized frequencies higher than 8, which are similar for both sensors, and are due to high noise levels at these frequencies. The constant spectral densities at the highest frequencies can also be attributed to aliasing as no low-pass filtering was applied during the measurement to reduce the energy above the Nyquist frequency.
Figure 5.7 shows averaged cospectra between vertical wind speed and temperature as well as ozone signals of the M1 and M4 sensor normalized by their respective covariance with w. Besides, the theoretic slope in the inertial subrange is given. The cospectra are more scattered compared to the power spectra as the flux can be directed up or downwards and thus, the cospectral densities can take positive as well as negative values. To allow plotting on a logarithmic scale, negative values have been inverted to positive values. The slope of the cospectrum between vertical wind and temperature (sensible heat flux) is less steep than the theoretic slope in the inertial subrange. A good agreement between the cospectra of sensible heat and ozone fluxes is visible for normalized frequencies up to about 0.3. For higher frequencies the ozone flux cospectra show again a steeper decline than the sensible heat flux spectrum, which is closer to the theoretic slope of -7/3. For the frequency range in which the power spectral densities in Figure 5.6 show a nearly constant value (n > 8), the cospectral densities in Figure 5.7 show a less steep decline with frequency than the cospectrum of sensible heat.
Two unsolicited effects can be observed in the power and cospectra measured by the closed-path systems, high-frequency noise and low-pass filtering. Low-pass filtering is observable in the power spectra of ozone as well as the cospectra between vertical wind and ozone by the lower power and cospectral densities compared to the temperature spectrum or heat flux cospectrum. The filtering is characterized by reduced spectral densities compared to the temperature spectrum and the sensible heat flux cospectrum for frequencies higher than 0.1 and 0.3, respectively. The effect is more distinctive for M4 than for M1 due to the lower power and cospectral densities, particularly observable in the power spectra.

5.3.1 Noise correction

The real signal of the ozone sensors is superimposed by white noise. It is caused by digitizing an analog signal, or it is caused by only a finite number of photons that are measured in the sampling intervals as a representation of the signal (Lenschow and Kristensen, 1985). White noise alters the shape of the power spectrum at high frequencies. When the spectral density of white noise is higher than the signal at a certain frequency, it is perceptible from the normal signal due to the zero gradient. The shape of the power spectra in Figure 5.6

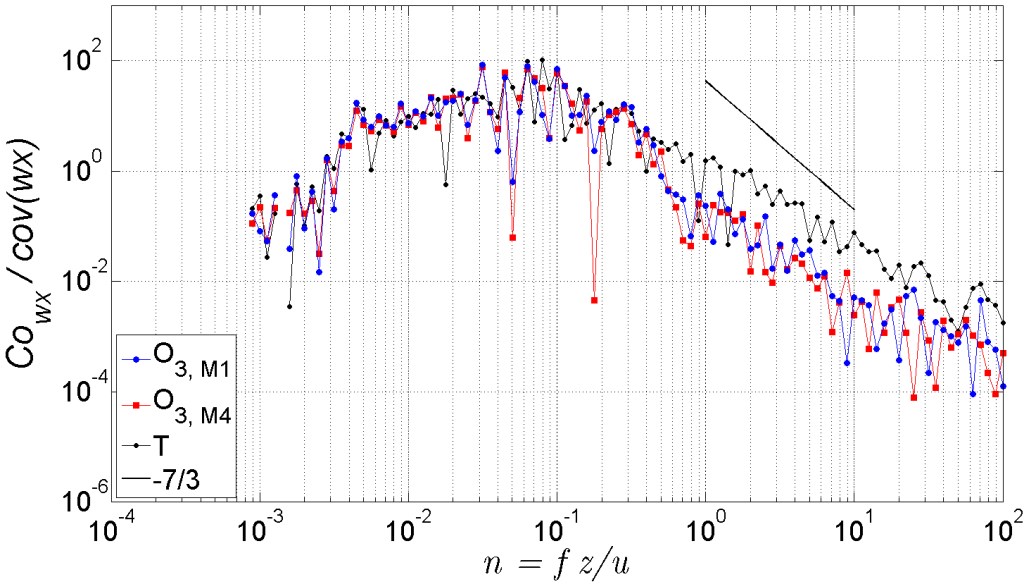

Figure 5.7: Averaged cospectral densities of vertical velocity (w) and temperature (T) as well as O_3 plotted against normalized frequency for the side-by-side experiment at the end of EGER-IOP3. Cospectra of the two ozone sensors applied during EGER-IOP3, labeled M1 and M4, are shown. The cospectra are normalized by the covariance $\overline{w'x'}$ of w and the scalar concentration x (either T or O_3). The measurement length for one cospectrum was 30 minutes and 17 cospectra are averaged. The measurement height was 2.25 m. The straight black solid line gives the theoretical slope of -7/3.

with a slope of n^0 at normalized frequencies larger than about 8 for M1 and M4 indicates high white noise levels at those frequencies (Muller et al., 2010). The frequency for which the noise becomes perceptible in the spectra depends on the sensitivity of the chemical disc inside the ozone sensor. For discs with a low sensitivity, the noise exceeds the real sensor signal at lower frequencies than for high-sensitivity discs.
The noise contributes to the ozone time series and is thus observable in the power spectra (see Fig. 5.6), however, it is not correlated to the wind speed (Hicks and McMillen, 1988). Therefore, the noise should not be visible in the cospectra. Nonetheless, the cospectra of M1 and M4 in Figure 5.7 reveal a change in the slope for frequencies higher than 8, which is a sign of some correlation between the white noise of the ozone measurement and the sampled wind speed time series.
The shape of the high-frequency part of the spectra would change with the application of low-pass filters. The filter reduces the contribution of the high-frequency fluctuations to the total flux and compensates for noise or aliasing during the digital sampling. As filter a moving average is applied on the ozone time series and the number of values leading to the best agreement of the spectra to their theoretic shape is determined. For the best agreement of the spectra to the theoretic slope in the inertial subrange, the moving average of the M1 sensor comprises 11 values and that of the M4 sensor 9 values.

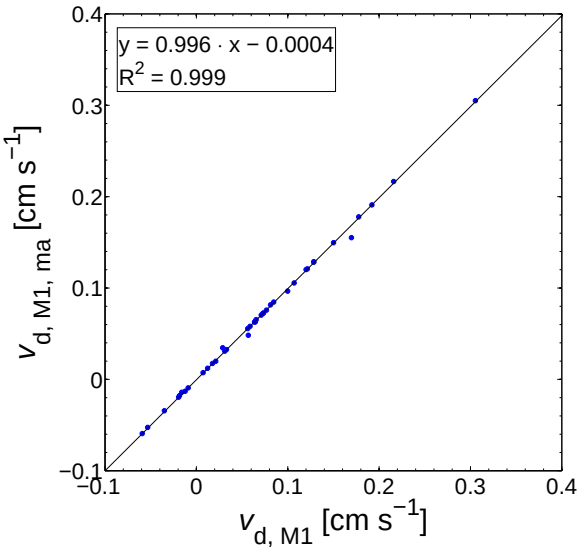

Figure 5.8: Scatterplot of O_3 deposition velocities, with the application of an anti-aliasing filter, against O_3 deposition velocities, without the application of an anti-aliasing filter for the M1 sensor during the side-by-side experiment at the end of EGER-IOP3. The measurement height was 2.25 m. The data was corrected by a series of standard steps. The black line gives the regression between the deposition velocities, the coefficients of the regression are given in the plot.

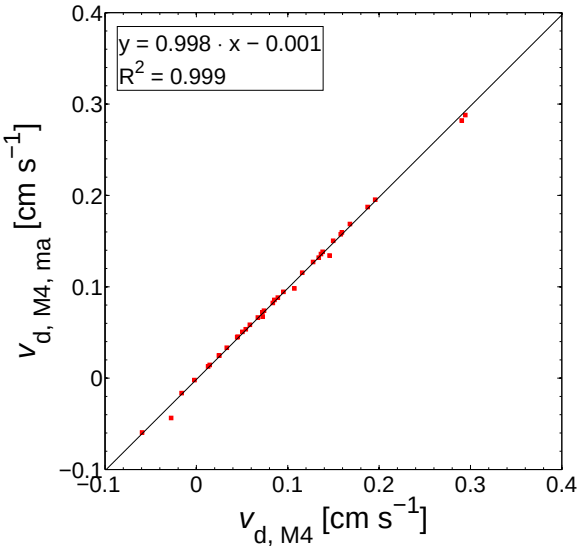

Figure 5.9: Same as Fig. 5.8 for M4.

The filtered time series are used to recalculate ozone deposition velocities. Figure 5.8 displays the scatterplot of the deposition velocities calculated from the filtered against the non-filtered time series of the M1 sensor. The regression performed between the deposition velocities shows a difference of less than 1 %. Figure 5.9 reveals the same for M4, where the difference is even smaller. Thus, the application of the moving average to compensate for the noise or aliasing alters the shape of the high-frequency part of the power and cospectra, but the correction shows only a small effect on the flux contribution from the inertial subrange. According to Massman (2000), it is even wrong to correct fluxes for aliasing as it results from digitizing a time series and will not influence the total flux.
For the following analysis, no moving average will be applied on the time series. While the application of the moving average could affect the determination of a transfer function for the effect of tube attenuation as it would remove the influence of noise on the cospectra, which are used for the determination of the transfer function, it does not improve the measured flux. Thus, as the aim of the analysis of system comparability is to compare experimental and theoretical correction factors for ozone fluxes, which are not influenced by noise, the application of a low-pass filter is not necessary.

5.3.2 Difference between EGER-systems

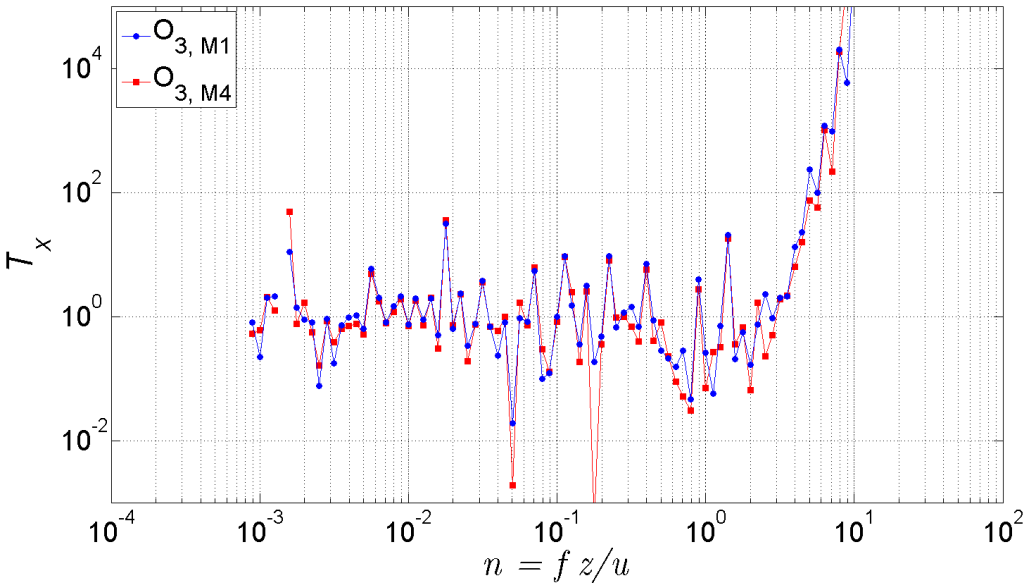

Figure 5.10: Coefficients of the transfer functions of O_3 sensors plotted against normalized frequency. Transfer functions of the two ozone sensors applied during EGER-IOP3, labeled M1 and M4, are shown.

In order to compare the ozone fluxes above the forest and on the clearing measured by the two EC systems M1 and M4 during EGER-IOP3, the systematic difference between the measured fluxes needs to be determined. Due to systematic differences between individual

chemiluminescence sensors as well as differences in the length of the applied tubes, the individual systems show different spectral distributions in the high-frequency range. Figure 5.10 shows transfer functions of the two ozone sensor systems. The transfer functions are determined from the averaged cospectra of the side-by-side experiment (see Fig. 5.7). The contribution of sensor separation to the high-frequency attenuation is not included in the transfer functions. Thus, the transfer functions represent the effect of attenuation of fluctuations in the tubing. Up to frequencies of about 0.3, the values of the transfer function fluctuate around or are close to 1. This indicates, that the contribution of these frequencies to the covariance is well represented. In the frequency range between 0.3 and about 2 to 3, the coefficients of the transfer function are lower than 1, indicating an underestimation of the contribution of these frequencies to the total covariance. With increasing frequency the values of the transfer function increase up to values larger than 10000, indicating an overestimation of the contribution of these frequencies to the covariance. Since the contribution of the highest frequencies to the covariance is small (see Fig. 5.7), an overestimation is of no consequence to the total covariance. Furthermore, the overestimation present in the ozone EC system transfer functions is due to the effect of noise, which is observable in the ozone flux cospectra as a less steep decline compared to the heat flux cospectrum (see Fig. 5.7), and for noise it was shown in section 5.3.1 that it does not considerably affect the flux.

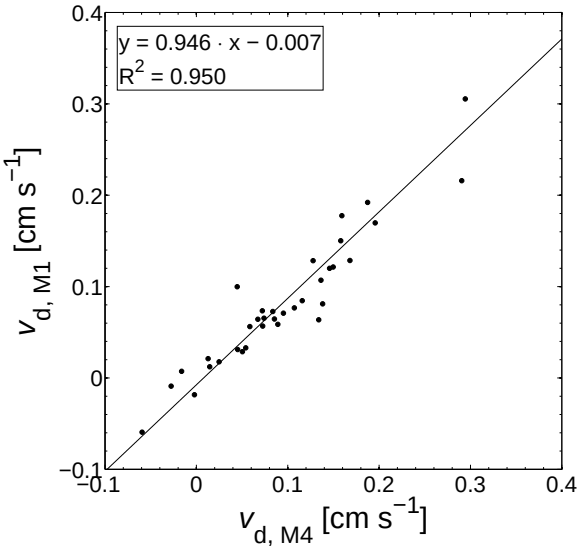

Figure 5.11: Scatterplot of O_3 deposition velocities, measured by the M1 sensor, against O_3 deposition velocities, measured by the M4 sensor during the side-by-side experiment at the end of EGER-IOP3. The measurement height was 2.25 m. The data was corrected by a series of standard steps. The black line gives the regression between the deposition velocities, the coefficients of the regression are given in the plot.

Figure 5.11 shows the scatterplot between the deposition velocities of the two sensors during the side-by-side campaign. Mostly, the deposition velocity shows values between 0 and 0.2 cm s^{-1}. Only a few negative values for v_d appear. A linear relation is evident between the ozone deposition velocities measured by the M1 and M4 sensor systems. To determine the difference between the deposition velocities, a linear regression is performed. The M4

sensor gives deposition velocities, which are slightly larger than those of the M1 sensor by about 5.4 %. This value can be used to adapt ozone fluxes measured at the same height for the difference between the EC systems by adjusting the flux results of one sensor to those of the other sensor. However, to correct for the total attenuation of fluctuations, the ozone flux cospectra need to be adjusted to the sensible heat flux cospectrum.

5.4 Difference between sensors

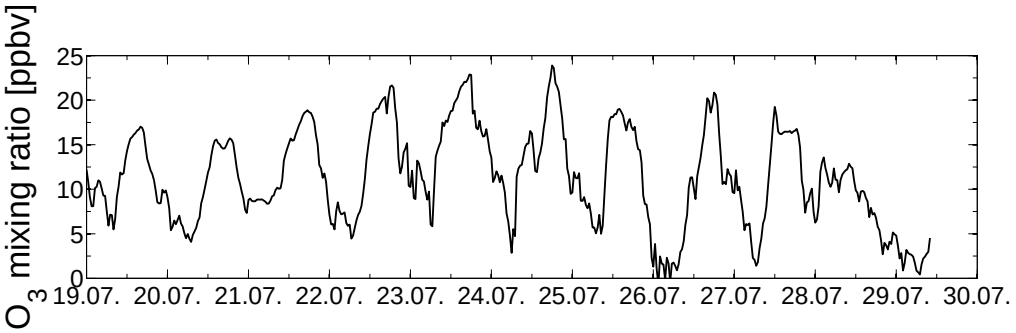

Figure 5.12: Time series of the ozone mixing ratio measured during the first phase of the experiment at the airfield Mainz-Finthen in summer 2013. The time series shows 30 minute averages measured at a height of 2.8 m.

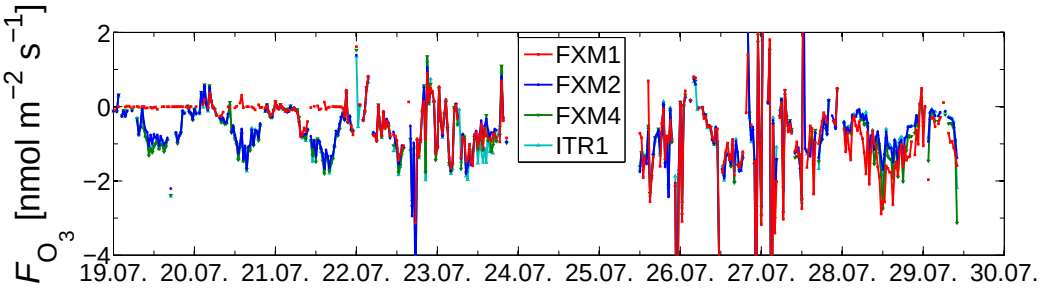

Figure 5.13: Time series of the ozone fluxes measured during the first phase of the experiment at the airfield Mainz-Finthen in summer 2013. The time series show 30 minute fluxes measured at a height of 2.8 m. From July 24 until noon of 25 a failure of the sonic prevented the calculation of fluxes.

The objective of the first phase of the side-by-side experiment at the airfield Mainz-Finthen was to investigate the difference between individual ozone EC systems by comparing the performance of individual O_3 sensors. Four fast ozone sensors were applied with tubes of an equal length of 3 m, which among others, were those used in EGER-IOP3. Sensor FXM1 is the one used at M4 and FXM2 that from M1.
Figure 5.12 shows the time series of the ozone mixing ratio measured during the Finthen

experiment. The mixing ratio shows a daily cycle with largest values in the afternoon, which is expected for ozone mixing ratios. The mixing ratios are generally low with maximum values of only 24 ppbv and during some nights nearly 0 ppbv are reached. Figure 5.13 gives the time series of the O_3 fluxes measured by the four sensors. Between July 24 and noon of July 25 there is no flux data available due to a failure of the sonic anemometer. The largest fluxes occur during the night and highest deposition around midday. The fluxes calculated from the measurements of the sensors FXM2, FXM4 and ITR1 agree fairly well over the course of the entire side-by-side experiment, while FXM1 agrees less, particularly at the beginning. The fluxes calculated from the measurements of the sensor FXM1 are close to zero until the morning of July 22, when the chemical discs inside the sensors have been replaced. Until July 22, all sensors were equipped with dye coated plates originating from the same large plate, but the output of the FXM1-sensor shows a smaller sensitivity. The sensitivity is determined as the ratio between the ozone sensor output and the ozone mixing ratio (expressed in mV ppbv^{-1}, not shown). The fluctuations in the time series of the FXM1-sensor are close to the minimum voltage difference that can be resolved by the instrument (not shown). Thus, small fluctuations cannot be resolved and result in a low covariance with vertical wind speed. After July 22, the FXM1 fluxes also agree well with those of the other sensors. The fluxes of the sensor FXM2 are highest. Those of FXM1 are lowest, but also show more fluctuations than the fluxes of the other sensors.

The averaged spectra of the campaign period are determined the same way as those during the EGER side-by-side experiment and thus include only spectra under same conditions. The maximum frequency of the spectra is higher than that of the spectra of the EGER campaign due to a higher sampling frequency of 50 Hz, resulting in a Nyquist frequency of 25 Hz instead of 10 Hz during EGER. However, for both campaigns a maximum normalized frequency of 100 is chosen for the presentation of the spectra. Figure 5.14 shows the distribution of power spectral densities of temperature and O_3 signals with normalized frequency. The power spectrum of the temperature measurement follows the theoretic $n^{-5/3}$ slope. The change in the slope for normalized frequencies higher than about 5 is due to the averaging process using normalized frequencies. Normalizing the frequency has the consequence that all 30 minute spectra give values for different frequency ranges and thus, for the highest as well as lowest frequencies less values are available for averaging. The power spectra of the sensors FXM2, FXM4 and ITR1 agree well with the temperature spectrum up to a normalized frequency of about 0.4. For higher frequencies, the power spectral densities of the ozone measurements decrease less and show constant values above a frequency of about 2. Due to the averaging process, the spectral densities decrease again with frequency for normalized frequencies higher than about 5. The power spectrum of sensor FXM1 is in agreement with the power spectra of the other sensors up to a frequency of 0.1, while it displays constant values for frequencies higher than 0.9 in contrast to a frequency of 2 for the other sensors. The different behavior is attributed to the characteristics of the ozone sensors, as FXM1 has a lower flow rate than the other sensors (see Tab. 5.1). Despite the ozone sensor itself, also the sensitivity of the chemical disc inside the instrument influences the lower limit of the frequencies affected by noise. Discs with a weak sensitivity increase the contribution of noise to the variance, which is recognizable by the constant power spectral densities starting at lower frequencies than for chemical discs with a high sensitivity. This was particularly distinctive in the observations of one chemical disc (data and spectra not shown) used between the first and second phase of the Finthen experiment,

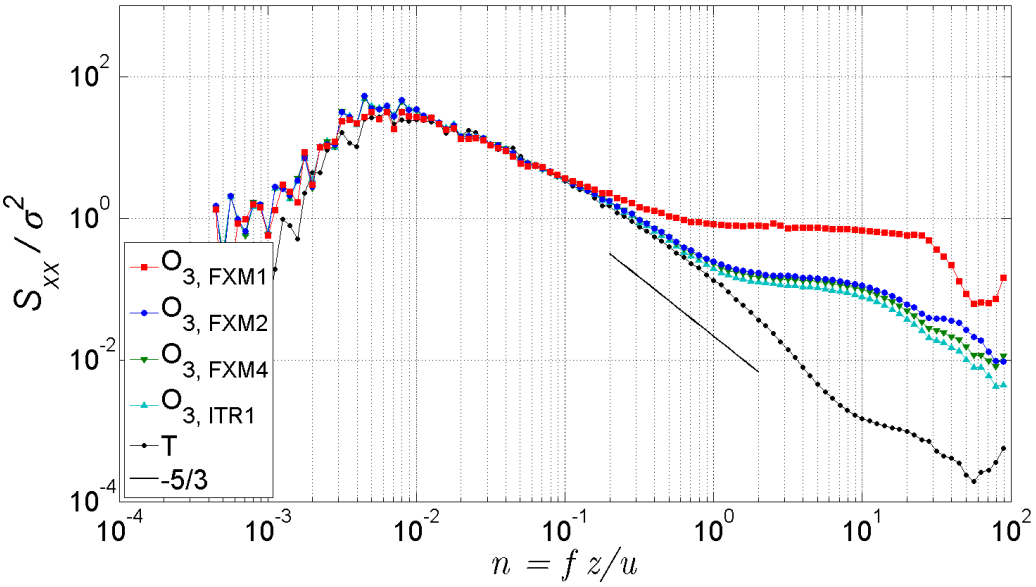

Figure 5.14: Averaged power spectral densities of temperature (T) as well as O_3 plotted against normalized frequency for the side-by-side experiment at the airfield Mainz-Finthen. Power spectra of the four ozone sensors, labeled FXM1, FXM2, FXM4 and ITR1, are shown. The spectra are normalized by the variance σ^2 of the scalar concentration x (either T or O_3). The measurement length for one power spectrum was 30 minutes and 77 power spectra are averaged. The measurement height was 2.8 m. The straight black solid line gives the theoretical slope of -5/3.

where the sensitivity was too low to be able to observe small fluctuations in the time series and the constant level of the power spectral densities started at frequencies a little higher than that of the peak in the spectra. Compared to the power spectra of the measurement at the end of EGER-IOP3 given in Figure 5.6, where the noise becomes obvious above a frequency of about 8, the noise becomes visible in the power spectra of the Finthen experiment already at lower normalized frequencies.
Figure 5.15 presents cospectral densities of vertical wind speed and temperature as well as O_3 signals. Alike the power spectrum of the temperature (see Fig. 5.14), the cospectrum of the sensible heat flux agrees with the theoretic shape for small n. The good agreement between the heat flux cospectrum and the theoretic shape of the cospectrum, where the decrease in the inertial subrange follows the theoretic slope, confirms a good quality of the measurement. However, for n larger than 20 the cospectrum also shows a smaller decrease with increasing frequency. The cospectra of the ozone fluxes determined from the measurements of the sensors FXM1, FXM2, FXM4 and ITR1 agree well with the sensible heat flux cospectrum for frequencies up to 0.2, while the decrease is steeper for frequencies between 0.2 and 2, which is due to the attenuation of fluctuations during the transport through the tubing with laminar tube flow as well as the effect of sensor separation. For frequencies higher than about 2 the cospectral densities of the ozone fluxes decrease less

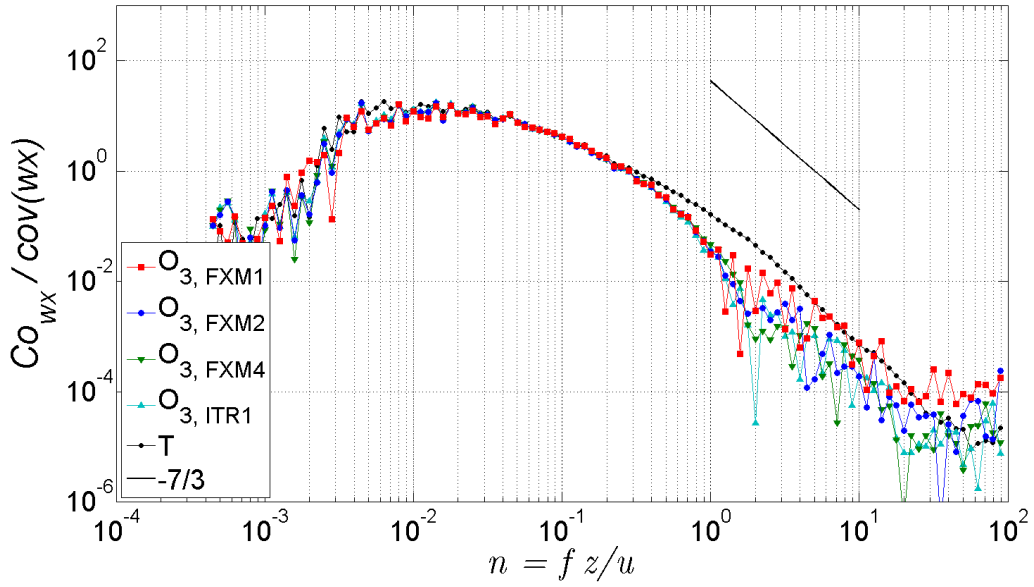

Figure 5.15: Averaged cospectral densities of vertical velocity (w) and temperature (T) as well as O_3 plotted against normalized frequency for the side-by-side experiment at the airfield Mainz-Finthen. Cospectra of the four ozone sensors, labeled FXM1, FXM2, FXM4 and ITR1, are shown. The cospectra are normalized by the covariance $\overline{w'x'}$ of w and the scalar concentration x (either T or O_3). The measurement length for one cospectrum was 30 minutes and 77 cospectra are averaged. The measurement height was 2.8 m. The straight black solid line gives the theoretical slope of -7/3.

than those of the sensible heat flux. This agrees with the frequency range at which noise is visible in the power spectra in Figure 5.14, indicating that the noise is not completely uncorrelated to the measurement of vertical wind speed fluctuations.

During the flux calculation by software packages, a correction procedure is performed, which comprises a spectral correction for sensor separation by a theoretic transfer function. As all ozone sensor inlets have the same distance from the middle of the sonic path, the influence of sensor separation is the same for all sensors. Figure 5.16 gives, representative for all sensors, the spectral correction of the fluxes of sensor FXM2 depending on stability. Under unstable conditions (z/L<0) the flux is increased by about 5 % due to the spectral correction, while stable conditions increase the influence of the sensor separation on the flux.
For the spectral correction due to the tube attenuation a transfer function can be determined as well as for sensor separation to correct for the resulting underestimation (Aubinet et al., 2001). The transfer function corrects for the different shape of the ozone cospectra in the higher frequency range compared to the ideal heat flux cospectrum. Figure 5.17 shows the transfer functions for the tube attenuation in the ozone sensor systems determined under unstable conditions. For frequencies up to 0.2, where the cospectra in Figure 5.15 agree, the coefficients of the transfer function take values close to 1. In the frequency range be-

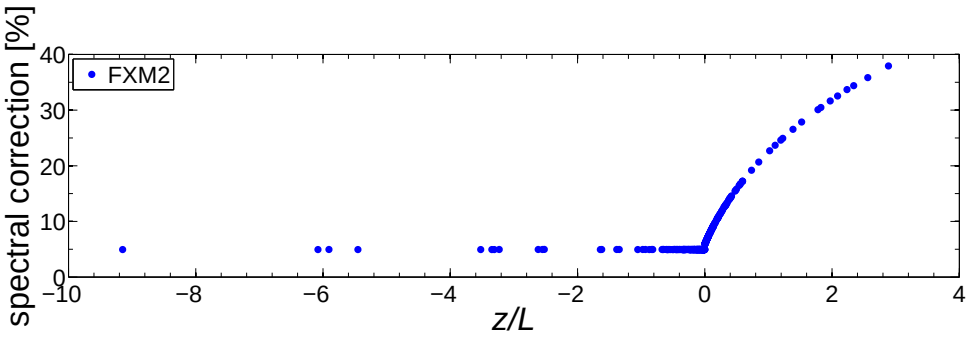

Figure 5.16: Spectral correction of the ozone flux depending on stability. The magnitude of the correction in relation to the uncorrected flux is calculated for the data of the ozone sensor FXM2.

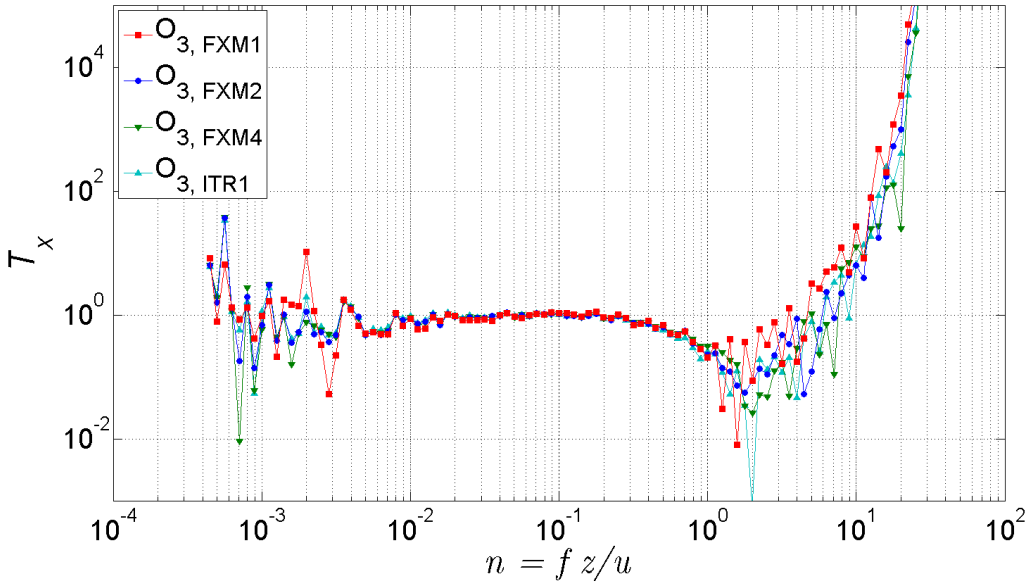

Figure 5.17: Coefficients of the transfer functions of O_3 sensors plotted against normalized frequency. Transfer functions for FXM1, FXM2, FXM4 and ITR1 are shown.

tween 0.2 and 2, the coefficients of the transfer function decrease due to the attenuation of fluctuations inside the tube and increase for higher frequencies due to the noise, only affecting the ozone flux cospectra. The transfer functions indicate that the tube attenuation decreases the cospectral densities to less than half of their real values for normalized frequencies higher than about 0.8-0.9.
Comparing the power and cospectra of the experiment at the airfield Mainz-Finthen (Figures 5.14 and 5.15; sampling frequency of 50 Hz) with those of the side-by-side comparison at the end of EGER-IOP3 (Figures 5.6 and 5.7; sampling frequency of 25 Hz) shows that a lower sampling frequency affects the noise in the flux measurement. A lower sampling frequency is obtained by averaging the respective number of sampled data points (e.g. 5 data points are averaged if a 10 Hz sampling frequency is chosen), which acts as a low-pass filter and reduces the white noise, but also the real fluctuations. The measurements of an additional ozone sensor with a lower sampling frequency during the Finthen experiment (results are not shown as the exact sampling frequency is not known) have shown higher attenuation and less noise compared to the 50 Hz ozone measurements, with spectra comparable to those of the side-by-side experiment at the end of EGER-IOP3.

In order to compare the effect of tube attenuation on the experimentally determined cospectra to the theoretic correction, correction factors (ϵ_x) for the ozone flux are determined for each flux averaging period. The factors are calculated as described in section 3.4.3, using the cospectra of the ozone fluxes and the heat flux cospectrum.
For mostly unstable daytime conditions the influence of stability on the correction factor is not significant and the horizontal wind speed u is found to be the only relevant controlling parameter. Therefore, the relation of the experimental correction factors to the wind speed is determined and compared to the relation obtained by using the theoretic transfer function for damping inside the tube and the theoretic spectra after Kaimal et al. (1972) presented in section 5.2. The relation is assumed to be linear with $\epsilon_x = au + b$, where a and b are parameters determined by linear fitting.
In the correction factors, the effect of sensor separation is not accounted for as it is already corrected for by the eddy-covariance software package. Not considering the effect of sensor separation reduces the axis intercept of the relation between ϵ_x and u such that it converges to the theoretic value of 1. For the comparison to the theoretic tube attenuation correction, it is assumed that the principle cause for the remaining high-frequency attenuation of the measured ozone flux is attenuation in the tubing, and thus contributions from slow response of the scalar sensor, from anemometer response and from the data aquisition system (Moore, 1986) are neglected. Another source for underestimating the fluxes is by high-pass filtering of the signals during data aquisition (linear trend removal, block averaging over a finite time period). Low frequency loss is not analyzed for the results presented in this thesis and so is not taken into account in the results. The estimated magnitude based on previous analyses is about 3 $\%$, depending for example on wind velocity and stability. Neglecting the differences between the cospectral densities in the low frequency range mainly reduces the slope of the relation between ϵ_x and u. The neglect also gives a small increase in the axis intercept and eliminates the few experimentally determined correction factors smaller than 1.
In field experiments as well as in the theoretic transfer function, the tube attenuation in different EC systems is affected by the length and inner diameter of the tube, the mean velocity of the flow and the Reynolds number. In the first phase of the Finthen experiment,

the factor distinguishing the systems from each other is the flow rate, which influences the mean velocity and the Reynolds number. It was already shown by the theoretic transfer functions that the tube Reynolds number has an effect on the dampening of the fluctuations by increasing the underestimation with decreasing Re.
To determine the relationships between correction factor and horizontal wind speed, only 30 minute values are taken into account where the fluxes of sensible heat and ozone of the particular sensor fulfill the quality criteria (see section 3.4.2). Thus, the number of correction factors considered for the relationship differs between the ozone sensors. Weighted fits and robust weighted fits are calculated. For the weighting, the standard deviation of the correction factor is used (see section 3.4.3 and appendix A).

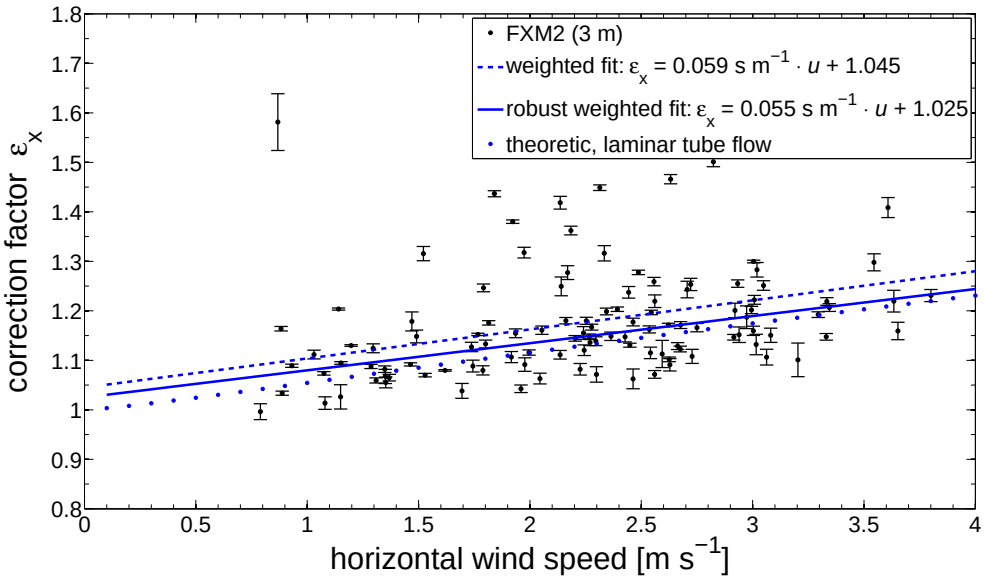

Figure 5.18: Relation between the correction factor and the horizontal wind speed for the fluxes measured by the sensor FXM2 at a height of 2.8 m during the first phase of the Finthen experiment. In blue the fitted linear regressions (weighted and robust weighted fit) and the theoretic relation for a sensor with the specific system characteristics are shown. For the fitting 113 correction factors are taken into account and the equations of the fits are given in the plot.

Figure 5.18 shows the relation between the correction factor and the wind speed for the sensor FXM2. The error bars denote the standard deviation of the correction factors. Linear fits (solid and dashed blue line) as well as the theoretic relation between ϵ_x and u (dotted blue line) are given. Most of the correction factors are close to the fitted lines. The correction factor with the largest distance to the fitted lines shows the largest error bars. The nearly parallel trends of the theoretic relation for laminar tube flow and the weighted as well as the robust weighted fit in Figure 5.18 indicate a good agreement of the measured data with theory. The coefficients of the fits are given in Table 5.2. The slope of the weighted fit is a little steeper and that of the robust weighted fit less steep than the slope of the theoretic fit. In both cases the correction factor gives an increase of the flux by less than 6 % for an increase of the wind speed of 1 m s^{-1}. The axis intercept is largest for the

Table 5.2: Fitting parameters of the linear relation $\epsilon_x = au + b$ between correction factor ϵ_x and horizontal wind speed u. The coefficients a and b are obtained by weighted and robust weighted fitting. All sensors are applied with a tube of a length of 3 m.

sensor	fitting method	slope [s m^{-1}]	axis intercept	R^2
FXM1	weighted	0.033±0.016	1.123±0.024	0.046
	robust weighted	0.067±0.008	1.011±0.012	0.759
FXM2	weighted	0.059±0.011	1.045±0.021	0.207
	robust weighted	0.055±0.006	1.025±0.012	0.764
FXM4	weighted	0.045±0.009	1.056±0.018	0.198
	robust weighted	0.051±0.006	1.025±0.012	0.666
ITR1	weighted	0.068±0.010	1.030±0.021	0.305
	robust weighted	0.065±0.006	1.017±0.013	0.710

weighted fit. It implicates a correction factor of already 1.045 at zero wind. The robust weighted fit reduces this value to 1.025. The application of a robust weighted fit increases the correlation coefficient and decreases the standard deviations of the slope and the axis intercept to about half the values of the weighted fit.
As the spectra agree well for the sensors FXM2, FXM4 and ITR1 (see Fig. 5.15), only the relation between ϵ_x and u of FXM2 is shown. For the sensors FXM4 and ITR1 the distribution of correction factors with wind speed looks similar to that of the sensor FXM2 in Figure 5.18. For the fitting of the FXM4 results 113 correction factors are taken into account and the fitting coefficients are given in Table 5.2. The slope is smaller than for the sensor FXM2 and also than the theoretic slope of 0.058 s m^{-1}. The intercept takes the same value as for the sensor FXM2. For the sensor ITR1 114 correction factors are used for the fitting, resulting in the coefficients given in Table 5.2. The intercept is smaller compared to the other sensors, however the slopes are larger, also compared to the theoretic slope of 0.058 s m^{-1}. As for the sensor FXM2, for the sensors FXM4 and ITR1 the standard deviations of the coefficients of the fit are nearly halved by the application of the robust weighted fitting instead of the weighted fitting. The robust weighted fit also shows an improvement of the correlation coefficient.
Figure 5.19 presents the scatterplot between ϵ_x and u for the sensor FXM1 as well as the linear fits (solid and dashed red line) and theoretic relation between ϵ_x and u (dotted red line). The correction factors have larger error bars and are more scattered than those of the other sensors, especially for wind speeds above 2 m s^{-1}. For the data from the sensor FXM1, there is also the largest deviation between the results of the weighted and the robust weighted fit. Table 5.2 gives the parameters obtained by the linear regression. The weighted fit gives a large axis intercept and only a small slope of the fitted line. Performing a robust weighted fit leads to a better agreement with the theoretic fit by decreasing the intercept and increasing the slope, such that the fit is nearly parallel to the theoretic fit. While the weighted fits of the sensor FXM1 and the other sensors deviate, the fits obtained by robust weighted fitting show a good agreement for all sensors.

The theoretic and experimentally determined relations between correction factor and horizontal wind speed show some differences. This raises the question of whether the difference between the measured and theoretic relation is significant. For the determination of

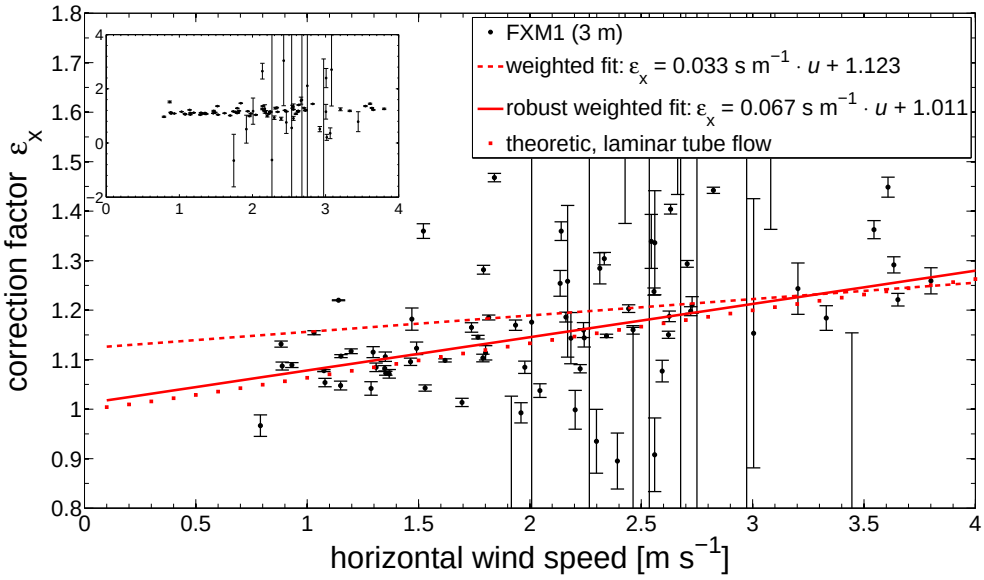

Figure 5.19: Relation between the correction factor and the horizontal wind speed for the fluxes measured by the sensor FXM1 at a height of 2.8 m during the first phase of the Finthen experiment. In red the fitted linear regressions (weighted and robust weighted fit) and the theoretic relation for a sensor with the specific system characteristics are shown. For the fitting 91 correction factors are taken into account (see small plot) and the equations of the fits are given in the plot.

the significance a student t test is applied. It tests if the difference is significant on a certain significance level and non-random. The test is performed for the slopes and axis intercepts of the fitted relations. Table 5.3 displays the significance levels on which an agreement cannot be rejected. For the first phase of the Finthen experiment, the difference between the fitted and the theoretic slopes is not significant and can thus be explained by randomness, i.e. too few data points. This is the case for all four sensors and for the weighted as well as the robust weighted fit. The axis intercepts show larger differences to their theoretic values. For the sensor FXM1 the difference between the axis intercept of the weighted fit and the theoretic one is highly significant (significance level of 99.9 %), while for the robust weighted fit the difference is not significant, which also applies for both fitting methods applied on the ITR1 data. For the axis intercepts of the sensors FXM2 and FXM4 a higher significance level is necessary to not reject the hypothesis that the measured and theoretic valus agree.

In contrast to the theory (see Fig. 5.3), the intercept of all fitted relations between ϵ_x and u is not 1 but crosses the ordinate at a higher value. The difference between the theoretic and the fitted axis intercept indicates that there might be another factor affecting the cospectra requiring further spectral correction or a modification of the applied one. A possible explanation for the difference is the execution of the sensor separation correction. The correction was performed by applying the theoretic transfer function, where the measurement height, among others, is required. The measurement height applied in the correction is the actual height above ground level minus the displacement height. For the analysis in this

Table 5.3: Significance levels on which an agreement between the fitted and theoretic coefficients of the linear relation between wind speed and correction factor cannot be rejected. All sensors are applied with a tube of a length of 3 m.

sensor	fitting method	slope	axis intercept
FXM1	weighted	95 %	-
	robust weighted	95 %	95 %
FXM2	weighted	95 %	99 %
	robust weighted	95 %	99 %
FXM4	weighted	95 %	99.9 %
	robust weighted	95 %	99 %
ITR1	weighted	95 %	95 %
	robust weighted	95 %	95 %

thesis, the displacement height is estimated as 2/3 of the actual canopy height. This rough estimate could partly be the reason for the deviation of the axis intercept from its theoretic value. This is due to the fact that the sensor separation correction affects rather the intercept than the slope as it is quite constant under unstable conditions without a dependency on wind speed.

5.5 Influence of tube length

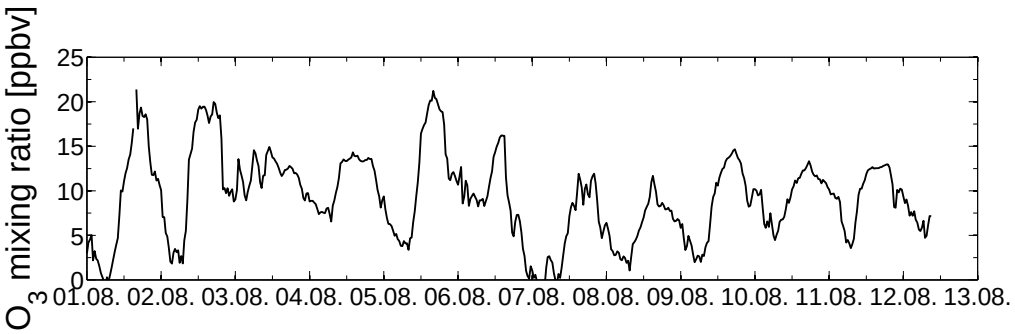

Figure 5.20: Time series of the ozone mixing ratio measured during the second phase of the experiment at the airfield Mainz-Finthen in summer 2013. The time series shows 30 minute averages measured at a height of 2.8 m.

During the second phase of the experiment at the airfield Mainz-Finthen in August 2013, the influence of the length of the inlet tubing on the flux was investigated. Therefore, in this phase the EC systems do not only differ in the flow rate of the ozone sensors, but also in the tube length. Figure 5.20 shows the ozone mixing ratios during the second phase of the experiment. The mixing ratios are even lower than during the first phase, with maximum daytime mixing ratios of about 20 ppbv until August 06 and lower than 15 ppbv afterwards. Figure 5.21 gives the ozone fluxes during the second experiment phase.

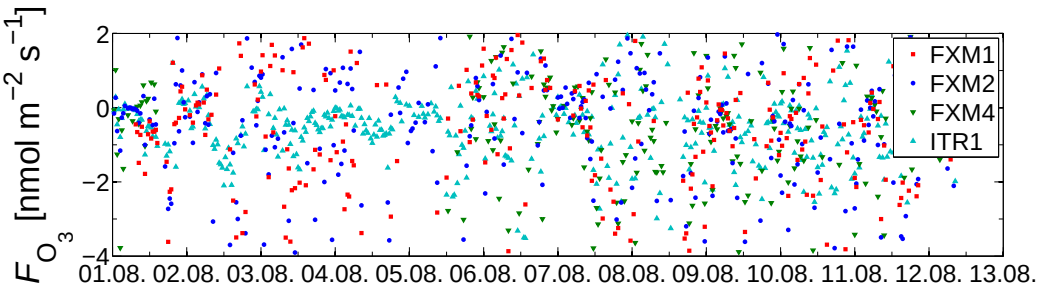

Figure 5.21: Time series of the ozone fluxes measured during the second phase of the experiment at the airfield Mainz-Finthen in summer 2013. The time series show 30 minute fluxes measured at a height of 2.8 m.

Due to the fluctuations in the time series of the ozone sensors not originating from actual fluctuations of ozone mixing ratio (see section 2.2 and 3.4.2), the calculation of fluxes does not give reliable results. There is a large scatter in the fluxes calculated from the data of all four ozone sensors, with also a lot of positive values. The best results are achieved by the sensor ITR1, which gives similar values as during the first phase of the Finthen experiment. Despite the disturbance of the ozone signals due to the broken instrument, the chemical discs applied during the second phase of the experiment also had a lower sensitivity.

Figures 5.22 and 5.23 show the averaged power and cospectra obtained for the analysis of the influence of tube length. They are more scattered than those of the first phase due to the usage of less spectra for the averaging. The spectra start at higher frequencies as shorter time periods are used for the determination of spectra. Only for the calculation of power spectra of temperature and cospectra of the heat flux 30 minute time series are used. Figure 5.22 displays the averaged power spectra of the temperature and the signals of the four ozone sensors. The temperature spectrum shows the same behavior in the high-frequency range as during the first phase of the experiment (see Fig. 5.14). However, it does not show the increase of spectral densities with increasing frequency in the low frequency range as for the first phase. The power spectra of the ozone sensors show a lot of scatter in the spectral densities on the frequency range, which is used for the determination of the normalization factor between temperature and ozone power spectra. Thus, the ozone power spectra as well as the ozone flux cospectra in Figure 5.23 might need to be shifted to higher or lower spectral densities for an exact agreement to the temperature or heat flux spectra. The scatter of the spectral densities of the ozone signals at lower frequencies also inhibit the determination of the frequency at which the power spectra of the ozone sensors start to differ from that of the temperature. The spectra show least scatter in the range of normalized frequencies between 0.1 and 40, where they already differ from the shape of the temperature power spectrum. The setup of the FXM2 system did not change between the two phases of the experiment and except for the more scattered course of the power spectrum, it agrees well with the power spectrum during the first phase of the experiment (see Fig. 5.14). The power spectrum of the sensor FXM1 shows constant values at a lower spectral density than during the first phase of the Finthen experiment. The data of this sensor shows the largest spectral density fluctuations of all ozone sensors in the frequency

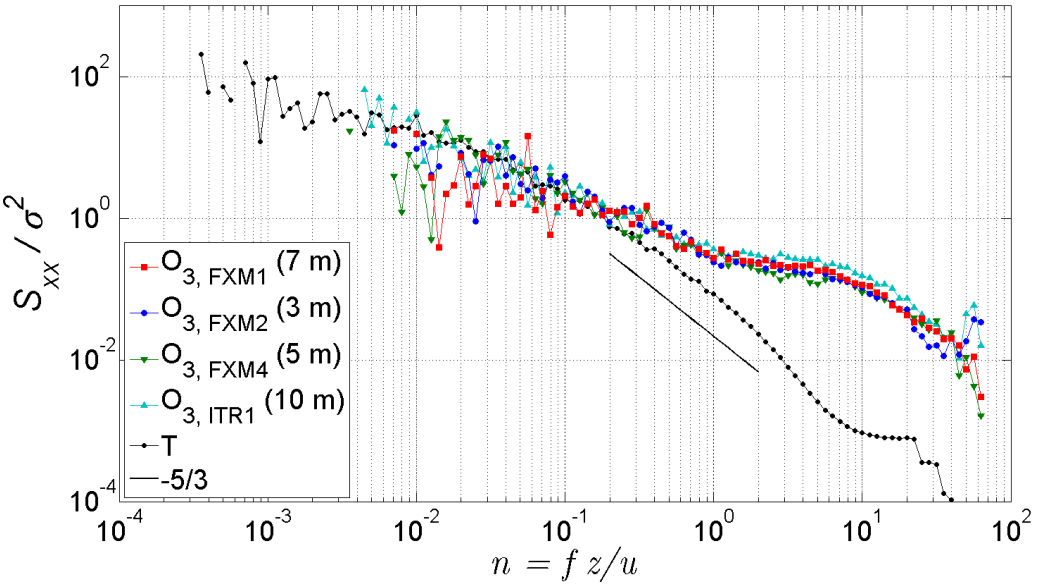

Figure 5.22: Averaged power spectral densities of temperature (T) as well as O_3 plotted against normalized frequency for the side-by-side experiment at the airfield Mainz-Finthen. Power spectra of the four ozone sensors, labeled FXM1, FXM2, FXM4 and ITR1, with different tube length are shown. The spectra are normalized by the variance σ^2 of the scalar concentration x (either T or O_3). The measurement length for one power spectrum was 30 minutes and 14 power spectra are averaged. The measurement height was 2.8 m. The straight black solid line gives the theoretical slope of -5/3.

range used for the normalization between power spectra of temperature and ozone. Thus, the determination of the normalization factor for the sensor FXM1 is most imprecise. Except for the power spectrum of the sensor FXM4, which shows the lowest constant spectral density, the level of the constant spectral density increases with tube length. This is due to the highest attenuation of ozone fluctuations in the longest tube, which increases the influence of noise as it becomes distinguishable from the real spectral densities at lower frequencies.

Figure 5.23 shows the averaged cospectra of sensible heat and ozone fluxes. The cospectra show the same scattered behavior as the power spectra. The cospectrum between vertical wind and temperature agrees well with the theoretic slope in the inertial subrange and with the cospectrum of the first phase of the experiment (see Fig. 5.15). The shapes of the cospectra of the ozone fluxes do not agree with the distribution of cospectral densities during the first phase. The cospectral densities are scattered around the heat flux cospectrum up to a normalized frequency of about 2. Thus, the ozone flux cospectra do not reveal a steeper decrease than the heat flux cospectrum due to the attenuation of fluctuations in the tubing. For frequencies higher than 2, the cospectra show about the same slope as during the first phase, but with spectral densities higher than those of the heat flux cospectrum.

Figure 5.24 presents the transfer functions of the ozone EC systems. In the system transfer

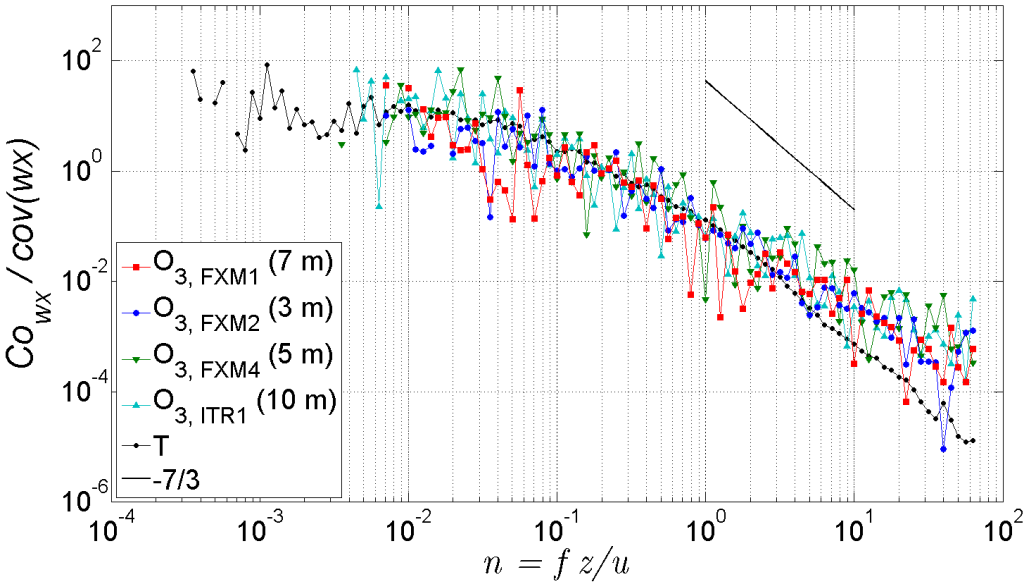

Figure 5.23: Averaged cospectral densities of vertical velocity (w) and temperature (T) as well as O_3 plotted against normalized frequency for the side-by-side experiment at the airfield Mainz-Finthen. Cospectra of the four ozone sensors, labeled FXM1, FXM2, FXM4 and ITR1, with different tube length are shown. The cospectra are normalized by the covariance $\overline{w'x'}$ of w and the scalar concentration x (either T or O_3). The measurement length for one cospectrum was 30 minutes and 14 cospectra are averaged. The measurement height was 2.8 m. The straight black solid line gives the theoretical slope of -7/3.

functions the effect of sensor separation is not included. For normalized frequencies up to about 2, the coefficients of the transfer function seem to fluctuate around 1. An attenuation of fluctuations due to the applied tube is not perceptible, as was already shown by the cospectra of the ozone fluxes. For frequencies higher than 2, the values of the transfer function increase with frequency to values higher than 10000 for all four sensors. The increase is due to the noise in the measurement of the ozone fluctuations and has no effect on the resulting ozone flux.

As a result of the more scattered cospectra of the ozone sensors and the more imprecise determination of the normalization factor between ozone and heat flux cospectra, the correction factors show a distribution over a larger range of values with also larger standard deviations. The standard deviations and also some values exceed the limit of the values displayed in the figures, therefore a smaller plot is inserted which contains all data points. Furthermore, the figures with the relations between correction factors and horizontal wind speed are shown for all four sensors, sorted by the length of the tubing.
Figure 5.25 gives the relation between the correction factors and the horizontal wind speed for the sensor FXM2, which was equipped with the shortest tube of 3 m as during the first phase of the experiment. The large figure contains all but two correction factors. Due to

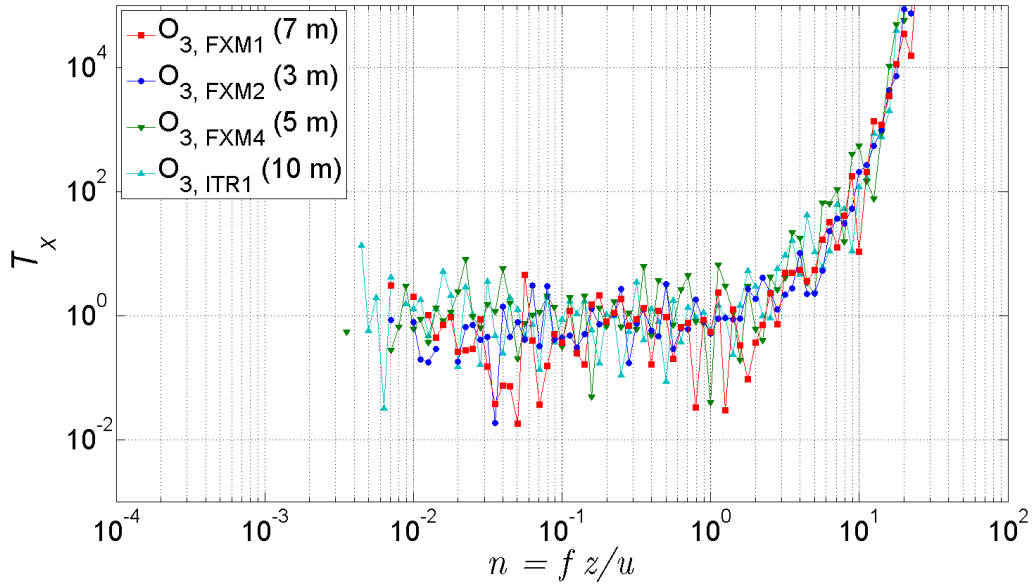

Figure 5.24: Coefficients of the transfer functions of O_3 sensors plotted against normalized frequency. Transfer functions for FXM1, FXM2, FXM4 and ITR1 with different tube length are shown.

the same system characteristics, the theoretic relation between ϵ_x and u is the same as in Figure 5.18. There is only a slight difference between the results of the weighted fit and the robust weighted fit, which are given in Table 5.4. The slope and axis intercept do not change much between the two fitting methods. In contrast to the results of the first phase the application of the robust weighted fit does not reduce the standard deviations and for the sensor FXM2 it even decreases the correlation coefficient. The fitted relations are nearly parallel to the theoretic relation between ϵ_x and u, but with a large offset of about 12 %.
The sensor FXM4 was applied with a tube of 5 m length. Figure 5.26 shows the result of the calculation of correction factors plotted against wind speed. All correction factors lie in the range displayed in the large figure, only some error bars exceed this range, which are shown in the small figure. The relations to the wind speed obtained by the fitting procedures are given in Table 5.4. The usage of a robust weighted fit improves the result by reducing the standard deviations of the coefficients of the fit and it increases the correlation coefficient. The axis intercepts are in good agreement with the theoretic one of 1.004, but the slope is larger than that received from the theoretic transfer function. The theoretic relation implies a necessary increase of the flux by 7.3 % per increase of the wind speed of 1 m s^{-1}, which is about half of the increase obtained by the fitting procedures.
The most scattered cospectra are obtained from the measurement of the sensor FXM1, which was applied with a tube of 7 m length. Figure 5.27 presents the correction factors for the FXM1 fluxes plotted against the horizontal wind speed. For this sensor the smallest number of correction factors is available. The large scatter of the correction factors is due to the imprecise determination of the normalization factor between the cospectra. The

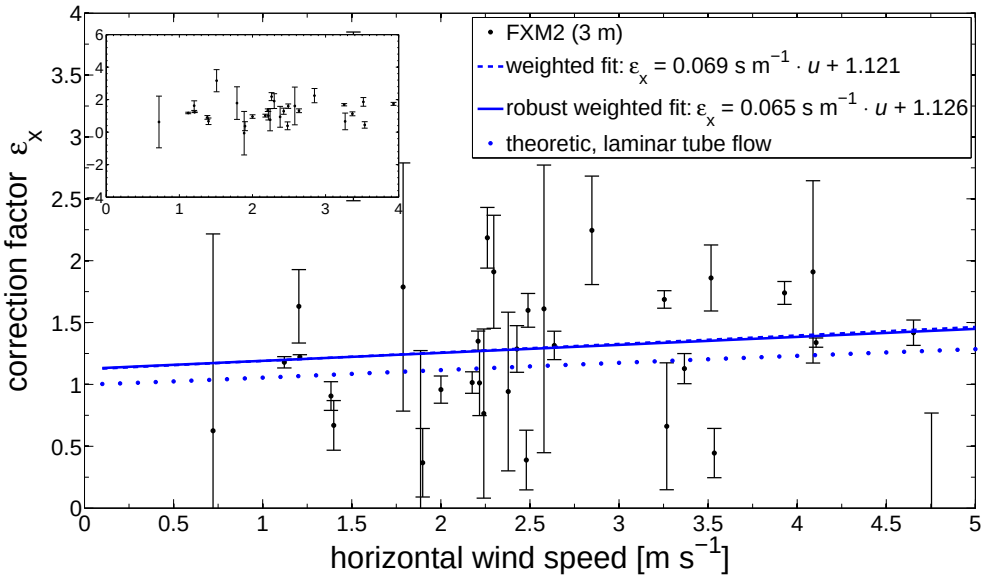

Figure 5.25: Relation between the correction factor and the horizontal wind speed for the fluxes measured by the sensor FXM2 and a tube of 3 m at a height of 2.8 m during the second phase of the Finthen experiment. In blue the fitted linear regressions (weighted and robust weighted fit) and the theoretic relation for a sensor with the specific system characteristics are shown. For the fitting 34 correction factors are taken into account (see small plot) and the equations of the fits are given in the plot.

fitted linear relations between ϵ_x and u show a differing trend for the two fitting procedures. Table 5.4 given the coefficients of the regressions. While the weighted fit gives the expected trend with an increase of the correction factor with increasing wind speed and a good agreement between the theoretic and fitted axis intercept, the robust weighted fit gives a decrease of the correction factor with increasing wind speed and a large axis intercept. Nonetheless, the correlation coefficient is improved by the application of the robust weighted fit and the standard deviations are reduced. Most of the correction factors with small standard deviations are located in the area between the weighted fit and the theoretic relation. The robust weighted fit agrees with the best data for horizontal wind speeds up to 2 m s^{-1}.

In Figure 5.28 the relation between correction factors and horizontal wind speed is shown for the sensor ITR1 with a tube length of 10 m. The measurement of the sensor ITR1 provides most correction factors for the determination of a linear fit, but most of the correction factors exhibit large standard deviations. The fitting parameters obtained by the two fitting procedures are given in Table 5.4. The fitted relations show the best agreement to the theoretic relation between ϵ_x and u. The axis intercepts differ from the theoretic one of 1.012 by about 0.03, but the slopes are both larger than the theoretic increase of 9.9 % per increase of the wind speed by 1 m s^{-1}. With the application of the robust weighted fit, the slope gets closer to the theoretic one and also the standard deviations and the correlation coefficient improve.

Table 5.4: Fitting parameters of the linear relation $\epsilon_x = au + b$ between correction factor ϵ_x and horizontal wind speed u. The coefficients a and b are obtained by weighted and robust weighted fitting. The sensors are applied with tubes of different length between 3 and 10 m.

sensor	fitting method	slope [s m^{-1}]	axis intercept	R^2
FXM1 (7 m)	weighted	0.209±0.053	0.999±0.132	0.397
	robust weighted	-0.067±0.036	1.424±0.091	0.715
FXM2 (3 m)	weighted	0.069±0.028	1.121±0.063	0.166
	robust weighted	0.065±0.029	1.126±0.067	0.067
FXM4 (5 m)	weighted	0.122±0.032	1.071±0.074	0.281
	robust weighted	0.144±0.025	1.033±0.057	0.573
ITR1 (10 m)	weighted	0.161±0.035	0.982±0.078	0.307
	robust weighted	0.136±0.029	1.042±0.066	0.512

Table 5.5: Significance levels on which an agreement between the fitted and theoretic coefficients of the linear relation between wind speed and correction factor cannot be rejected. The sensors are applied with tubes of different length between 3 and 10 m.

sensor	fitting method	slope	axis intercept
FXM1 (7 m)	weighted	99 %	95
	robust weighted	-	-
FXM2 (3 m)	weighted	95 %	95 %
	robust weighted	95 %	95 %
FXM4 (5 m)	weighted	95 %	95 %
	robust weighted	99.9 %	95 %
ITR1 (10 m)	weighted	95 %	95 %
	robust weighted	95 %	95 %

Table 5.5 summarizes the significance levels for the agreement between the fitted relations between correction factor and horizontal wind speed during the second phase of the Finthen experiment and the theoretic relations. Only the difference between the robust weighted fit and the theoretic fit for the sensor FXM1 is found to be highly significant. The robust weighted fit of the sensor FXM1 is the only fit giving a negative trend of the correction factor with increasing wind speed. The differences between the other fitted and theoretic axis intercepts are not found to be statistically significant. Regarding the slopes, the sensors FXM2, ITR1 and the weighted fit for FXM4 show best agreement with the theoretic relation and the difference is not significant. For the other slopes the difference is significant and a higher significance level is necessary to not reject the agreement between theoretic and fitted slope.

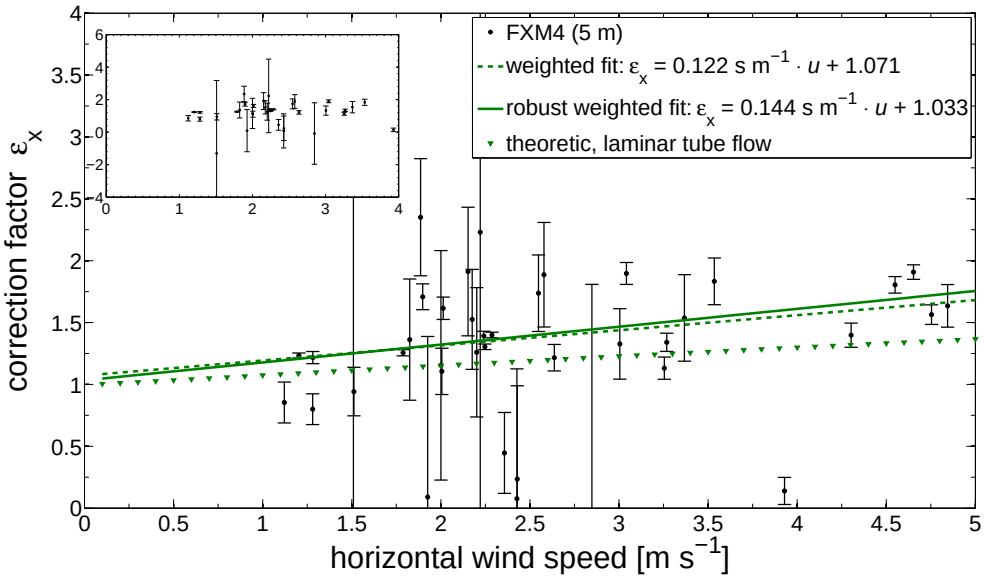

Figure 5.26: Relation between the correction factor and the horizontal wind speed for the fluxes measured by the sensor FXM4 and a tube of 5 m at a height of 2.8 m during the second phase of the Finthen experiment. In green the fitted linear regressions (weighted and robust weighted fit) and the theoretic relation for a sensor with the specific system characteristics are shown. For the fitting 40 correction factors are taken into account (see small plot) and the equations of the fits are given in the plot.

5.6 Discussion

The following discussion deals with the weaknesses of closed-path EC systems with laminar tube flow for the measurement of turbulent fluxes of ozone and with implications of the findings for the results of the EGER campaign and future flux measurements. The objective was to provide a robust and simple method that considers the variability in low-pass filtering by a closed-path ozone EC system and corrects the EGER dataset for it.

The theoretic corrections for laminar and turbulent tube flow have shown that the ozone fluxes need to be corrected less for turbulent than for laminar tube flow (see Fig. 5.3 and 5.4). Thus, the high-frequency response of the closed-path EC system can be improved substantially by ensuring turbulent flow in the tube, using a combination of high volumetric flow rate (e.g. by using a powerful pump) and small tube diameter (Leuning and King, 1992) as well as keeping the length of the tubing short (Lenschow and Raupach, 1991). Nevertheless, a large air flow volume in the inlet tubing might require a large spatial separation between the inlet of the tube and the sonic anemometer head, leading to another loss of covariance (see Moore, 1986 for the specific contributions of the diverse characteristics of an EC system to the total damping). The Reynolds number is a relevant factor to consider when estimating the high-frequency cospectral attenuation of ozone fluxes. In particular, decreasing Reynolds numbers increase the high-frequency attenuation. Figure 5.29 taken from Zahn et al. (2012) displays the approximate Reynolds number of the flow

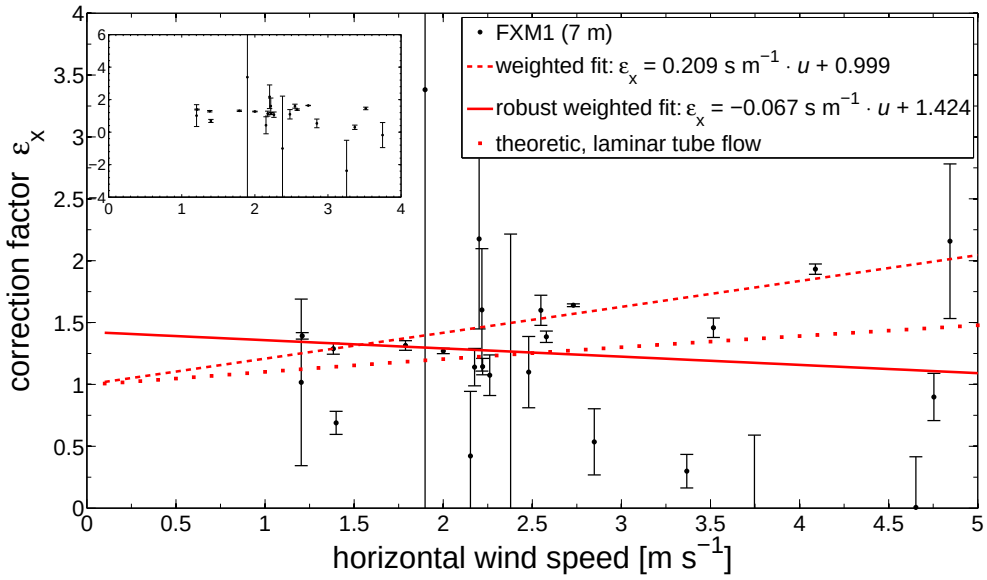

Figure 5.27: Relation between the correction factor and the horizontal wind speed for the fluxes measured by the sensor FXM1 and a tube of 7 m at a height of 2.8 m during the second phase of the Finthen experiment. In red the fitted linear regressions (weighted and robust weighted fit) and the theoretic relation for a sensor with the specific system characteristics are shown. For the fitting 27 correction factors are taken into account (see small plot) and the equations of the fits are given in the plot.

in the tubing of the fast-response ozone sensor, where the x-axes is either flow rate or Reynolds number. It has to be considered that the inner diameter of the 3/8" tube used by Zahn et al. (2012) is smaller than that of the applied tubes. Thus, in the side-by-side experiment the same flow rate results in a slightly smaller Reynolds number. The values are well below the critical Reynolds number for turbulent flow (~2300 for straight tubing). The figure gives the response times of sensor systems with different tube lengths. For the shortest and longest applied tubes, it shows that the measured response times are in between those for pure laminar or tubulent flow. According to Lenschow and Raupach (1991) the radial mixing in the tube is enhanced by elbows and soft bendings in the tube, which converges the diffusion coefficient to the one for turbulent flow. This was also shown by Zahn et al. (2012) for changes in the inlet line cross section within sampling blocks. Therefore, it can be assumed that the tube flow during the Finthen experiment was not completely laminar, which should reduce the tube attenuation.

The effect of high-frequency attenuation is evaluated using the cospectral correction method. It assumes originally equal spectral distribution of ozone and sensible heat flux (Panofsky and Dutton, 1984) and that dampening starts at frequencies exceeding 0.15 Hz (upper limit for the determination of the normalization factor). The cospectra between w and T during the Finthen experiment follow the theoretic shape (see Fig. 5.15 and 5.23). Thus, they could be well used for the cospectral correction method of ozone fluxes. The attenuation of ozone fluctuations in the tube is found to considerably change the shape of the cospectra

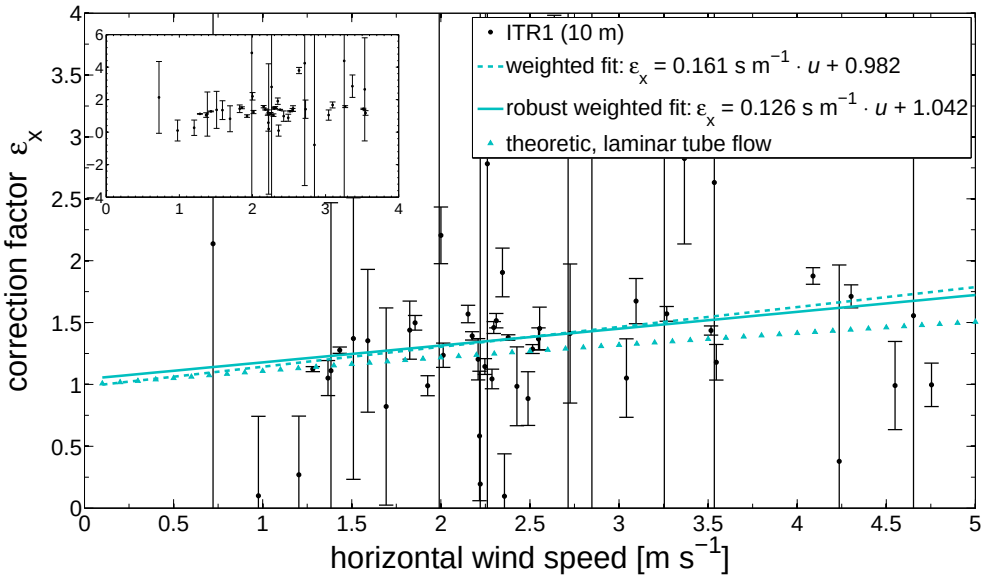

Figure 5.28: Relation between the correction factor and the horizontal wind speed for the fluxes measured by the sensor ITR1 and a tube of 10 m at a height of 2.8 m during the second phase of the Finthen experiment. In turquoise the fitted linear regressions (weighted and robust weighted fit) and the theoretic relation for a sensor with the specific system characteristics are shown. For the fitting 52 correction factors are taken into account (see small plot) and the equations of the fits are given in the plot.

(see Fig. 5.15).
With the cospectral correction method, correction factors for the measured ozone fluxes between 0 and 2.5 are determined for the different EC system setups. This factor is calculated as a function of measuring height z, mean horizontal wind speed u, Monin-Obukhov stability z/L, tube length l and flow rate, whereof measuring height and flow rate have been constant throughout the campaign. For sensor systems with a laminar tube flow and tubes of 3 m length, most of the correction factors are in the range beween 1 and 1.3 for sensors FXM2, FXM4 and ITR1, and between 0.9 and about 1.5 for sensor FXM1 with the lowest flow rate. The attenuation effect of ozone fluxes is tested against theoretic functions, which are found to be a good estimate for determining the correction factor. For most of the fitting parameters, the fitted relation of the correction factor to the horizontal wind speed by robust weighted fitting is not significantly different from the theoretic relation between ϵ_x and u, which is determined using the theoretic transfer function for tube attenuation after Lenschow and Raupach (1991) and the model cospectra after Kaimal et al. (1972). For the sensor systems with different tube lengths, the determined correction factors allow no clear implication for an accordance with the theoretic correction factors. Except for the sensor FXM1, the differences between fitted and theoretic relation of the correction factors to wind speed are not highly significant, but the correction factors are scattered between 0 and about 2.5.
A direct comparison of the observed correction factors to literature values is not possible, as factors influencing the correction need to be taken into account, which are not neces-

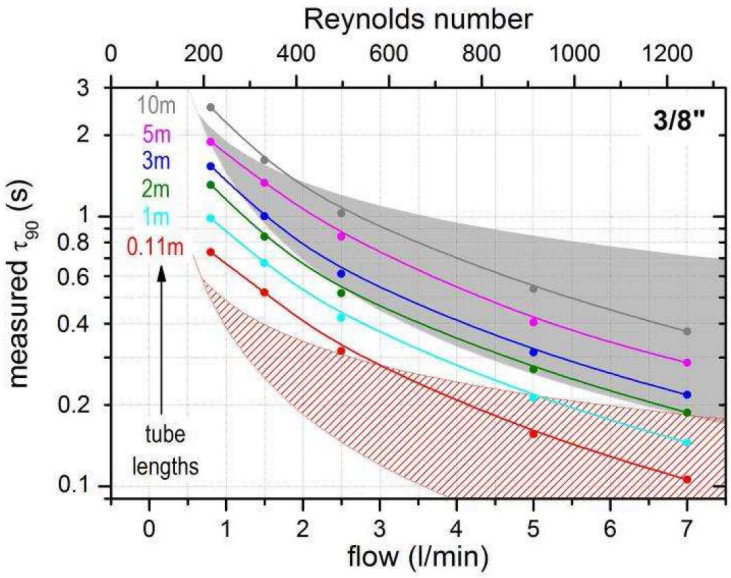

Figure 5.29: Measured response times for inlet tube lengths l between 0.11 m and 10 m and for 3/8" (ID=6 mm) sampling tubes. The upper x-axis indicates the Reynolds number. The colored areas are solutions of the diffusion equation (Eq. (8) in Zahn et al., 2012), the upper border for pure laminar flow, the lower border for turbulent flow, in grey for an inlet tube length of l=10 m and in red of l=0.11 m (taken from Zahn et al., 2012).

sarily given in the literature. A longer tubing, larger diameter of the tube as well as lower flow rate/Reynolds number increase the correction. The measurement height needs to be considered as well, as the influence of high-frequency attenuation decreases with increasing measurement height. In addition, as already emphasized by Runkle et al. (2012), a short-term paired-device calibration experiment may be insufficient to capture attenuation changes outside the range of meteorological conditions experienced during the campaign period. However, the range of the correction factors should be comparable. Correction factors for ozone flux measurements are rare in the literature, therefore the obtained results for the correction of ozone fluxes are also compared to those obtained for other gas flux measurements (e.g. CO_2, NO_2) as for these scalars comparable values to ozone are expected. Values for water vapor are given as well, for which several studies reported an additional dependency of the correction on relative humidity by adsorption and desorption processes on the tube walls, which increases the correction compared to a passive tracer (Ibrom et al., 2007; Massman and Ibrom, 2008; Runkle et al., 2012).
Massman (1991) and Massman (1993) report ozone measurements performed by Zeller et al. (1989), where a lengthening of the response time was found for a sensor system of sensor and intake tube compared to the sensor alone. The longer response time could be accounted for by allowing interactions of ozone with the tube wall (Massman, 1991), like sorption/desorption and/or destruction of ozone by the tube walls. The finding of possible interactions with the tube walls could be the reason for a larger flux underestimation for ozone as expected for a passive tracer by the theoretic correction factors. However, it was mentioned that the dampening of fluctuations is not likely to cause significant errors in the flux measurement (Massman, 1991). Tuovinen et al. (1998) report a typical total spectral correction factor of 1.15 for ozone fluxes, with a relatively unimportant effect of tube

attenuation due to turbulent tube flow. Keronen et al. (2003) estimated systematic errors due to the imperfect frequency response of the instrumentation based on one year of ozone measurements with a 12 m long Teflon tube with a mean diameter of 9 mm. For unstable stratification, the estimated underestimation correction factors are 1.03-1.19, also revealing a linear dependency to wind speed and being independent on stability for unstable stratification. In stable cases, larger corrections of 1.13-1.33 occured. Those were cases, when absolute flux values were nearly zero. Muller et al. (2010) investigated sources of uncertainty using two fast-response dry chemiluminescence ozone sensors side-by-side over grassland and compared the fluxes calculated with the same method for the two sensors. Differences of up to a factor of 2 for half-hourly flux values were observed. The agreement between the fluxes was excellent for some days, when also the cospectra showed a good agreement, but there is an underlying uncertainty as a result of variable analyzer performance and of non-linear sensitivity of the chemical discs.
Moravek et al. (2013) tested the flux loss due to high-frequency attenuation for O_3, CO_2 and H_2O by applying low-pass filters with different cut-off frequencies to the 20 Hz scalar time series. A flux loss between less than 5 and 30 $\%$ was found, with similar results for all scalar quantities. They used the same ozone sensor (enviscope GmbH, Germany; ITR1 in this thesis) with an inlet tube of 2.5 m length, which is a little shorter than the tube used for this study.
The attenuation of water vapor and CO_2 fluctuations was investigated in several studies. The influence of the attenuation of fluctuations was not only investigated by the cospectral transfer function method, but also by comparison with open-path EC systems, where no tube is applied and hence they are not prone to gas transport effects and no tube attenuation takes place. Lenschow and Raupach (1991) investigated the attenuation of humidity fluctuations in straight tubing in a laboratory investigation and thereby developed simple formulations for the use in turbulent flux measurements with turbulent and laminar tube flow. Their transfer functions have been used in this thesis for the determination of theoretic relations between correction factors and horizontal wind speed. Massman and Ibrom (2008) examined the effect of tube attenuation with turbulent tube flow for both, passive and sorbing tracers. They found the theoretic transfer function to be most applicable to a straight horizontal tube, but closed-path flux systems are rarely implemented in this way. In general, the departure from the ideal tube led to the suggestion that the present attenuation model for sorption/desorption at the tube wall may need to be calibrated against spectra of trace gases on site specific basis. Mammarella et al. (2009) found the age of the sampling tube to be another relevant factor for the spectral correction, at least for water vapor fluxes. For used tubes the relative humidity affects the response time. For a 7 m tube, the correction of water vapor fluxes was 7 $\%$ on average over a Scots pine forest with an unused tube and 10-15 $\%$ in summer with a 4 year old tube. They concluded that the effective transfer function should be estimated experimentally at least once per year and that high correction can be avoided by periodic maintenance of the tube. Aubinet et al. (2001) found slopes in the equation for the correction factors due to sensor separation and fluctuation attenuation in the tube to be 0.044 $\mathrm{s\,m^{-1}}$ for CO_2 and 0.063 $\mathrm{s\,m^{-1}}$ for H_2O, the factor varies between 1.04 and 1.25 for CO_2 and between 1.06 and 1.35 for water vapor flux, depending on the wind velocity. Those values are in good agreement with the correction factors determined for the Finthen experiment. For the passive tracer CO_2 numerous studies report lower correction factors than for ozone fluxes. Over a Beech forest in Denmark, the correction for

water vapor accounted on average to 42 % of the measured flux due to interactions between H_2O and the tube wall, while it was only 4 % for the CO_2 flux (Ibrom et al., 2007). Leuning and King (1992) compared open- and closed-path CO_2 flux measurements with a laminar tube flow. The fluxes obtained with the closed-path analyzer were on average 16 % lower than those obtained with the adjacent open-path analyzer. Goulden et al. (1997) obtained comparable values over a black spruce forest. The values ranged between 1.02 and 1.5 depending on wind speed and atmospheric stratification. The correction was linearly related to wind speed under unstable and near neutral conditions with $\epsilon_x = 1.02 + 0.017\,\mathrm{s\,m^{-1}} \cdot u$. Basically the same approach and a closed-path EC system was used by Hollinger et al. (1999) to measure fluxes above a red spruce dominated forest. The dependency of the correction factor to wind speed was found to be smaller with $\epsilon_x = 1.03 + 0.007\,\mathrm{s\,m^{-1}} \cdot u$, with an average daytime correction of 6 % and 11 % at nighttime. Ammann et al. (2006) corrected water vapor fluxes using empirical ogive analysis. For their correction an upper limiting frequency of 0.065 Hz corresponding to a period of 15 s was chosen and the dampening of the water vapor flux measurement is assumed to start at frequencies exceeding this limit. For the correction, which is presented in this thesis, an average upper limit of 0.15 Hz is chosen for the measurement at the airfield Mainz-Finthen and of 0.07 Hz for the EGER spectra. As the spectra and transfer functions depend on measurement height and wind speed, it is necessary and useful to adapt the frequency range for scaling (Ammann et al., 2006). In the analysis of Ammann et al. (2006), the frequencies below the upper limiting frequency contribute by about 40 % to the undisturbed heat flux and around 60 % to the damped water vapor flux. Adopting their analysis to the averaged cospectra of the Finthen experiment results in the undisturbed heat flux reaching 71.45 % of its total value up to the frequency limit. This value is larger due to the higher upper limiting frequency. For the single ozone sensors the average uncorrected value is 80.90 % (FXM1), 81.49 % (FXM2), 81.12 % (FXM4) and 82.57 % (ITR1), still including the effect of sensor separation on the high-frequency attenuation of the cospectra. Like in the correction of water vapor fluxes determined by Ammann et al. (2006), the fractions of the flux in the lower frequency range up to the limiting frequency are overestimated. While on average the higher frequencies should have an influence of about 30 % to the total flux, they only contribute to the calculated ozone flux by about 20 %.
Eugster and Senn (1995) observed a daily average of the correction factor for NO_2 of 1.2 (range 1.12-1.31) for August and September, and 1.14 (range 1.05-1.22) in May. For the measurements a 5 m long 0.6 cm Teflon tube with a flow rate of 2.2 $\mathrm{l\,min^{-1}}$ was used to not influence the wind measurement significantly. The disadvantage of the small air flow is a laminar tube flow (Re ~600), which mainly causes the high-frequency loss in the measuring path.

The comparison of the results of the sensor comparison to those of previous studies emphasizes the importance of correcting closed-path ozone fluxes for attenuation at high frequencies caused by dampening of fluctuations in the tubing as otherwise the ozone fluxes might still include a considerable uncertainty. The cospectral correction method was demonstrated to improve closed-path ozone flux estimates and the exact functions and parameters of the relationships found here are highly dependent on the characteristics of the flux measurement system (tube length, flow rate, etc.). The results described above show that the correction factors under unstable stratification presented in this thesis are reasonable compared to values obtained for other flux measurements with closed-path EC systems, and

that they are in good agreement to theoretic correction factors.

6 Ozone exchange during the EGER campaign

6.1 Meteorological conditions during EGER-IOP3

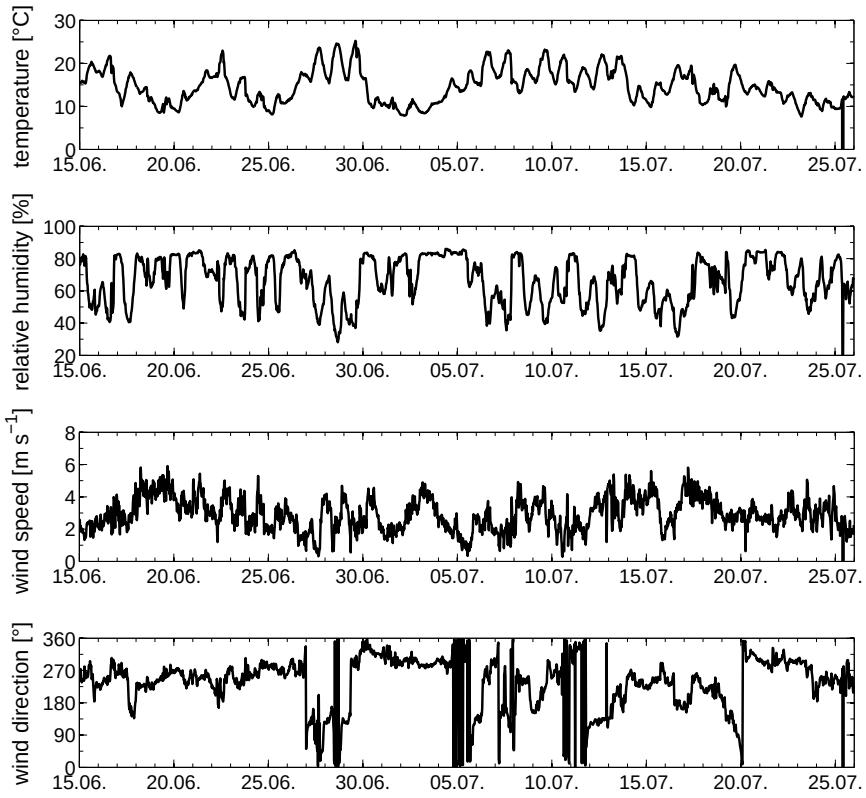

Figure 6.1: Meteorological conditions during the campaign EGER-IOP3 in summer 2011. Displayed from top to bottom are the time series of 10 minute averages of temperature, relative humidity, wind speed and wind direction measured on the main tower M1 at a height of 32 m.

The weather during the EGER campaign in summer 2011 was characterized by warm and sunny days as well as overcast days and rain. Figure 6.1 shows the time series of temperature, relative humidity, wind speed and direction for the entire time period from June 15 until July 25, 2011. The maximum temperatures during daytime ranged between 8 and

Table 6.1: Synoptical conditions on the "golden days" (from Serafimovich et al., 2011).

N	Period	Conditions	Wind speed	Wind directions
1	June 26 - 29, 2011	good (cloudless) conditions mainly on 27, 28 and 29 up to 2 p.m.	moderate winds	26/27 from west, 28/29 from east
2	July 04 - 08, 2011	best conditions on 06 and 07, other days partly cloudy, on 08 in the morning short power off	low winds	04/07/08 from west, 05/06 from east
3	July 14 - 17, 2011	best conditions on 15 and 16, on 14 and 17 partly cloudy	moderate winds	south-west

27 °C. The relative humidity during the campaign was higher than 40 % except for some days. The time series of the relative humidity and the temperature act anticorrelated, as relative humidity decreases with increasing temperature. The driest and warmest days with best radiation conditions were those from June 27 until the afternoon of June 29 followed by a thunderstorm and a high relative humidity over the next days. The mean wind speed reached values up to 6 $\mathrm{m\,s^{-1}}$. The wind was coming mainly from westerly directions. It turned to easterly directions over a longer period during the dry and warm days mentioned before. Over the period from July 5 to 14, the wind directions as well as the wind speeds were strongly fluctuating. This time period was characterized by a mixed high and low pressure influence.
From the entire campaign period, three periods have been selected as "golden days" based on radiation, wind, precipitation measurements and instrumental performance. Some synoptical observations of the "golden days" are summarized in Table 6.1 (from Serafimovich et al., 2011). The first period is after the passage of a warm front with still some rain on June 26. The site was under high pressure influence until the passage of a cold front on June 29 accompanied by a thunderstorm and rain. The second period is characterized by little rain on all days with an occlusion approaching from north-east, which passed the site on July 05, and a cold front in the night of July 06/07. The third period still showed some rain on July 14 after the passage of a cold front and more rain on July 17 due to the passage of another cold front.

6.2 Comparison of TK3 and MPIC software packages

Two eddy-covariance software packages have been applied for the calculation of ozone fluxes during the EGER campaign. The MPIC software package was used as it was already applied for the calculation of ozone fluxes during previous EGER campaigns. Whereas, for all other fluxes (sensible and latent heat, as well as CO_2) measured and calculated by participants from the University of Bayreuth in EGER-IOP3, the EC software package TK3 has been applied. The main difference between both software packages, favoring TK3 over MPIC software, is the spike detection, which is not applied by the MPIC software and

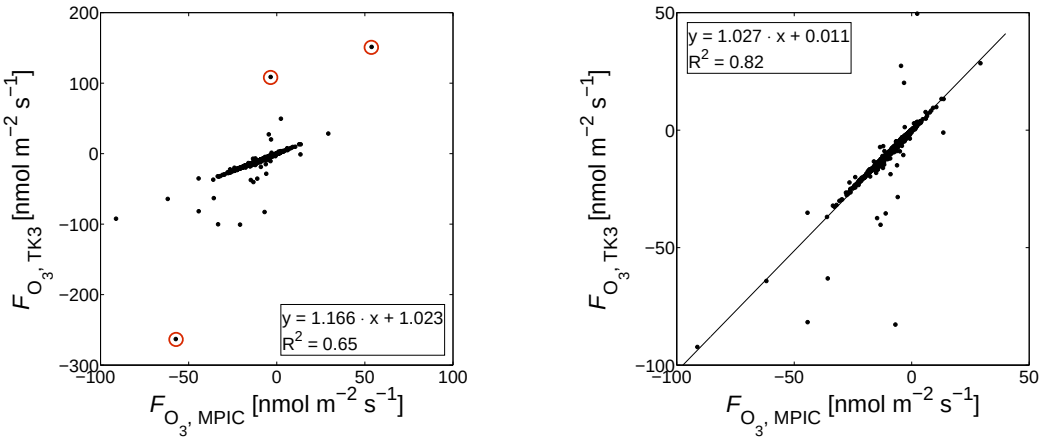

Figure 6.2: Scatterplot of measured O_3 fluxes, processed by TK3, against O_3 fluxes, processed by the MPIC software package. For (a) all fluxes measured at mast M1 and M4 over the entire measurement period are used and for (b) the three obvious outliers marked in (a) are neglected.

the additional QA/QC module of TK3. However, TK3 has no functioning O_3 channel, therefore the N_2O channel is applied and the fluxes are corrected for differences in the molar masses. In order to determine if the ozone fluxes of TK3's N_2O channel agree with those of the MPIC software and if TK3 is suitable to be used for all further calculations, the O_3 fluxes processed by both software packages are compared. For the comparison of the software packages, all ozone fluxes calculated for the masts M1 and M4 during EGER-IOP3 and with quality flags given by TK3 between 1 and 6 are used. Figure 6.2 shows a scatterplot between the O_3 fluxes processed by both software packages. The regression between the fluxes shows a good agreement between the software packages. Neglecting three obvious outliers gives a deviation of less than 5 %, which is within the range of differences found in software intercomparisons (Mauder et al., 2008).
The good agreement indicates that both packages give reliable flux estimates and for the further analysis only the EC software package TK3 will be used.

6.3 Effect of corrections

In order to estimate the impact of the correction procedure on the resulting flux, fluxes are calculated with and without the application of corrections. A number of corrections have been applied to the raw fluxes, which are described in section 3.3.2. By comparing the results of the current and an older version of the software package TK3, the influence of corrections on the resulting flux is determined. In the older version no application of corrections was included in the N_2O channel applied for the ozone flux calculation. Figure 6.3 shows a scatterplot between corrected and uncorrected ozone fluxes from the masts M1 and M4. The regression shows that the absolute values of the corrected EGER fluxes are on average about 6.6 % larger than those of the uncorrected fluxes with a small offset.

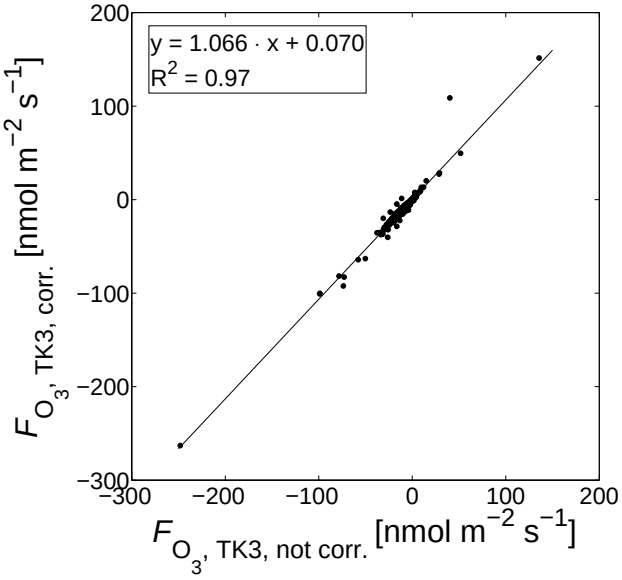

Figure 6.3: Scatterplot of measured ozone fluxes with and without the application of corrections. For the linear relation given in the plot, the fluxes from the masts M1 and M4 during EGER-IOP3 with quality flags between 1 and 6 are considered.

The sites and the setup of the measurements at M1 and M4 are different. Thus, the actual lag and spectral correction as well as coordinate rotation are different for both sites and for changing meteorological conditions. Especially the spectral correction under stable conditions shows large differences for fluxes from M1 and M4. Figure 6.4 gives the magnitude of the spectral correction plotted against the stability (displayed by the dimensionless length parameter z/L). While under unstable conditions ($z/L < 0$) the effect of the spectral correction is nearly constant with values lower than 5 % on both masts, for stable conditions, the influence of the spectral correction increases and is considerably larger for M4 than for M1. The corrections are different for the two masts due to the different measurement heights, which result in different turbulence spectra. The lower measurement height of M4

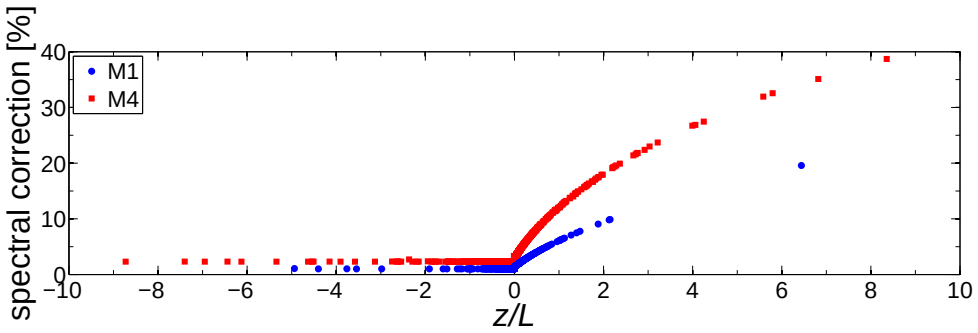

Figure 6.4: Spectral correction of the ozone flux depending on stability. The magnitude of the correction in relation to the uncorrected flux is calculated for masts M1 and M4 of EGER-IOP3.

results in a spectrum that is shifted to higher frequencies. Thus, the spectral corrections, which affect the high-frequency part of the spectrum, result in larger corrections.
The comparison shows that there is a large variation in the size of the flux correction, but the average effect of the correction on the flux is comparably small.

6.4 Measured ozone exchange during EGER-IOP3

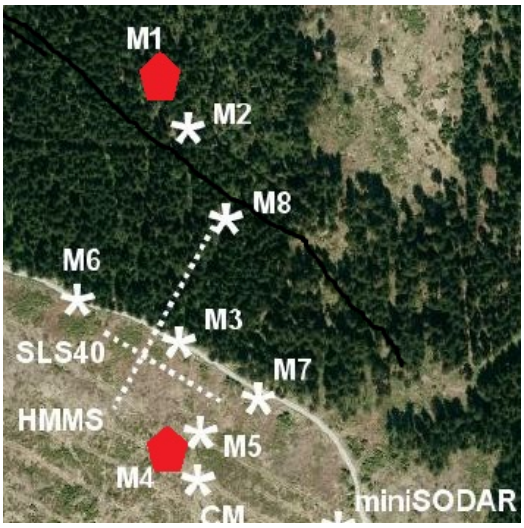

Figure 6.5: Close-up view of the site where the EGER-IOP3 measurements have been performed. The total site is shown in Figure 2.1(a). The red points mark the positions of the main tower M1 and the turbulence mast M4.

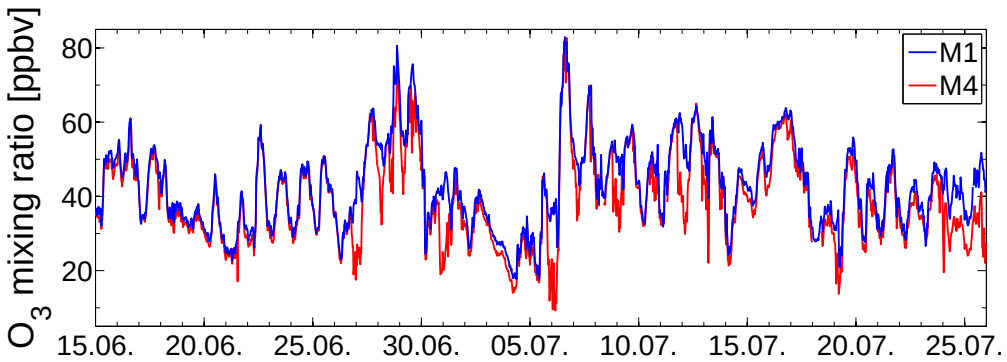

Figure 6.6: Time series of the ozone mixing ratios measured during EGER-IOP3 at M1 and M4. The time series show 30 minute averages measured at a height of 32 m at M1 and 5.5 m at M4.

In EGER-IOP3, the ozone exchange between the atmosphere and the biosphere has been investigated during 41 days on the masts M1 and M4. Figure 6.5 displays a close-up

view on the positions of the two masts. Figure 6.6 shows the ozone mixing ratios for the entire campaign period. Until June 20 the mixing ratios show no pronounced diurnal cycles. Afterwards, there is a clear difference between day- and nighttime mixing ratios. The daytime mixing ratios are about 15 to 20 ppbv higher than during the night. Highest daytime mixing ratios are present on June 28 to 29 and on July 06 with values up to 80 ppbv. Lowest daytime mixing ratios occur on June 18 and 19 and on July 03 and 04 with values around 30 ppbv. The mixing ratios measured above the forest and on the clear-cut agree well during daytime except for the last days of the measurement campaign. The nighttime mixing ratios are similar at both sites or the mixing ratios at M4 are lower than above the forest and thus show a more pronounced diurnal cycle. The trend of the mixing ratios agrees with the trend of the meteorological conditions during the campaign (see Fig. 6.1). The mixing ratios are highest under high radiation conditions, indicated by high temperature and low RH, due to the increased production of ozone under these conditions.

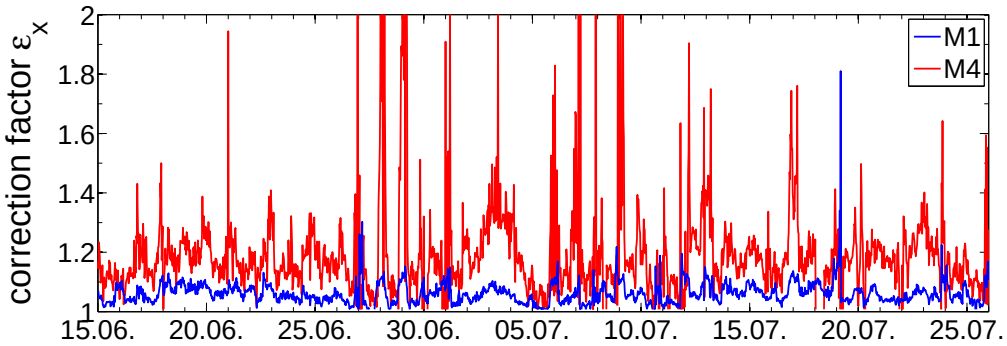

Figure 6.7: Theoretic correction factors for the attenuation of fluctuations inside the tube during EGER-IOP3. The correction factors are determined using the measured values of z/L, u, z and l. The sensor at M1 was equipped with an inlet tubing of 6.96 m and the sensor at M4 with an inlet tubing of 9.47 m length.

In order to be able to compare the fluxes at M1 and M4 measured by different EC systems, the measured fluxes need to be corrected for the influence of dampening of fluctuations in the tubes. The tube correction is not included in the post-processing routine of the software package. However, it was shown in chapter 5 that the correction is necessary due to the laminar tube flow in the long tubes and that the theoretic transfer function for laminar tube flow is suitable to be used for the correction of ozone fluxes. Using the measured meteorological data of wind speed and stability as well as the actual measurement height and tube length, correction factors (ϵ_x) are obtained from the theoretic transfer functions for laminar tube flow and the spectra after Kaimal et al. (1972), which have been modified to consider the spectral corrections already performed by the EC software package. Figure 6.7 shows the correction factors of the entire campaign period for the ozone fluxes measured at M1 and M4. For the M1 fluxes, the correction factor takes values between 1 and 1.1 except for some spikes. The correction factors for the M4 fluxes reach values up to 1.5, but most of the time they vary around 1.2, indicating that the flux is underestimated by about 20 %. Between July 02 and 05 there is a period of increased ϵ_x values at both sites due to an increased wind speed (see Fig. 6.1). The correction factors are higher during the night than during the day, and the correction factors for the ozone fluxes at M4 are higher than

for those at M1. Both is due to a shift of the cospectra to higher frequencies under stable conditions and for lower measurement heights.

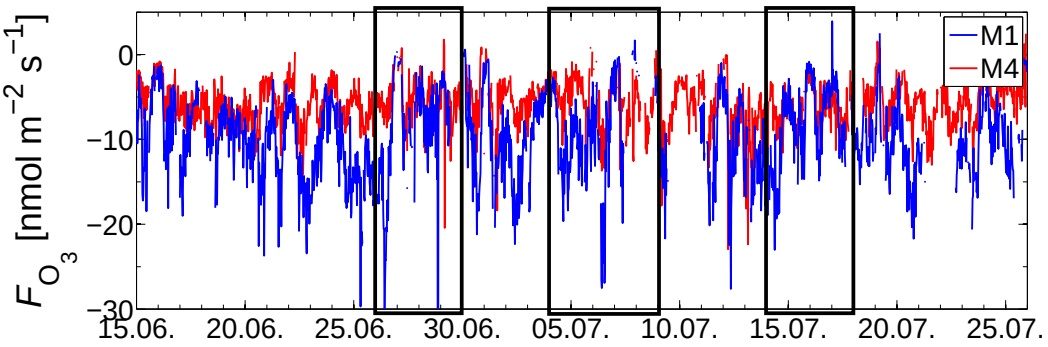

Figure 6.8: Time series of the tube attenuation corrected ozone fluxes measured during EGER-IOP3 at M1 and M4. The time series show 30 minute fluxes measured at a height of 32 m at M1 and 5.5 m at M4. The black boxes mark the three "golden day" periods.

The correction factors are used for the correction of EGER fluxes for the dampening of fluctuations inside the inlet tubings. The corrected flux F_{O_3} is determined from the flux calculated by TK3 by

$$F_{O_3}(t) = \epsilon_x(t) \cdot F_{O_3,TK3}(t) \; . \tag{6.1}$$

Figure 6.8 shows the time series of the corrected ozone fluxes measured at M1 and M4. There are gaps in the time series due to the quality control module of TK3, the neglection of 30 minute fluxes in which the chemical disc of the ozone sensor has been exchanged and the manual expection of the raw data for periods where the chemical discs have given erroneous data. From all measured 30 minute fluxes 7.32 % of the values at M1 are neglected due to quality control and exchange of discs, at M4 9.25 % are neglected. The manual inspection leads to the neglection of another 1.32 % at M4 and at M1 even 13.67 % of the values are discarded due to the inspection of the raw time series. The general trend of the ozone fluxes at both sites agrees well. The downward directed fluxes measured above the forest are lower than those measured on the clearing. The fluxes are closest to zero during the night with similar values at M1 and M4. The nighttime fluxes show a good agreement during some nights with low relative humidity. The daytime fluxes reach values down to about -20 nmol m^{-2} s^{-1} at M1 and only about -12 nmol m^{-2} s^{-1} at M4 with some spikes in between. During the day, the deposition increases because of an increased stomatal activity. The decrease of the flux is higher above the forest than on the clearing. The three "golden day" periods are marked in Figure 6.8 by the black boxes. During the first period, the ozone fluxes are not as low as on the surrounding days due to the high temperatures and low relative humidities which result in a minor aperture of the stomata to avoid the loosing of water by the plant. The ozone fluxes during the second period show a large decrease on July 06, which corresponds to an increase in the ozone mixing ratio (see Fig. 6.6). Best

data quality and availability is present during the third period and hence, this period will be described in more detail in the following section.

6.4.1 The third "golden day" period

The ozone flux time series in Figure 6.8 have shown a decrease of the ozone flux during the day due to an increased stomatal activity. In addition to the ozone fluxes, also the turbulent fluxes of CO_2 and latent heat depend on the stomatal aperture. Therefore, their fluxes are compared to the ozone fluxes measured on the masts M1 and M4 during the third "golden day" period of four days from July 14 to 17. In Figure 6.9 the fluxes of ozone, carbon dioxide and latent heat are shown. Figure 6.9(a) gives the four day time series of the ozone fluxes. The ozone fluxes on the clearing show similar minimum daytime values for all four days of about -10 nmol m^{-2} s^{-1}. The nighttime fluxes are about -5 nmol m^{-2} s^{-1}, except for the night of July 15/16 with only a small deposition close to zero. However, this night shows the best agreement to the flux above the forest. The other nights also show similar values for the forest and the clearing, but during the day the deposition to the forest is higher than to the clear-cut. On July 14, the deposition to the forest is highest with fluxes of -20 nmol m^{-2} s^{-1}. During the further course of the "golden day" period, the minimum daytime downward directed fluxes to the forest increase to about -14 nmol m^{-2} s^{-1} on July 17, where there is no data available in the evening due to rain. The difference between the fluxes to the forest and the clearing is largest on July 14, where the flux to the forest already showed decreased nighttime values. On the remaining days, the difference is highest on July 16.
In Figure 6.9(b) the fluxes of CO_2 are displayed. For CO_2, the fluxes measured above the forest are lower than those measured on the clearing, which means less respiration during the night and a higher deposition during the day. On the first three days, the deposition to the forest shows similar cycles and a less pronounced cycle on the last day. The flux decreases down to about -0.02 mmol m^{-2} s^{-1} on the first days. A flux of the same size is reached on the last day for one 30 minute flux, but the fluxes during the remains of the day reach values around -0.012 mmol m^{-2} s^{-1}. On the clear-cut the daytime fluxes take values of about -0.012 mmol m^{-2} s^{-1} around noon during the first two days and of about -0.009 mmol m^{-2} s^{-1} on the third day. On the last day, there is only a slight difference between the fluxes measured at M1 and M4. The difference between the fluxes to the forest and to the clearing is highest on July 16 as well.
Figure 6.9(c) shows the latent heat fluxes. The time series shows higher values for the fluxes measured on the clearing than for the fluxes measured above the forest as well. However, in contrast to the ozone and CO_2 fluxes, the daytime latent heat fluxes are directed upwards. During the day, the latent heat flux increases to maximum values between 200 and 250 W m^{-2} on the first three days at M1 and above 250 W m^{-2} at M4. On the last day of the third "golden day" period the latent heat flux on the clearing reaches values as high as during the other days, but above the forest the flux only increases to about 150 W m^{-2} around noon and is more scattered as on the other days due to cloudy conditions. The nighttime latent heat fluxes of forest and clearing agree well except for the first and last night, where the fluxes at M4 are more scattered. The fluxes take values close to zero at night.

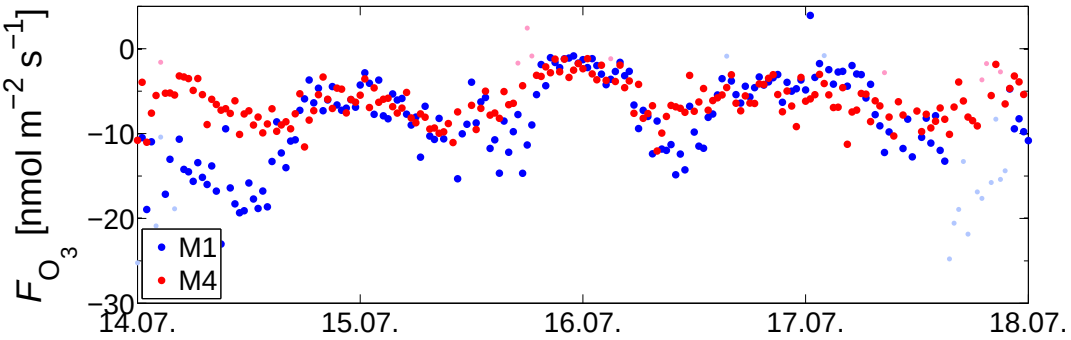

(a)

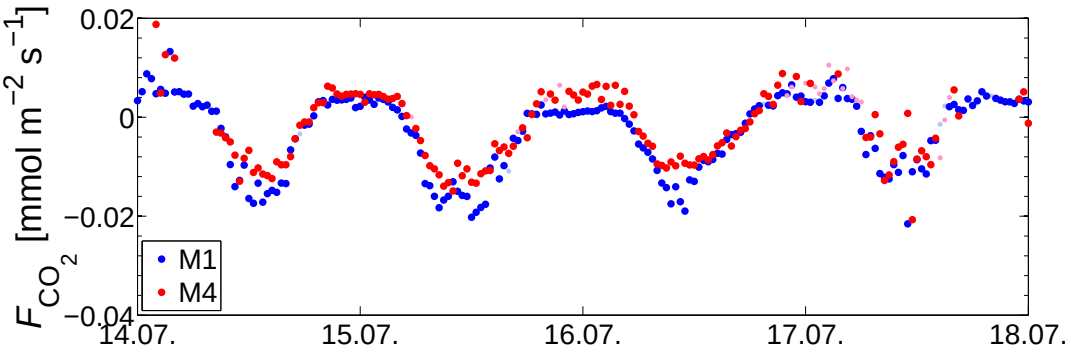

(b)

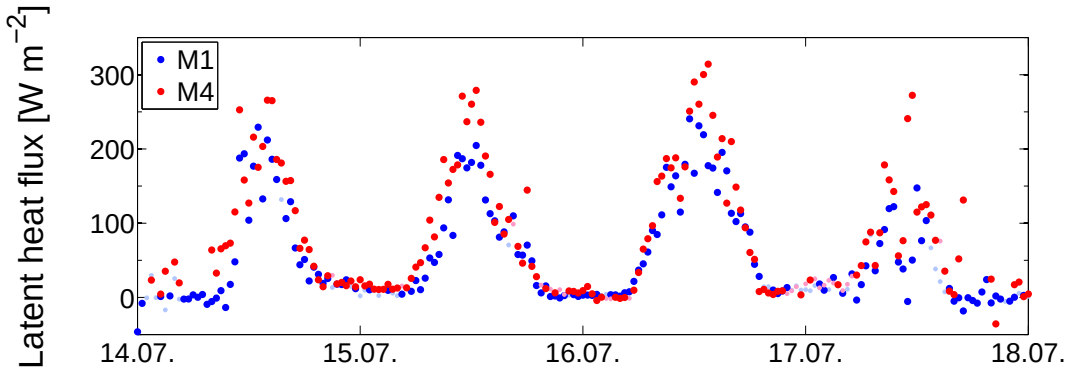

(c)

Figure 6.9: Time series of fluxes of (a) ozone, (b) CO_2 and (c) latent heat measured during the third "golden day" period of EGER-IOP3 at M1 and M4. The time series show 30 minute fluxes measured at a height of 32 m at M1 and 5.5 m at M4.

The fluxes depend on the same factors like radiation or humidity, which affect plant activity. Over the third "golden day" period, the fluxes of O_3, CO_2 and latent heat show a quite good agreement in the general shape of their time series. From the first to the third day, the respective fluxes have a comparable size, except for the ozone flux at M1 on the first day compared to the second and third day. On the last day, all fluxes show smaller absolute values and are more scattered. During the day, the ozone as well as the CO_2 flux show that there is a higher deposition to the forest than to the clear-cut vegetation. However, in contrast to the difference in the ozone fluxes between the forest and the clearing, there is a less obvious difference for carbon dioxide with even higher upward directed fluxes from the clearing due to respiration during the night. For the latent heat flux, the relation between the fluxes from M1 and M4 looks different. Over the entire course of the third "golden day" period, the fluxes from the clearing are higher than from the forest. Particularly on the clearing it is noticable, that the latent heat flux not only represents the transpiration from plants, but also the evaporation of water. As the surface of the clearing is wet with also some space with open water, a large portion of the latent heat flux at this site is probably caused by evaporation.

6.4.2 Diurnal variation in fluxes, deposition and mixing ratios

In order to allow a better analysis of the connection between ozone fluxes, deposition velocities and mixing ratios as well as the comparison of the fluxes of O_3, CO_2 and latent heat of the forest and the clearing, mean diel cycles are determined from the 41 days of the measurement in EGER-IOP3. The mean cycles are displayed as boxplots, which contain hourly medians. Figure 6.10 presents mean diel cycles of the ozone flux, the deposition velocity and the mixing ratio, determined from the ozone measurements performed above the forest. The ozone flux in plot (a) shows the expected diel cycle with highest fluxes during the night and lowest fluxes during the day. The median ozone flux takes a nearly constant value of -6 to -7 nmol m^{-2} s^{-1} from 20 CET until 6 CET with a small decrease at 22 CET. In the morning hours between 6 and 8 CET, there is a sharp increase in the deposition to a flux of about -11 nmol m^{-2} s^{-1}. The highest deposition is present at 12 CET with about -13 nmol m^{-2} s^{-1}. Afterwards the deposition decreases, but increases again to a second maximum at 16 CET of about the same magnitude as that at 12 CET. However, with a larger interquartile ranges in the afternoon than around noon. During the further course, the downward directed flux shows a slow increase to its nighttime values. The deposition velocity in Figure 6.10(b) also shows nearly constant values of about 0.6 cm s^{-1} during the night with a small increase at 22 CET. In the morning it shows the same sharp increase between 6 and 8 CET as the ozone flux and takes its maximum value of 0.8 cm s^{-1} from 8 to 9 CET. The deposition velocity decreases until 15 CET, exhibits another smaller maximum of about 0.7 cm s^{-1} at 17 CET and then decreases to its nighttime values. Largest amplitudes of the interquartile range appear in the night, when the deposition velocity has the lowest values. During the day, when the deposition velocity is larger, the interquartile range is smaller. In plot (c) the ozone mixing ratios are presented, which show a sinusoidal diel cycle. Minimum median mixing ratios are present between 6 and 7 CET with values of about 34 ppbv. The mixing ratio increases in the course of the day and takes its maximum values of about 48 ppbv in the afternoon between 15 and 16 CET. In the evening and during

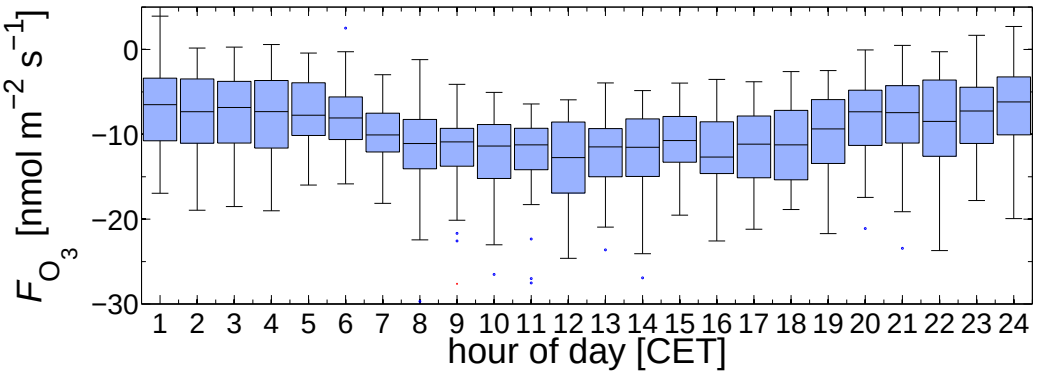

(a)

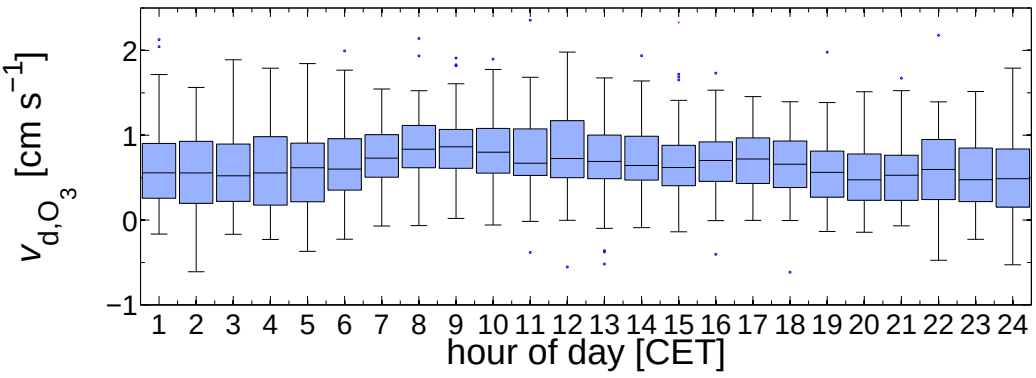

(b)

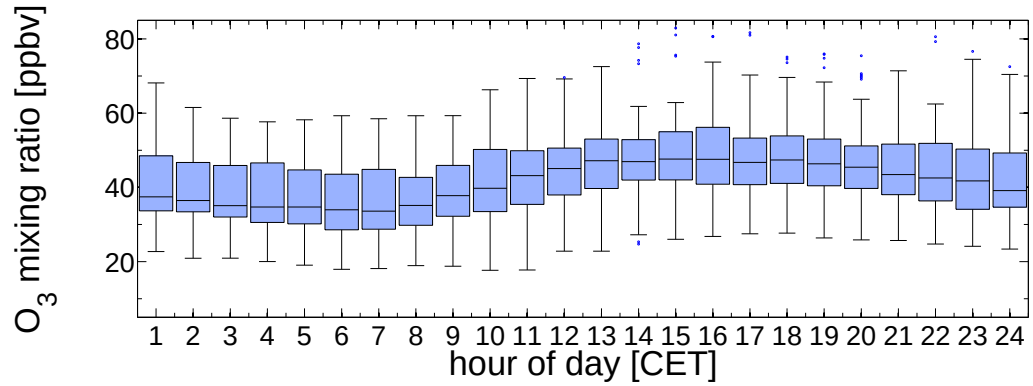

(c)

Figure 6.10: Mean diel cycles of (a) ozone flux, (b) deposition velocity and (c) ozone mixing ratio, measured at M1 at a height of 32 m and averaged over 41 days (15.06.-25.07.2011). Shown is the median with 25 % and 75 % quartiles, the whiskers display the quartiles +/- 1.5 times the interquartile range. Outliers are marked as dots.

the night the mixing ratio decreases down to its minimum values in the morning. The interquartile range is largest during the night and has slightly smaller amplitudes during the day.
The diurnal variation of the flux can be explained by the cycles of deposition velocity and mixing ratio, as it is calculated as the product of deposition velocity and concentration. The sharp flux decrease in the morning is correlated to the increases in deposition velocity as well as mixing ratio. The increase in deposition velocity is due to the sunrise. The increase in radiation makes the stomata open up such that the stomatal deposition starts to add to the total deposition. The mixing ratio increases due to the photochemical production of ozone driven by radiation. The decrease of radiation also leads to the decrease in mixing ratio in the late afternoon and evening. The maximum in the mixing ratio correlates with the second minimum found in the ozone flux cycle at 16 CET.

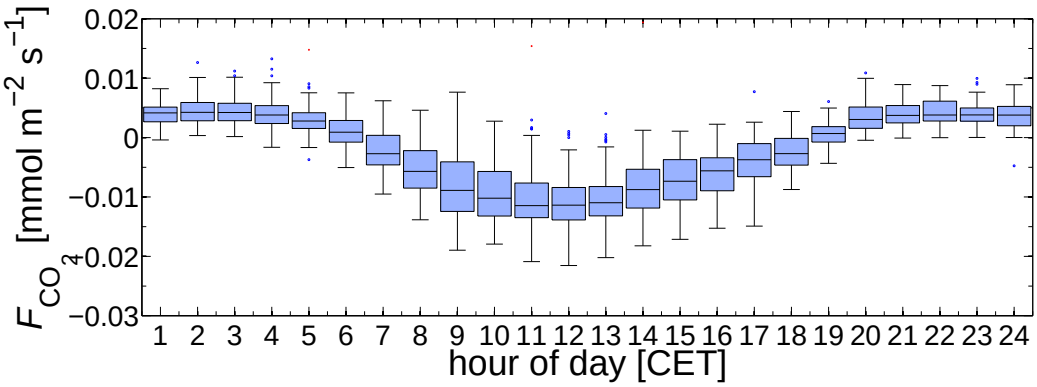

(a)

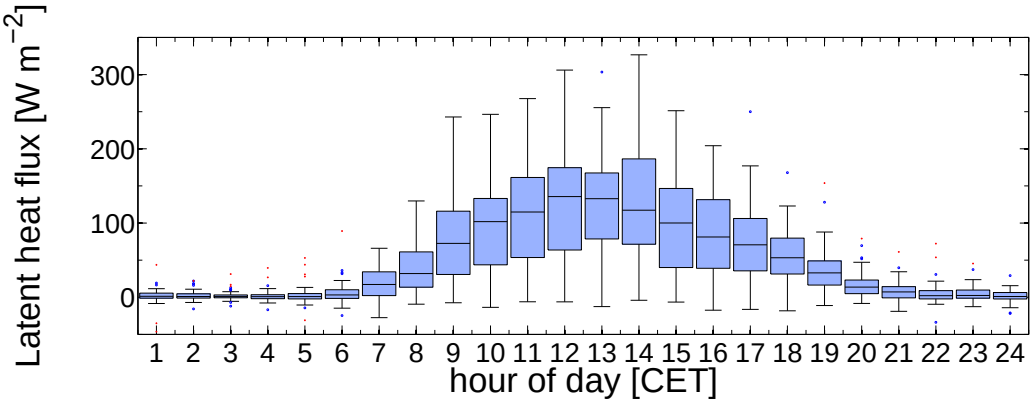

(b)

Figure 6.11: Mean diel cycles of (a) CO_2 flux and (b) latent heat flux, measured at M1 at a height of 32 m and averaged over 41 days (15.06.-25.07.2011). Shown is the median with 25 % and 75 % quartiles, the whiskers display the quartiles +/- 1.5 times the interquartile range. Outliers are marked as dots.

In Figure 6.11 the mean diel cycles of the carbon dioxide and latent heat flux measured at M1 are displayed. The CO_2 flux in plot (a) shows a clear diurnal variation of the median flux with nearly constant upward directed fluxes of about 0.004 mmol m^{-2} s^{-1} during the night from 20 CET to 4 CET due to the respiration of the forest canopy. After sunrise the flux shows the same sharp decrease as the ozone flux, and between 6 and 7 CET it becomes negative until between 18 and 19 CET. The minimum median downward directed flux of -0.012 mmol m^{-2} s^{-1} appears between 11 and 12 CET. The latent heat flux in Figure 6.11(b) shows values close to zero during the night from 22 CET until 5 CET. The flux increases to its maximum median value at 12 CET of about 140 W m^{-2} and afterwards decreases to its nighttime values. For both fluxes the smallest interquartile range is present during the night and increases towards noon, where the fluxes reach their maximum absolute values. The diel cycles show a good agreement with the mean diel ozone flux cycle in Figure 6.10(a) with a maximum of the absolute flux at the same time. However, in contrast to the ozone flux, the CO_2 as well as the latent heat flux show no second peak at 16 CET as this was due to the maximum in the ozone mixing ratio and not to a maximum in the plant activity.

Figure 6.12 shows the averaged fluxes, deposition velocities and mixing ratios of the ozone measurements performed on the clear-cut. Plot (a) shows that the highest median flux of about -4 nmol m^{-2} s^{-1} is evident during the night between 20 CET and 6 CET. The flux decreases until 10 CET and stays nearly constant until 13 CET at a value of -7.5 nmol m^{-2} s^{-1}. In the afternoon and evening the flux increases until 20 CET. The size of the interquartile range shows no dependence on the size of the flux and is about constant throughout the day. The deposition velocity in Figure 6.12(b) presents a similar diel cycle as the ozone flux but with inverse sign. The nighttime deposition velocity is about 0.3 cm s^{-1}. During the day, the deposition velocity increases and reaches its maximum value of about 0.5 cm s^{-1} between 8 and 10 CET. The decrease of the deposition velocity until 20 CET is slower than the increase in the morning. In Figure 6.12(c) the ozone mixing ratio measured at M4 is shown. The cycle of the mixing ratio on the clearing shows some differences to the cycle measured above the forest. The smallest mixing ratio of about 30 ppbv is present between 5 and 6 CET. The increase of the mixing ratio is slow and the highest mixing ratio is present between 14 and 16 CET with about 45 ppbv. However, the daytime values are more constant than above the forest (see Fig. 6.10(c)) and the mixing ratio does not change much between 13 and 18 CET.
The decrease in the diurnal variation of the ozone flux is due to the increase in deposition velocity and the simultaneous increase in mixing ratio. Although the deposition velocity starts to decrease after 10 CET, the further increase in the mixing ratio results in a later maximum of the absolute flux than of the deposition velocity. The nearly constant ozone mixing ratio in the afternoon and the decreasing deposition velocity lead to an increase in the flux without a second minimum.

Figure 6.13 shows the averaged diel cycles of the fluxes of CO_2 and latent heat. The diurnal variation of the carbon dioxide flux in Figure 6.13(a) agrees well with that of the ozone flux. The cycle of CO_2 flux shows the same sharp decrease as that of the ozone flux, but the decrease starts already after 4 CET. The minimum is reached at 12 CET, where the median CO_2 flux has a value of -0.009 mmol m^{-2} s^{-1}. In the further course of the day, the flux increases and stays nearly constant at about 0.004 mmol m^{-2} s^{-1} during the night.

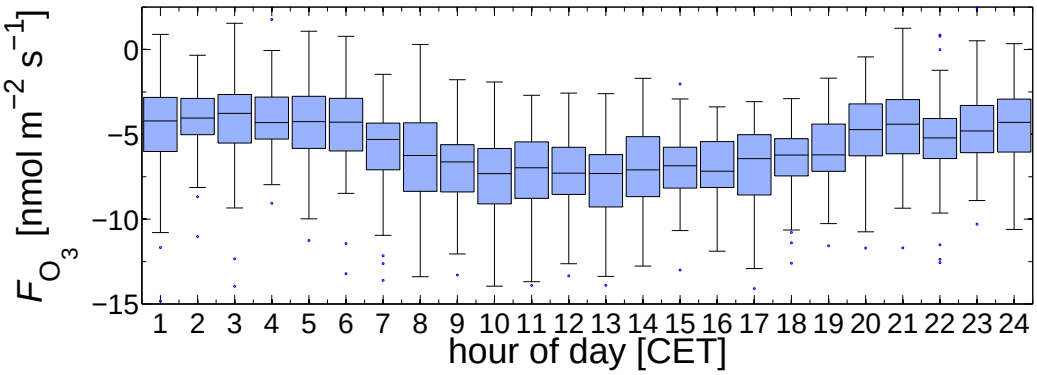

(a)

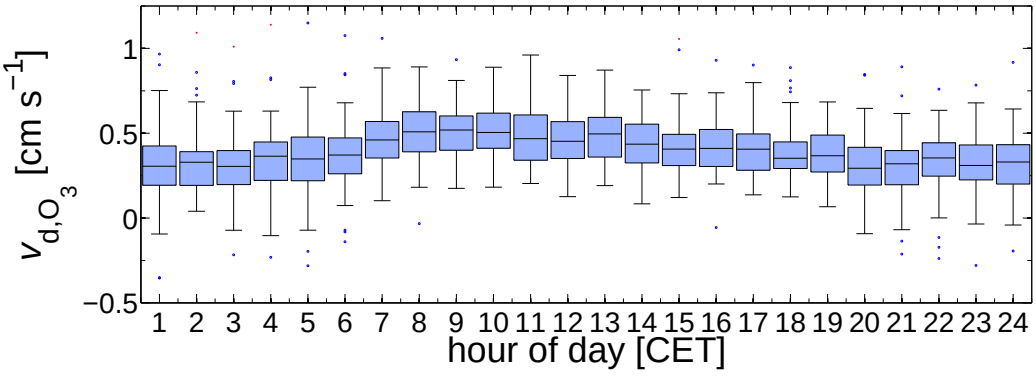

(b)

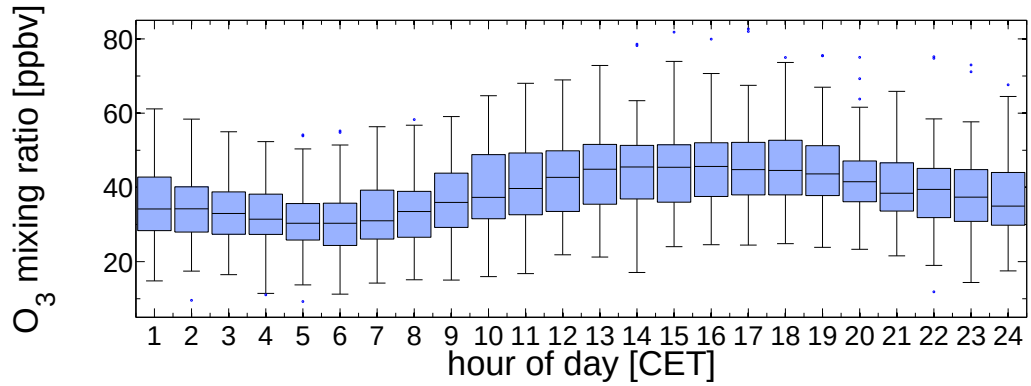

(c)

Figure 6.12: Mean diel cycles of (a) ozone flux, (b) deposition velocity and (c) ozone mixing ratio, measured at M4 at a height of 5.5 m and averaged over 41 days (15.06.-25.07.2011). Shown is the median with 25 % and 75 % quartiles, the whiskers display the quartiles +/- 1.5 times the interquartile range. Outliers are marked as dots.

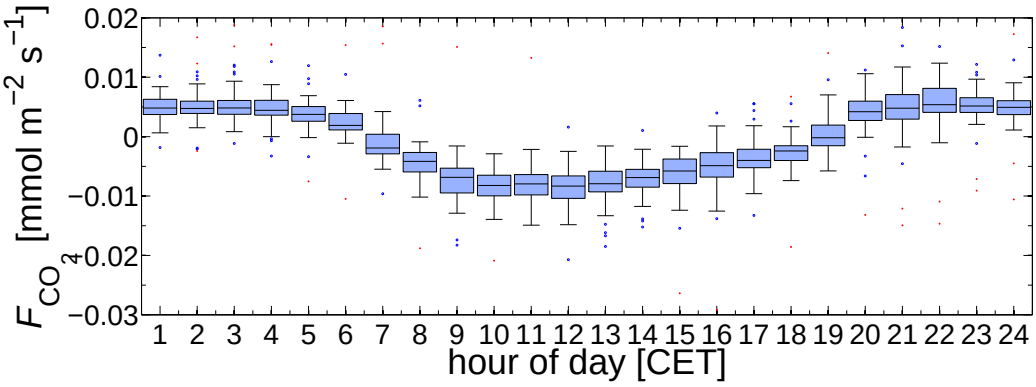

(a)

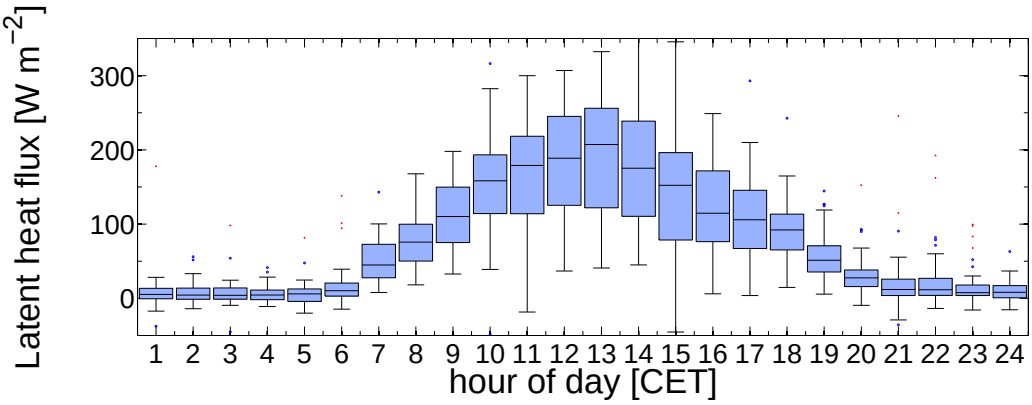

(b)

Figure 6.13: Mean diel cycles of (a) CO_2 flux and (b) latent heat flux, measured at M4 at a height of 5.5 m and averaged over 41 days (15.06.-25.07.2011). Shown is the median with 25 % and 75 % quartiles, the whiskers display the quartiles +/- 1.5 times the interquartile range. Outliers are marked as dots.

The interquartile range is small and shows no relation to the size of the flux. The small interquartile range of the CO_2 flux indicates only a small fluctuation of the flux among the days of the campaign. In Figure 6.13(b) the median latent heat flux cycle is presented. The flux starts to increase after 5 CET and reaches its maximum median value of about 200 W m^{-2} at 13 CET. Until 21 CET the flux decreases and stays close to zero during the night. The size of the interquartile range has a large diurnal variation, with the largest range around noon, when also the flux is highest. The latent heat flux shows a larger variation throughout the campaign than the CO_2 flux, resulting in a maximum interquartile range of about 140 W m^{-2}. The variation in the latent heat flux is due to the changing humidity conditions.

Comparing the results of the ozone measurements above the forest (M1) and on the clearing (M4), it is apparent that the flux to the forest is about twice the flux to the clear-cut

vegetation. The median ozone mixing ratios above the forest are only slightly higher than on the clearing due to the differences on some days (see Fig. 6.6). As the ozone mixing ratios are comparable, the difference in the ozone fluxes between M1 and M4 is mainly due to the difference in the deposition velocity. At both sites there is a sharp rise at dawn and the deposition velocity reaches its maximum already in the morning. This indicates the importance of stomatal processes for the deposition of ozone. The decrease to nighttime values still higher than zero indicates the significant influence of other non-stomatal processes on the removal of ozone. The nighttime ozone flux takes values of about -6 to -7 nmol m^{-2} s^{-1} above the forest and about -4 nmol m^{-2} s^{-1} on the clearing. Thus, the processes causing the deposition during the night are barely doubled between the clear-cut vegetation and the forest. The decrease of the flux to the daytime minimum above the forest (difference of 6-7 nmol m^{-2} s^{-1}) is also a little less than doubled compared to the decrease on the clearing (difference of 3.5 nmol m^{-2} s^{-1}). The median deposition velocities show a nighttime factor of two between the forest and clear-cut vegetation and at 8 CET, where the deposition velocity is at its maximum, there is a nearly equal difference of about 0.2 cm s^{-1} to the respective nighttime values. The ratio between the fluxes to the forest and clear-cut vegetation is in good agreement with the ratio of the biomass expressed by the leaf area index, which is 6 m^2 m^{-2} for the forest and 3.34 m^2 m^{-2} for the clearing. The fluxes as well as the deposition velocities show that the influence of the non-stomatal processes is larger than that of the stomatal deposition. At noon, when the flux reaches its minimum, the flux composes in nearly equal shares of stomatal and non-stomatal fluxes.

6.4.3 Discussion

In the following discussion, the results of the ozone measurements during EGER-IOP3 will be compared to findings of previous studies dealing with the atmosphere-biosphere exchange of ozone.
During the measurements in EGER-IOP3, the mixing ratios of O_3 were generally high (up to 80 ppbv), indicating that the air was polluted. The nearly identical mixing ratios above the forest and at the middle of the clearing also indicate no advection between the forest and the clearing for most of the intensive observation period.

The ozone fluxes of EGER-IOP3 show a clear diurnal variation at M1 (Fig. 6.10(a)) and M4 (Fig. 6.12(a)) with minima around noon. The median minimum ozone flux is -13 nmol m^{-2} s^{-1} above the forest and -7.5 nmol m^{-2} s^{-1} above the clearing. Also the deposition velocities of O_3 show a clear diurnal pattern, indicating that stomatal uptake might be an important process contributing to the deposition. The median observed deposition velocities vary between 0.6 and 0.8 cm s^{-1} above the forest and between 0.3 and 0.5 cm s^{-1} above the clearing with maxima in the morning. The high nighttime deposition suggests a significant non-stomatal portion to the total ozone flux. The closure of the stomata during the night is indicated by water vapor fluxes close to zero (Fig. 6.11(b)). Pilegaard et al. (1995) and Mikkelsen et al. (2000) observed a high nighttime deposition as well and related it to reactions with plant surfaces, particles and gases like NO emitted from the soil.
For grassland and low vegetation, Cieslik (2004) report fluxes down to about -8 to -9 nmol m^{-2} s^{-1}. The values are only slightly lower than observed in this study for the clearing with heterogeneous low vegetation. For moorland species Fowler et al. (2001) report

deposition velocities between 0.2 and 0.7 cm s^{-1}, which show the same shape as the observed daily cycle with a sharper rise than decrease, but a maximum around noon instead of the morning hours. The observed values are in the upper range of literature values reported for grasslands of -4 to -8 nmol m^{-2} s^{-1} and 0.2-0.6 cm s^{-1} (Massman et al., 1995; Meyers et al., 1998; Horvath et al., 1998; Cieslik, 1998; Fowler et al., 2001; Sorimachi et al., 2003; Cieslik, 2004). Considering that the clear-cut vegetation not only consisted of grasses, the relatively high O_3 deposition rates are plausible due to a large plant area with a large stomatal conductance of the vegetation, although it has been demonstrated that stomatal ozone deposition represents only a part of the total flux (Fowler et al., 2001).
Norway spruce canopies have been the target area of several ozone flux measurements, using either the eddy-covariance or the gradient method. The studies report the same sharp rise in flux and deposition velocity in the morning as during EGER-IOP3. Averaged fluxes varied between -4 and -17 nmol m^{-2} s^{-1} in the daily course, with deposition velocities between 0.2 and 0.8-0.9 cm s^{-1} (Pilegaard et al., 1995, 1998; Mikkelsen et al., 2000, 2004). Mikkelsen et al. (2004) observed highest canopy ozone uptake during the day and during the summer, which is interpreted as increased stomatal uptake and physical and chemical reactions. The ozone fluxes at the EGER-IOP3 forest site have been investigated in previous campaign. Klemm and Mangold (2001) measured ozone fluxes in July and September between 0 and -10 nmol m^{-2} s^{-1} as well as -6 and -27 nmol m^{-2} s^{-1}, respectively. For the two previous EGER campaigns, Foken et al. (2012) report ozone fluxes classified by coupling regimes. For EGER-IOP1 the median fluxes of the regimes vary between -4 and -9 nmol m^{-2} s^{-1} and in IOP2 between -2 and -6 nmol m^{-2} s^{-1}. For IOP1, Zhu (2008) gives daily ozone flux cycles in the range between -5.8 and -9.6 nmol m^{-2} s^{-1} and deposition velocities with nighttime values of 0.52 cm s^{-1} and daytime values of 0.75 cm s^{-1}. The depositions are lower than during IOP3 as in June and July 2011 the stomatal activity was higher than during IOP1, performed later in the course of the year. Moreover, the reported deposition for other coniferous forest stands (e.g. ponderosa pine, Engelmann spruce-subalpine fir, Scots pine), is in the same range as observed in this study. Summer daytime mean fluxes of -10 to -13 nmol m^{-2} s^{-1} were reported, with deposition velocities between less than 0.05 and 0.7 cm s^{-1} (Kurpius and Goldstein, 2003; Zeller and Hehn, 1996; Zeller and Nikolov, 2000; Aurela et al., 1996; Keronen et al., 2003).

The observed ozone deposition to the vegetation on the disturbed part of the ecosystem agrees well with the deposition to the same vegetation type under undisturbed conditions. The difference to the deposition to the undisturbed ecosystem thus depends on the species that can be found on the clearing after the disturbance. Post-clear-cut dynamics of carbon, water and energy exchanges in a deciduous forest environment have been investigated by Williams et al. (2014). They found the clearcutting and other forest disturbances to perturb the carbon, water and energy balance in significant ways, with corresponding influence on Earth's climate system through biogeochemical and biogeophysical effects. Their findings underscore the highly dynamic nature of vegetation composition during the regrowth following a severe forest disturbance.

6.5 Modeled atmosphere-biosphere exchange of ozone

6.5.1 Ozone fluxes modeled by MLC-CHEM

In addition to the measurement of ozone fluxes, the model MLC-CHEM is applied to model canopy top fluxes at M1 and M4 during EGER-IOP3 in June and July 2011. For the modeling of ozone fluxes over the spruce forest canopy and the heterogeneously vegetated clearing, the model is driven by observations, which have been collected during EGER-IOP3 (see section 2.1). The modeled ozone fluxes of 41 days starting on June 15 are analyzed. Figure 6.14 shows time series of the modeled fluxes for M1 above the forest and M4 above the clearing. Nighttime fluxes are between 0 and -4 nmol m^{-2} s^{-1} and are similar for both masts for most nights. During daytime, there is a larger difference between the fluxes for M1 and M4. The model gives a higher deposition to the forest over the entire time period used for the modeling study. Above the forest, the daily minimum flux is in the range between -12 and -32 nmol m^{-2} s^{-1}. Above the clearing, this range is between -5 and -15 nmol m^{-2} s^{-1}. The distribution of the fluxes is similar at both masts, such that the deposition is largest for M1 when it is also largest for M4 (e.g. July 06). The daytime fluxes also take their smallest absolute values on the same day (July 03). Figure 6.15 shows the ratio between the fluxes modeled for M4 to the fluxes modeled for M1. For the days with the highest and lowest daytime fluxes, the ratio between the M1 and M4 flux is about the same. Around noon the ratio is close to 0.5 for all days, which indicates a downward directed flux to the clearing which is about half of that to the forest. This ratio is in good agreement with the ratio of LAI of 0.56, which would be expected, if the ozone would only deposit to leaf surfaces (expressed by stomatal, mesophyll and cuticular resistance). The deviation from the ratio of 0.56 is due to the contributions to the deposition by other pathways like the deposition to the soil. Approaching nighttime, the ratio increases to values close to or even higher than 1, which means a higher deposition to the clear-cut vegetation than to the forest. Due to the small absolute nighttime fluxes, already small differences between the M1 and M4 fluxes can cause a large change in the ratio. Obvious differences between the modeled nighttime fluxes for M1 and M4 are found in the nights of July 05/06 and July 17/18, when the deposition to the forest is higher than to the clear-cut vegetation. The difference in the night 05/06 is due to the low mixing ratio on the clearing of less than 10 ppbv, which is about 10-15 ppbv lower than above the forest (see Fig. 6.6). In the night between July 17 and 18 the mixing ratios reveal no difference. Thus, the difference in the flux cannot always be explained by the difference in the mixing ratios between the two masts. Furthermore, a difference in the mixing ratio between M1 and M4 does not always result in a difference of the modeled fluxes. The modeled nighttime flux is mainly controlled by differences in the mixing ratio between the canopy layers used for the turbulent flux and not by the absolute mixing ratio. The latter one is used for the modeling of deposition by the canopy model. In the night, the canopy deposition pathways are reduced to the deposition to the cuticle and the soil and the deposition is thus smaller than during the day.

In order to consider changing humidity conditions in the modeling of ozone fluxes, two changes needed to be applied to the model code in advance of the modeling study. The

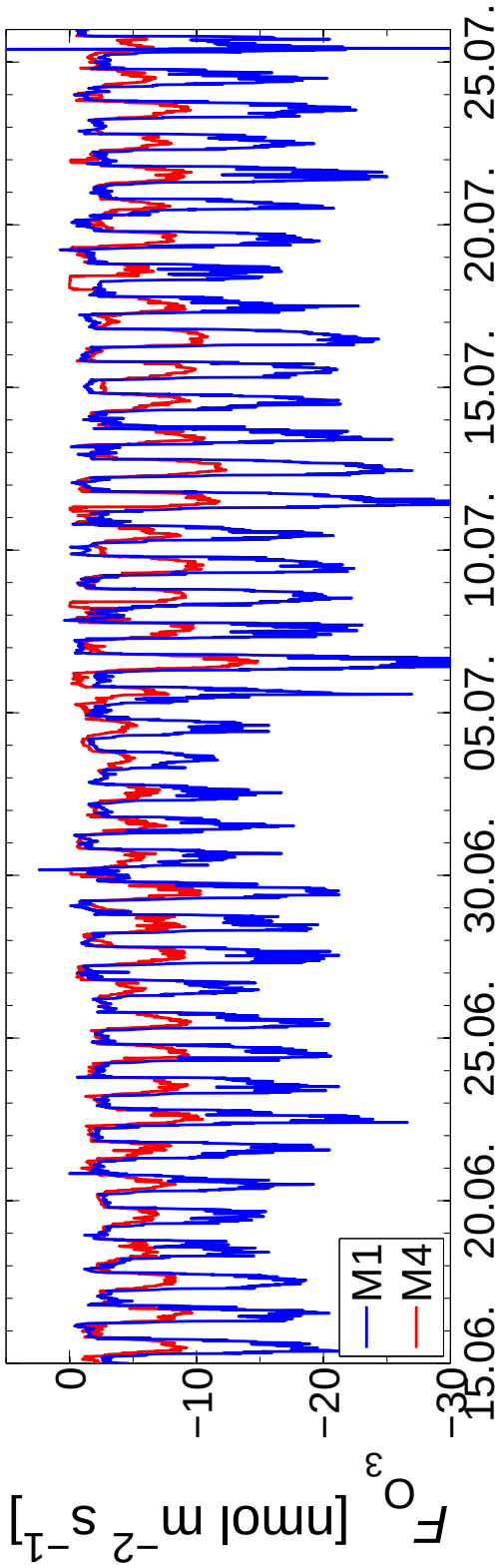

Figure 6.14: Time series of the ozone fluxes modeled for M1 and M4 during EGER-IOP3. The time series show 10 minute fluxes modeled for a height of 32 m at M1 and 5.5 m at M4.

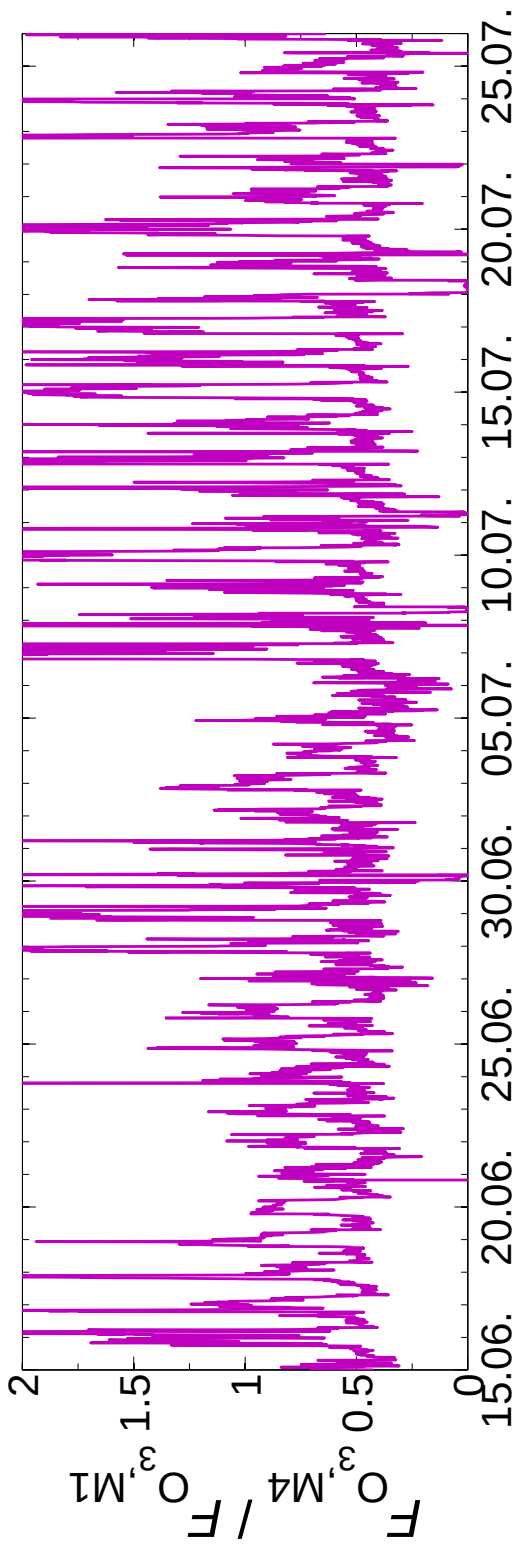

Figure 6.15: Time series of the ratio of the ozone fluxes modeled for M1 and M4 during EGER-IOP3.

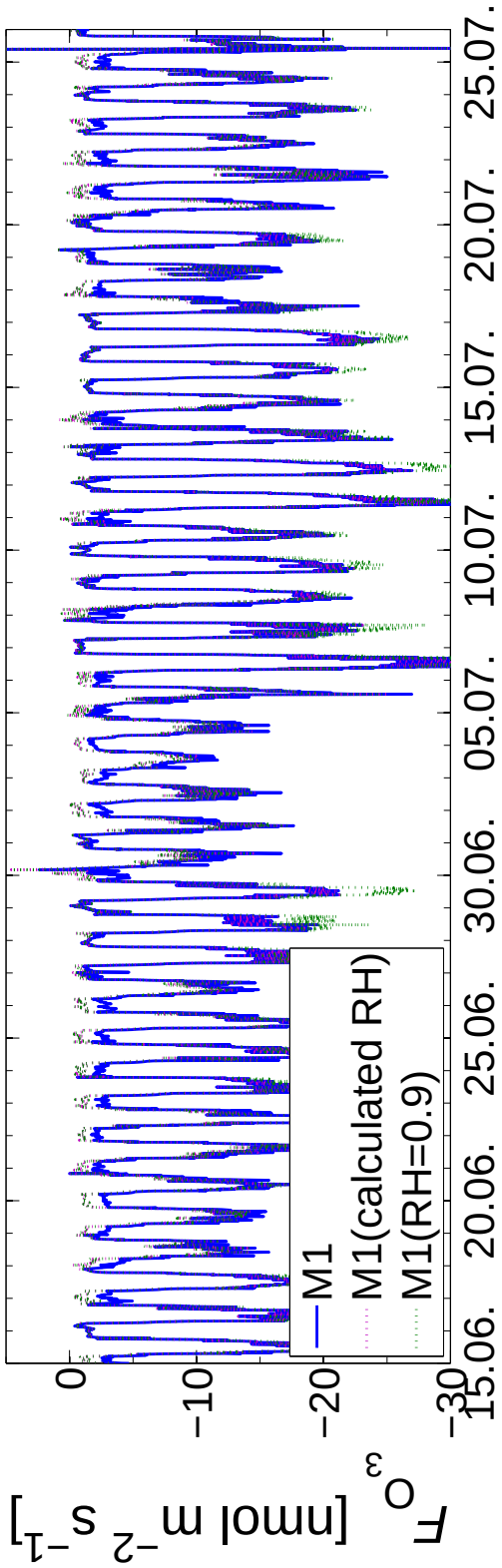

Figure 6.16: Time series of the ozone fluxes modeled for M1 (blue) during EGER-IOP3. The purple dotted line gives the flux with a calculated relative humidity, the green dotted line with a fixed relative humidity. In both cases no wet skin fraction is assumed. The time series show 10 minute fluxes modeled for a height of 32 m.

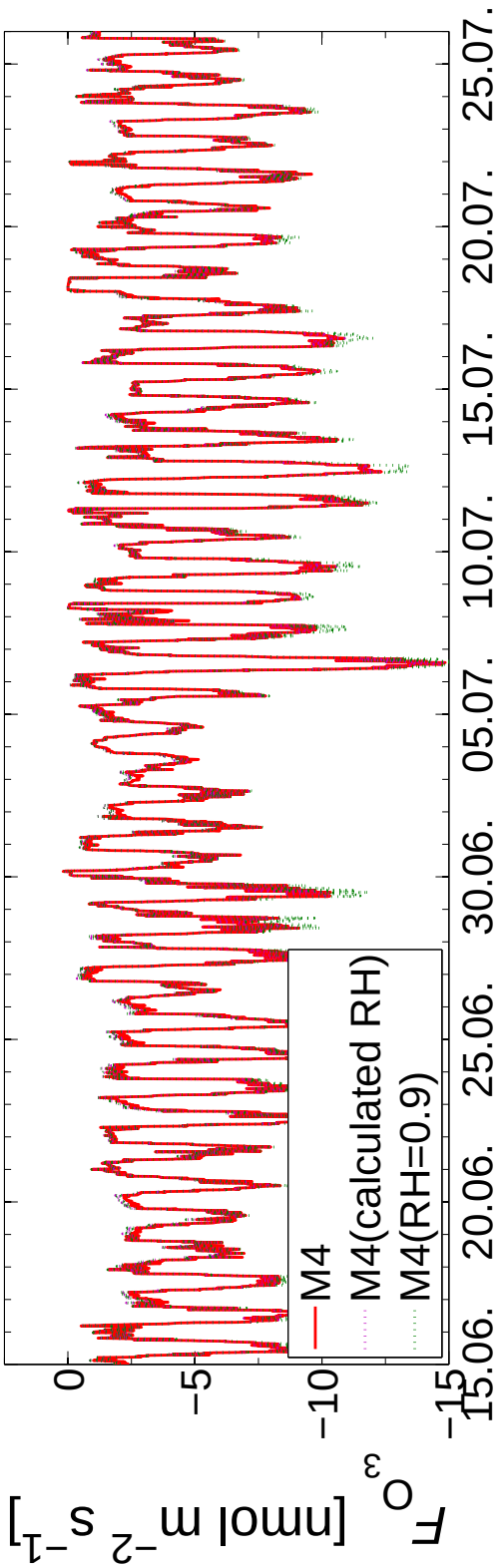

Figure 6.17: Time series of the ozone fluxes modeled for M4 (red) during EGER-IOP3. The purple dotted line gives the flux with a calculated relative humidity, the green dotted line with a fixed relative humidity. In both cases no wet skin fraction is assumed. The time series show 10 minute fluxes modeled for a height of 5.5 m.

first change was the replacement of a fixed relative humidity of 90 % by the calculation of relative humidity from the specific humidity given as input (see Fig. 6.1). The second change was the consideration of this changing relative humidity for the fraction of wet surfaces, which was zero by default. Figure 6.16 shows the time series of the ozone flux at M1 with and without considering the changes made to the relative humidity part of the model code. The green dotted line gives the flux using the fixed relative humidity and to obtain the flux given by the purple dotted line the relative humidity is calculated from specific humidity. In both cases the wet skin fraction is set to zero. For the final modeling, the wet skin fraction is calculated depending on relative humidity. The first change to the code (difference between dotted green and purple line) mainly affects the daytime fluxes by reducing the deposition. This is visible especially from June 27 to 29, when the relative humidity was lowest, thus showing the largest difference to the default RH of 90 %. On these days, the deposition is reduced by up to 6 nmol m^{-2} s^{-1}. On the following days with rain and a high RH, the calculation of RH has only a small or no effect. The remaining daytime fluxes show a decrease in deposition between 0 and 6 nmol m^{-2} s^{-1}, depending on the difference of the calculated relative humidity to the default value of 90 %. During the night, when the relative humidity is usually high, the calculation of RH results only in a change in the flux for individual nights.
In contrast to the first change, the second change to the model code has a larger effect on the modeled nighttime fluxes than on the daytime fluxes. During the day, the increase in the wet surface fraction has only an effect on some days with high humidity, as the change becomes effective for relative humidities higher than 80 %. The calculation of wet surface fraction is more effective in the modeling of nighttime fluxes, where the deposition increases due to an increased wet surface fraction. The flux changes by about 1-2 nmol m^{-2} s^{-1} for most nights.
Figure 6.17 presents the modeled ozone flux time series with and without the application of the changes for M4. The modeled fluxes to the clearing are less affected by the changes in the consideration of humidity. The highest increase in the flux between using the default and the calculated RH is present from June 27 to 29 as well. In contrast to the fluxes above the forest, the calculation of wet skin fraction shows only small differences in the M4 fluxes. While the increase in the nighttime deposition above the forest by this step is quite obvious, the increase of the clear-cut deposition is hardly perceptible.

6.5.2 Model evaluation by comparison with observations

In order to use the model MLC-CHEM for the determination of ozone fluxes for different time periods or other sites than M1 and M4 of the entire 4 km^2 measurement site, it is necessary to evaluate the model output by comparison with measured fluxes. For the evaluation, the modeled ozone fluxes are compared to those observed at M1 and M4 during EGER-IOP3. The comparison is done for the same 41 days in June and July 2011 shown before.

Figure 6.18 presents the measured fluxes including their error bars together with the modeled fluxes for the main tower M1. The general size of the fluxes is in good agreement. The most obvious difference is that the modeled fluxes show clear daily cycles, while the measured fluxes also show nearly constant values between day and night (e.g. June 24/25,

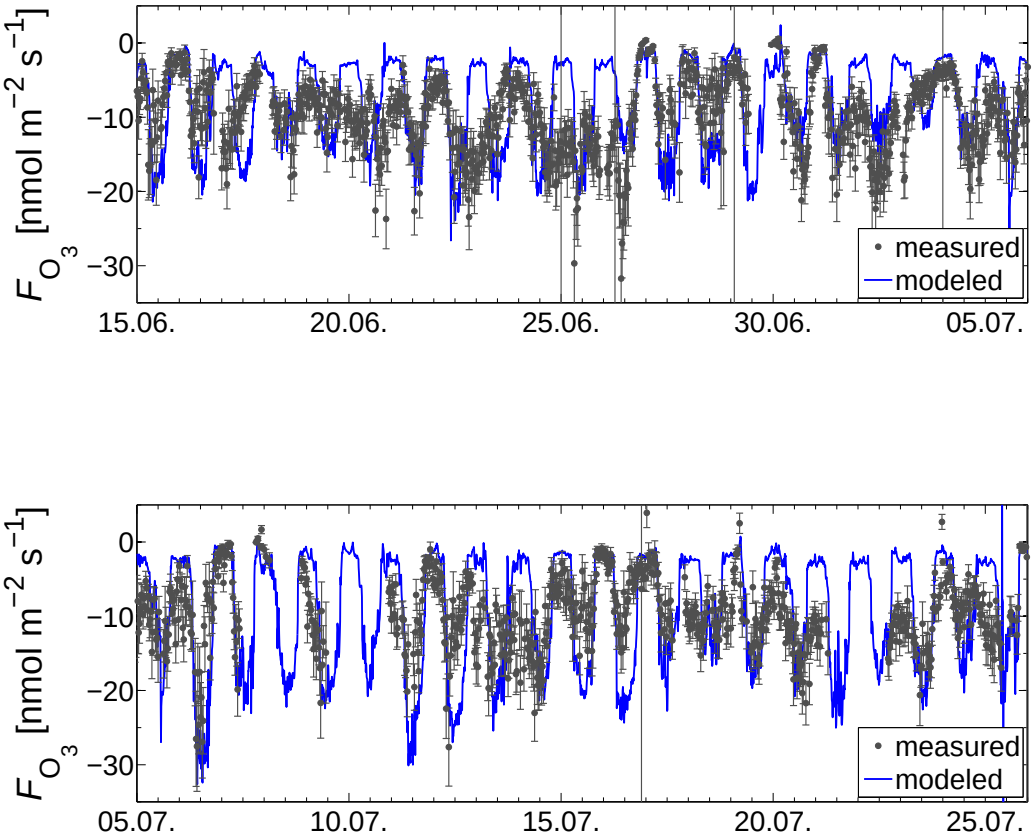

Figure 6.18: Time series of the measured and modeled ozone fluxes at M1 during EGER-IOP3. The time series show 30 minute measured and 10 minute modeled fluxes for a height of 32 m.

July 13/14) or cycles that appear to last over more than one day (e.g. June 22/23). This behavior results in a large difference between measurement and modeling for these time periods. On days where the measured fluxes follow the expected diel cycle, there is a good agreement between modeling and measurement within the margin of error. The period from July 05 until noon of July 07 shows the best agreement, but it is noticeable that the measured nighttime deposition is higher than the modeled deposition. The best agreement during nighttime is found for nights with a low relative humidity (e.g. June 26/27).
In Figure 6.19 the time series of the measured and modeled ozone fluxes at M4 are displayed. For the turbulence mast on the clearing, the modeled ozone fluxes show a better agreement with the fluxes measured during EGER-IOP3 than for M1. As was observed for the modeling for M1, the nighttime deposition is underestimated by the model. On the days where a well developed daily cycle is visible for the measured fluxes, there is a good agreement to the daytime model results. Between June 16 and 19 the measured fluxes show nearly constant values or only a slight difference between day and night, such that there is only little agreement to the modeled fluxes. There is also only partial agreement between

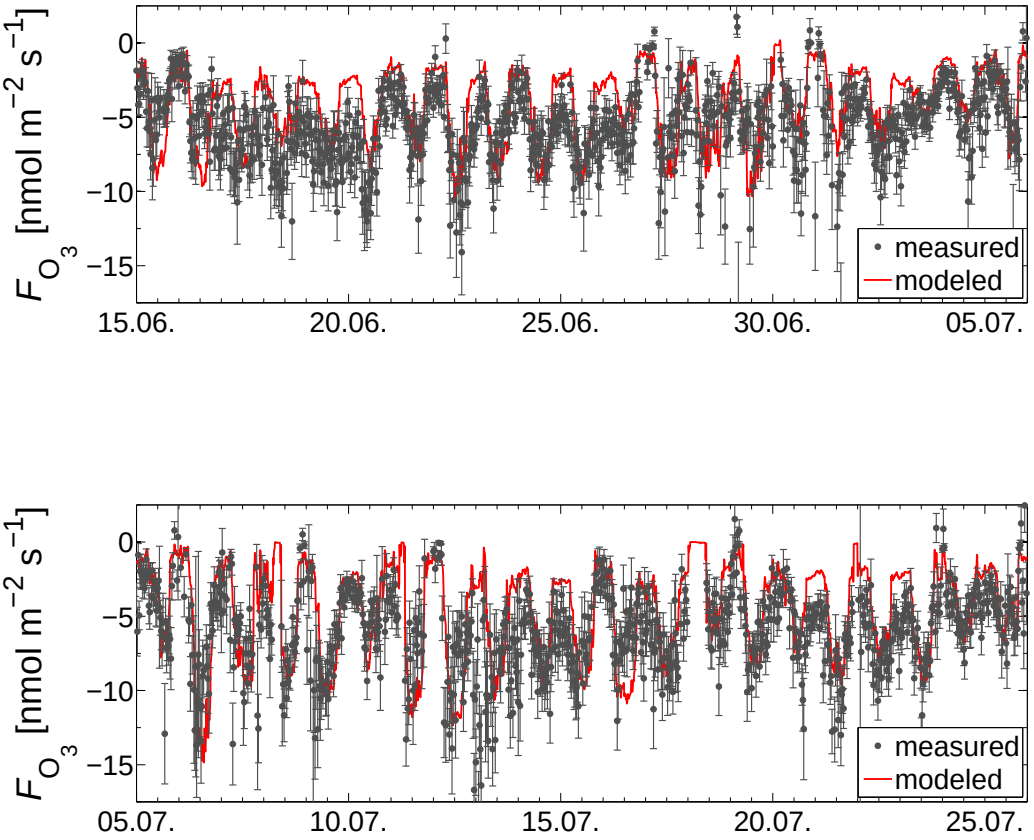

Figure 6.19: Time series of the measured and modeled ozone fluxes at M4 during EGER-IOP3. The time series show 30 minute measured and 10 minute modeled fluxes for a height of 5.5 m.

June 27 and July 01, when the measured fluxes are more scattered than on the other days.

To investigate whether the modeled ozone fluxes show the same qualitative diurnal cycle as the measured fluxes, averaged diel cycles are calculated, comprising the 41 days of EGER-IOP3. Figures 6.20 and 6.21 show the mean diel cycles obtained from the modeled ozone flux timeseries of M1 and M4, respectively. For M1, the median nighttime fluxes between 21 and 5 CET are about -2 nmol m^{-2} s^{-1} and show only small variations. The interquartile range is small as well. The modeled ozone flux decreases to its minimum value of -18 nmol m^{-2} s^{-1} at 13 CET. The flux decreases faster to the minimum value than it increases in the afternoon. Between 19 and 20 CET there is a jump in the flux cycle, whereat for 20 CET there are several outliers. Compared to the measured diel ozone flux cycle in Figure 6.10(a), the modeled cycle shows a higher deposition during the day and a lower deposition during the night, which was already observed in the time series. In contrast to the diel cycles of the measurement, the interquartile range of the modeled flux cycle increases with increasing deposition, as a difference in the flux between different days is mainly found for modeled daytime fluxes, while the nighttime fluxes are similar for

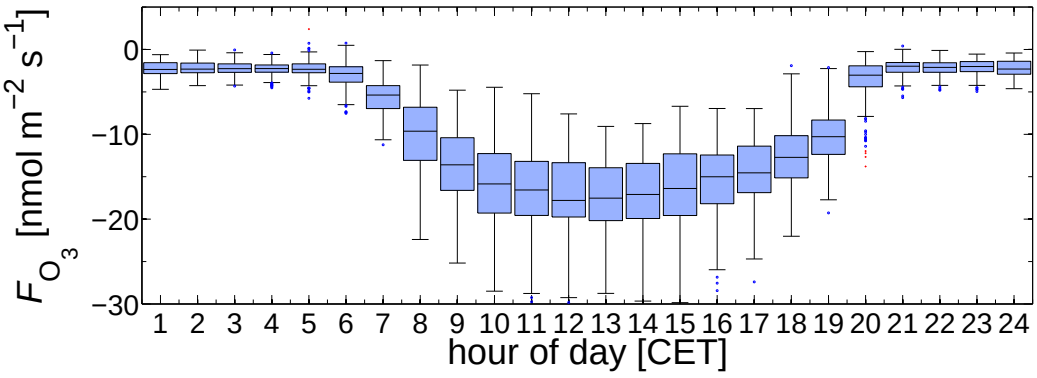

Figure 6.20: Mean diel ozone flux cycle modeled for M1 at a height of 32 m and averaged over 41 days (15.06.-25.07.2011). Shown is the median with 25 % and 75 % quartiles, the whiskers display the quartiles +/- 1.5 times the interquartile range. Outliers are marked as dots.

most nights. Except for the amplitude between night- and daytime fluxes, there is also a difference in the course of the diel cycles. Besides the minimum of the flux reached after the sharp rise in deposition until noon, the measured diel cycle has a second flux minimum at 16 CET, due to the maximum in ozone mixing ratio at this time, which is not reproduced by the model.

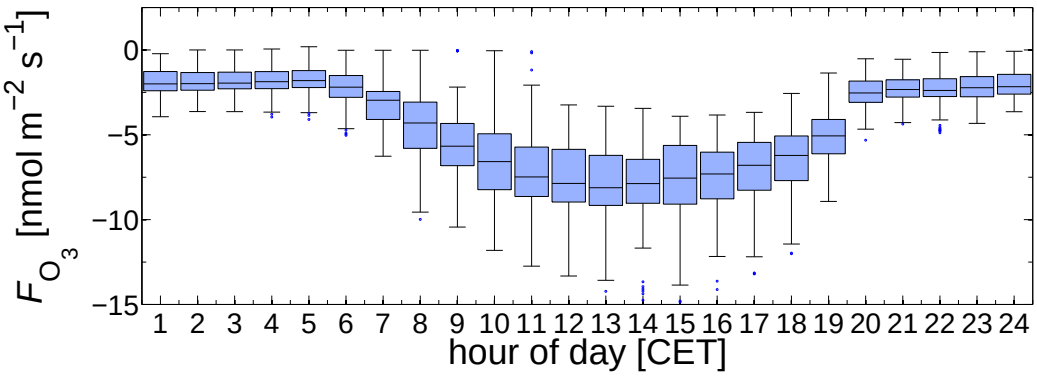

Figure 6.21: Same as Figure 6.20 for M4 at a height of 5.5 m.

Figure 6.21 shows the mean modeled diel ozone flux cycle on the clearing. The shape of the diel cycle is similar to above the forest, also showing the jump between 19 and 20 CET, but without the outliers at 20 CET. The median nighttime fluxes are similar to those modeled for M1, which indicates only minor influence of the leaf area on the modeled nighttime deposition. The flux is most negative at 13 CET with about -8 nmol m^{-2} s^{-1}. The decrease of the flux to its minimum value is not as sharp as above the forest, such

that the decrease and the increase of the flux have a similar shape. In the diel cycle of the measurement at M4 (see Fig. 6.12(a)), the flux reaches its minimum of -7.5 nmol m^{-2} s^{-1} already at 10 CET with a second slightly higher minimum at 13 CET. The modeled value at 13 CET is only about 0.5 nmol m^{-2} s^{-1} smaller than the measured one, but before noon the model underestimates the sharp increase in the deposition. As for the forest, the model underestimates the nighttime deposition to the clearing. The difference between measured and modeled ozone fluxes is more pronounced for M1 than for M4, but during the night the model overestimates the flux at both sites.

6.5.2.1 Causes of the difference to the measurement

To determine the causes of the deviations between measured and modeled ozone fluxes, the difference $F_{\text{measured}} - F_{\text{modeled}}$ is analyzed for its dependence on various parameters. Seven wind direction sectors are chosen, which comprise different vegetation types (see Fig. 2.1(a)):

- (1) 115 - 140° – mainly forest
- (2) 140 - 210° – clearing around M4
- (3) 210 - 235° – mixed vegetation; mainly forest
- (4) 235 - 270° – mixed vegetation; mainly clearings, stone pit
- (5) 270 - 290° – mainly forest
- (6) 290 - 310° – Pflanzgarten clearing
- (7) 310 - 15° – mixed vegetation

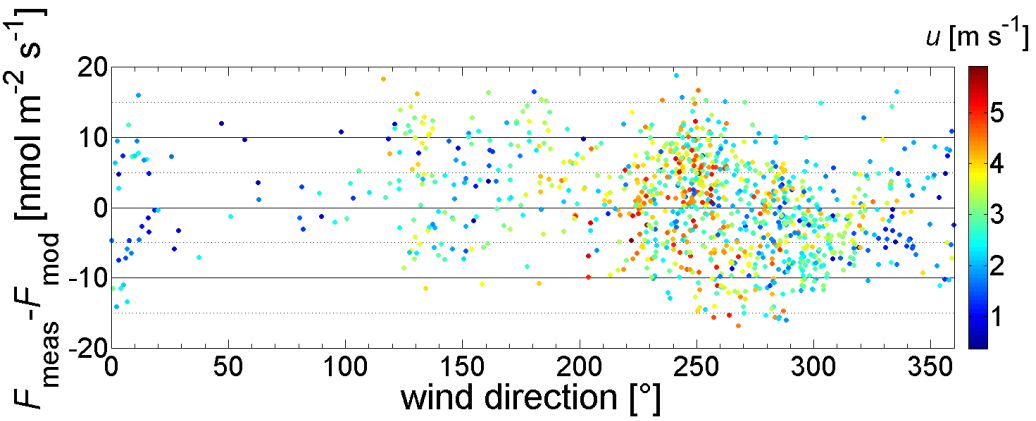

Figure 6.22: Difference between measured and modeled daytime ozone fluxes at M1 in relation to wind direction. The color coding gives the wind speed.

Figures 6.22 and 6.23 show the dependence of the difference between measured and modeled M1 ozone fluxes on the wind direction. In addition, the color coding gives the relation to wind speed and relative humidity, respectively. A relation between the difference and

the wind direction would imply an effect of the flux footprint on the difference. For the second sector, when the wind is coming from the clearing, the differences are shifted more towards positive values. For the bulk of the measurement period, the wind is coming from directions between 220 and 300° (sectors (3)-(6)). Most of the differences are distributed between -15 and 10 nmol m^{-2} s^{-1}. Most negative differences are observed for wind coming from 250-290° (middle of sector (4) and sector (5)) and most positive differences for wind directions around 250°, when the wind is coming mainly from clearings or the unvegetated stone pit, which cause a small measured flux. For the last sector, the differences are equally distributed. Amongst the wind direction sectors, only a small influence on the difference is observed with more positive differences for wind coming from less vegetated areas, while for the modeling a forest vegetation is assumed.
In Figure 6.22 the color coding shows the effect of the wind speed in addition to the wind direction. Except for the first sector, where the highest wind speeds give the lowest difference, all other sectors show wind speeds, which are equally distributed over the whole range. Thus, Figure 6.22 shows that the wind speed has no clear effect on the difference.

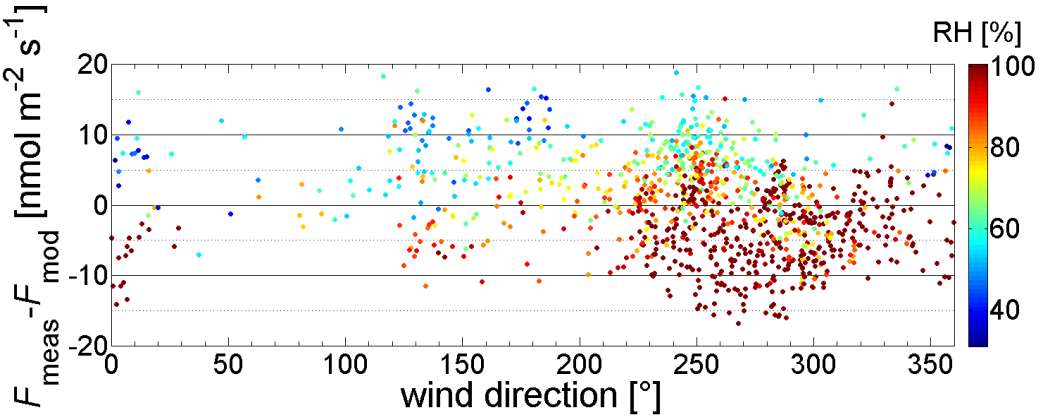

Figure 6.23: Difference between measured and modeled daytime ozone fluxes at M1 in relation to wind direction. The color coding gives the relative humidity.

In Figure 6.23 the difference between measurement and modeling plotted against wind direction and additionally relative humidity is presented. The difference shows a dependence on relative humidity with most positive differences for lowest relative humidity and most negative differences for highest RH. Amongst the wind direction sectors, the relative humidities, which cause the same difference between measurement and modeling, are different. Wind directions from less vegetated areas generally give a more positive difference already at higher humidities (e.g. sector (4)). Particularly for wind directions, where most data is available, an overlapping between relative humidities causing the same difference is observable. Therefore, it is tested whether the relative humidities belonging to negative differences are significantly higher than those belonging to positive differences between measured and modeled ozone fluxes. Table 6.2 gives the mean and standard deviation of the relative humidities and the number of observations belonging to positive or negative differences in each wind direction sector. The mean relative humidities belonging to a positive difference between measurement and modeling are always below 82 %, while those

Table 6.2: Mean relative humidity and standard deviation for a positive and negative difference between measured and modeled ozone flux (F_{measured}-F_{modeled}) for the 7 wind direction sectors. The last column gives the probability that there is no influence of relative humidity on the difference.

wind sector	pos. difference	N_{pos}	neg. difference	N_{neg}	probability
(1)	58.244 ± 12.545	37	82.846 ± 13.823	17	$4.276 \cdot 10^{-7}$
(2)	63.796 ± 14.435	78	82.469 ± 10.741	33	$3.479 \cdot 10^{-11}$
(3)	77.682 ± 11.857	64	92.108 ± 8.815	42	$5.224 \cdot 10^{-12}$
(4)	75.747 ± 15.440	199	97.013 ± 7.765	119	$9.099 \cdot 10^{-44}$
(5)	81.073 ± 17.760	69	95.555 ± 9.637	95	$8.741 \cdot 10^{-9}$
(6)	76.696 ± 17.129	24	94.053 ± 10.668	97	$2.908 \cdot 10^{-5}$
(7)	76.580 ± 26.141	55	98.223 ± 5.427	81	$5.848 \cdot 10^{-8}$

belonging to a negative difference are higher than 82 %. The last column gives the probability that there is no influence of relative humidity on the difference and that the observed differences are random. For all wind direction sectors, it is highly significant that the relative humidities causing a negative difference are higher than the relative humidities causing a positive difference between measurement and modeling. Thus, an influence of relative humidity cannot be rejected. Most data is available for the fourth sector, with wind from the south-west. For this sector, the influence of relative humidity is most obvious, which is also shown by the very small probability of the randomness of the difference. Disregarding sector (4), the probabilities span eight orders of magnitude.

For a detailed analysis of the effect of relative humidity on the difference between measured and modeled ozone fluxes at both masts, the data is grouped into RH blocks of 10 % width, with a further separation into day- and nighttime values. Figure 6.24 shows the boxplot for the differences at M1. The figure also gives the number of observations and the level of significance for the deviation of the difference between measurement and modeling from zero. The upper plot gives the daytime differences. The highest positive median difference appears for relative humidities between 40 and 50 % with about +10 nmol m^{-2} s^{-1}. The median for relative humidities lower than 40 % is a little lower, which might be due to the low number of observations in this block. For relative humidities higher than 40 %, the median decreases with increasing relative humidity. The difference is still slightly positive around +1 to +2 nmol m^{-2} s^{-1} for relative humidities between 80 and 90 % and only becomes negative for relative humidities higher than 90 %. The scatter in the data, displayed by the whiskers and outliers, is similar for RH blocks higher than 50 % and is much larger than the errors determined for the fluxes. Thus, the fluctuations in the difference cannot be explained by the uncertainty of the measurement. For the nighttime fluxes given in the lower plot of Figure 6.24, the median difference is always negative, implicating an underestimation of the nighttime deposition. The difference also decreases with increasing relative humidity, not considering relative humidities lower than 50 % as too few measurements are available. For the highest relative humidities, the underestimation of the measured deposition is highest, with a median of about -6 nmol m^{-2} s^{-1}. During the night, the scatter in the differences increases with decreasing difference and increasing relative humidity. Only for RH between 80 and 90 % during the day and 40 and 60 % dur-

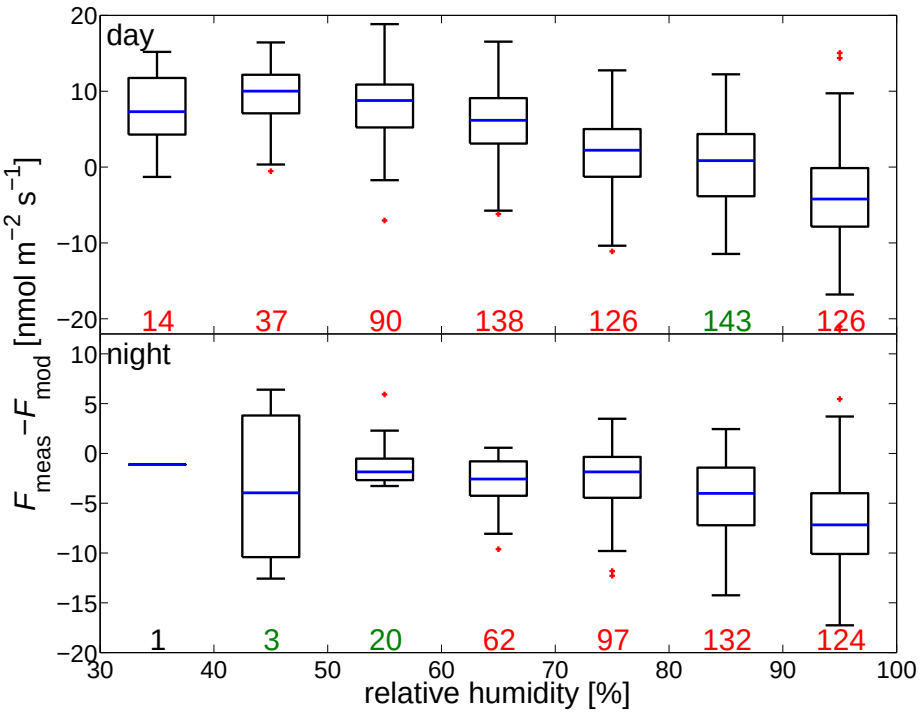

Figure 6.24: Boxplot giving the difference between measured and modeled ozone fluxes at M1 for relative humidity blocks of 10 %. Shown is the median with 25 % and 75 % quartiles, the whiskers display the quartiles +/- 1.5 times the interquartile range. Outliers are marked as crosses. The numbers at the bottom of the figures give the number of observations used for the boxplot and their colors indicate the significance level on which the differences are different from zero. Green: difference is not significant on a level of β=0.1; red: difference is highly significant (β=0.01).

ing the night, the differences are not statistically significant from zero, although the block between 40 and 50 % can be neglected due to the low number of observations. For all other differences, the deviation from zero is highly significant.
Figure 6.25 shows the boxplot of the difference between measured and modeled fluxes for M4 and its dependence on relative humidity. The number of available fluxes in the relative humidity blocks is given as well. As was observed for M1, the difference decreases with increasing relative humidity, but the differences are much lower. For the lowest daytime relative humidity, the overestimation of the measured deposition is highest with about 4 nmol m^{-2} s^{-1}. For relative humidities between 70 and 80 %, the median difference is negative and closest to zero. For higher RH the difference is negative as well, but the median value is still higher than -2 nmol m^{-2} s^{-1}. Except for the RH block from 30 to 40 %, which comprises the lowest number of observations, all deviations of the difference between measurement and modeling from zero are highly significant. During the night, the model underestimates the deposition, indicated by the negative difference between measurement and modeling for all humidity blocks. As for M1, the difference decreases with increasing relative humidity. The minimum median difference is about -3 nmol m^{-2} s^{-1} for the highest RH blocks. For the RH blocks with a sufficient number of data points, the deviation from zero is highly significant.

Overall the nighttime differences, where no stomatal pathway is considered for the flux modeling, show that the non-stomatal deposition is underestimated by the model. Furthermore, the daytime fluxes, which are mainly caused by the stomatal fluxes, show that the deposition to stomata is highly overestimated by the model. Comparing the upper plots of Figures 6.24 and 6.25, which give the daytime differences between measured and modeled ozone fluxes, it is noticeable that the differences change from positive to negative values at different relative humidities. For the fluxes above the forest, only the RH block for 90 to 100 % gives a negative difference, while on the clearing the change in sign is present for RH higher than 70 %.

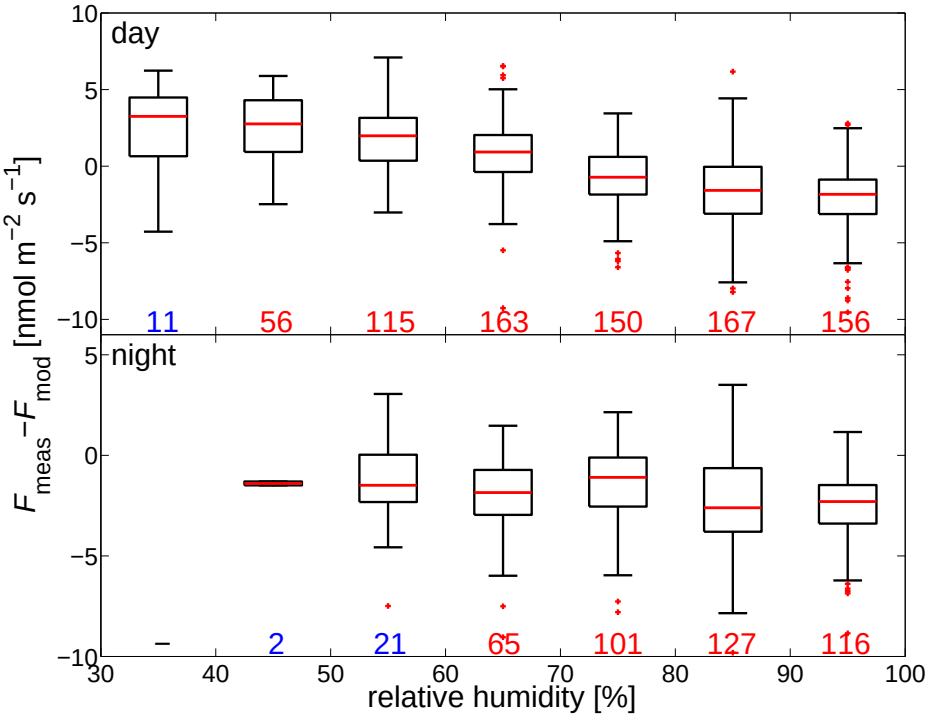

Figure 6.25: Same as Figure 6.24 for M4. The numbers at the bottom of the figures give the number of observations used for the boxplot and their colors indicate the significance level on which the differences are different from zero. Blue: difference is very significant (β=0.05); red: difference is highly significant (β=0.01).

The differences between measurement and modeling have been affected by the changes made to the model code. These changes mainly consisted of the consideration of actual relative humidity in the flux calculation. Figure 6.26 presents the day- and nighttime median differences at M1 for RH blocks of 10 % as well as the median of the measured fluxes in the blocks. The different colors represent different model versions. The corresponding ozone flux time series are shown in Figure 6.16 using the same color coding. The medians represented by the blue bars are the same medians presented in Figure 6.24, as this is the model version used for the modeling studies. During daytime, the calculation of relative humidity from specific humidity (purple bars) decreases the difference and thus improves the model behavior compared to the original model code (green bars), especially for low relative humidities. The highest decrease of about 5 nmol m^{-2} s^{-1} is found for the lowest relative humidity block. With increasing RH, the change in the median difference decreases

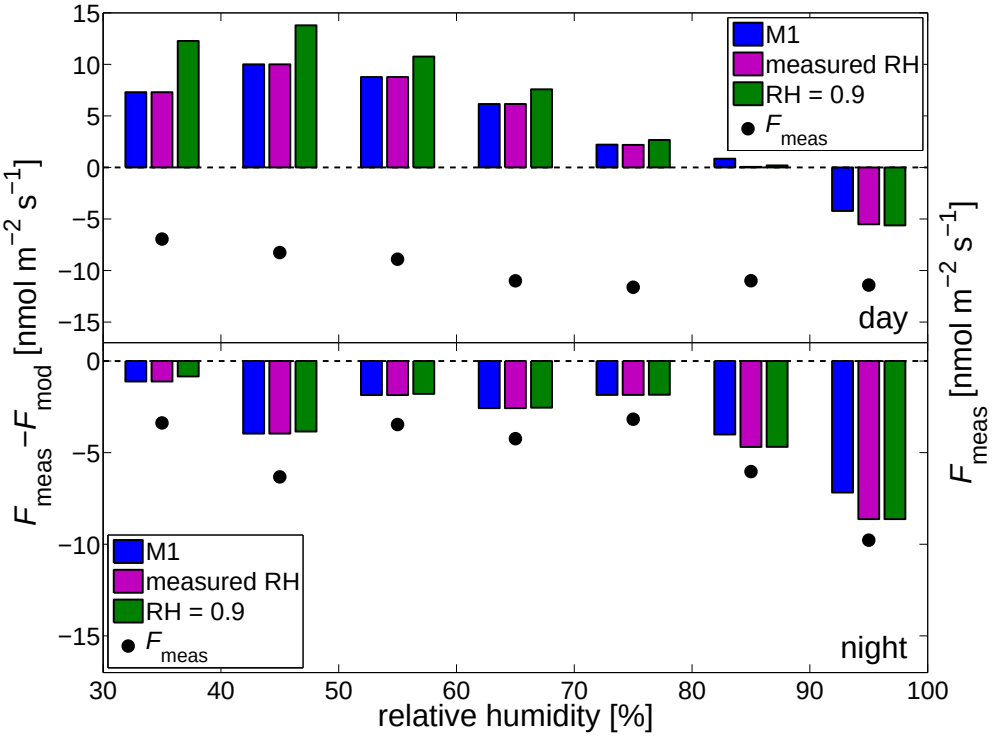

Figure 6.26: Barplot giving the median difference between measured and modeled ozone fluxes at M1 for relative humidity blocks of 10 %. Shown are the differences for the original model code (in green), using the measured relative humidity (RH) (in purple) and the model version using the measured RH and considering RH for determination of wet skin fraction (in blue). The number of observations in each RH block are the same as in Fig. 6.24. The black dots give the median of the measured M1 fluxes in each RH block.

and for relative humidities higher than 70 %, the change in the difference becomes lower than 1 nmol m^{-2} s^{-1}. For RH higher than 90 %, the difference is increased by the use of the different model versions. For the nighttime fluxes, the calculation of the relative humidity shows hardly any changes to the difference between measurement and modeling. During daytime, the decrease in the median difference between the model versions is mainly due to the use of the relative humidity for the calculation of the vapor pressure deficit, which is considered in the stomatal resistance. The lower the RH, the higher is the deficit and thus the higher is the resistance to ozone and the lower becomes the modeled deposition. Furthermore, the decreasing change in the median difference with increasing humidity is due to the difference between the calculated relative humidity and the default value of 90 %. Thus, for the lowest RH, the difference to the default value is highest and the change is largest. This also explains the increase of the difference for RH > 90 %, where the default value underestimates the measured RH. During nighttime, the stomata are closed and therefore, the effect of the calculation of relative humidity is negligible. The consideration of the calculated relative humidity for the determination of the wet skin fraction (fr_{ws}), which is zero by default, is included in the version of the model code used for the blue bars. As the wet skin fraction increases for relative humidities higher than 80 %, there is no effect on the lower RH blocks. The change in the code increases the difference between

measurement and modeling for day- as well as nighttime fluxes. While for the two previous model versions the daytime difference is nearly zero between 80 and 90 % RH, it increases to about 1 nmol m^{-2} s^{-1} including the last change. For higher RH, the increase is a little higher than 1 nmol m^{-2} s^{-1}. During nighttime, the increases are of comparable size, but the total difference between measurement and modeling is more negative. The black dots in Figure 6.26, which give the median fluxes observed in the relative humidity blocks, show that for low RH during daytime the differences are as large as the observed fluxes. For relative humidities higher than 70 %, the absolute differences are at most half as large as the absolute fluxes. During the night, the size of the differences follows the size of the fluxes. The fluxes are about 1 to 3 nmol m^{-2} s^{-1} smaller than the differences, which is due to a small, nearly constant modeled nighttime flux.

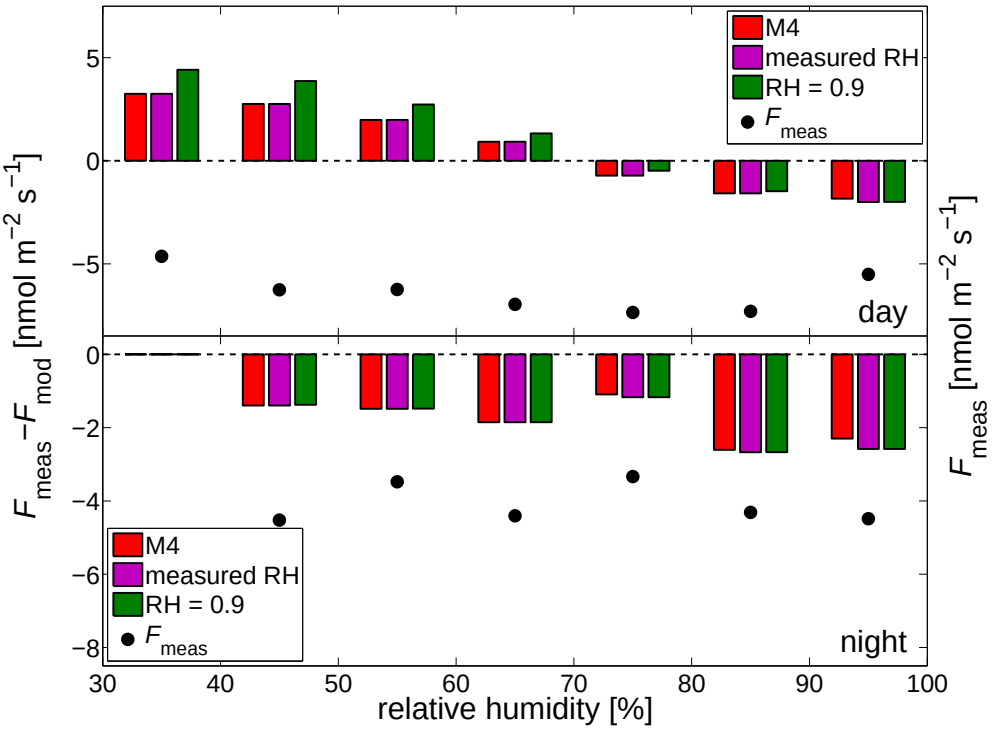

Figure 6.27: Barplot giving the median difference between measured and modeled ozone fluxes at M4 for relative humidity blocks of 10 %. Shown are the differences for the original model code (in green), using the measured relative humidity (RH) (in purple) and the model version using the measured RH and considering RH for determination of wet skin fraction (in red). The number of observations in each RH block are the same as in Fig. 6.25. The black dots give the median of the measured M4 fluxes in each RH block.

Figure 6.27 presents the barplot of the difference between the measured and modeled ozone fluxes for RH blocks of 10 % width as well as the median ozone fluxes on the clearing. The upper plot gives the difference for the daytime fluxes, showing the effect of the changes to the consideration of RH in the model code on the difference. The calculation of relative humidity from specific humidity has the largest effect on the difference compared to the original model version with a fixed RH of 90 %. For the lowest two RH blocks, using the correct RH as input decreases the difference by about 1.1 nmol m^{-2} s^{-1}. With increasing

relative humidity the decrease in the difference decreases and for the highest RH block the change in the model even increases the difference by 0.15 nmol m^{-2} s^{-1}. The consideration of relative humidity for the wet skin fraction affects only the two highest RH blocks. For the lowest blocks, there is no difference as all surfaces are considered dry for RH up to 80 %. The difference between measurement and modeling considering both changes (red bars) decreases from 3.3 nmol m^{-2} s^{-1} in the 30-40 % RH block to -1.8 nmol m^{-2} s^{-1} in the highest RH block. For relative humidities between 80 and 90 % the calculation of wet skin fraction shows only a small increase of less than 0.01 nmol m^{-2} s^{-1}, but for the highest RH block the increase in the difference is of about 0.16 nmol m^{-2} s^{-1}. Solely for the lowest RH block, the difference is of the same order of magnitude as the absolute flux. For higher relative humidities, the differences are at most half as large as the fluxes. During the night, which is shown in the lower plot of Figure 6.27, none of the changes to the original model version produces a large change in the difference. The largest change in the difference is present in the RH block from 90 to 100 %, due to the calculation of wet skin fraction. The calculation increases the difference by about 0.3 nmol m^{-2} s^{-1}. The difference shows no trend with relative humidity, but the size of the differences follows the trend of the size of the flux, except for the RH block of 40-50 % with the lowest number of observations (N = 2). The difference is about half as large as the flux with the exception that for the highest humidities, the flux is less than twice the difference. As was observed for the nighttime values at M1 (see Fig. 6.26), the deviation between difference and flux is similar for all relative humidities.

The presentation of the modeled fluxes as mean diel cycles should partly compensate for the daytime over- and underestimations due to different RH. For the fluxes above the clearing, there is a good agreement between the measured and modeled diel cycles during the day. Above the forest, the modeled deposition is higher than the measured deposition, which could indicate that there is an additional cause for the overestimation of the ozone deposition by the model. The overestimation could be due to the application of a LAI for the modeling, which is too high to accurately represent the actual vegetation cover. The footprint area of the forest tower was not completely covered with vegetation (e.g. a stone pit) or only with lower vegetation (clearings), which results in a lower LAI than that of the forest applied for the modeling. In contrast, the footprint area of M4 consisted mainly of the clear-cut vegetation, whose data was used as input for the model. Therefore, instead of a leaf area index of 6 m^2 m^{-2}, which was measured during EGER-IOP3 for the area around the main tower M1, a lower LAI is used to analyse its effect on the mean diel cycle. For the modeling, a lower LAI could also indicate a lower vegetation fraction. An average vegetation fraction of 80 % or a LAI of 4.8 m^2 m^{-2} is assumed. Figure 6.28 displays the mean diel ozone flux cycle above the forest using the afore mentioned LAI. The maximum downward directed flux is present at 12 CET with about -15 nmol m^{-2} s^{-1}, compared to -18 nmol m^{-2} s^{-1} at 13 CET with the measured LAI and -13 nmol m^{-2} s^{-1} at 12 CET during the EGER-IOP3 measurement. The diel cycle in Figure 6.28 shows a better agreement with the measured diel cycle in Figure 6.10(a). Between 9 and 19 CET the mean diel cycles of the measured flux and that modeled with a lower LAI show comparable values. The deposition during the night is only a little lower than using the LAI measured around the main tower and thus still underestimates the nighttime deposition.
The decrease in the deposition using a lower LAI reduces the daytime difference between measurement and modeling. Therefore, the relation between daytime difference and RH

shows a better agreement with the relation for M4 (see Fig. 6.25). However, the stomatal deposition remains overestimated by the model.

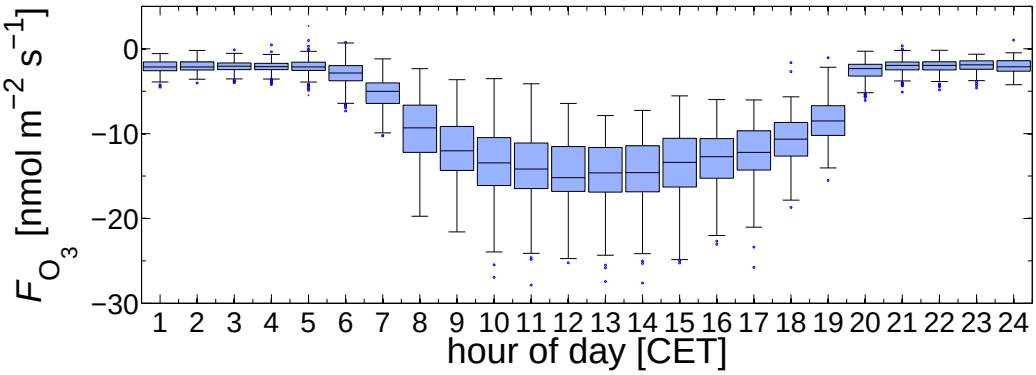

Figure 6.28: Mean diel ozone flux cycle modeled for M1 at a height of 32 m and with a vegetation fraction of 0.8, averaged over 41 days (15.06.-25.07.2011). Shown is the median with 25 % and 75 % quartiles, the whiskers display the quartiles +/- 1.5 times the interquartile range. Outliers are marked as dots.

6.5.2.2 Further possible model improvements

For the modeled ozone fluxes presented in section 6.5.1, only some changes have been performed to the original model version, which concerned the calculation of relative humidity and the further usage of the calculated value. To improve the accordance between measurement and modeling, additional modifications of some model parameters are possible. The modifications are tested for M1, where the larger absolute fluxes are observed and larger effects of the modifications are expected compared to M4.

Under wet conditions, the cuticular resistance r_{cut} is replaced by the wet surface resistance r_{ws} in the calculation of the surface resistance. The default value of $r_{\mathrm{ws}} = 2000$ s m^{-1} is high in relation to the value of r_{cut}. Therefore, the value of r_{ws} is reduced to 997 s m^{-1}, according to Eq. 12 in Wesely (1989) to calculate wet from dry cuticular resistance. The decrease in r_{ws} only affects time periods with a relative humidity higher than 80 % as only under this condition part of the surface is considered as wet. Figure 6.29 shows the time series of the ozone flux at M1 using the default and the reduced value of r_{ws}. Reducing the resistance has an effect on the night- as well as on the daytime fluxes. The nighttime fluxes show an increased deposition, except for some nights. The largest difference is visible on the night June 29/30 with about 2 nmol m^{-2} s^{-1}. On average, the deposition is increased by about 1 nmol m^{-2} s^{-1}. The affected nights are those, which have also shown the highest difference to the measured flux before and thus, the nighttime difference between measurement and modeling is increased and shifted closer to zero. During daytime, the deposition is also increased by up to 2 nmol m^{-2} s^{-1} (e.g. June 30-July 02), but the increase is usually lower or there is no increase at all. In general, the daytime relative humidity is lower than in the

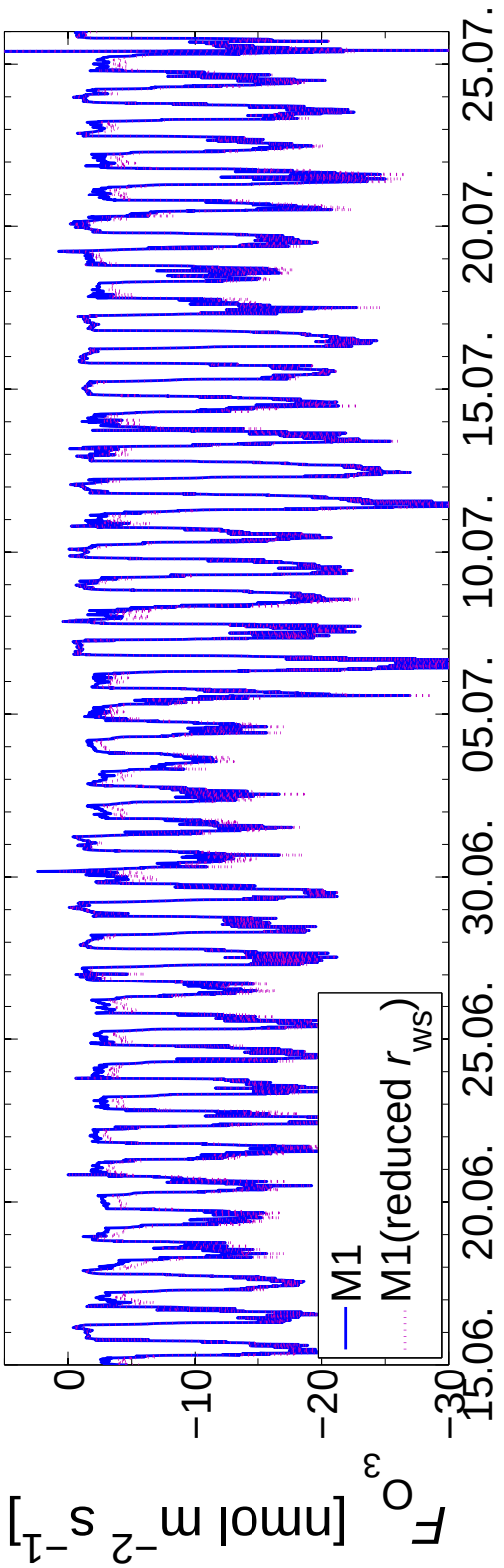

Figure 6.29: Time series of the ozone fluxes modeled for M1 (blue) during EGER-IOP3. The purple dotted line gives the flux with a reduced wet surface resistance. The time series show 10 minute fluxes modeled for a height of 32 m.

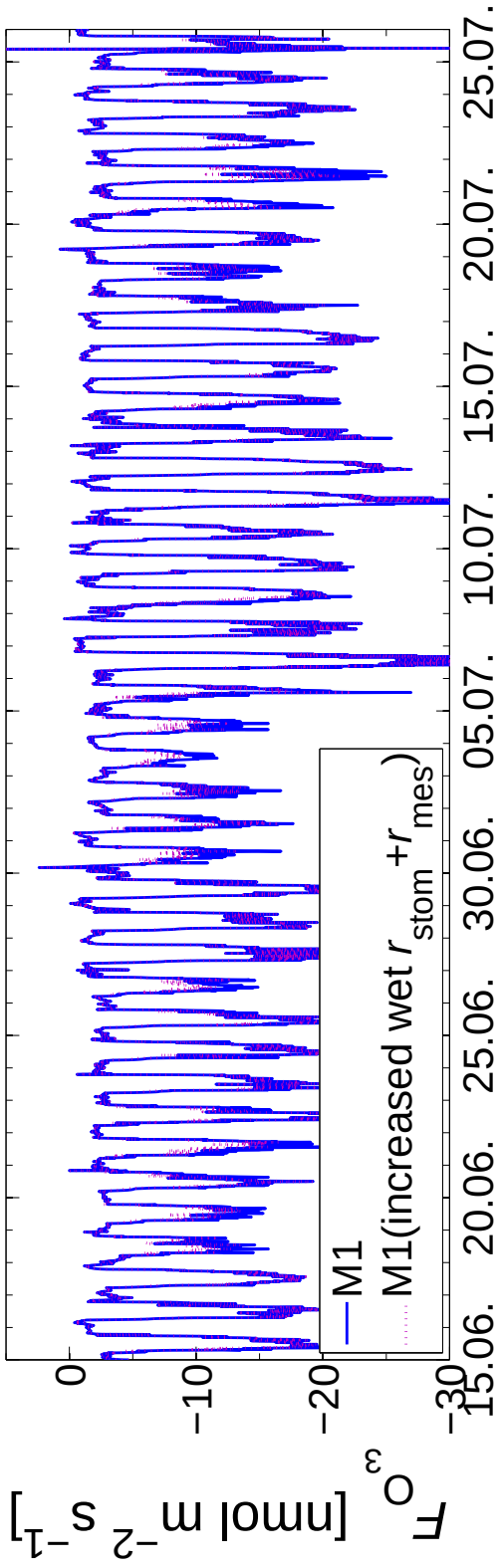

Figure 6.30: Time series of the ozone fluxes modeled for M1 (blue) during EGER-IOP3. The purple dotted line gives the flux with an increased resistance of stomata and mesophyll under wet conditions. The time series show 10 minute fluxes modeled for a height of 32 m.

night and thus, a relative humidity higher than 80 % ($fr_{\text{ws}} > 0$ for $RH > 80\%$) is reached not as often as during night. Thus, the decrease of the wet surface resistance decreases the nighttime underestimation and also the daytime underestimation for the highest relative humidities, but it increases the overestimation for relative humidities between 80 and 90 %.

Dew and rain also have the effect of covering the leaf stomata and thus cutting-off the direct gas exchange when stomata are open (Wesely, 1989). According to Wesely (1989) the value of $r_{\text{stom}} + r_{\text{mes}}$ should be increased by a factor of 3 under these conditions. In Figure 6.30 the ozone flux time series obtained with and without an increased value of $r_{\text{stom}} + r_{\text{mes}}$ are given. Increasing the resistance has no effect on the nighttime fluxes as the stomata are closed anyway. Thus, only the daytime flux in affected. The daytime deposition is reduced due to the increase in resistance. The reduction is highest on July 04 with up to 2.5 nmol $\text{m}^{-2}\,\text{s}^{-1}$. The highest reductions are observed for low absolute ozone fluxes. For the highest absolute fluxes about no reduction of the flux is observed. A high deposition is related to a high PAR, as the stomatal resistance decreases with increasing PAR. Usually, high PAR is observed in combination with a relatively low relative humidity and thus, no or only little change of the flux is observed. Under cloudy conditions, a lower PAR and thus lower deposition is observed. Hence, the higher relative humidity under these conditions leads to a decrease in deposition by the humidity dependent increase in resistance. The decrease in deposition for relative humidities higher than 80 % decreases the difference between measurement and modeling, which is already negative for the highest humidities and close to zero for RH between 80 and 90 % (see Fig, 6.24). Therefore, the increase of the resistance does not improve the agreement between measurement and modeling.

A number of additional parameters can be changed, but the changes shown above are those with the largest effect on the modeled flux. Not using a more precise parameterization of the stomatal resistance is the largest limitation of the current model version, but changing it in the model code is more complex and time-consuming.

6.5.3 Sensitivity analysis

The effect of different parameters on the flux can be analyzed by switching on and off the parameters in the model. Thus, the effect of chemistry on the flux is investigated by switching off chemical reactions and photolysis. Figure 6.31 shows the time series of the M1 ozone flux with and without considering chemical reactions. Chemical reactions decrease the flux, both at day and night, except for a few time steps. This indicates that chemistry is a sink for ozone, the way that more ozone is destroyed by chemical reactions than produced. In general, the effect of chemical reactions is higher during the day than during the night. The highest effect of chemistry is observable for June 27 and 28, which are the days with the highest radiation. However, only slight differences are visible and at least in the model the effect of chemistry on the flux can be assumed as negligible.

The total ozone flux is composed of a stomatal as well as a non-stomatal component. The portion of the non-stomatal to the total modeled ozone flux can be determined by switching off the stomatal pathway. Closed stomata are simulated by increasing the stomatal and mesophyll resistance to values larger than 10^5 s m^{-1}. The non-stomatal portion is obtained by

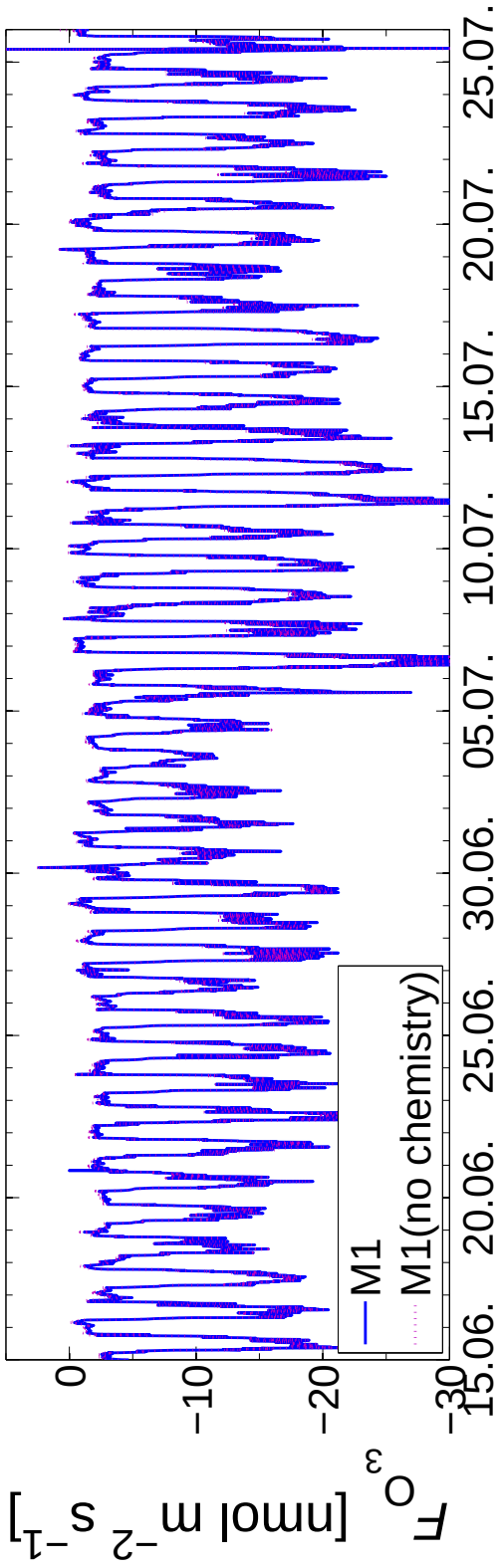

Figure 6.31: Time series of the ozone fluxes modeled for M1 (blue) during EGER-IOP3. The purple dotted line gives the flux without considering chemical reactions. The time series show 10 minute fluxes modeled for a height of 32 m.

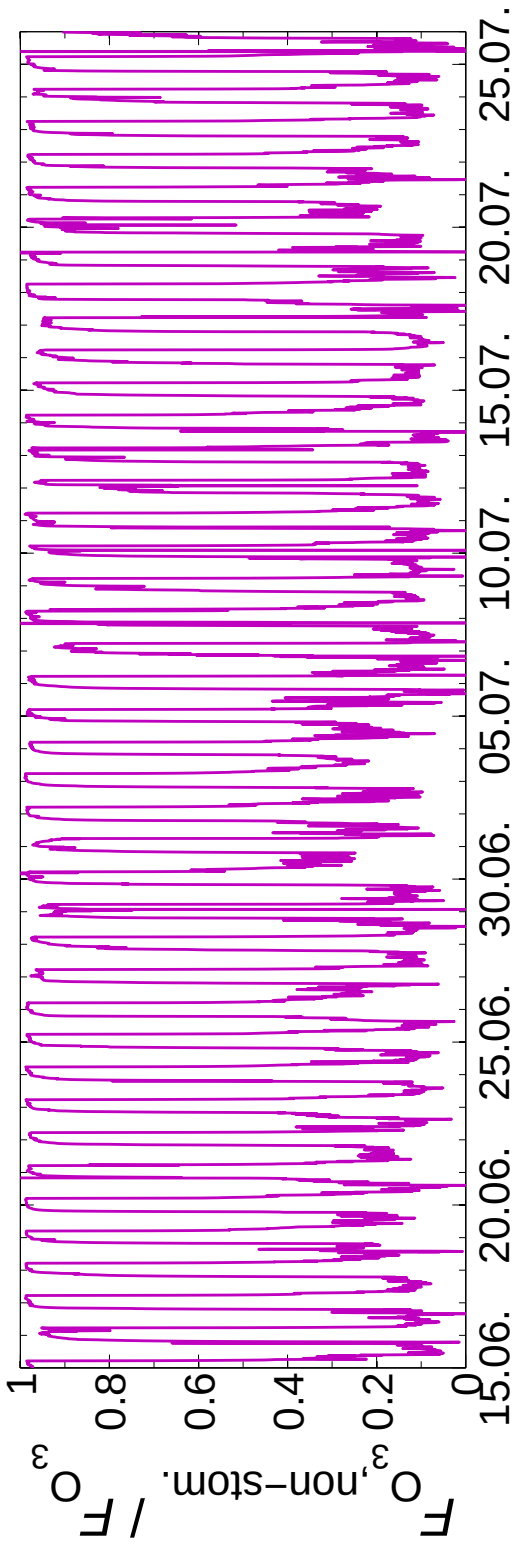

Figure 6.32: Time series of the fraction of non-stomatal deposition modeled for M1 during EGER-IOP3. The fraction is the ratio of the ozone flux without considering stomatal deposition ($F_{O_3,\text{non-stom.}}$) to the total ozone flux (F_{O_3}). The time series shows 10 minute fractions modeled for a height of 32 m.

comparing the flux assuming no stomatal contribution to the ozone flux considering all deposition pathways. Disregarding the stomatal deposition decreases the daytime deposition (time series not shown). At M1, the lowest non-stomatal flux is about -11 nmol m^{-2} s^{-1}, while the total flux is about -28 nmol m^{-2} s^{-1}. The non-stomatal flux shows similar values during day and night and a good agreement to the total nighttime ozone flux, where no stomatal deposition is assumed anyway. Figure 6.32 presents the time series of the fraction of the non-stomatal to the total M1 ozone flux. During nighttime, the non-stomatal deposition is the main pathway for the ozone deposition indicated by a fraction close to 1. The nighttime fraction is lowest for some dry nights (e.g. nights from June 26 to 29), whereas for wet nights especially the cuticular resistance decreases, which decreases the total leaf resistance and increases the fraction of the non-stomatal to the total flux. The stomatal ozone deposition is mainly contributing to the total flux during the day and the fraction of the non-stomatal flux decreases. It reaches minimum values of about 0.1 on most of the days. The maximum fraction to the total flux around noon is present on June 30 with up to 40 %. The daytime fraction of the non-stomatal flux depends on the humidity and the radiation, which affect the stomatal resistance (see Fig. 4.3). For low humidity/high radiation the fraction is low and for increasing humidity/decrasing radiation the fraction increases, amongst others, due to an increased fraction of wet surfaces, which decreases the cuticular resistance and thus increases the non-stomatal flux. For the campaign period of 41 days the total deposition of ozone to the forest sums up to 30.8 mmol m^{-2} (1.5 g m^{-2}). The non-stomatal deposition accounts for 8.1 mmol m^{-2} (387.8 mg m^{-2}). Thus, the non-stomatal deposition accounts for 26.23 % of the total modeled deposition.
In Figure 6.33 the fraction of the non-stomatal to the total flux on the clearing is presented. The nighttime flux is dominated by the non-stomatal flux like above the forest. The only difference is that a fraction of 1 is reached in all nights. During the day, the contribution of the stomatal to the total deposition increases and thus, the fraction of the non-stomatal deposition decreases. At midday, the fraction ranges between about 40 and 50 %. The course of the midday fractions at M4 is similar to the course above the forest, but with smaller differences between the days. The fraction of the non-stomatal to the total deposition is higher for M4 than for M1 due to the lower LAI of the clearing, which gives a lower stomatal deposition. The modeled non-stomatal depositions are similar at both sites. The total amount of ozone deposited to the clear-cut during the campaign period is 15.5 mmol m^{-2} (743.7 mg m^{-2}). Thereof, the non-stomatal deposition accounts for 59.36 %, which means a deposition of 9.2 mmol m^{-2} (441.4 mg m^{-2}).
The real fractions of the non-stomatal to the total ozone flux might be even higher, as the nighttime/non-stomatal deposition is underestimated by the model. Furthermore, the average daytime deposition to the forest is overestimated. An improvement in the calculation of the stomatal flux would reduce the stomatal deposition and thus increase the non-stomatal fraction.

6.5.4 Discussion

For a future use of the model MLC-CHEM for the modeling of ozone fluxes between atmosphere and biosphere, the model is evaluated using the measurements during EGER-IOP3. In the following section, the results of the evaluation are discussed and compared to previ-

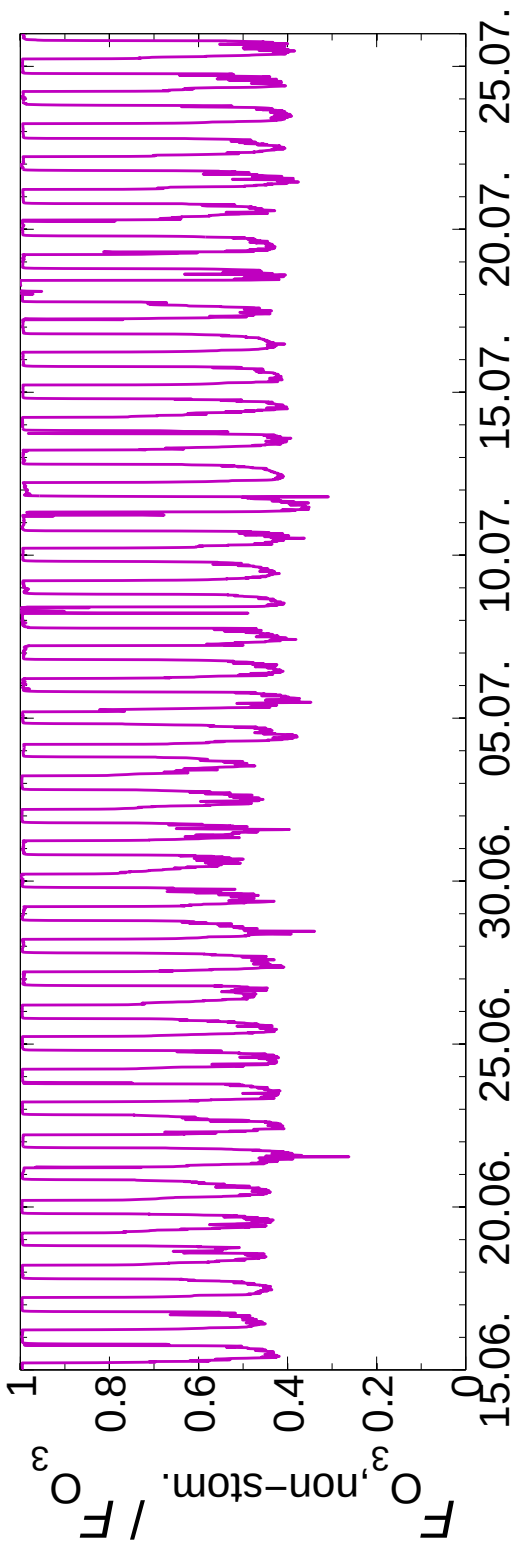

Figure 6.33: Time series of the fraction of non-stomatal deposition modeled for M4 during EGER-IOP3. The fraction is the ratio of the ozone flux without considering stomatal deposition ($F_{O_3,\text{non-stom.}}$) to the total ozone flux (F_{O_3}). The time series shows 10 minute fractions modeled for a height of 5.5 m.

ous studies.
On average, the modeled fluxes show a good agreement to the measured fluxes, with a better agreement for the fluxes to the clearing than to the forest. Particularly the averaged daytime fluxes agree well with the measured fluxes, while the nighttime deposition is underestimated. However, the difference between measurement and modeling shows large variations depending on relative humidity. The comparison of measurement and modeling above the forest shows a larger overestimation of the measured deposition, which changes to an underestimation at higher RH than for the modeling on the clearing. The deviations in the relation between relative humidity and the difference between measurement and modeling for M1 and M4 could be explained by the simplified assumption of a complete forest canopy at M1, while the footprint area of the M1 measurement was also covered with lower or no vegetation. In addition to the footprint, coherent structures, which are non-periodic, organized eddy structures in canopy flows (Eder et al., 2013), could be a reason for the difference in averaged measured and modeled fluxes. Eder et al. (2013) analyzed the appearance of coherent structures during the EGER campaign. MLC-CHEM presumes a full coupling between the forest and the atmosphere, but this is rarely the case. Mostly, high vegetation and atmosphere are only coupled by turbulent eddies during the day, allowing the exchange of energy and matter of the soil and stem area with the atmospheric layers above the stand. Regarding the effect of relative humidity, Ganzeveld et al. (2002b) discussed the relevance of changes in surface cover properties due to rainfall or dew and the consequent increase in the wet skin fraction. Depending on the solubility of the trace gas, an increase in the wet skin fraction induces significant changes in the modeled canopy top fluxes. The process of uptake or release of trace gases by wet canopies is not well understood with a complex mechanism controlling the uptake. There is a difference, whether the surface is wetted by dew or rain as both have a different acidity and chemical composition (Baldocchi, 1993). Wesely et al. (1990) noted that aqueous phase chemistry such as the oxidation of SO_2 by O_3 can enhance the uptake of gases which are not very soluble (e.g. ozone). The lack of understanding the mechanism driving the O_3 deposition to the wet foliage constrains its quantification and leads to its parameterization as constant values (Ganzeveld and Lelieveld, 2004). Fuentes et al. (1992) showed by flux measurements over a deciduoous forest that there is still significant uptake of ozone by a wet canopy. Whereas in many deposition models, a reduced uptake for wet surfaces is assumed. Furthermore, Altimir et al. (2006) even showed an enhancement of the total ozone deposition to Scots pine foliage under moist conditions. The clearest connection with ambient relative humidity was shown for the non-stomatal sink, and they suggest that the non-stomatal ozone sink on the foliage is modulated by the surface films and that different mechanisms of ozone decomposition are expected to happen in acidic or alkaline solutions (Sehested et al., 1991). Many conclusions on the non-stomatal sinks are drawn from nighttime data based on the assumption that the stomatal conductance is negligible and therefore all nocturnal deposition is non-stomatal. The nighttime underestimation of the deposition shows that the parameterization of the non-stomatal resistance is overestimated. While the modeled deposition is only slightly increasing with relative humidity, there is a sharper increase in the measured flux with RH. The results of Altimir et al. (2006) suggest that the model results could indeed be improved by incorporating the moisture effect in the parameterization of non-stomatal surface conductance.
In contrast to the nighttime differences, the daytime differences between measured and

modeled ozone fluxes show that the stomatal resistance is mainly underestimated by the model. The model evaluation shows that the representation of stomatal exchange, which largely controls the dry deposition flux of ozone, results in an overestimation of the daytime deposition. Ganzeveld et al. (2002b) have already shown, that the modeled stomatal exchange is very sensitive to the selected soil moisture and in this thesis also the sensitivity of the stomatal resistance parameterization to the vapor pressure deficit (depending on RH) is shown. Several other parameterizations are available for the stomatal resistance considering additional parameters affecting the resistance, e.g. the CO_2 concentrations. Alike in the model applied in this thesis, most of the parameterizations of the stomatal resistance applied in one-dimensional SVAT models only consider the dependence of stomatal resistance on radiation, temperature, the vapor pressure deficit and soil water potential in relative terms between 0 and 1, described by the Jarvis-Stewart approach (Jarvis, 1976; Stewart, 1988) as well as modifications due to phenological change (Emberson et al., 2000; Grünhage et al., 2000). However, in nature the stomatal aperture is regulated to gain as much carbon as possible, while minimizing the loss of water for a given set of microclimate conditions (Launiainen et al., 2013). Therefore, the parameterization can be improved by also considering the influence of ambient air CO_2. A semi-empirical equilibrium model of stomatal conductance was proposed by Ball et al. (1987) and Ball (1988), which is based on a number of gas exchange experiments. The model used by Zeller and Nikolov (2000) (Nikolov et al., 1995; Nikolov and Zeller, 2003) uses the Ball-Berry stomatal model for the calculation of stomatal conductance:

$$g_s = m \cdot A_n \frac{h_s}{c_a} + b_s \ , \tag{6.2}$$

where m is a species specific non-dimensional parameter that determines the composite of g_s to net CO_2 assimilation (A_n), relative humidity (h_s) and CO_2 concentration (c_a) at the leaf surface. b_s is the stomatal conductance that remains unaffected by the atmospheric environment or leaf biochemistry. The model also simulates the effect of leaf water deficit on stomatal conductance and net photosynthesis. The variables are estimated as a solution to a system of four simultaneous equations. The model is advantageous over more empirical photosynthesis models (e.g. Jarvis, 1976), as it explicitely accounts for feedbacks between leaf energy balance, stomatal conductance and CO_2 assimilation processes. The proposed model for stomatal conductance was also used by Collatz et al. (1991) as well as by Falge et al. (1996) and Falge et al. (1997) for the calculation of foliage gas exchange in a slightly different form:

$$g_s = g_{min} + g_{fac} \cdot 1000 \cdot (NP + 0.5R_d) \cdot \frac{h_s}{c_s} \ , \tag{6.3}$$

where NP is the net CO_2 fixation rate, $0.5R_d$ is the rate of dark respiration assumed to continue in the light, h_s is relative humidity as decimal fraction, c_s is the CO_2 partial pressure at the leaf surface, g_{min} is the cuticular conductance with closed stomata (as b_s in Eq. 6.2) and g_{fac} is the dimensionless sensitivity of stomata to change in NP, h_s and c_s (Tenhunen et al., 1994; Falge et al., 1996).

For the modeling of fluxes in the first phase of the EGER project, the ACASA model (Advanced Canopy-Atmosphere-Soil Algorithm; Pyles, 2000; Pyles et al., 2000) was used. The plant physiological response to ambient conditions was calculated as well by the use of the Ball-Berry stomatal conductance (Collatz et al., 1991) and the Farquhar and Von Caemmerer (1982) photosynthesis equation following Su et al. (1996) and a soil module adapted

from MAPS (Mesoscale Analysis and Prediction System; Smirnova et al., 1997, 2000).
Launiainen et al. (2013) used a stomatal conductance model, which is based on stomatal optimization theories and the economics of leaf gas exchange coupled together with a Farquhar-type photosynthesis model (Farquhar et al., 1980). The stomatal conductance is (Launiainen et al., 2011):

$$g_s = \frac{a_1}{a_2 + sc_a}\left(-1 + \sqrt{\frac{c_a - c_p}{a_c \lambda D}}\right) , \tag{6.4}$$

where $a_c = 1.6$ is the relative molecular diffusivity of water vapor with respect to carbon dioxide, c_a is the ambient CO_2 concentration, c_p is the CO_2 compensation point, D is the vapor pressure deficit between the leaf and the air, and a_1 and a_2 are parameters of the photosynthesis model. Besides the photosynthetic parameters, the only parameters that require specification are λ (the marginal water use efficiency) and s, a constant that reflects the long-term average ratio of the leaf intercellular and ambient atmospheric CO_2 concentrations.
The models additionally considering the availability of CO_2 seem to be more accurate in the representation of stomatal resistance than the one considering mainly radiation and humidity effects. A newer version of MLC-CHEM will include an option to simulate stomatal uptake as a function of CO_2. However, this model version was still tested by the model developer at the time of the modeling studies for this thesis.

In a sensitivity study performed with MLC-CHEM, the effect of chemistry on the ozone flux was found to be small. Kurpius and Goldstein (2003) determined the influence of gas-phase chemistry on the total ozone flux to a forest and found that the flux due to gas-phase chemistry was exponentially dependent on temperature. The functionality is the same as for biogenic hydrocarbon emissions, which implies that reactions with those are the likely gas-phase chemical process within the canopy. The reaction leads to hydroxyl radical formation and secondary aerosol growth, which affect atmospheric chemistry and climate. In summer, the chemistry was found as the dominant daytime loss process with 45-55 % and decreases to minor importance in winter (15 %). This result for the summer is contrary to the results of the study in this thesis.
In addition, the contribution of the non-stomatal to the total ozone flux was determined. The absolute amount of ozone deposited to the forest and the clearing on non-stomatal pathways is comparable. Above the forest, the model gives a non-stomatal portion of 26 % to the total flux, while on the clearing, the non-stomatal portion accounts for 59 %. The latter value for low vegetation is closer to the value of 70 % found by Fowler et al. (2001) for moorland species. For the various surface types in Southern Europe observed by Cieslik (2004), the stomatal ozone fluxes accounted for less than 50 % of the total flux. Essential was the role of water supply, which influenced the stomatal activity. For Scots pine foliage, Altimir et al. (2006) estimated stomatal deposition accounting for one third of the canopy scale removal. Mikkelsen et al. (2004) observed the yearly stomatal uptake over a Norway spruce ecosystem to have a minimum contribution of 21 % to the total deposition. Highest values of 30-33 % are found between May and August and between November and February low values of 4-9 % are found. Zeller and Nikolov (2000) report a non-stomatal ozone uptake of only 41 % of the total annual flux. Their model predicts most of the ozone to be actively taken up by foliage via leaf stomata. The ozone comes into direct contact with the leaf mesophyll cells and can adversely affect plant photosynthesis and growth.

The remaining amount is estimated to be deposited to non-transpiring surfaces such as tree stems, branches and soil. An improved parameterization of the stomatal and non-stomatal ozone flux in the model MLC-CHEM would increase the contribution of the non-stomatal to the total ozone flux, thus showing a better agreement to the observed fractions.

7 Conclusions

Eddy-covariance measurements of ozone fluxes with today's commercially available O_3 analyzers are still a challenge, and careful consideration of instrument performance is needed. Four dry chemiluminescence fast-response ozone sensors (enviscope GmbH) have been run side-by-side for eddy-covariance ozone flux measurements at a grassland site on the airfield Mainz-Finthen, Germany, during July and August 2013. The same sonic anemometer, logging and analysis software was used for all fast-response sensors, thus some source of error could be eliminated or can at least be considered the same for the ozone fluxes obtained by the four sensor systems. Absolute ozone concentration measurements have been made by a reliable UV-absorption instrument, thus errors in the absolute ozone concentrations are assumed negligible. One potential source of error arises from the attenuation of fluctuations in the tubing, when the flow in the tube is laminar. It has been assumed here that attenuation of fluctuations in the tubing of the scalar sensor dominates the high-frequency attenuation of the EC flux measurement performed for this thesis. Other causes of high-frequency attenuation, e.g. a separation between the sonic and the inlet of the O_3 sensor, need to be considered and minimized as well, and in these cases, an accurate estimate of the flux attenuation requires numerical integration of the cospectrum between the vertical wind speed and the signal of the scalar sensor multiplied with multiple transfer functions.

The comparison of the four ozone sensors shows that on average the diurnal trend of the ozone flux is well captured. However, the absolute values of the fluxes measured by the sensors differ. As the ozone fluxes measured by all sensors seem reasonable compared to previously measured fluxes for similar ecosystem types, each dataset would be accepted as a good estimate of the flux, if only one sensor would have been applied. However, the results of this and previous studies show that although the range of the data is reasonable and quality assurance and quality control measures have been applied, the ozone fluxes might still include a considerable uncertainty up to about 50 $\%$ due to the high-frequency attenuation in the tubing with laminar tube flow.

As a consequence of the flux underestimation under laminar tube flow conditions, a turbulent flow in the tubing should be ensured for future ozone flux measurements with closed-path instruments, as the correction for high-frequency attenuation becomes negligibly small. A higher flow rate not only decreases the attenuation in the tubing, but it also decreases the lagtime between the measurements of the sonic and the ozone analyzer. In order to ensure a turbulent tube flow, it is important to determine the flow rate/Reynolds number for the flow inside the tube. Furthermore, the flow rate should be kept constant using a mass flow controller. In case of an unavoidable laminar tube flow, several points have to be taken into account. Especially at low measurement heights as well as under stable conditions and for high wind speeds, where there are large contributions of the high frequencies to the total covariance, the influence of the damping inside the tube should be considered during post-processing, even for short tubes, which would have no large effect

at larger measurement heights, such as above forest canopies. The corrections and error considerations might be inevitable for nighttime fluxes, when mainly stable conditions prevail and a high accuracy is required as scalar fluxes are generally lower due to reduced turbulent mixing.
In order to analyze and correct the fluxes obtained with closed-path EC systems with laminar tube flow and to assure the reliability and comparability of long-term flux measurements between different years and across ecological gradients, it is suggested to use the cospectral correction method applied in this thesis. The measurements have shown that the correction factors differ for different EC system setups. They have also shown that these are not significantly different from the available theoretical corrections, if those reflect the present state of the measurement setup (e.g. tube length, flow rate) as accurately as possible. Therefore, for ozone fluxes of long-term measurement campaigns, when the application of the cospectral correction method for each flux averaging period would be too time-consuming, the application of the theoretic transfer function is suitable to correct for the underestimation of the measured ozone fluxes.

During the 41-day EGER field campaign in summer 2011 at a forest ecosystem disturbed by a storm, ozone concentrations and EC fluxes have been measured using dry chemiluminescence fast-response ozone sensors. The eddy-covariance instrumentation and measurement setup at the EGER site in the Fichtelgebirge worked well giving results comparable to other studies using both different and similar instrumentation. The eddy-covariance system has been shown to provide reliable flux estimates provided that an adequate correction is applied to high-frequency losses. Distinct diurnal patterns of ozone mixing ratios, fluxes, and deposition velocities have been observed with highest absolute values during daytime and lowest values at night. The clear diurnal variation indicates stomatal activity as a major regulating factor. The fluxes have been lowest around noon with minimum fluxes of -13 nmol m^{-2} s^{-1} above the forest and -7.5 nmol m^{-2} s^{-1} above the clear-cut. The average daily maximum deposition velocity of O_3 was 0.8 and 0.5 cm s^{-1}, respectively. The absolute flux and deposition velocity showed maxima in the morning or around noon, which is in contrast to the ozone mixing ratio that showed highest values in the afternoon. The large nighttime deposition leads to the conclusion that other ozone sinks exist, and it has already been suggested by Pilegaard et al. (1995) that the most important of these are destruction at surfaces and chemical reactions with NO emitted from the forest floor and with terpenes emitted from the coniferous trees.
The measurements during the EGER campaign have shown the high impact of disturbed ecosystems on the regional ozone exchange. It can be concluded that the reduction of vegetation due to a disturbance reduces the deposition of ozone to a canopy according to the ratio of LAIs between the canopy before and after the change in the ecosystem. This change in the ozone exchange is not negligible and emphasizes the importance to consider forest disturbances for the regionalization of fluxes.

In addition to the EGER measurements, the chemistry model MLC-CHEM has been applied to determine ozone fluxes above the forest and the clearing. Originally, the model was designed for a use in larger areas (grid size of about 100 km), comprising several kinds of vegetation types. Despite the coarse scaling of the applied model, the order of magnitude of the measured and modeled fluxes agrees. The mean modeled daytime fluxes show a small underestimation of the measured daytime ozone fluxes, particularly for the

fluxes on the clearing, but the detailed analysis has shown that the modeled fluxes deviate from the measured ones, with a deviation up to the same size as the absolute fluxes. The analysis revealed that the parameterization of the stomatal deposition needs to be adjusted to better represent the relation to relative humidity. With the present parameterization, the difference between measured and modeled fluxes is significant and shows a dependence on the relative humidity, with decreasing difference with increasing humidity. Changes to the model regarding the consideration of the relative humidity for the deposition processes already decreased the difference between measured and modeled ozone fluxes.
The modeled nighttime fluxes reveal an overestimation of the flux. In contrast to the measured flux, the modeled flux is similar for all nights. As the nighttime fluxes are mainly caused by non-stomatal sinks, the overestimation indicates that the representation of non-stomatal ozone sinks needs to be improved.
As the footprint area of the measurement above the forest changed depending on the wind direction, assuming a footprint area fully covered with forest leads to an underestimation of the flux by the model. A realistic representation of the forest fraction was shown to be of importance to obtain reliable modeled fluxes. With the use of an average forest fraction in the footprint area, the difference between measured and modeled mean daytime ozone fluxes above the forest decreased.
The evaluation of the model MLC-CHEM has shown that the model with its present parameterization of deposition processes is not yet suitable for the correct representation of measured ozone fluxes. Before the model can be used for the modeling of ozone fluxes for the entire 4 km^2 EGER measurement site, it is necessary to improve the consideration of stomatal and non-stomatal processes in the deposition modeling.

A Statistical analysis

The results obtained during the measurements and post-processing are analyzed statistically. In the following, the calculation of statistical moments will be described. For a variable x the temporal mean $\overline{x}$ and the standard deviation $\sigma(x)$ from N data points are defined by

$$\overline{x} = \frac{1}{N} \sum_{i=1}^{N} x_i \tag{A.1}$$

and

$$\sigma(x) = \sqrt{\frac{1}{N} \sum_{i=1}^{N} (x_i - \overline{x})^2} \, . \tag{A.2}$$

For a large number of measurements (N > 10), N in the denominator of the standard deviation calculation is replaced by N-1. This inheres in a reduced number of independent data points (Borrmann, 2012). The median x_{med} of a quantity is the value where half of the total data is below.

To determine the relation between two quantities, the linear least squares method is used. It minimizes the summed square of the residuals. To improve the fit if not all data is of equal quality, a weighted least squares regression is performed. The weights w are included as additional scaling factors and are obtained from the standard deviation of each measured value y by $w = \sigma(y)^{-2}$. The weights indicate differing levels of quality present in the data and are used to determine how much each response value influences the final fitting parameter estimate. A high-quality data point influences the fit more than a low-quality data point.
The main disadvantage is the sensitivity of least squares fitting to outliers. Outliers have a large influence on the fit, because squaring the residuals magnifies the effects of those extreme data points. To minimize the influence, the data can be fitted using robust least squares regression. The bisquare weights method minimizes a weighted sum of squares, where the weight depends on how far the point is from the fitted line. Full weight is given to points near the line and points farther from the line get reduced weight, down to zero. The robust fitting with bisquare weights uses an iteratively reweighted least squares algorithm.
For the linear regressions a correlation coefficient R is calculated, which is a measure of the goodness of the linear relation. R^2 ranges between 0 and 1. A value of 1 implies that the relationship between two variables can perfectly be described by a linear equation. If no linear correlation exists between the variables, it is implied by a value of 0.

In order to verify experimental results against theoretical values or to compare different samples, statistical testing is performed for test parameters like mean, standard deviation or fitting parameters. It is used to quantify the differences between samples and determine

whether they are close enough to both represent the same underlying situation. The declaration about the confidence that two samples are the same or different is associated with numbers for the level of confidence. For each statistical test, the test statistic follows a specific probability density distribution and contains information about the available sample sets. The values for the test statistic depending on the confidence level and the number of measurements can be found in tables.
For the distribution of sampled estimator values λ^* around the true one λ, a probability density function $f(\lambda^*)$ is defined, which has its maximum at $\lambda^* = \lambda$ and decreases with increasing distance between λ and λ^* following a bell shape. The spread of the curve decreases with increasing number of observations (N). A cumulative probability β is chosen with a certain limiting value $S(\beta)$, which follows from the particular distribution $f(\lambda^*)$ and takes the role of quantiles of the distribution. It gives a range, where it is unlikely to find a sampled estimator further away from its true value than given by β:

$$\begin{aligned}\beta = \beta(\text{left side}) + \beta(\text{right side}) &= \int_{-\infty}^{(\lambda - S(\beta))} f(\lambda^*) d\lambda^* + \int_{(\lambda + S(\beta))}^{\infty} f(\lambda^*) d\lambda^* \\ &= 1 - \int_{(\lambda - S(\beta))}^{\lambda + S(\beta)} f(\lambda^*) d\lambda^* \,. \end{aligned} \tag{A.3}$$

The β-values are termed "levels of significance". A value of β = 0.1 implies a significance level of 90%, which is termed "significant", β = 0.05 is termed "very significant" and β = 0.01 is named "highly significant". If the probability density function is symmetric, two-sided limits can be defined for a probability P:

$$P(|\lambda - \lambda^*| \geq S(\beta)) \leq \beta \tag{A.4}$$

and the interval

$$\lambda^* - S(\beta) \leq \lambda \leq \lambda^* + S(\beta) \tag{A.5}$$

is called "confidence limit".
The width of the confidence interval indicates how uncertain the sampled estimator values or fitted coefficients are.

A Student t test is applied if the number of samples is small (lower than 200) and no normal distribution can be used as probability density distribution. The test statistic t is

$$t = \frac{\overline{x} - \mu_0}{s} \cdot \sqrt{N} \,, \tag{A.6}$$

where s is the dispersion of the real data from the sample of N measurements. A probability density function of Student t distribution for $-\infty < t < \infty$ has a mean of zero and for $n > 2$ a spread of $\sigma^2 = n/(n-2)$, where the number of degress of freedom is $n = (N-1)$. The lobes are wider than for a Gaussian normal distribution and thus the levels of significance are further away from the mean than for Gaussian normal distribution. The larger the number of degrees of freedom, the more the Student t distribution approaches a Gaussian normal distribution. The fewer data is available, the more difficult it becomes to reject a hypothesis.
The deviation of a sample mean $\overline{x}$ (of N data sample points) from the mean μ_0 of a hypothetical population mean is statistically significant on a significance level of β, if

$$t = \frac{|\overline{x} - \mu_0|}{s} \cdot \sqrt{N} > t_\beta(n) \,, \text{with } n = (N-1) \,. \tag{A.7}$$

Rearranging the equation gives the confidence limits of the sample mean, which give the range on both sides of $\overline{x}$ within which the expectation value μ_0 of the underlying population should be found under the given significance level:

$$\overline{x} - t_\beta(n) \cdot \frac{s}{\sqrt{N}} \leq \mu_0 \leq \overline{x} + t_\beta(n) \cdot \frac{s}{\sqrt{N}} \tag{A.8}$$

or in form of error bars

$$\mu_0 = \overline{x} \pm t_\beta(n) \cdot \frac{s}{\sqrt{N}} \,. \tag{A.9}$$

A detailed description of the methods for statistical analyses can be found in Borrmann (2012) and literature therein.

B List of Symbols

Abbreviations

ABL	Atmospheric boundary layer
CBL	Convective boundary layer
DC	Dry chemiluminescence
EC	Eddy-Covariance
EGER	ExchanGE processes in mountainous Regions
FFT	Fast Fourier transform
GPC	Gas-phase chemiluminescence
ID	Inner diameter
IOP	Intensive observation period
ITC	Integral turbulence characteristics
LAD	Leaf area density
LAI	Leaf area index
MAD	Median Absolute Deviation
MPIC	Max Planck Institute for Chemistry
PAI	Plant area index
QA/QC	Quality assurance and quality controle
RH	Relative humidity
SL	Surface layer
TK3	Third version of the "Turbulence Knight" (eddy-covariance software)
TKE	Turbulent kinetic energy
UV	Ultraviolet
VOC	Volatile organic compound

Chemical species

CO_2	Carbon dioxide
H_2O	Water
NO_x	Nitrogen oxides
O_3	Ozone

Greek symbols

ϵ_x	Correction factor for spectral flux correction
ν	Kinematic viscosity
ρ	Density of air
τ	Time constant
σ	Standard deviation

Latin symbols

Co_{xy}	Cospectrum of variables x and y
c	Scalar component concentration
d	Displacement height
E	Saturation vapor pressure
e	Vapor pressure
F_x	Flux of variable x
f	Natural frequency
f_N	Nyquist frequency
h_c	Canopy height
K_{H}	Turbulent diffusion coefficient for heat
L	Monin Obukhov length
l	Tube length
N	Number of observations
n	Normalized frequency
p	Pressure/sampling path length
Pr	Prandtl number
q	Specific humidity
R_a	Aerodynamic resistance to turbulent transport
R_b	Quasi-laminar boundary layer resistance
R_c	Surface resistance
r_{cut}	Cuticular resistance
r_{leaf}	Leaf resistance
$r_{\text{leaf,wet}}$	Leaf resistance for wet vegetation
r_{mes}	Mesophyll resistance
r_{soil}	Soil resistance
r_{stom}	Stomatal resistance
r_{ws}	Wet skin resistance
Re	Reynolds number

Re_{crit}	Critical Reynolds number
S_x	Power spectrum of variable x
s	Sensor separation length
Sc	Schmidt number
T	Actual temperature
$T_{i,x}$	Specific transfer function of variable x, $i \in \{\tau, p, s\}$
U	Mean flow velocity in a tube
u, v, w, u_i	Components of the wind vector, $i \in \{1, 2, 3\}$
u_*	Friction velocity
v_d	Deposition velocity
$\overline{w'c'}$	Vertical flux of scalar component
z	Measurement height

Averages and indices applied on a variable Ψ

Ψ_m	Measured component
$\overline{\Psi}$	Temporal mean
Ψ'	Fluctuation (deviation from the mean)

Operators

∂	Partial differential-operator
$\int$	Integral-operator
$\sum$	Sum-operator

Bibliography

Altimir, N., Vesala, T., Keronen, P., Kulmala, M., and Hari, P.: Methodology for direct field measurements of ozone flux to foliage with shoot chambers, Atmospheric Environment, 36, 19–29, 2002.

Altimir, N., Kolari, P., Tuovinen, J.-P., Vesala, T., Bäck, J., Suni, T., Kulmala, M., and Hari, P.: Foliage surface ozone deposition: a role for surface moisture?, Biogeosciences, 3, 209–228, 2006.

Amiro, B., Orchansky, A., Barr, A., Black, T., Chambers, S., Chapin III, F., Goulden, M., Litvak, M., Liu, H., McCaughey, J., et al.: The effect of post-fire stand age on the boreal forest energy balance, Agricultural and Forest Meteorology, 140, 41–50, 2006.

Amiro, B., Barr, A., Barr, J., Black, T., Bracho, R., Brown, M., Chen, J., Clark, K., Davis, K., Desai, A., et al.: Ecosystem carbon dioxide fluxes after disturbance in forests of North America, Journal of Geophysical Research, 115, 2010.

Ammann, C., Brunner, A., Spirig, C., and Neftel, A.: Technical note: Water vapour concentration and flux measurements with PTR-MS, Atmospheric Chemistry and Physics, 6, 4643–4651, 2006.

Ashmore, M.: Assessing the future global impacts of ozone on vegetation, Plant, Cell & Environment, 28, 949–964, 2005.

Aubinet, M., Grelle, A., Ibrom, A., Rannik, U., Moncrieff, J., Foken, T., Kowalski, A., Martin, P., Berbigier, P., Bernhofer, C., et al.: Estimates of the annual net carbon and water exchange of forests: the EUROFLUX methodology., Advances in Ecological Research, 30, 113–175, 2000.

Aubinet, M., Chermanneb, B., Vandenhauteb, M., Longdoza, B., Yernauxa, M., and Laitatb, E.: Long term carbon dioxide exchange above a mixed forest in the Belgian Ardennes, Agricultural and Forest Meteorology, 108, 293–315, 2001.

Aurela, M., Laurila, T., and Tuovinen, J.-P.: Measurements of O_3, CO_2 and H_2O fluxes over a Scots pine stand in eastern Finland by the micrometeorological eddy covariance method, Silva Fennica, 30, 97–108, 1996.

Baldocchi, D.: Measuring fluxes of trace gases and energy between ecosystems and the atmosphere–the state and future of the eddy covariance method, Global Change Biology, 20, 3600–3609, 2014.

Baldocchi, D., Falge, E., Gu, L., Olson, R., Hollinger, D., Running, S., Anthoni, P., Bernhofer, C., Davis, K., Evans, R., et al.: FLUXNET: A new tool to study the temporal

and spatial variability of ecosystem-scale carbon dioxide, water vapor, and energy flux densities, Bulletin of the American Meteorological Society, 82, 2415–2434, 2001.

Baldocchi, D. D.: Deposition of gaseous sulfur compounds to vegetation, Sulfur nutrition and assimilation and higher plants, pp. 271–293, 1993.

Baldocchi, D. D., Hicks, B. B., and Camara, P.: A canopy stomatal resistance model for gaseous deposition to vegetated surfaces, Atmospheric Environment, 21, 91–101, 1987.

Ball, J. T.: An analysis of stomatal conductance, Ph.D. thesis, Stanford University Stanford, 1988.

Ball, J. T., Woodrow, I. E., and Berry, J. A.: A model predicting stomatal conductance and its contribution to the control of photosynthesis under different environmental conditions, in: Progress in Photosynthesis Research, pp. 221–224, Springer, 1987.

Bassin, S., Calanca, P., Weidinger, T., Gerosa, G., and Fuhrer, J.: Modeling seasonal ozone fluxes to grassland and wheat: model improvement, testing, and application, Atmospheric Environment, 38, 2349–2359, 2004.

Bauer, M., Hultman, N., Panek, J., and Goldstein, A.: Ozone deposition to a ponderosa pine plantation in the Sierra Nevada Mountains (CA): a comparison of two different climatic years, Journal of Geophysical Research, 105, 22 123–22 136, 2000.

Bonn, B. and Moortgat, G. K.: Sesquiterpene ozonolysis: Origin of atmospheric new particle formation from biogenic hydrocarbons, Geophysical Research Letters, 30, 2003.

Borrmann, S.: Fundamentals of Statistics and Data Analyses in Meteorology, Lecture notes, WS 2011/2012, 2012.

Burba, G. and Anderson, D.: A brief practical guide to eddy covariance flux measurements: principles and workflow examples for scientific and industrial applications, Li-Cor Biosciences, 2010.

Cieslik, S.: Energy and ozone fluxes in the atmospheric surface layer observed in Southern Germany highlands, Atmospheric Environment, 32, 1273–1281, 1998.

Cieslik, S. A.: Ozone uptake by various surface types: a comparison between dose and exposure, Atmospheric Environment, 38, 2409–2420, 2004.

Collatz, G. J., Ball, J. T., Grivet, C., and Berry, J. A.: Physiological and environmental regulation of stomatal conductance, photosynthesis and transpiration: a model that includes a laminar boundary layer, Agricultural and Forest Meteorology, 54, 107–136, 1991.

Dabberdt, W., Lenschow, D., Horst, T., Zimmerman, P., Oncley, S., and Delany, A.: Atmosphere-surface exchange measurements, Science, 260, 1472–1481, 1993.

Derwent, R., Simmonds, P., Manning, A., and Spain, T.: Trends over a 20-year period from 1987 to 2007 in surface ozone at the atmospheric research station, Mace Head, Ireland, Atmospheric Environment, 41, 9091–9098, 2007.

Dore, S., Montes-Helu, M., Hart, S. C., Hungate, B. A., Koch, G. W., Moon, J. B., Finkral, A. J., and Kolb, T. E.: Recovery of ponderosa pine ecosystem carbon and water fluxes from thinning and stand-replacing fire, Global Change Biology, 18, 3171–3185, 2012.

Duyzer, J., Meyer, G., and van Aalst, R.: Measurement of dry deposition velocities of NO, NO_2 and O_3 and the influence of chemical reactions, Atmospheric Environment, 17, 2117–2120, 1983.

Eder, F., Serafimovich, A., and Foken, T.: Coherent structures at a forest edge: Properties, coupling and impact of secondary circulations, Boundary-Layer Meteorology, 148, 285–308, 2013.

Emberson, L., Ashmore, M., Cambridge, H., Simpson, D., and Tuovinen, J.-P.: Modelling stomatal ozone flux across Europe, Environmental Pollution, 109, 403–413, 2000.

Erisman, J. W. and Draaijers, G.: Deposition to forests in Europe: most important factors influencing dry deposition and models used for generalisation, Environmental Pollution, 124, 379–388, 2003.

Ermel, M., Oswald, R., Mayer, J.-C., Moravek, A., Song, G., Beck, M., Meixner, F., and Trebs, I.: Preparation methods to optimize the performance of sensor discs for fast chemiluminescence ozone analyzers, Environmental Science & Technology, 47, 1930–1936, 2013.

Eugster, W. and Senn, W.: A cospectral correction model for measurement of turbulent NO_2 flux, Boundary-Layer Meteorology, 74, 321–340, 1995.

Falge, E., Graber, W., Siegwolf, R., and Tenhunen, J.: A model of the gas exchange response of Picea abies to habitat conditions, Trees, 10, 277–287, 1996.

Falge, E., Ryel, R. J., Alsheimer, M., and Tenhunen, J.: Effects of stand structure and physiology on forest gas exchange: a simulation study for Norway spruce, Trees, 11, 436–448, 1997.

Farquhar, G. and Von Caemmerer, S.: Modelling of photosynthetic response to environmental conditions, in: Physiological Plant Ecology II, pp. 549–587, Springer, 1982.

Farquhar, G., von Caemmerer, S. v., and Berry, J.: A biochemical model of photosynthetic CO_2 assimilation in leaves of C_3 species, Planta, 149, 78–90, 1980.

Finkelstein, P. L. and Sims, P. F.: Sampling error in eddy correlation flux measurements, Journal of Geophysical Research, 106, 3503–3509, 2001.

Foken, T.: Der Bayreuther Turbulenzknecht, Arbeitsergebnisse, University of Bayreuth, Dept. of Micrometeorology, 1999.

Foken, T.: Micrometeorology, Springer, 2008.

Foken, T. and Wichura, B.: Tools for quality assessment of surface-based flux measurements, Agricultural and Forest Meteorology, 78, 83–105, 1996.

Foken, T., Skeib, G., and Richter, S.: Dependence of the integral turbulence characteristics on the stability of stratification and their use for Doppler-Sodar measurements, Z. Meteorol., 41, 1991.

Foken, T., Dlugi, R., and Kramm, G.: On the determination of dry deposition and emission of gaseous compounds at the biosphere-atmosphere interface, Meteorologische Zeitschrift, 4, 91–118, 1995.

Foken, T., Meixner, F., Falge, E., Zetzsch, C., Serafimovich, A., Bargsten, A., Behrendt, T., Biermann, T., Breuninger, C., Dix, S., et al.: ExchanGE processes in mountainous Regions (EGER)–overview of design, methods, and first results., Atmospheric Chemistry and Physics Discussions, 11, 2011.

Foken, T., Meixner, F., Falge, E., Zetzsch, C., Serafimovich, A., Bargsten, A., Behrendt, T., Biermann, T., Breuninger, C., Dix, S., et al.: Coupling processes and exchange of energy and reactive and non-reactive trace gases at a forest site–results of the EGER experiment, Atmospheric Chemistry and Physics, 12, 1923–1950, 2012.

Forster, P., Ramaswamy, V., Artaxo, P., Berntsen, T., Betts, R., Fahey, D. W., Haywood, J., Lean, J., Lowe, D. C., Myhre, G., et al.: Changes in atmospheric constituents and in radiative forcing. Chapter 2, in: Climate Change 2007. The Physical Science Basis, Cambridge University Press, Cambridge, United Kingdom and New York, NY, USA, 2007.

Fowler, D., Flechard, C., Cape, J. N., Storeton-West, R. L., and Coyle, M.: Measurements of ozone deposition to vegetation quantifying the flux, the stomatal and non-stomatal components, Water, Air, and Soil Pollution, 130, 63–74, 2001.

Fuentes, J., Gillespie, T., Den Hartog, G., and Neumann, H.: Ozone deposition onto a deciduous forest during dry and wet conditions, Agricultural and Forest Meteorology, 62, 1–18, 1992.

Fuhrer, J.: Ozone risk for crops and pastures in present and future climates, Naturwissenschaften, 96, 173–194, 2009.

Gallagher, M., Beswick, K., and Coe, H.: Ozone deposition to coastal waters, Quarterly Journal of the Royal Meteorological Society, 127, 539–558, 2001.

Ganzeveld, L. and Lelieveld, J.: Dry deposition parameterization in a chemistry general circulation model and its influence on the distribution of reactive trace gases, Journal of Geophysical Research, 100, 20 999–21, 1995.

Ganzeveld, L. and Lelieveld, J.: Impact of Amazonian deforestation on atmospheric chemistry, Geophysical Research Letters, 31, 2004.

Ganzeveld, L., Lelieveld, J., and Roelofs, G.-J.: A dry deposition parameterization for sulfur oxides in a chemistry and general circulation model, Journal of Geophysical Research, 103, 5679–5694, 1998.

Ganzeveld, L., Lelieveld, J., Dentener, F., Krol, M., Bouwman, A., and Roelofs, G.-J.: Global soil-biogenic NO_x emissions and the role of canopy processes, Journal of Geophysical Research, 107, 4298, 2002a.

Ganzeveld, L., Lelieveld, J., Dentener, F., Krol, M., and Roelofs, G.-J.: Atmosphere-biosphere trace gas exchanges simulated with a single-column model, Journal of Geophysical Research, 107, 4297, 2002b.

Ganzeveld, L., Bouwman, L., Stehfest, E., van Vuuren, D. P., Eickhout, B., and Lelieveld, J.: Impact of future land use and land cover changes on atmospheric chemistry-climate interactions, Journal of Geophysical Research, 115, 2010.

Gerosa, G., Marzuoli, R., Cieslik, S., and Ballarin-Denti, A.: Stomatal ozone fluxes over a barley field in Italy. "Effective exposure" as a possible link between exposure- and flux-based approaches, Atmospheric Environment, 38, 2421–2432, 2004.

Goldstein, A., McKay, M., Kurpius, M., Schade, G., Lee, A., Holzinger, R., and Rasmussen, R.: Forest thinning experiment confirms ozone deposition to forest canopy is dominated by reaction with biogenic VOCs, Geophysical Research Letters, 31, L22 106, 2004.

Goulden, M. L., Daube, B. C., Fan, S.-M., Sutton, D. J., Bazzaz, A., Munger, J. W., and Wofsy, S. C.: Physiological responses of a black spruce forest to weather, Journal of Geophysical Research, 102, 28 987–28 996, 1997.

Grünhage, L., Haenel, H.-D., and Jäger, H.-J.: The exchange of ozone between vegetation and atmosphere: micrometeorological measurement techniques and models, Environmental Pollution, 109, 373–392, 2000.

Guenther, A., Hewitt, C. N., Erickson, D., Fall, R., Geron, C., Graedel, T., Harley, P., Klinger, L., Lerdau, M., McKay, W., et al.: A global model of natural volatile organic compound emissions, Journal of Geophysical Research, 100, 8873–8892, 1995.

Guenther, A., Baugh, W., Davis, K., Hampton, G., Harley, P., Klinger, L., Vierling, L., Zimmerman, P., Allwine, E., Dilts, S., et al.: Isoprene fluxes measured by enclosure, relaxed eddy accumulation, surface layer gradient, mixed layer gradient, and mixed layer mass balance techniques, Journal of Geophysical Research, 101, 18 555–18 567, 1996.

Güsten, H., Heinrich, G., Schmidt, R. W., and Schurath, U.: A novel ozone sensor for direct eddy flux measurements, Journal of Atmospheric Chemistry, 14, 73–84, 1992.

Hanisch, F. and Crowley, J.: Ozone decomposition on Saharan dust: an experimental investigation, Atmospheric Chemistry and Physics, 3, 119–130, 2003.

Heck, W. W., Taylor, O., Adams, R., Bingham, G., Miller, J., Preston, E., and Weinstein, L.: Assessment of crop loss from ozone, Journal of the Air Pollution Control Association, 32, 353–361, 1982.

Hicks, B. and McMillen, R.: On the measurement of dry deposition using imperfect sensors and in non-ideal terrain, Boundary-Layer Meteorology, 42, 79–94, 1988.

Hicks, B., Baldocchi, D., Meyers, T., Hosker Jr, R., and Matt, D.: A preliminary multiple resistance routine for deriving dry deposition velocities from measured quantities, Water, Air, and Soil Pollution, 36, 311–330, 1987.

Hojstrup, J.: A statistical data screening procedure, Measurement Science and Technology, 4, 153–157, 1993.

Hollinger, D., Goltz, S., Davidson, E., Lee, J., Tu, K., and Valentine, H.: Seasonal patterns and environmental control of carbon dioxide and water vapour exchange in an ecotonal boreal forest, Global Change Biology, 5, 891–902, 1999.

Horvath, L., Nagy, Z., and Weidinger, T.: Estimation of dry deposition velocities of nitric oxide, sulfur dioxide, and ozone by the gradient method above short vegetation during the tract campaign, Atmospheric Environment, 32, 1317–1322, 1998.

Ibrom, A., Dellwik, E., Flyvbjerg, H., Jensen, N. O., and Pilegaard, K.: Strong low-pass filtering effects on water vapour flux measurements with closed-path eddy correlation systems, Agricultural and Forest Meteorology, 147, 140–156, 2007.

Jarvis, P.: The interpretation of the variations in leaf water potential and stomatal conductance found in canopies in the field, Philosophical Transactions of the Royal Society of London. B, Biological Sciences, 273, 593–610, 1976.

Kaimal, J., Wyngaard, J., Izumi, Y., and Coté, O.: Spectral characteristics of surface-layer turbulence, Quarterly Journal of the Royal Meteorological Society, 98, 563–589, 1972.

Kaimal, J. C. and Finnigan, J. J.: Atmospheric boundary layer flows: their structure and measurement, Oxford University Press, 1994.

Keronen, P., Reissell, A., Rannik, U., Pohja, T., Siivola, E., Hiltunen, V., Hari, P., Kulmala, M., and Vesala, T.: Ozone flux measurements over a Scots pine forest using eddy covariance method: performance evaluation and comparison with flux-profile method, Boreal Environment Research, 8, 425–444, 2003.

Kerstiens, G. and Lendzian, K. J.: Interactions between ozone and plant cuticles, New Phytologist, 112, 21–27, 1989.

Klemm, O. and Mangold, A.: Ozone deposition at a forest site in NE Bavaria, Water, Air, and Soil Pollution: Focus, 1, 223–232, 2001.

Knohl, A., Kolle, O., Minayeva, T. Y., Milyukova, I. M., Vygodskaya, N. N., Foken, T., and Schulze, E.-D.: Carbon dioxide exchange of a Russian boreal forest after disturbance by wind throw, Global Change Biology, 8, 231–246, 2002.

Kolmogorov, A. N.: The local structure of turbulence in incompressible viscous fluid for very large Reynolds numbers, in: Dokl. Akad. Nauk SSSR, vol. 30, pp. 299–303, 1941.

Kraus, H.: Die Atmosphäre der Erde: Eine Einführung in die Meteorologie, Springer, 2004.

Kraus, H.: Grundlagen der Grenzschicht-Meteorologie, Springer, 2008.

Kristensen, L., Mann, J., Oncley, S., and Wyngaard, J.: How close is close enough when measuring scalar fluxes with displaced sensors?, Journal of Atmospheric and Oceanic Technology, 14, 814–821, 1997.

Kurpius, M. R. and Goldstein, A. H.: Gas-phase chemistry dominates O_3 loss to a forest, implying a source of aerosols and hydroxyl radicals to the atmosphere, Geophysical Research Letters, 30, 2003.

Lammel, G.: Formation of nitrous acid: parameterisation and comparison with observations, Max-Planck-Institut für Meteorologie, Hamburg (Germany), 1999.

Launiainen, S., Katul, G. G., Kolari, P., Vesala, T., and Hari, P.: Empirical and optimal stomatal controls on leaf and ecosystem level CO_2 and H_2O exchange rates, Agricultural and Forest Meteorology, 151, 1672–1689, 2011.

Launiainen, S., Katul, G., Grönholm, T., and Vesala, T.: Partitioning ozone fluxes between canopy and forest floor by measurements and a multi-layer model, Agricultural and Forest Meteorology, 173, 85–99, 2013.

Lee, X., Massman, W., and Law, B. E.: Handbook of Micrometeorology: A Guide for Surface Flux Measurement and Analysis, vol. 29, Kluwer Academic Publishers: Springer Science+ Business Media, Inc., 2004.

Lenschow, D. and Raupach, M.: The attenuation of fluctuations in scalar concentrations through sampling tubes, Journal of Geophysical Research, 96, 15 259–15 268, 1991.

Lenschow, D., Mann, J., and Kristensen, L.: How long is long enough when measuring fluxes and other turbulence statistics?, Journal of Atmospheric and Oceanic Technology, 11, 661–673, 1994.

Lenschow, D. H. and Kristensen, L.: Uncorrelated noise in turbulence measurements, Journal of Atmospheric and Oceanic Technology, 2, 68–81, 1985.

Lenschow, D. H., Wulfmeyer, V., and Senff, C.: Measuring second- through fourth-order moments in noisy data, Journal of Atmospheric and Oceanic Technology, 17, 1330–1347, 2000.

Leuning, R. and Judd, M.: The relative merits of open- and closed-path analysers for measurements of eddy fluxes, Global Change Biology, 2, 241–253, 1996.

Leuning, R. and King, K.: Comparison of eddy-covariance measurements of CO_2 fluxes by open- and closed-path CO_2 analysers, Boundary-Layer Meteorology, 59, 297–311, 1992.

Leuning, R. and Moncrieff, J.: Eddy-covariance CO_2 flux measurements using open- and closed-path CO_2 analysers: corrections for analyser water vapour sensitivity and damping of fluctuations in air sampling tubes, Boundary-Layer Meteorology, 53, 63–76, 1990.

Leuning, R., Neumann, H., and Thurtell, G.: Ozone uptake by corn (*Zea mays* L.): a general approach, Agricultural Meteorology, 20, 115–135, 1979.

Lindauer, M., Schmid, H., Grote, R., Mauder, M., Steinbrecher, R., and Wolpert, B.: Net ecosystem exchange over a non-cleared wind-throw-disturbed upland spruce forest–Measurements and simulations, Agricultural and Forest Meteorology, 197, 219–234, 2014.

Loescher, H. W., Oberbauer, S. F., Gholz, H., and Clark, D. B.: Environmental controls on net ecosystem-level carbon exchange and productivity in a Central American tropical wet forest, Global Change Biology, 9, 396–412, 2003.

Mammarella, I., Launiainen, S., Gronholm, T., Keronen, P., Pumpanen, J., Rannik, Ü., and Vesala, T.: Relative humidity effect on the high-frequency attenuation of water vapor flux measured by a closed-path eddy covariance system, Journal of Atmospheric and Oceanic Technology, 26, 1856–1866, 2009.

Massman, W.: Partitioning ozone fluxes to sparse grass and soil and the inferred resistances to dry deposition, Atmospheric Environment. Part A. General Topics, 27, 167–174, 1993.

Massman, W.: Toward an ozone standard to protect vegetation based on effective dose: a review of deposition resistances and a possible metric, Atmospheric Environment, 38, 2323–2337, 2004.

Massman, W. and Ibrom, A.: Attenuation of concentration fluctuations of water vapor and other trace gases in turbulent tube flow, Atmospheric Chemistry and Physics, 8, 6245–6259, 2008.

Massman, W., MacPherson, J., Delany, A., Den Hartog, G., Neumann, H., Oncley, S., Pearson Jr, R., Pederson, J., and Shaw, R.: Surface conductances for ozone uptake derived from aircraft eddy correlation data, Atmospheric Environment, 29, 3181–3188, 1995.

Massman, W. J.: The attenuation of concentration fluctuations in turbulent flow through a tube, Journal of Geophysical Research, 96, 15 269–15 273, 1991.

Massman, W. J.: A simple method for estimating frequency response corrections for eddy covariance systems, Agricultural and Forest Meteorology, 104, 185–198, 2000.

Mauder, M. and Foken, T.: Documentation and instruction manual of the eddy covariance software package TK3, Arbeitsergebnisse, University of Bayreuth, Dept. of Micrometeorology, 2011.

Mauder, M., Foken, T., Clement, R., Elbers, J., Eugster, W., Grünwald, T., Heusinkveld, B., Kolle, O., et al.: Quality control of CarboEurope flux data? Part 2: Inter-comparison of eddy-covariance software, Biogeosciences, 5, 451–462, 2008.

Mauder, M., Cuntz, M., Drüe, C., Graf, A., Rebmann, C., Schmid, H. P., Schmidt, M., and Steinbrecher, R.: A strategy for quality and uncertainty assessment of long-term eddy-covariance measurements, Agricultural and Forest Meteorology, 169, 122–135, 2013.

McMillen, R. T.: An eddy correlation technique with extended applicability to non-simple terrain, Boundary-Layer Meteorology, 43, 231–245, 1988.

Meyers, T. P.: The sensitivity of modeled SO_2 fluxes and profiles to stomatal and boundary layer resistances, Water, Air, and Soil Pollution, 35, 261–278, 1987.

Meyers, T. P., Finkelstein, P., Clarke, J., Ellestad, T. G., and Sims, P. F.: A multilayer model for inferring dry deposition using standard meteorological measurements, Journal of Geophysical Research, 103, 22 645–22 661, 1998.

Mikkelsen, T. N., Ro-Poulsen, H., Pilegaard, K., Hovmand, M., Jensen, N., Christensen, C., and Hummelshøj, P.: Ozone uptake by an evergreen forest canopy: temporal variation and possible mechanisms, Environmental Pollution, 109, 423–429, 2000.

Mikkelsen, T. N., Ro-Poulsen, H., Hovmand, M. F., Jensen, N. O., Pilegaard, K., and Egeløv, A. H.: Five-year measurements of ozone fluxes to a Danish Norway spruce canopy, Atmospheric Environment, 38, 2361–2371, 2004.

Moncrieff, J. B., Massheder, J., De Bruin, H., Elbers, J., Friborg, T., Heusinkveld, B., Kabat, P., Scott, S., Søgaard, H., and Verhoef, A.: A system to measure surface fluxes of momentum, sensible heat, water vapour and carbon dioxide, Journal of Hydrology, 188, 589–611, 1997.

Monks, P. S.: Gas-phase radical chemistry in the troposphere, Chemical Society Reviews, 34, 376–395, 2005.

Moore, C.: Frequency response corrections for eddy correlation systems, Boundary-Layer Meteorology, 37, 17–35, 1986.

Moravek, A., Trebs, I., and Foken, T.: Effect of imprecise lag time and high-frequency attenuation on surface-atmosphere exchange fluxes determined with the relaxed eddy accumulation method, Journal of Geophysical Research, 118, 10–210, 2013.

Muller, J., Percival, C., Gallagher, M., Fowler, D., Coyle, M., and Nemitz, E.: Sources of uncertainty in eddy covariance ozone flux measurements made by dry chemiluminescence fast response analysers, Atmospheric Measurement Techniques, 3, 163–176, 2010.

Nikolov, N. and Zeller, K. F.: Modeling coupled interactions of carbon, water, and ozone exchange between terrestrial ecosystems and the atmosphere. I: Model description, Environmental Pollution, 124, 231–246, 2003.

Nikolov, N. T., Massman, W. J., and Schoettle, A. W.: Coupling biochemical and biophysical processes at the leaf level: an equilibrium photosynthesis model for leaves of C_3 plants, Ecological Modelling, 80, 205–235, 1995.

Norman, J.: Modeling the complete crop canopy, in: Modification of the Aerial Environment of Crops, pp. 249–280, American Society of Agricultural Engineers Michigan, 1979.

Panofsky, H. A. and Dutton, J. A.: Atmospheric turbulence. Models and methods for engineering applications, 1984.

Pearson Jr, R.: Measuring ambient ozone with high sensitivity and bandwidth, Review of Scientific Instruments, 61, 907–916, 1990.

Philip, J.: The theory of dispersal during laminar flow in tubes. I., Australian Journal of Physics, 16, 287–299, 1963a.

Philip, J.: The theory of dispersal during laminar flow in tubes. II., Australian Journal of Physics, 16, 300–310, 1963b.

Pilegaard, K.: Air–soil exchange of NO, NO_2 and O_3 in forests, Water, Air, and Soil Pollution: Focus, 1, 79–88, 2001.

Pilegaard, K., Jensen, N., and Hummelshøj, P.: Seasonal and diurnal variation in the deposition velocity of ozone over a spruce forest in Denmark, Water, Air, and Soil Pollution, 85, 2223–2228, 1995.

Pilegaard, K., Hummelshøj, P., and Jensen, N.: Fluxes of ozone and nitrogen dioxide measured by Eddy correlation over a harvested wheat field, Atmospheric Environment, 32, 1167–1177, 1998.

Pyles, R. D.: The development and testing of the UCD Advanced Canopy-Atmosphere-Soil Algorithm (ACASA) for use in climate prediction and field studies, Ph.D. thesis, UC Davis, 2000.

Pyles, R. D., Weare, B. C., and Pawu, K. T.: The UCD Advanced Canopy-Atmosphere-Soil Algorithm: Comparisons with observations from different climate and vegetation regimes, Quarterly Journal of the Royal Meteorological Society, 126, 2951–2980, 2000.

Reich, P. B.: Quantifying plant response to ozone: a unifying theory, Tree Physiology, 3, 63–91, 1987.

Reich, P. B. and Amundson, R. G.: Ambient levels of ozone reduce net photosynthesis in tree and crop species, Science, 230, 566–570, 1985.

Rinne, H., Guenther, A., Warneke, C., De Gouw, J., and Luxembourg, S.: Disjunct eddy covariance technique for trace gas flux measurements, Geophysical Research Letters, 28, 3139–3142, 2001.

Roelofs, G.-J. and Lelieveld, J.: Tropospheric ozone simulation with a chemistry-general circulation model: Influence of higher hydrocarbon chemistry, Journal of Geophysical Research, 105, 22 697–22 712, 2000.

Rummel, U., Ammann, C., Kirkman, G., Moura, M., Foken, T., Andreae, M., and Meixner, F.: Seasonal variation of ozone deposition to a tropical rain forest in southwest Amazonia, Atmospheric Chemistry and Physics, 7, 5415–5435, 2007.

Runkle, B. R., Wille, C., Gažovič, M., and Kutzbach, L.: Attenuation correction procedures for water vapour fluxes from closed-path eddy-covariance systems, Boundary-Layer Meteorology, 142, 401–423, 2012.

Running, S. W.: Ecosystem disturbance, carbon, and climate, Science, 321, 652–653, 2008.

Sandermann Jr, H.: Ozone and plant health, Annual Review of Phytopathology, 34, 347–366, 1996.

Schmid, S., Thürig, E., Kaufmann, E., Lischke, H., and Bugmann, H.: Effect of forest management on future carbon pools and fluxes: A model comparison, Forest Ecology and Management, 237, 65–82, 2006.

Schurath, U., Speuser, W., and Schmidt, R.: Principle and application of a fast sensor for atmospheric ozone, Fresenius' Journal of Analytical Chemistry, 340, 544–547, 1991.

Sehested, K., Corfitzen, H., Holcman, J., Fischer, C. H., and Hart, E. J.: The primary reaction in the decomposition of ozone in acidic aqueous solutions, Environmental Science & Technology, 25, 1589–1596, 1991.

Seidl, R., Rammer, W., Jäger, D., and Lexer, M. J.: Impact of bark beetle (*Ips typographus* L.) disturbance on timber production and carbon sequestration in different management strategies under climate change, Forest Ecology and Management, 256, 209–220, 2008.

Seidl, R., Schelhaas, M.-J., and Lexer, M. J.: Unraveling the drivers of intensifying forest disturbance regimes in Europe, Global Change Biology, 17, 2842–2852, 2011.

Sellers, P., Mintz, Y., Sud, Y. e. a., and Dalcher, A.: A simple biosphere model (SiB) for use within general circulation models, Journal of the Atmospheric Sciences, 43, 505–531, 1986.

Serafimovich, A., Siebicke, L., Staudt, K., Lüers, J., Biermann, T., Schier, S., and Foken, T.: ExchanGE processes in mountainous Regions (EGER) Documentation of the Intensive Observation Period (IOP1) September, 6th to October, 7th 2007, Arbeitsergebnisse, University of Bayreuth, Dept. of Micrometeorology, 2008a.

Serafimovich, A., Siebicke, L., Staudt, K., Lüers, J., Hunner, M., Gerken, T., Schier, S., Biermann, T., Rütz, F., and Buttlar, J. v.: ExchanGE processes in mountainous Regions (EGER) Documentation of the Intensive Observation Period (IOP2) June, 1st to July, 15th 2008, Arbeitsergebnisse, University of Bayreuth, Dept. of Micrometeorology, 2008b.

Serafimovich, A., Eder, F., Hübner, J., Falge, E., Voß, L., Sörgel, M., Held, A., Liu, Q., Eigenmann, R., Huber, K., Ferro Duarte, H., Werle, P., Gast, E., Cieslik, S., Heping, L., and Foken, T.: ExchanGE processes in mountainous Regions (EGER) Documentation of the Intensive Observation Period (IOP3) June, 13th to July, 26th 2011, Arbeitsergebnisse, University of Bayreuth, Dept. of Micrometeorology, 2011.

Simpson, D., Tuovinen, J.-P., Emberson, L., and Ashmore, M.: Characteristics of an ozone deposition module II: Sensitivity analysis, Water, Air, and Soil Pollution, 143, 123–137, 2003.

Smirnova, T. G., Brown, J. M., and Benjamin, S. G.: Performance of different soil model configurations in simulating ground surface temperature and surface fluxes, Monthly Weather Review, 125, 1870–1884, 1997.

Smirnova, T. G., Brown, J. M., Benjamin, S. G., and Kim, D.: Parameterization of cold-season processes in the MAPS land-surface scheme, Journal of Geophysical Research, 105, 4077–4086, 2000.

Solomon, S., Qin, D., Manning, M., Chen, Z., Marquis, M., Averyt, K., Tignor, M., and Miller, H. L.: Climate change 2007: the physical science basis. Contribution of working group I to the fourth assessment report of the intergovernmental panel on climate change, Cambridge University Press, Cambridge, United Kingdom and New York, NY, USA, 2007.

Sorimachi, A., Sakamoto, K., Ishihara, H., Fukuyama, T., Utiyama, M., Liu, H., Wang, W., Tang, D., Dong, X., and Quan, H.: Measurements of sulfur dioxide and ozone dry deposition over short vegetation in northern China–a preliminary study, Atmospheric Environment, 37, 3157–3166, 2003.

Spathelf, P., van der Maaten, E., van der Maaten-Theunissen, M., Campioli, M., and Dobrowolska, D.: Climate change impacts in European forests: the expert views of local observers, Annals of Forest Science, 71, 131–137, 2014.

Stewart, J.: Modelling surface conductance of pine forest, Agricultural and Forest Meteorology, 43, 19–35, 1988.

Stier, P., Feichter, J., Kinne, S., Kloster, S., Vignati, E., Wilson, J., Ganzeveld, L., Tegen, I., Werner, M., Balkanski, Y., et al.: The aerosol-climate model ECHAM5-HAM, Atmospheric Chemistry and Physics, 5, 1125–1156, 2005.

Stull, R. B.: An introduction to boundary layer meteorology, vol. 13, Springer, 1988.

Su, H.-B., Paw U, K. T., and Shaw, R. H.: Development of a coupled leaf and canopy model for the simulation of plant-atmosphere interaction, Journal of Applied Meteorology, 35, 733–748, 1996.

Taylor, G.: Dispersion of soluble matter in solvent flowing slowly through a tube, Proceedings of the Royal Society of London. Series A. Mathematical and Physical Sciences, 219, 186–203, 1953.

Taylor, G.: The dispersion of matter in turbulent flow through a pipe, Proceedings of the Royal Society of London. Series A. Mathematical and Physical Sciences, 223, 446–468, 1954.

Tenhunen, J., Hanano, R., Abril, M., Weiler, E., and Hartung, W.: Above- and below-ground environmental influences on leaf conductance of *Ceanothus thyrsiflorus* growing in a chaparral environment: drought response and the role of abscisic acid, Oecologia, 99, 306–314, 1994.

Thomas, C. and Foken, T.: Organised motion in a tall spruce canopy: temporal scales, structure spacing and terrain effects, Boundary-Layer Meteorology, 122, 123–147, 2007.

Tuovinen, J.-P., Aurela, M., and Laurila, T.: Resistances to ozone deposition to a flark fen in the northern aapa mire zone, Journal of Geophysical Research, 103, 16 953–16 966, 1998.

Tuovinen, J.-P., Simpson, D., Mikkelsen, T. N., Emberson, L., Ashmore, M., Aurela, M., Cambridge, H., Hovmand, M., Jensen, N., Laurila, T., et al.: Comparisons of measured and modelled ozone deposition to forests in Northern Europe, Water, Air, and Soil Pollution: Focus, 1, 263–274, 2001.

Vickers, D. and Mahrt, L.: Fetch limited drag coefficients, Boundary-Layer Meteorology, 85, 53–79, 1997.

Webb, E. K., Pearman, G. I., and Leuning, R.: Correction of flux measurements for density effects due to heat and water vapour transfer, Quarterly Journal of the Royal Meteorological Society, 106, 85–100, 1980.

Weiss, A. and Norman, J.: Partitioning solar radiation into direct and diffuse, visible and near-infrared components, Agricultural and Forest Meteorology, 34, 205–213, 1985.

Wesely, M.: Parameterization of surface resistances to gaseous dry deposition in regional-scale numerical models, Atmospheric Environment, 23, 1293–1304, 1989.

Wesely, M. and Hicks, B.: A review of the current status of knowledge on dry deposition, Atmospheric Environment, 34, 2261–2282, 2000.

Wesely, M., Sisterson, D., and Jastrow, J.: Observations of the chemical properties of dew on vegetation that affect the dry deposition of SO_2, Journal of Geophysical Research, 95, 7501–7514, 1990.

WHO: Health Aspects of Air Pollution with Particulate Matter, Ozone and Nitrogen Dioxide: Report on a WHO Working Group; Bonn, Germany, World Health Organization, Regional Office for Europe, 2003.

Wilczak, J. M., Oncley, S. P., and Stage, S. A.: Sonic anemometer tilt correction algorithms, Boundary-Layer Meteorology, 99, 127–150, 2001.

Williams, C. A., Collatz, G. J., Masek, J., and Goward, S. N.: Carbon consequences of forest disturbance and recovery across the conterminous United States, Global Biogeochemical Cycles, 26, 2012.

Williams, C. A., Vanderhoof, M. K., Khomik, M., and Ghimire, B.: Post-clearcut dynamics of carbon, water and energy exchanges in a midlatitude temperate, deciduous broadleaf forest environment, Global Change Biology, 20, 992–1007, 2014.

Wittig, V. E., Ainsworth, E. A., Naidu, S. L., Karnosky, D. F., and Long, S. P.: Quantifying the impact of current and future tropospheric ozone on tree biomass, growth, physiology and biochemistry: a quantitative meta-analysis, Global Change Biology, 15, 396–424, 2009.

Yanai, R. D., Currie, W. S., and Goodale, C. L.: Soil carbon dynamics after forest harvest: an ecosystem paradigm reconsidered, Ecosystems, 6, 197–212, 2003.

Yienger, J. and Levy, H.: Empirical model of global soil-biogenic NO_x emissions, Journal of Geophysical Research, 100, 11 447–11 464, 1995.

Zahn, A., Weppner, J., Widmann, H., Schlote-Holubek, K., Burger, B., Kühner, T., and Franke, H.: A fast and precise chemiluminescence ozone detector for eddy flux and airborne application, Atmospheric Measurement Techniques, 5, 363–375, 2012.

Zeller, K. and Hehn, T.: Measurements of upward turbulent ozone fluxes above a subalpine spruce-fir forest, Geophysical Research Letters, 23, 841–844, 1996.

Zeller, K. and Nikolov, N.: Quantifying simultaneous fluxes of ozone, carbon dioxide and water vapor above a subalpine forest ecosystem, Environmental Pollution, 107, 1–20, 2000.

Zeller, K., Massman, W., Stocker, D., Fox, D. G., Stedman, D., and Hazlett, D.: Initial results from the Pawnee eddy correlation system for dry acid deposition research, United States Department of Agriculture (USDA), Forest Service, RM-282, 1989.

Zhu, Z.: Turbulent ozone fluxes and ozone deposition velocities within and above a spruce forest (Waldstein/Fichtelgebirge), Geophysical Research Abstracts 10, EGU2008-A-04768, 2008.

Acknowledgment

Regarding privacy laws, the acknowledgment was removed from the online version.